TOPOLOGICAL DEFECTS IN CONFINED NEMATIC LIQUID CRYSTAL SYSTEMS AND THE TRANSITIONS BETWEEN THEM

A Dissertation
Presented to
The Academic Faculty

By

Shengnan Huang

In Partial Fulfillment
of the Requirements for the Degree
Doctor of Philosophy in the
School of Physics

Georgia Institute of Technology

August 2019

TOPOLOGICAL DEFECTS IN CONFINED NEMATIC LIQUID CRYSTAL SYSTEMS AND THE TRANSITIONS BETWEEN THEM

Approved by:

Dr. Paul M. Goldbart, Advisor
Department of Physics
The University of Texas at Austin

Dr. Elisabetta Matsumoto
School of Physics
Georgia Institute of Technology

Dr. Kurt Wiesenfeld
School of Physics
Georgia Institute of Technology

Dr. Peter Yunker
School of Physics
Georgia Institute of Technology

Dr. Haomin Zhou
School of Mathematics
Georgia Institute of Technology

Date Approved: April 29, 2019

Strive to enter through the narrow door.

Luke 13:24 ESV

(also quoted in "La Porte Étroite" by André Gide)

To my parents.

ACKNOWLEDGEMENTS

First and foremost, I would like to express my deepest gratitude to my advisor Prof. Paul Goldbart. His profound knowledge in both physics and mathematics has expanded my horizons greatly; and his quick mind and deep insights have inspired me constantly. I am deeply grateful to his patience with me, especially during my first two years: when I was dazzled by the deep concepts and difficult calculations in the vulcanization theory invented by him, he provided me with detailed explanations and helped me through tedious calculations. I appreciate that Paul has encouraged me to pursue my research interests, and that many times he patiently listened to my crazy ideas and steered me into the right directions. Moreover, I am grateful to the financial support he has allocated to me over the years.

I would also like to express my gratitude and thanks to Prof. Alberto Fernandez-Nieves for letting me attend his group meetings and providing me with the research topic which eventually became my thesis topic. It was a great pleasure to work with his group members Jayalakshmi Vallamkondu and Perry Ellis, who patiently explained their experiments and generously offered their experimental data.

I would like to thank my group members Fangfu Ye, Bing-Sui Lu, Anton Souslov, Rafael Hipolito, Benjamin Loewe, Michael Dimitriyev and Boli Zhou. Especially, Fangfu Ye and Bing-Sui Lu helped me enormously when I got started with research in my first year.

It has been my great fortune to attend lectures by many excellent professors at Georgia Tech and thus have the access to a wide range of perspectives. Special thanks go to Prof. Kurt Wiesenfeld, Prof. Christopher Heil, Prof. Galyna Livshyts, Prof. Predrag Cvitanović, Prof. Shina Tan, Prof. Roman Grigoriev, Prof. Michael Pustilnik, Prof. Zhigang Jiang, Prof. Matt Baker, Prof. Kirsten Wickelgren, Prof. Igor Belegradek, Prof. Joseph Rabinoff, Prof. Andrzej Swiech. The skills I acquired from them have helped me explore my research from different angles. Also, I would like to thank Jane Chisholm from the Language Institute for her encouragement and the wonderful course she designed.

I am deeply grateful to Prof. Andrew Zangwill and Prof. David Ballantyne for their commitment and dedication to graduate students. I am also grateful to Prof. James Sowell for his dedication to graduate admissions. I would like to thank Chinneta Willis for helping me making numerous appointments with Paul. I would also like to thank Dr. Hang Chen for his hospitality when I first came to Atlanta.

I feel fortunate to have received training from Emily Alicea-Munoz to be a teaching assistant. I would like to thank Suo Yang for great advice on graduate courses, and Prof. Haomin Zhou for career advice.

I am also thankful to many friends who are working or have worked here as physics graduate students: Di Chen, Zhe Guang, Yuxuan Jiang, Xi Lv, Shangguo Zhu and Shengkai Li, for the discussions about homework and research.

I would like to thank Adam Kamor and Simon Berman for being wonderful officemates. And I believe, if there were elections of the spokespersons for the office W503 in Howey, they would be the ones we would choose.

Also, I consider myself very lucky for always having wonderful roommates (lots of them were great chefs, in my opinion). In particular, Lu Xu, as one of my very first roommates, offered me a great deal of help during my first two years at Atlanta. He and another roommate Liren Xu drove me to grocery store, and took me to the weekly dinners with their friends from the School of Chemical & Biomolecular Engineering. Then, years later, I was fortunate to have Jiangtao Wu and Xiaona Li as my great roommates and friends.

I would like to thank Han Li and Xiuli Sun who used to live in the same building with me (at that time Han Li was also my officemate). They helped me go through the tough times in 2013 and sometimes carried on the "duty" of taking me to grocery store (I regret being too dependent). I would also like to thank Xiaofeng Shi who used to live in the same community with me. He always gave me honest advice, whether I liked it or not, and he took me to the hospital when I had a high fever in the summer of 2014.

From May 2012 to January 2014, I commuted to and from school by Bus Route 26. It was my great pleasure to meet bus drivers everyday. They were the nicest people I have ever seen in Atlanta. They were professional, sympathetic and cheerful, always creating a welcoming vibe. How nice to meet them at the beginning and end of a workday!

I owe a debt of gratitude to my parents who have made every effort to make sure I received a good education. They haven't seen me in person for many years; they have never put any pressure on me and always encouraged me to pursue the career that I liked.

Last, I would like to thank my decayed wisdom tooth, which got pulled out in March 2018. *Without it*, I immediately experienced months of happy research with constant inspirations, as if my wisdom was refilled. Now, with three other wisdom teeth waiting to make sacrifice, my future as a researcher looks promising (*starry-eyed*).

TABLE OF CONTENTS

LIST OF FIGURES

SUMMARY

The major theme of this thesis is the treatment of defect cores in uniaxial nematic liquid crystals. For simplicity, we prefer the Oseen-Frank formalism, where the orientational order of the uniaxial nematics is represented by unit vectors with head-tail symmetry. However, the defect core in this formalism is a tiny region where the unit vectors are not defined. This implies that when we evaluate the Oseen-Frank free-energy functional and solve the corresponding Euler-Lagrange equation, we should not admit differentiation and integration cross the defect core. In fact, we should either treat the defect core as a boundary or put it at the coordinate singularity of a special coordinate system. The first treatment is used in our numerical study of the defect transitions in the nematic bridges. The finite-difference method (with the use of the successive over-relaxation method) enables us to select the ground state after exhausting many possible defect structures. Our results confirm the existence of different types of equilibrium defect structures in the cylindrical bridge. Our results further imply that some different shapes of the lateral surfaces preserve the qualitative features of the defect structure diagram yet they can change the positions of the transition lines.

However, the above-mentioned two treatments impede a general analytical theory of defects in nematics since they usually require exhaustive search or special geometries. Therefore, a better treatment may be to create the defect core during the calculation process. To test its feasibility, we conduct a numerical experiment by designing a special multigrid method for the study of equilibrium defect structures in the cylindrical bridge, where the crudest information of the defect core is expected to be contained on the coarsest grid and better information of the defect core is expected to be contained on the finer grid. Then, for the analytical study, we first experiment on the one-dimensional analog, where the solution is represented by Fourier series and the defect core is the jump discontinuity. We observe that the correct energy function can be obtained by properly eliminating an infinitely large

part, and the resulting regularized energy function is equally effective with a finite number of its Fourier modes for the purpose of determining the equilibrium state. Based on that, some calculations are performed for two-dimensional nematics. We speculate that a finite number of Fourier modes of the regularized energy function may be enough to determine the equilibrium defect structures in nematics.

CHAPTER 1

INTRODUCTION AND BACKGROUND

1.1 Liquid Crystal and its Order Parameter

Liquid crystals, whose basic microscopic components are rod-like or disc-like molecules, exhibit unusual emergent phenomena in which spatial and orientational correlations present over short distances may or may not fade away at large distances. In this sense, they are partially reminiscent of liquids and solids. Distinct phases of liquid crystals include isotropic, nematic, cholesteric, smectic and columnar. As a result of their different types of ordering, they have distinctive elastic, electric and optical properties; see Refs. [1–4].

Liquid crystal phases, such as isotropic and nematic, whose translational symmetry is maintained while the rotational symmetry may or may not be broken, can be characterized by the order parameter $\mathbf{Q}$, which is a symmetric traceless tensor and can be represented by a 3×3 matrix diagonalized as

$$\mathbf{Q} = \frac{1}{3}\begin{bmatrix} 2S_1 - S_2 & 0 & 0 \\ 0 & -S_1 - S_2 & 0 \\ 0 & 0 & -S_1 + 2S_2 \end{bmatrix}, \tag{1.1}$$

where S_1 and S_2 are scalars; see Refs. [1, 5, 6]. If the system is in the isotropic phase then $\mathbf{Q} = 0$, i.e., $S_1 = S_2 = 0$. If it is in the uniaxial nematic phase then $S_1 \neq 0$, $S_2 = 0$, and $\mathbf{Q}$ simplifies to

$$\mathbf{Q} = S\,(\mathbf{n} \otimes \mathbf{n} - \frac{1}{3}\mathbf{I}), \tag{1.2}$$

and in terms of Cartesian coordinate, it becomes

$$Q_{ij} = S\,(n_i\,n_j - \frac{1}{3}\delta_{ij}), \tag{1.3}$$

where i, j are Cartesian indices, δ_{ij} is the Kronecker delta, S is a scalar, and $\mathbf{n}$ is a unit vector, also known as the director [1]. The scalar S is a second moment average of the distribution of the orientations of the molecules near some particular spatial point $\mathbf{r}$ and is defined as

$$S(\mathbf{r}) = \frac{1}{2}\langle 3\cos^2\theta - 1\rangle = \frac{1}{2}\int (3\cos^2\theta - 1) f(\theta, \mathbf{r}) \mathrm{d}\theta, \tag{1.4}$$

where $\langle\cdots\rangle$ is a statistical-mechanical average, θ is the angle between $\mathbf{n}$ and the orientation of each molecule, and $f(\theta, \mathbf{r})$ is the distribution of the θ near the point $\mathbf{r}$, which satisfies $f(\theta, \mathbf{r}) = f(\pi - \theta, \mathbf{r})$ because $\mathbf{n}$ and $-\mathbf{n}$ represent the same local direction of molecular alignment (i.e., head-tail symmetry). If the molecules are fully oriented in some particular direction then $S = 1$; if the molecules are fully randomly oriented in 3-dimensional space (so that the system is in an isotropic phase) then $S = 0$; and if the molecules are fully randomly oriented in an 2-dimensional plane perpendicular to some axis then $S = -1/2$; see Refs. [1, 5].

If the system is, however, in the *biaxial* nematic phase then $S_1 \neq 0$ and $S_2 \neq 0$. Equation (1.1) can be written compactly as

$$\mathbf{Q} = S_1\, \mathbf{n} \otimes \mathbf{n} + S_2\, \mathbf{m} \otimes \mathbf{m} - \frac{1}{3}(S_1 + S_2)\, \mathbf{I}, \tag{1.5}$$

or equivalently,

$$Q_{ij} = S_1\, n_i\, n_j + S_2\, m_i\, m_j - \frac{1}{3}(S_1 + S_2)\, \delta_{ij}, \tag{1.6}$$

where $\mathbf{m}$ is a unit vector perpendicular to $\mathbf{n}$ [5].

1.2 Isotropic-Nematic Phase Transition

In the Landau-de Gennes formalism, when the temperature of the system is close to the isotropic-nematic transition temperature, the bulk free energy density $\mathcal{F}_b$ can be expanded in terms of (a) powers of $\mathbf{Q}$, and (b) gradients of $\mathbf{Q}$. This is because the order parameter $\mathbf{Q}$ is typically rather small despite the discontinuous character of the transition, and the gradients of $\mathbf{Q}$ represents the small energy cost due to the long-wavelength spatial distortion of the spatially uniform equilibrium states [1]. To determine the spatially uniform equilibrium states below and above the transition point, we can ignore the gradients of $\mathbf{Q}$ and express $\mathcal{F}_b$ as

$$\mathcal{F}_b = \frac{3}{2}a(T - T^*)\,\mathrm{Tr}(\mathbf{Q}^2) - \frac{9}{2}b\mathrm{Tr}(\mathbf{Q}^3) + \frac{9}{4}c\mathrm{Tr}(\mathbf{Q}^4), \tag{1.7}$$

where a, b, c and T^* are approximately independent of temperature and pressure. $\mathcal{F}_b$ is known as the Landau-de Gennes free-energy density; see Refs. [5, 7].

If we assume that the nematic phase is uniaxial, then Eq. (1.7) becomes [by using Eq. (1.2)]

$$\mathcal{F}_b = a(T - T^*)S^2 - bS^3 + cS^4. \tag{1.8}$$

At the transition temperature $T_p = T^* + b^2/ac$, the scalar S has the value $S_p = b/2c$. For the common nematic material 5CB, one has $a \approx 5.2 \times 10^4 \mathrm{Jm}^{-3}\mathrm{K}^{-1}$, $b \approx 5.3 \times 10^5 \mathrm{Jm}^{-3}$, $c \approx 9.7 \times 10^5 \mathrm{Jm}^{-3}$, $T^* \approx 307.55\mathrm{K}$, and $T_p \approx 308.94\mathrm{K}$, $S_c \approx 0.27$ [8–10].

1.3 Elasticity of the Uniaxial Nematic Phase in the Low-Temperature Regime

In the Landau-de Gennes formalism, the distortion free-energy density $\mathcal{F}_d$ is part of the free energy density composed of the lowest gradients of $\mathbf{Q}$ that are symmetry-invariant. For the uniaxial or biaxial nematic state, $\mathcal{F}_b$ can be expressed as

$$\mathcal{F}_d = \frac{L_1}{2}\Big(\frac{\partial Q_{ij}}{\partial x_k}\Big)^2 + \frac{L_2}{2}\frac{\partial Q_{ij}}{\partial x_j}\frac{\partial Q_{ik}}{\partial x_k} + \frac{L_3}{2}\frac{\partial Q_{ik}}{\partial x_j}\frac{\partial Q_{ij}}{\partial x_k} + \frac{L_6}{2}Q_{lk}\frac{\partial Q_{ij}}{\partial x_l}\frac{\partial Q_{ij}}{\partial x_k}, \tag{1.9}$$

where L_1, L_2, L_3 and L_6 are constants.

In the Oseen-Frank formalism, when the system is so much lower than the nematic-isotropic transition temperature that fluctuations of S are weak and S is approximately a constant, the distortion free-energy density $\mathcal{F}_d$ can be expressed in terms of $\mathbf{n}$:

$$\mathcal{F}_d = \frac{K_{11}}{2}(\nabla\cdot\mathbf{n})^2 + \frac{K_{22}}{2}(\mathbf{n}\cdot(\nabla\times\mathbf{n}))^2 + \frac{K_{33}}{2}(\mathbf{n}\times(\nabla\times\mathbf{n}))^2$$

$$+ K_{13}\nabla\cdot[\mathbf{n}(\nabla\cdot\mathbf{n})] - K_{24}\nabla\cdot[(\mathbf{n}\times(\nabla\times\mathbf{n}) + \mathbf{n}(\nabla\cdot\mathbf{n}))], \tag{1.10}$$

where the five terms represent, respectively, the contributions of the splay, twist, bend, splay-bend and saddle-splay, and the first three are illustrated in Fig. 1.1; see Refs. [5, 11–14]. This is known as the Oseen-Frank free-energy density [15, 16].

The distortion free energy functional is the integration of the free energy density over a domain, i.e.,

$$F_d = \int \mathrm{d}^3V\ \mathcal{F}_d, \tag{1.11}$$

where $\mathcal{F}_d$ is either Eq. (1.9) or (1.10).

In Eq. (1.10), the terms corresponding to the contributions of splay-bend and saddle-splay are beyond the scope of this thesis, because they are surface energies (by the use of divergence theorem) and the examples we are studying have fixed outer boundary conditions.

For example, note that the saddle-splay contribution to the functional can be written, by using the divergence theorem, as a surface integral

$$-\int K_{24}[\mathbf{n}\times(\nabla\times\mathbf{n}) + \mathbf{n}(\nabla\cdot\mathbf{n})]\cdot\mathbf{v}\mathrm{d}S, \tag{1.12}$$

where $\mathbf{v}$ is the vector normal to the boundary. As this term does not contain any derivatives of $\mathbf{n}$ in the normal direction of the boundary (see Refs. [17, 18]), it therefore is a constant when the boundary conditions are given. Thus, instead of using Eq. (1.10), we usually consider

$$\mathcal{F}_d = \frac{K_{11}}{2}(\nabla\cdot\mathbf{n})^2 + \frac{K_{22}}{2}(\mathbf{n}\cdot(\nabla\times\mathbf{n}))^2 + \frac{K_{33}}{2}\left|\mathbf{n}\times(\nabla\times\mathbf{n})\right|^2. \tag{1.13}$$

Now, to obtain the equilibrium state, we need to derive the Euler-Lagrange equation corresponding to the functional Eq. (1.11), and solve it subject to the prescribed boundary conditions.

One tricky issue is that the tensor field $\mathbf{Q}$ and the unit vector field $\mathbf{n}$ are not equivalent in characterizing a uniaxial nematic state since $\mathbf{n}$ is not an order parameter. The fact that $\mathbf{n}$ and $-\mathbf{n}$ equivalently characterize the local direction of molecular alignment means that $\mathbf{n}$ or $-\mathbf{n}$ hide the head-tail symmetry. In some cases, $\mathbf{n}$ cannot replace $\mathbf{Q}$ without flipping through π rad on some lines or planes, i.e., there is a branch cut. To illustrate this situation, we use "arrows" and "sticks" to represent $\mathbf{n}$ and $\mathbf{Q}$, respectively, in schematic diagrams. Figures 1.2 and 1.3 illustrate the tensor fields and their corresponding unit vector fields assuming homeotropic boundary conditions (i.e., $\mathbf{n}$ perpendicular to the boundary). The former represents a state where both $\mathbf{n}$ and $\mathbf{Q}$ are continuous, while the latter is a state where $\mathbf{n}$ inevitably flips through π rad on a line while the corresponding $\mathbf{Q}$ is continuous. This issue is related to the existence of a defect core [11, 19–22].

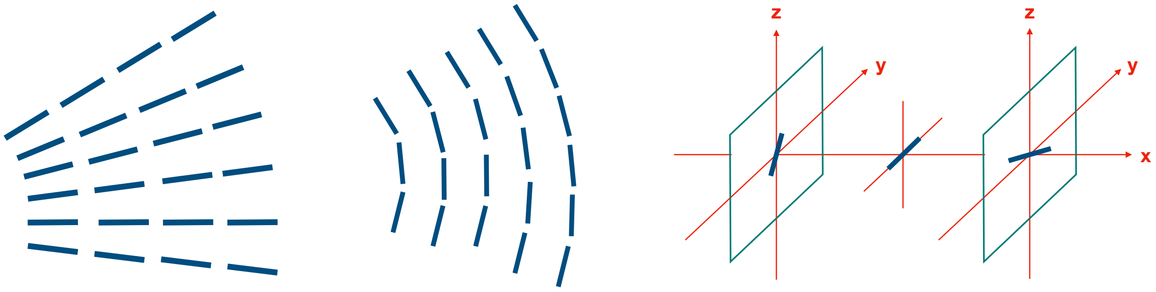

(a) Splay

(b) Bend

(c) Twist

Figure 1.1: Distortion types (based on Figs. 3.1. and 3.7. in Ref. [1])

1.4 Defects in Uniaxial Nematics and their Topologies

The defect in a uniaxial nematic is characterized by its topology. In the Oseen-Frank formalism, the defect core is characterized by a tiny region where the orientation of the order is undefined, i.e., the unit vector $\mathbf{n}$ is undefined. However, in the Landau-de Gennes for-

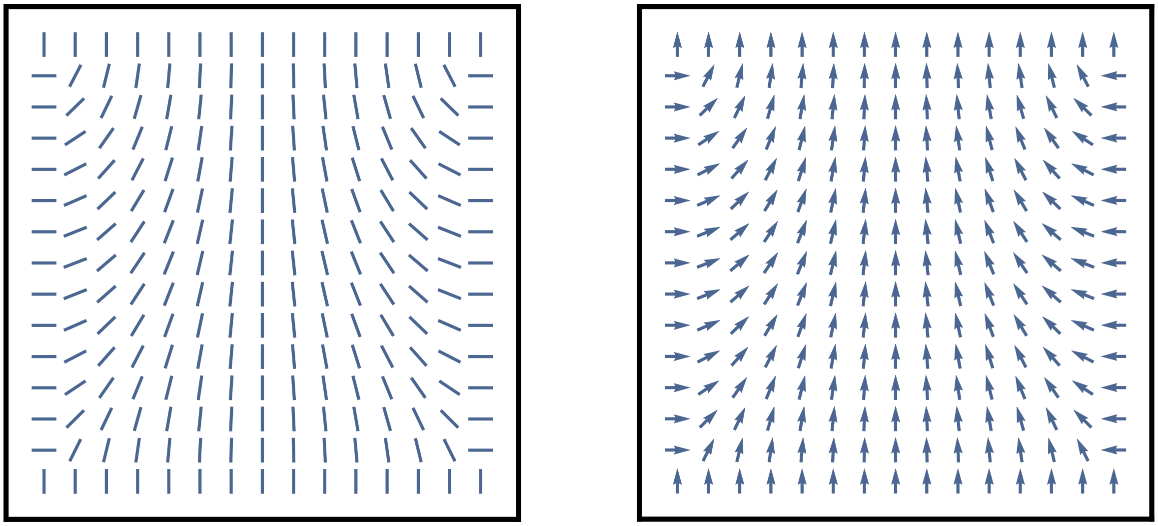

(a) Uniaxial tensor field #1

(b) Unit vector field #1

Figure 1.2: Uniaxial tensor field #1 (left) and its corresponding unit vector field #1 (right), for the case in which there are no topological defects

malism, the defect core is in a different state, i.e., the biaxial state; see Refs. [23–29]. The Oseen-Frank formalism is more convenient in the study of the topology, as the defect core can be treated as a hole in a manifold, which can be studied by homotopy theory.

1.4.1 Topology of Defects in Two-Dimensional Uniaxial Nematics

In a spatially two-dimensional uniaxial nematic, the defect core is a point. The vector field $\mathbf{n}$ can be parametrized as

$$\mathbf{n} = \cos\theta(x,y)\,\hat{\mathbf{x}} + \sin\theta(x,y)\,\hat{\mathbf{y}}, \tag{1.14}$$

subject to the head-tail symmetry, i.e., $\mathbf{n}$ and $-\mathbf{n}$ are equivalent. θ is the angle between the vector and the $\hat{\mathbf{x}}$ direction. Therefore the order parameter space is the real projective line $\mathbb{R}P^1$, i.e., a circle with antipodal points being identified. Its topology can be captured by the fundamental group, i.e., the first homotopy group,

$$\pi_1(\mathbb{R}P^1) = \mathbb{Z} \equiv \{0, \pm 1, \pm 2, \ldots\}. \tag{1.15}$$

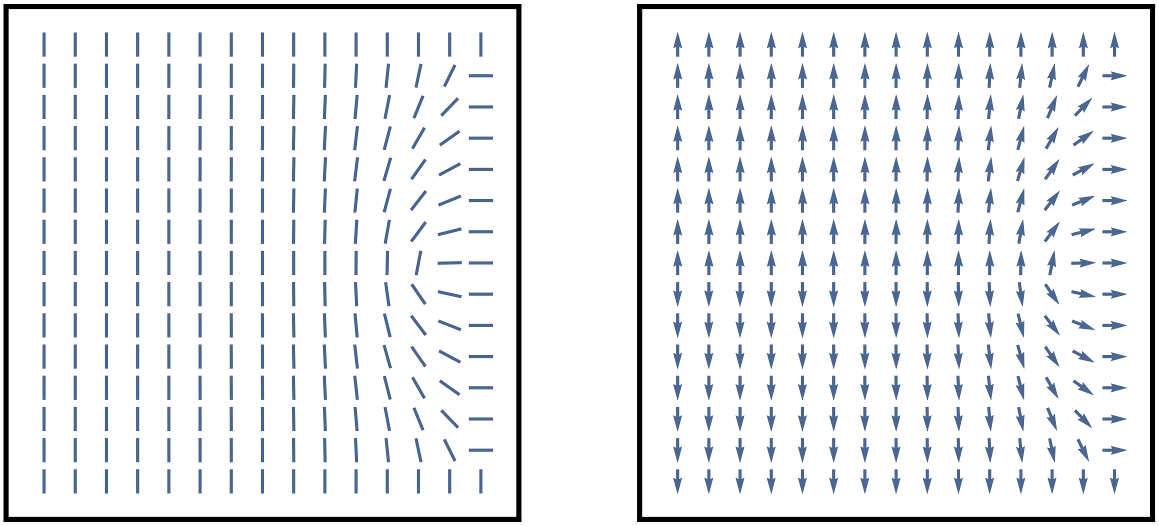

(a) Uniaxial tensor field #2

(b) Unit vector field #2

Figure 1.3: Uniaxial tensor field #2 (left) and its corresponding unit vector field #2 (right), for the case in which there is a topological defect

Each element of the group represents an topologically equivalence class of configuration that cannot be transformed into another by continuously deforming the vector field $\mathbf{n}$ in two dimensions [30–34].

The topology can also be accessed by a winding number m, which is defined to be the total number of turns through which a vector rotates when one travels counterclockwise around the defect core; then

$$m \in \frac{1}{2} \cdot \mathbb{Z} \equiv \{0, \pm\frac{1}{2}, \pm 1, \dots\}. \tag{1.16}$$

We can think of the different winding numbers as representing different elements in the fundamental group $\pi_1(\mathbb{R}P^1)$ [1, 34, 35]. Defects with different winding numbers are illustrated in Fig. 1.4.

1.4.2 Topology of Defects in Three-Dimensional Uniaxial Nematics

In a three-dimensional uniaxial nematic, the defect core can be a point or a line. The order parameter space is now the real projective plane $\mathbb{R}P^2$, i.e., a sphere with antipodal points being identified.

If the defect core is a line then its topology can be captured by the first homotopy group

$$\pi_1(\mathbb{R}P^2) = \mathbb{Z}/2\mathbb{Z} \equiv \{0, 1\}. \tag{1.17}$$

However, contrary to the two–dimensional counterpart, two defect structures whose two–dimensional projections are topologically equivalent can belong to the same topologically equivalent class in three dimensions [32, 34–36]. In Fig. 1.5, (a) – (c) are line defects whose two-dimensional projections are the point defects with winding numbers $1/2$, $-1/2$ and 1 respectively. However, in three dimensions, (a) and (b) are topologically equivalent, represented by the element 1 in $\pi_1(\mathbb{R}P^2)$; and (c) is topologically equivalent to a homogeneous state, represented by the element 0 in $\pi_1(\mathbb{R}P^2)$.

If the defect core is a point then its topology can be captured by the second homotopy group

$$\pi_2(\mathbb{R}P^2) = \mathbb{Z} \equiv \{0, \pm 1, \pm 2, \dots\}. \tag{1.18}$$

Since the elements with the same absolute value but opposite signs represent the same defect, the topologically equivalent classes are therefore represented by the set of nonzero integers. Again, two apparently different defect structures can belong to the same class.

If the defect core is a ring then we need the automorphism classes of $\pi_1(\mathbb{R}P^2) \rtimes \pi_2(\mathbb{R}P^2)$ to understand its topology [30–32, 34, 35].

Inside one topologically equivalence class, one defect structure can be continuously deformed into another defect structure, which means there exists a path between two defects with a finite energy barrier. Experimentally, we can use this information to predict the defect structures under certain topological constraints imposed by the boundary conditions. Furthermore, homotopy theory helps us predict the result of the merger of several defects by the rules of group multiplication [32, 34, 37–39].

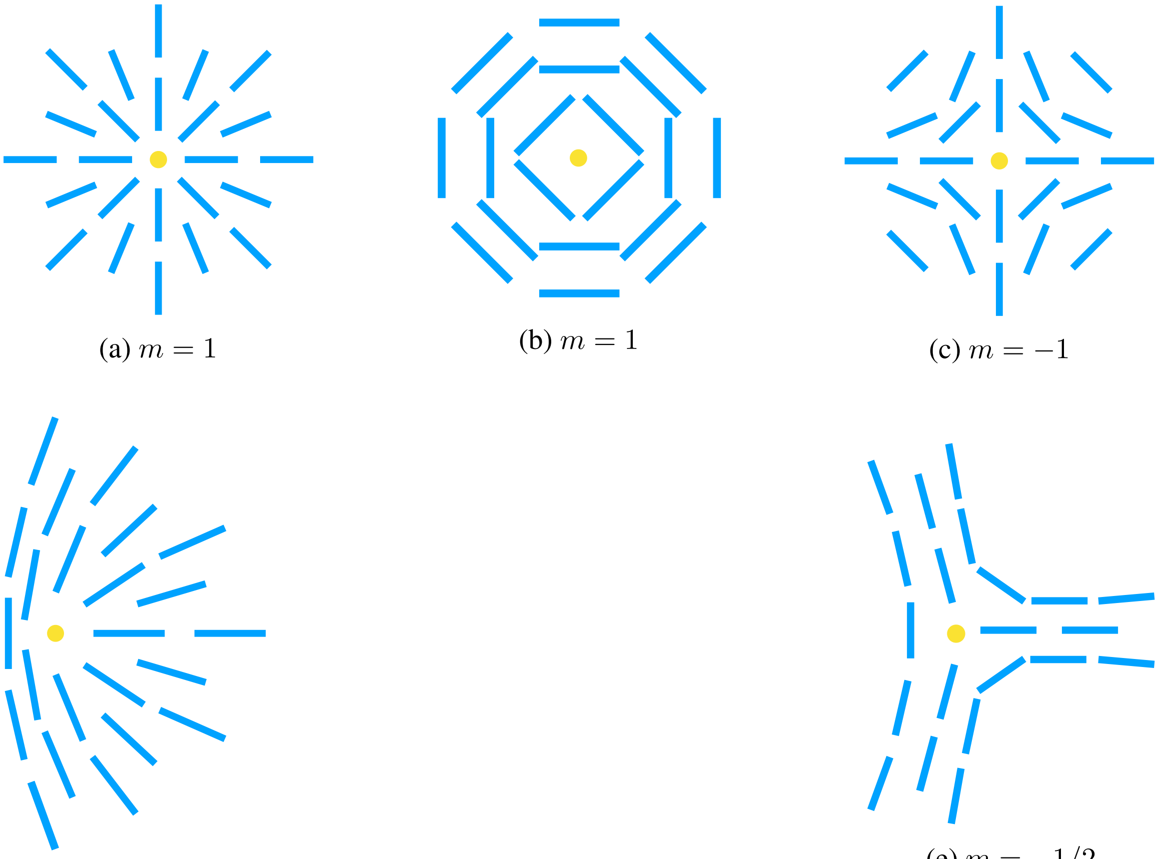

(a) $m = 1$ (b) $m = 1$ (c) $m = -1$

(d) $m = 1/2$ (e) $m = -1/2$

Figure 1.4: Defects with different winding numbers m

1.5 Equilibrium Defect Structures in Uniaxial Nematics

The equilibrium defect structure is defined to be the spatial equilibrium configuration of $\mathbf{Q}$ or $\mathbf{n}$ in the presence of defects. Thus, to determine it, we are required to minimize the distortion free-energy functional [i.e., Eq. (1.11)]. A necessary step is to solve the corresponding Euler-Lagrange equation, subject to prescribed boundary conditions, plus a treatment for the defect cores.

The Landau-de Gennes formalism [i.e., Eq. (1.9)] is straightforward, in principle, because it will always give us a continuous solution showing that the small defect core is actually not in the uniaxial nematic state, and therefore no special treatment for the defect core is needed [7, 23–29]. In contrast, by using fewer variables, the Oseen-Frank formal-

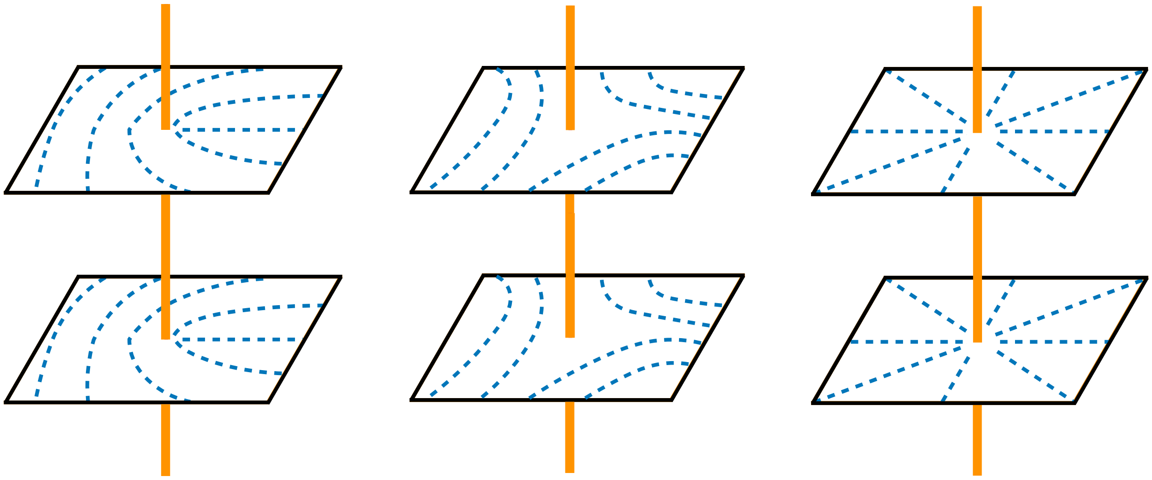
(a) $m = 1/2$ (b) $m = -1/2$ (c) $m = 1$

Figure 1.5: Line defect (based on Fig. 5. in Ref. [32])

ism [i.e., Eq. (1.13)] only considers the uniaxial nematic state, and the small defect cores are not included in the integration domain of the functional. Our purpose is to determine the number and locations of the defect cores regardless of their fine structures, which is a small step forward in studying the topology, the Oseen-Frank formalism is being used. As a result, we are faced with a problem about how to deal with the defect core in the Oseen-Frank formalism. Here, we summarize three general schemes.

1.5.1 Defect Cores as Inner Boundaries

The distortion free-energy functional [i.e., Eq. (1.11)] is an integration of an energy density composed of derivatives of a field (i.e., $\mathbf{Q}$ or $\mathbf{n}$). For a given field, in order to get the energy functional, we should do the differentiation and integration with respect to this field. Since the Oseen-Frank formalism is not supposed to give us the energy for the defect core, the derivative of the field at the location of the defect core is undefined and cannot be included in the domain of integration. One scheme is to treat the defect core as a boundary.

This scheme requires the number and locations of the defect cores to be prescribed. In practice, in order to determine the equilibrium defect structure, one has to guess all the possible numbers and locations of the defect cores and solve the many corresponding boundary value problems. Therefore it often occurs in numerical computations. One example is the study of defects in nematic bridges introduced later in this thesis [40–45]. Another example is the study of a long cylindrical cavity, where defect cores exist along the cylinder axis, and the cylinder segment between the two defect cores is the domain where the numerical computation is conducted [46–50].

1.5.2 Defect Cores as Coordinate Singularities

To make sure the defect cores are not in the domain of integration, we can also choose a special coordinate system such that the defect cores are located at the coordinate singularities. This scheme still requires the numbers and locations of the defect cores to be prescribed, since the coordinate singularities are determined for a given coordinate system. However, for some special cases, the special coordinate system is easy to construct.

***Example 1**: One Point Defect in an Infinitely Large Disk*

We consider a point defect (with a point-like defect core at the origin) in an infinitely large disk with radius $R \to \infty$ [1]. The boundary condition is

$$\mathbf{n}|_{R\to\infty} = \hat{\mathbf{r}}, \tag{1.19}$$

where $\hat{\mathbf{r}}$ is the radial unit vector in the polar coordinate system. Within the one-constant approximation, i.e., $K_{11} = K_{22} = K_{33}$, the distortion free energy for two dimensions [see Eqs. (1.11) and (1.13)] becomes

$$F_d = \frac{K}{2} \int \mathrm{d}^2 S \, [(\nabla \cdot \mathbf{n})^2 + (\nabla \times \mathbf{n})^2], \tag{1.20}$$

and the domain of integration is an annulus, i.e., the complement of the origin in the infinitely large disk. Substituting Eq. (1.14) into Eq. (1.20), we have

$$F_d = \frac{K}{2} \int \mathrm{d}^2 S \; (\nabla \theta)^2. \tag{1.21}$$

Its Euler-Lagrange equation is

$$\Delta \theta = 0. \tag{1.22}$$

For a two-dimensional nematic, if we choose the polar coordinate system with the coordinate singularity coinciding with the defect core then Eq. (1.22) becomes

$$\frac{1}{\rho} \frac{\partial}{\partial \rho} \left(\rho \frac{\partial \theta}{\partial \rho} \right) + \frac{1}{\rho^2} \frac{\partial^2 \theta}{\partial \phi^2} = 0. \tag{1.23}$$

It is straightforward to check that

$$\theta = m \cdot \phi + C, \tag{1.24}$$

is a solution to Eq. (1.23), where m is the winding number and C is a constant. The boundary condition Eq. (1.19) requires that $m = 1$ and $C = 0$. Therefore the solution to the boundary value problem [i.e., Eqs. (1.22) and (1.19)] is

$$\theta = \phi. \tag{1.25}$$

Example 2*: One Point Defect in an Infinitely Large Ball* B^3

We consider a point defect (with a point-like defect core at the origin) in an infinitely large ball B^3 with radius $R \to \infty$ [49]. The boundary condition is

$$\mathbf{n}|_{R \to \infty} = \hat{\mathbf{r}}, \tag{1.26}$$

where $\hat{\mathbf{r}}$ is the radial unit vector in the spherical coordinate system. With one-constant approximation, the distortion free energy for three dimensions becomes

$$F_d = \frac{K}{2} \int \mathrm{d}^3 V \; [(\nabla \cdot \mathbf{n})^2 + (\nabla \times \mathbf{n})^2], \tag{1.27}$$

and the domain of integration is $S^2 \times I$, i.e., the complement of the origin in the infinitely large ball. The vector field $\mathbf{n}$ can be parametrized as

$$\begin{aligned} \mathbf{n} = {} & \sin \alpha(x, y, z) \cos \beta(x, y, z) \; \hat{\mathbf{x}} + \sin \alpha(x, y, z) \sin \beta(x, y, z) \; \hat{\mathbf{y}} \\ & + \cos \alpha(x, y, z) \; \hat{\mathbf{z}}. \end{aligned} \tag{1.28}$$

Here, $\{x, y, z\}$ are Cartesian coordinates and $\{\hat{\mathbf{x}}, \hat{\mathbf{y}}, \hat{\mathbf{z}}\}$ are Cartesian basis vectors.

If we consider the one-constant approximation then by substituting Eq. (1.28) into Eq. (1.27) we have

$$F_d = \frac{K}{2} \int \mathrm{d}^3 V \; [(\nabla \alpha)^2 + \sin^2 \alpha (\nabla \beta)^2]. \tag{1.29}$$

Its Euler-Lagrange equations are

$$\frac{1}{2} \sin 2\alpha (\nabla \beta)^2 = \Delta \alpha, \tag{1.30}$$

$$\sin 2\alpha (\nabla \alpha \cdot \nabla \beta) + \sin^2 \Delta \beta = 0. \tag{1.31}$$

If we choose the spherical coordinate system with the coordinate singularity coinciding with the defect core then Eqs. (1.30) and (1.31) become

$$\begin{aligned} & \frac{1}{2} \sin 2\alpha \Big[\Big(\frac{\partial \beta}{\partial r} \Big)^2 + \frac{1}{r^2} \Big(\frac{\partial \beta}{\partial \theta} \Big)^2 + \frac{1}{r^2 \sin^2 \theta} \Big(\frac{\partial \beta}{\partial \phi} \Big)^2 \Big] \\ & = \frac{\partial^2 \alpha}{\partial r^2} + \frac{2}{r} \frac{\partial \alpha}{\partial r} + \frac{1}{r^2} \frac{\partial^2 \alpha}{\partial \theta^2} + \frac{\cos \theta}{r^2 \sin \theta} \frac{\partial \alpha}{\partial \theta} + \frac{1}{r^2 \sin^2 \theta} \frac{\partial^2 \alpha}{\partial \phi^2}, \end{aligned} \tag{1.32}$$

$$\sin 2\alpha\Big(\frac{\partial\alpha}{\partial r}\frac{\partial\beta}{\partial r}+\frac{1}{r^2}\frac{\partial\alpha}{\partial\theta}\frac{\partial\beta}{\partial\theta}+\frac{1}{r^2\sin^2}\frac{\partial\alpha}{\partial\phi}\frac{\partial\beta}{\partial\phi}\Big)+\sin^2\alpha\Big(\frac{\partial^2\beta}{\partial r^2} \tag{1.33}$$

$$+\frac{2}{r}\frac{\partial\beta}{\partial r}+\frac{1}{r^2}\frac{\partial^2\beta}{\partial\theta^2}+\frac{\cos\theta}{r^2\sin\theta}\frac{\partial\beta}{\partial\theta}+\frac{1}{r^2\sin^2\theta}\frac{\partial^2\beta}{\partial\phi^2}\Big)=0.$$

It is straightforward to check that

$$\begin{cases}\alpha=\theta,\\ \\ \beta=\phi+C,\end{cases} \tag{1.34}$$

is a solution to Eqs. (1.32) and (1.33), where C is a constant. The boundary condition Eq. (1.26) requires that $C=0$. Therefore the solution to the boundary value problem [i.e., Eqs. (1.32), (1.33) and (1.26)] is

$$\begin{cases}\alpha=\theta,\\ \\ \beta=\phi,\end{cases} \tag{1.35}$$

***Example 3**: A Ring Defect in an Infinitely Large Ball B^3*

We consider a ring defect in an infinitely large ball B^3 with radius $R\to\infty$ [31, 51–54]. Assume the ring-like defect core of radius a lying in the x-y plane with the center coinciding with the origin of the Cartesian coordinate system. The boundary condition is Eq. (1.26). Then we can choose a spheroidal coordinate system (u, v, ϕ), for which

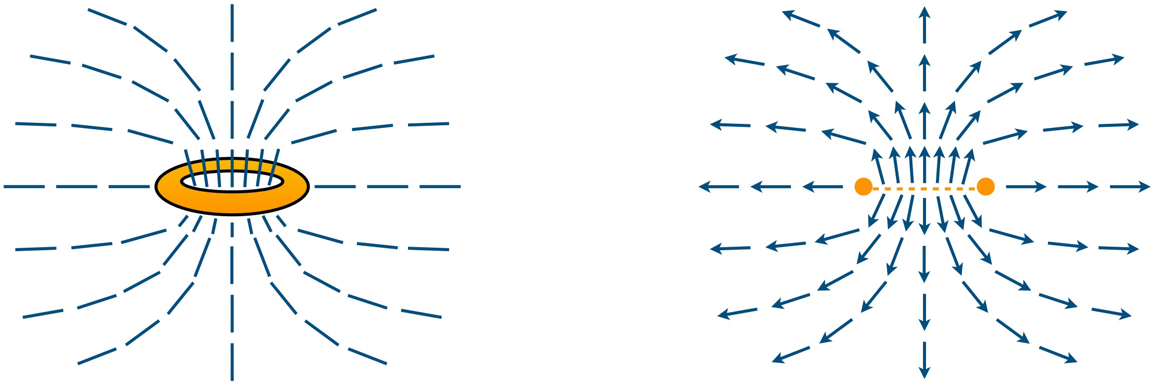

(a) Ring defect in three-dimensions (b) Cross section of a ring defect

Figure 1.6: Ring defect (based on Figs. 2 and 3. in Ref. [31])

$$x = a\cosh u \cos v \cos\phi,$$
$$y = a\cosh u \cos v \sin\phi, \tag{1.36}$$
$$z = a\sinh u \sin v;$$

see Ref. [55]. Then we can choose the unit vector field $\mathbf{n}$ to be perpendicular to the oblate spheroids

$$\frac{x^2+y^2}{a^2\cosh^2 u} + \frac{z^2}{a^2\sinh^2 u} = 1. \tag{1.37}$$

This Ansatz does not satisfy the Euler-Lagrange equation, and therefore it can only provide an upper bound for the free energy. However, one good thing about writing $\mathbf{n}$ in terms of (u, v, ϕ) is that the differentiation and integration never cross the ring-like defect core and the disk bounded by the ring (i.e., the branch cut), and therefore there is no fictitious infinite free energy.

1.5.3 Defect Cores as Contained in the Solutions to the Boundary Value Problems

In the Landau-de Gennes formalism, the defect core is contained in the solution to the boundary value problem, and it is created as the emergence of a different state in a tiny region. The equilibrium defect structure can be obtained by directly solving the Euler-Lagrange equation corresponding to Eq. (1.9). In contrast, lots of computations are spent on the many non-equilibrium defect structures by using Oseen-Frank formalism (since the defect core is not in the domain of integration). However, this convenience from Landau-de Gennes formalism comes with an expense of intense computations for the fine structure of the defect core, which is deemed by us as unnecessary for our purpose since we are interested in the equilibrium location of the defect core. When using the Oseen-Frank formalism, we can ask: Can we create the inner boundaries during the process of solving the Euler-Lagrange equation? A substantial part of this thesis is to provide a partial answer to this question.

Contrary to the schemes introduced in the last two subsections, where the complement of the defect cores in the whole domain is considered as the domain of integration, the scheme arising from a positive answer to the question in the last paragraph would require us to consider the whole domain, which results in some unphysical contributions to the free-energy functional. An essential part of this scheme involves how to cancel these unphysical contribution out, as will be introduced in Chapter 5.

The above three schemes are for general considerations. For two-dimensional nematics within the one-constant approximation, there is a simple method, as introduced below, which bears some resemblance to the second scheme.

1.5.4 Two-Dimensional Nematics within the One-Constant Approximation

An important observation is that Eq. (1.22) is a *linear* PDE, which means that we can get the vector field $\mathbf{n}$ of many defect cores via superposition of the vector fields associated with each defect core. However, we should be careful about the multiplicity of θ, as there exist branch cuts. For two-dimensional nematics within the one-constant approximation, there are two methods for determining the equilibrium defect structures, as shown in the following [1, 56, 57].

Method 1

First, we let N be the number of the defect cores and introduce m_i ($i = 1, 2, \ldots, N$) as the associated winding numbers (and these numbers need to be compatible with the topology imposed by the boundary conditions). Then, we connect each pair of defect cores by a straight line segment which can be the branch cut. As a result, the whole domain is divided into patches, in each of which θ is single valued, and this makes it safe to solve Eq. (1.22). Let us mark each patch, and focus our following discussion on an arbitrary patch, say patch j. Since Eq. (1.22) is linear, we can write its solution as:

$$\theta^{(j)} = \theta_1^{(j)} + \theta_2^{(j)} + \cdots + \theta_N^{(j)}, \tag{1.38}$$

where

$$\theta_i^{(j)} = m_i \phi_i + C_i^{(j)} \tag{1.39}$$

is the contribution from defect-core i with ϕ_i being the polar angle of its particular polar coordinate system and $C_i^{(j)}$ being a constant. m_i should be prescribed while $C_i^{(j)}$ can be determined by the prescribed values on the two sides of the branch cuts. Following the same procedure, we can find θ in every patch. Then, to compute the free energy in patch j, we use the following relation for the continuous function θ^j:

$$\frac{K}{2}\int_{S_j} \mathrm{d}\mathbf{r}_j \, (\nabla\theta^{(j)})^2 = -\frac{K}{2}\int_{S_j} \mathrm{d}\mathbf{r}_j \, \theta^{(j)}\Delta\theta^{(j)} + \frac{K}{2}\int_{\partial S_j} \mathrm{d}\mathbf{r}_j \, \theta^{(j)}\nabla\theta^{(j)}, \tag{1.40}$$

where S_j and ∂S_j are the area and boundary of the patch j, repectively. Because of Eq. (1.22), the first term on the RHS of Eq. (1.40) vanishes, and therefore the bulk energy of patch j can be transformed to a surface energy. Thus, the total free energy is related to the length of each branch cut; see Refs. [1, 58].

Method 2

Let θ_i be the contribution from defect-core i in an arbitrary patch. Then, Eq. (1.39) shows that θ_i is determined up to a constant, and $\nabla\theta_i$ can be made continuous throughout the whole domain [56]. (To be specific, when crossing the branch cut, θ^j and each of its terms θ_i^j are changed by a multiple of $\pi/2$, while $\nabla\theta^j$ and $\nabla\theta_i^j$ are unchanged.)

The total energy can then be written as

$$F = \frac{K}{2}\int \mathrm{d}\mathbf{r}\ (\nabla\theta_1 + \nabla\theta_2 + \cdots + \nabla\theta_N)^2 \tag{1.41}$$

$$= \sum_{i=1}^{N} \frac{K}{2}\int \mathrm{d}\mathbf{r}\ (\nabla\theta_i)^2 + \sum_{i=1,k=1,j\neq k}^{N} K\int \mathrm{d}\mathbf{r}\ (\nabla\theta_i)(\nabla\theta_k).$$

These two methods are equivalent. Method 1 computes the boundary integral, emphasizing the fact that the function θ is discontinuous at the branch cut, while Method 2 computes the bulk integral, taking advantage of the fact that $\nabla\theta$ can be made continuous at the branch cut. To better elucidate the above two methods, let us revisit an example introduced in de Gennes' book [1].

Problem: Compute the free energy of two parallel straight-line defect cores having winding numbers m and $-m$, respectively, and separated by a distance d, which is illustrated in Fig. 1.7.

Solution via Method 1: Choose the Cartesian coordinate system for the whole domain, and let the defect core with winding number m be at $(-d/2, 0)$ and the other defect core be at $(d/2, 0)$. Then the whole domain can be divided as two patches: one with $x > 0$ (patch 1) and one with $x < 0$ (patch 2). Then, on patch 1 and patch 2, we have, respectively,

$$\theta^{(1)} = \theta_1^{(1)} + \theta_2^{(1)} = m\phi_1 - m\phi_2 + D^{(1)}, \tag{1.42}$$

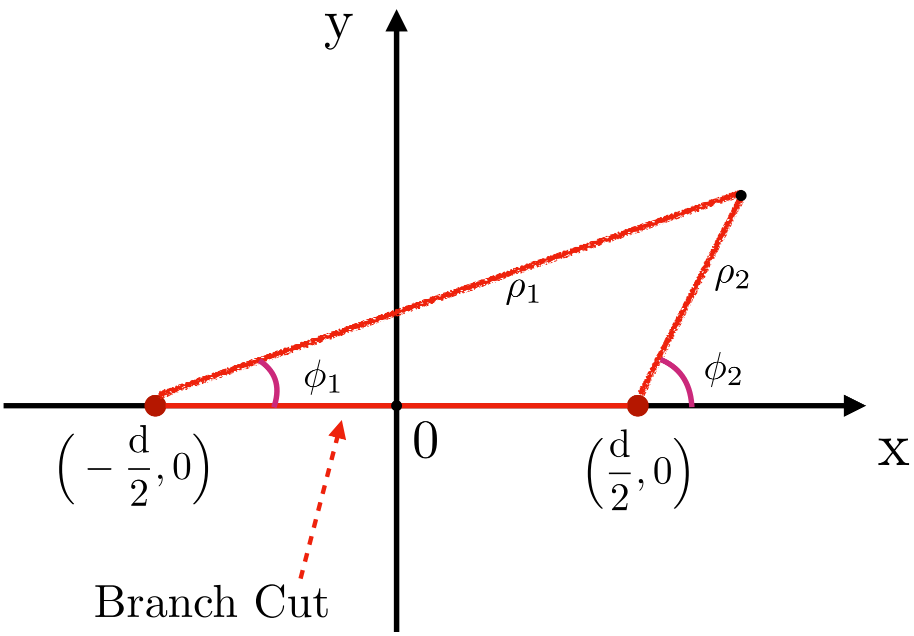

Figure 1.7: Problem of two parallel straight-line defects (based on Fig. 4.9 in Ref. [1])

$$\theta^{(2)} = \theta_1^{(2)} + \theta_2^{(2)} = m\phi_1 - m\phi_2 + D^{(2)}, \tag{1.43}$$

where $D^{(1)}$ and $D^{(2)}$ are constants. We choose the line segment connecting $(-d/2, 0)$ and $(d/2, 0)$ be the branch cut. Then, due to symmetry, $D^{(1)}$ and $D^{(2)}$ can be chosen such that $\theta^{(1)} = \theta^{(2)}$ on the intervals $(-\infty, -d/2)$ and $(d/2, \infty)$, and $\theta^{(2)} - \theta^{(1)} = 2\pi m$ on the interval $(-d/2, d/2)$. Then we can compute the total energy as follows:

$$\begin{aligned} F &= \frac{K}{2}\int_{S_1} (\nabla\theta^{(1)})^2 \, \mathrm{d}\mathbf{r}_1 + \frac{K}{2}\int_{S_2} (\nabla\theta^{(2)})^2 \, \mathrm{d}\mathbf{r}_2 \\ &= \frac{K}{2}\int_{-\infty}^{\infty} \theta^{(1)}\nabla\theta^{(1)} \cdot \mathrm{d}\mathbf{r}_1 + \frac{K}{2}\int_{-\infty}^{\infty} \theta^{(2)}\nabla\theta^{(2)} \cdot \mathrm{d}\mathbf{r}_2 \\ &= \frac{K}{2}\int_{-d/2}^{d/2} \theta^{(1)}\nabla\theta^{(1)} \cdot \mathrm{d}\mathbf{r}_1 + \frac{K}{2}\int_{-d/2}^{d/2} \theta^{(2)}\nabla\theta^{(2)} \cdot \mathrm{d}\mathbf{r}_2 \\ &= \frac{K}{2}\int_{a}^{d-a} \theta^{(1)}\frac{m}{\rho_1}\hat{\phi}_1 \cdot \mathrm{d}\mathbf{r}_1 + \frac{K}{2}\int_{a}^{d-a} \theta^{(2)}\Big(-\frac{m}{\rho_2}\Big)\hat{\phi}_2 \cdot \mathrm{d}\mathbf{r}_2 \end{aligned} \tag{1.44}$$

$$= -\frac{K}{2}\int_a^{d-a} \theta^{(1)}\frac{m}{\rho_1}\,\mathrm{d}\rho_1 + \frac{K}{2}\int_a^{d-a} \theta^{(2)}\Big(-\frac{m}{\rho_2}\Big)\,\mathrm{d}\rho_2$$

$$= \frac{K}{2}\int_a^{d-a} 2\pi m\Big(\frac{m}{\rho_1} + \frac{m}{d-\rho_1}\Big)\,\mathrm{d}\rho_1$$

$$= 2\pi K m^2 \ln\Big(\frac{d}{a}\Big),$$

where a is the radius of the defect cores.

Solution via Method 2: We can compute the total energy in the following way:

$$F = \frac{K}{2}\int \mathrm{d}\mathbf{r}\ (\nabla\theta_1 + \nabla\theta_2)^2 \tag{1.45}$$

$$= \frac{K}{2}\int \mathrm{d}\mathbf{r}\ (\nabla\theta_1)^2 + \frac{K}{2}\int \mathrm{d}\mathbf{r}\ (\nabla\theta_2)^2 + K\int \mathrm{d}\mathbf{r}\ (\nabla\theta_1)(\nabla\theta_2)$$

$$= \frac{K}{2}\int_a^R \rho_1\mathrm{d}\rho_1 \int_0^{2\pi}\mathrm{d}\phi_1\Big(\frac{1}{\rho_1}\frac{\partial\theta_1}{\partial\phi_1}\Big)^2 + \frac{K}{2}\int_a^R \rho_2\mathrm{d}\rho_2 \int_0^{2\pi}\mathrm{d}\phi_2\Big(\frac{1}{\rho_2}\frac{\partial\theta_2}{\partial\phi_2}\Big)^2$$

$$+ K\int_a^R \rho_1\mathrm{d}\rho_1 \int_0^{2\pi}\mathrm{d}\phi_1\Big(\frac{1}{\rho_1}\frac{\partial\theta_1}{\partial\phi_1}\hat{\phi}_1\Big)\Big(\frac{1}{\rho_2}\frac{\partial\theta_2}{\partial\phi_2}\hat{\phi}_2\Big)$$

$$= K\pi m^2\int_a^R \frac{1}{\rho_1}\mathrm{d}\rho_1 + K\pi m^2\int_a^R \frac{1}{\rho_2}\mathrm{d}\rho_2 - Km^2\int_a^R \mathrm{d}\rho_1\int_1^{2\pi}\frac{1}{\rho_2}\cos(\phi_2-\phi_1)$$

$$= 2\pi K m^2\ln\Big(\frac{R}{a}\Big) + Km^2\int_a^R\mathrm{d}\rho_1\int_0^{2\pi}\mathrm{d}\phi_1\frac{-\rho_1 + d\cos\phi_1}{\rho_1^2 + d^2 - 2\rho_1 d\cos\phi_1}$$

$$= 2\pi K m^2\ln\Big(\frac{R}{a}\Big) - Km^2\int_a^R\mathrm{d}\rho_1\frac{2\pi\rho_1}{|\rho_1^2 - d^2|} - Km^2\int_a^R\mathrm{d}\rho_1\frac{\pi}{\rho_1}$$

$$+ Km^2\int_a^R\mathrm{d}\rho_1\frac{\pi(\rho_1^2 + d^2)}{\rho_1|\rho_1^2 - d^2|}$$

$$= 2\pi K m^2\ln\Big(\frac{R}{a}\Big) + \pi K m^2\ln\Big(\frac{d}{a}\Big) - \pi K m^2\ln\Big(\frac{R}{a}\Big) - \pi K m^2\ln\Big(\frac{R}{d}\Big)$$

$$= 2\pi K m^2 \ln\Big(\frac{d}{a}\Big),$$

where $R(\to\infty)$ is the size of the whole domain.

Another interesting example is to find the equilibrium locations of two point defects of winding number $1/2$ and $-1/2$, respectively, in a disk [57]. The only difference from the above example is that this example considers a finite domain, and we need to use the method of images, similar to the one used in electrostatics. Based on this method, there is a Green function formalism, as we now discuss.

Green Function Formalism

In a two-dimensional space, for a point charge q, we have the following electrostatic potential:

$$V_{el} = kq \ln\Big(\frac{\rho}{a}\Big); \tag{1.46}$$

by contrast, for a single defect core of winding number m, the distortion potential is

$$V_d = 2\pi K m \ln\Big(\frac{\rho}{a}\Big). \tag{1.47}$$

This implies we may borrow the Green function formalism from electrostatics to study defects in two-dimensional nematics [59–64]. The procedure is as follows.

Let us assume that there is a defect core located at (x_1, y_1) of winding number m_1. Then we can draw a contour around it and use Stokes' theorem:

$$\oint \mathrm{d}\theta = \oint \Big(\frac{\partial\theta}{\partial x}\mathrm{d}x + \frac{\partial\theta}{\partial y}\mathrm{d}y\Big) = 2\pi m_1 \tag{1.48}$$

$$\Longrightarrow \int \mathrm{d}x\,\mathrm{d}y\Big(\frac{\partial}{\partial x}\frac{\partial\theta}{\partial y} - \frac{\partial}{\partial y}\frac{\partial\theta}{\partial x}\Big) = 2\pi m_1 \int \mathrm{d}x\,\mathrm{d}y\,\delta(x-x_1, y-y_1)$$

$$\Longrightarrow \frac{\partial}{\partial x}\frac{\partial\theta}{\partial y} - \frac{\partial}{\partial y}\frac{\partial\theta}{\partial x} = 2\pi m_1\,\delta(x-x_1, y-y_1).$$

By Eqs. (1.22) and (5.17), we have

$$\frac{\partial \theta}{\partial x} = -2\pi m_1 \frac{\partial}{\partial y} \int \mathrm{d}x' \mathrm{d}y' \; G(x, y; x', y') \; \delta(x' - x_1, y' - y_1), \tag{1.49}$$

$$\frac{\partial \theta}{\partial y} = 2\pi m_1 \frac{\partial}{\partial x} \int \mathrm{d}x' \mathrm{d}y' \; G(x, y; x', y') \; \delta(x' - x_1, y' - y_1), \tag{1.50}$$

where $G(x, y; x', y')$ is the Green function that satisfies

$$\left(\frac{\partial^2}{\partial x^2} + \frac{\partial^2}{\partial y^2} \right) G(x, y; x', y') = \delta(x - x', y - y'). \tag{1.51}$$

Next, we let

$$\eta(x, y) = \sum_{i=1}^{N} 2\pi m_i \cdot \delta(x' - x_i, y' - y_i) \tag{1.52}$$

By superposition, Eqs. (5.18) and (5.19) generalize to

$$\frac{\partial \theta}{\partial x} = -\frac{\partial}{\partial y} \int \mathrm{d}x' \mathrm{d}y' \; G(x, y; x', y') \; \eta(x', y'), \tag{1.53}$$

$$\frac{\partial \theta}{\partial y} = \frac{\partial}{\partial x} \int \mathrm{d}x' \mathrm{d}y' \; G(x, y; x', y') \; \eta(x', y'). \tag{1.54}$$

Thus, Eq. (1.21) becomes

$$F[\theta] = -\frac{K}{2} \int G(x, y; x', y') \, \eta(x, y) \, \eta(x', y') \, \mathrm{d}x \, \mathrm{d}y \, \mathrm{d}x' \, \mathrm{d}y'. \tag{1.55}$$

1.6 Defects in Nematic Liquid-Crystal Capillary Bridges

The main objects to be studied in this thesis are defects in nematic liquid-crystal capillary bridges [40–44]. In experiments, these are created by the confinement of nematic liquid crystal droplets (e.g., 5CB) between two parallel glass microscope slides [45].

Since the energy functional [i.e., Eq. (1.11)] is an integral, in order to determine the equilibrium defect structures, we need to first specify the domain of integration. Apparently in experiments, the bridge has a cylindrical symmetry, and therefore we can focus our discussion on the axial plane. We then notice that the bridge is symmetrical with respect to the mid-plane, which is due to the fact that the gravity is far smaller than surface tension in its effect. Experimentally, it is easy to measure the height H of the bridge as well as the radius R of the mid-plane. Therefore, the first important rescaled parameter we know is the aspect ratio defined by $\Gamma = 2R/H$.

The lateral surface is determined by the Young-Laplace equation, i.e.,

$$\Delta P = 2\gamma M, \tag{1.56}$$

where ΔP is the Laplace pressure, γ is the surface tension between the outer medium and the inside liquid crystal, and M is the mean curvature, written as

$$M = \frac{1}{2}\Big(\frac{1}{R_1} + \frac{1}{R_2}\Big), \tag{1.57}$$

where $1/R_1$ and $1/R_2$ are the two principal curvatures. As the pressures inside and outside the surface are approximately uniform, the Laplace pressure is a constant, and therefore the surface is a mean-curvature surface. The contact angle θ_C, which is the angle between the glass and the lateral surface, is given by the Young equation

$$\gamma_{SG} - \gamma_{SL} - \gamma_{LG} \cos\theta_C = 0, \tag{1.58}$$

where γ_{SG}, γ_{SL} and γ_{LG} are the surface tensions between solid and outer medium, between glass and liquid crystal, and between liquid crystal and outer medium, respectively, as illustrated in Fig. 1.8. Detailed calculations based on Eq. (1.56) shows that the rescaled shape of the lateral surface (regardless of its location) is determined by the contact angle θ_C and the rescaled mean curvature M/H, where the latter can be replaced by the aspect ratio Γ.

Therefore, the rescaled domain is determined by Γ and θ_C; see Ref. [65–68].

(a) Sharp angle

(b) Obtuse angle

Figure 1.8: Contact angles

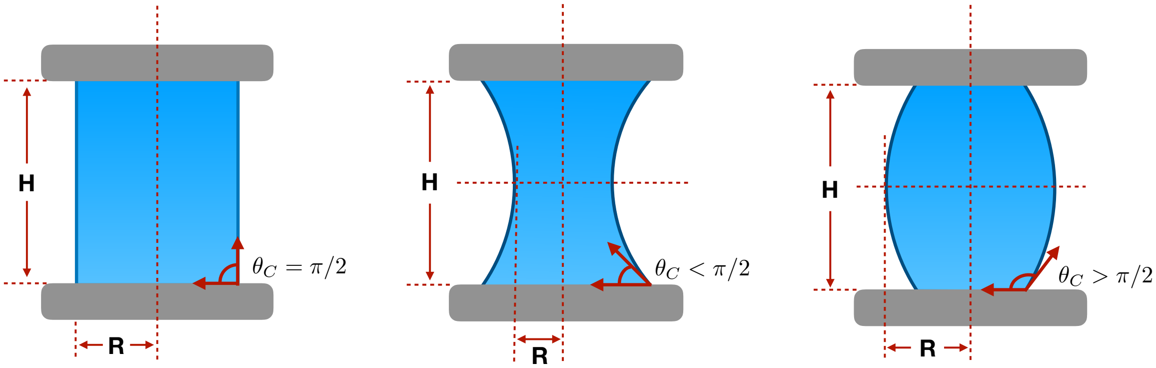

(a) Cylindrical bridge

(b) Waist-shaped bridge

(c) Barrel-shaped bridge

Figure 1.9: Nematic bridges

From Eq. (1.13), we can see that the equilibrium defect structures are also related to the Frank constants K_{11}, K_{22} and K_{33}. For nematic liquid-crystal capillary bridges, we will show later that K_{11}/K_{33} is another important parameter.

1.6.1 Defects in Cylindrical Nematic Bridges

A cylindrical nematic bridge, as shown in Fig. 1.9a, requires that $\theta_C = \pi/2$, which implies $\gamma_{SG} = \gamma_{SL}$ by Eq. (1.57). That means that the outer medium may have to be the same as the nematics inside the bridge and thus it is impossible for this type of experiments. However, we can consider a similar experiment, which is nematics confined inside a short cylindrical tube with end caps. In this case, if the unit vectors $\mathbf{n}$ are made to be perpendicular to the boundary, i.e., the homeotropic boundary conditions, then defect cores will be inevitably formed inside the tube and at the cusps of the boundary [69–74]. Numerical study of the shapes of the defects in this short cylinder with end caps was carried out by Liang and Chen [42].

Their study claims the existence of four different types of defects: radial point, radial ring, hyperbolic point and hyperbolic ring, as illustrated in Fig. 1.10. The phase diagram they obtained further shows that:

(1) When the aspect ratio Γ is large, the ring defect is preferred over the point defect.

(2) When the Frank constant ratio K_{11}/K_{33} is large, the hyperbolic type defect is preferred over the radial type defect.

(3) There exist a transition between hyperbolic point and hyperbolic ring defects at $\Gamma \approx 7.5$, and a transition between hyperbolic point and hyperbolic ring defects at $\Gamma \approx 4.5$.

Qualitative explanations for these findings are:

(1) For the ring defect, the unit vector field $\mathbf{n}$ in the cylindrical region bounded by the ring-like defect core is only slightly distorted, and this region is large when Γ is large.

(2) The bend distortion free energy is dominant in the hyperbolic type defect while the splay distortion free energy is dominant in the radial type defect.

However, their predictions of the existence of defect transition lines require quantitative explanations. Their numerical strategy is that: by using the finite difference method, they obtained the distortion free energy for each defect at each Γ and K_{11}/K_{33}, and then they determined which one cost the least free energy. As computations shown before, the ring-like defect cores in the center and at the edges cost infinite free energy if no cut-off length scale is introduced. It is not obvious that they introduced this cut-off length; instead, they computed the relative free energy, which is the energy difference between the ring defect and the point defect at each Γ and K_{11}/K_{33}. This relative free energy can still be infinite. Our numerical work for the cylindrical bridge will be introduced in Chapter 2.

(a) Radial point (b) Radial ring

(c) Hyperbolic point (d) Hyperbolic ring

Figure 1.10: Nematic configuration on diametrical planes for the four types of defect structure. Black dots represent defect cores, yellow annular regions represent rapidly varying uniaxial nematic regions, and blue rods represent the unit vector field

1.6.2 Defects in Waist-Shaped and Barrel-Shaped Bridges

The study of defects in waist-shaped and barrel-shaped bridges, as shown in Figs. 1.9b and 1.9c, was done in Prof. Fernandez-Nieves' lab [45]. The bridge was made of 5CB with $K_{11}/K_{33} = 0.74$, therefore certain defect transition points can be obtained though the defect structure diagram was not recreated experimentally.

To make a waist-shaped bridge, the outer medium was chosen to be the air; and to make a barrel-shaped bridge, the outer medium was chosen to be water. By tuning the aspect ratio Γ, they discovered that

(1) Hyperbolic type defects exist in waist-shaped bridges and radial type defects exist in barrel-shaped bridges.

(2) There is a transition between hyperbolic point and hyperbolic ring defects at $\Gamma = 2.7 \pm 0.3$ while no radial point to radial ring transition is observed.

A qualitative explanation for (1) is that bend distortion is dominant in waist-shaped bridges and splay distortion if dominant in barrel-shaped bridges. However, (2) seems drastically different from the results of the previous numerical study by Liang and Chen, even though the shapes of the bridges are not exactly the same. Our numerical work for the waist-shaped and barrel-shaped bridges will be introduced in Chapter 3.

CHAPTER 2

NUMERICAL STUDY OF NEMATIC LIQUID-CRYSTAL BRIDGES PART I – FINITE DIFFERENCE METHOD FOR CYLINDRICAL NEMATIC BRIDGES

The experimental setting is that nematic liquid-crystal fills up a short cylindrical tube with homeotropic anchoring at the upper, lower and lateral surfaces. The important parameters are the aspect ratio Γ and the Frank constant ratio K_{11}/K_{33}. The main question is: what are the equilibrium states of defect structures for different parameters? This was answered by Liang and Chen in their numerical study of defect structures inside a closed cylinder filled with nematics [42] (for other similar numerical studies, please see Refs. [69, 70, 75–78]). In this chapter, we obtain better results by using a modified version of their original numerical strategy.

2.1 Theoretical Preparations

This is characterized as a problem of calculus of variations, and the computation process involves solving the boundary value problem (Euler-Lagrange equations subject to outer and inner boundary conditions) and evaluating the Oseen-Frank free energy functional [1, 6, 79, 80]. There are two tricky issues: (1) how to deal with the inner boundaries which include the defect cores and the branch cuts; and (2) when to introduce the cut-off length in order to make the energy finite. The short answer is: Issue (1) can be resolved by symmetry or empirical considerations; and for Issue (2), we can introduce the cut-off length either when setting up the inner boundary conditions or evaluating the energy functional.

2.1.1 Symmetry Assumptions and the Euler-Lagrange Equations

Subject to the homeotropic outer boundary conditions, the unit vector field $\mathbf{n}$ in a cylindrical nematic bridge is assumed to have cylindrical symmetry. For simplicity, we neglect the contributions from the twist distortion. Therefore we can choose an arbitrary plane through the axis of the cylinder and parametrize $\mathbf{n}$ via cylindrical coordinates (r, ϕ, z) as

$$\mathbf{n} = \cos\theta(r,z)\,\hat{\mathbf{r}} + \sin\theta(r,z)\,\hat{\mathbf{z}}. \tag{2.1}$$

We see that there is only one angular variable left (i.e., θ), and it only depends on two spatial coordinates (i.e., r and z). Furthermore, $\mathbf{n}$ is assumed to be symmetric with respect to the mid-plane (i.e., $z = 0$ plane), which enables us to restrict our consideration to one quarter of any axial plane as indicated by the purple region of Fig. 2.1.

According to the structures of the four types of defects shown in Fig. 2.2, the order parameter field $\mathbf{Q}$ can be replaced by a continuous vector field $\mathbf{n}$ on this region. Therefore, it is safe to use the Oseen-Frank free energy which is written as

$$F_d = 2\pi \int \mathrm{d}r \int \mathrm{d}z\, \mathcal{F}_d(r, z, \theta, \frac{\partial\theta}{\partial r}, \frac{\partial\theta}{\partial z}), \tag{2.2}$$

where

$$\begin{aligned}\mathcal{F}_d \equiv\, & K_{11}\frac{\cos^2\theta}{r} - r(K_{11}\sin^2\theta + K_{33}\cos^2\theta)\Big(\frac{\partial\theta}{\partial r}\Big)^2 - r(K_{11}\cos^2\theta + K_{33}\sin^2\theta)\Big(\frac{\partial\theta}{\partial z}\Big)^2 \\ & - K_{11}\sin 2\theta\frac{\partial\theta}{\partial r} + K_{11}(\cos 2\theta + 1)\frac{\partial\theta}{\partial z} - (K_{11} - K_{33})r\sin 2\theta\frac{\partial\theta}{\partial r}\frac{\partial\theta}{\partial z}.\end{aligned} \tag{2.3}$$

The associated Euler-Lagrange equation is

$$\begin{aligned}& K_{11}\frac{\sin 2\theta}{r} + r\sin 2\theta(K_{11} - K_{33})\Big(\Big(\frac{\partial\theta}{\partial r}\Big)^2 - \Big(\frac{\partial\theta}{\partial z}\Big)^2\Big) \\ & - 2r\cos 2\theta(K_{11} - K_{33})\frac{\partial\theta}{\partial r}\frac{\partial\theta}{\partial z} + 2(K_{11}\sin^2\theta + K_{33}\cos^2\theta)\frac{\partial\theta}{\partial r} \\ & - \sin 2\theta(K_{11} - K_{33})\frac{\partial\theta}{\partial z} + 2r(K_{11}\sin^2\theta + K_{33}\cos^2\theta)\frac{\partial^2\theta}{\partial r^2}\end{aligned} \tag{2.4}$$

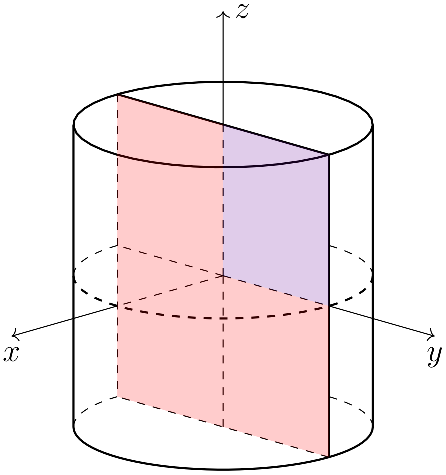

Figure 2.1: An axial plane in a cylinder

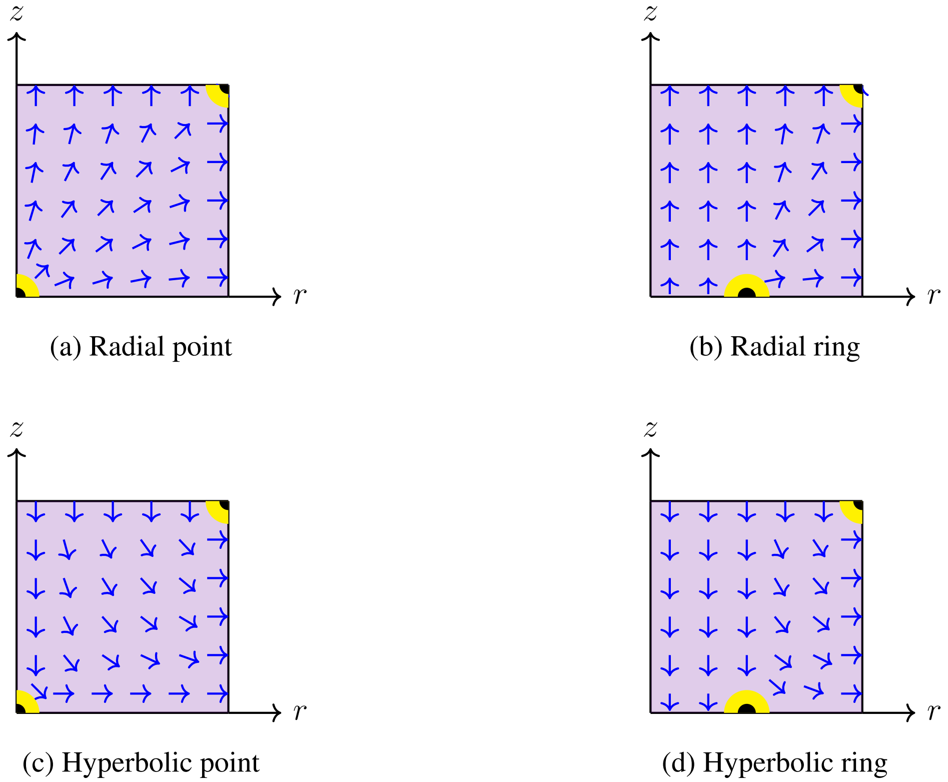

(a) Radial point

(b) Radial ring

(c) Hyperbolic point

(d) Hyperbolic ring

Figure 2.2: One quarter of the axial planes for the four types of defect structures; blue arrows represent unit vectors

$$+ 2r(K_{11}\cos^2\theta + K_{33}\sin^2\theta)\frac{\partial^2\theta}{\partial z^2} - 2r\sin 2\theta(K_{11} - K_{33})\frac{\partial^2\theta}{\partial r\partial z} = 0.$$

2.1.2 Boundary Conditions

Let a denote the radius of the ring-like defect core. Based on whether the cut-off length is introduced at this stage, there are two types of boundary conditions for the defect structures.

Boundary Conditions (A)

No cut-off length is introduced, therefore the vector field $\mathbf{n}$ can experience a jump in its direction when crossing the defect core. As a result, the complete boundary conditions are written as

Radial Point

$$\begin{cases} \theta(r,0) = 0 \\ \theta(r,\frac{H}{2}) = \frac{\pi}{2} \\ \theta(0,z) = \frac{\pi}{2} \\ \theta(R,z) = 0 \end{cases} \tag{2.5}$$

Hyperbolic Point

$$\begin{cases} \theta(r,0) = 0 \\ \theta(r,\frac{H}{2}) = -\frac{\pi}{2} \\ \theta(0,z) = -\frac{\pi}{2} \\ \theta(R,z) = 0 \end{cases} \tag{2.6}$$

Radial Ring

$$\begin{cases} \theta(r<a,0)=\frac{\pi}{2} \\ \theta(r>a,0)=0 \\ \theta(r,\frac{H}{2})=\frac{\pi}{2} \\ \theta(0,z)=\frac{\pi}{2} \\ \theta(R,z)=0 \end{cases} \tag{2.7}$$

Hyperbolic Ring

$$\begin{cases} \theta(r<a,0)=-\frac{\pi}{2} \\ \theta(r>a,0)=0 \\ \theta(r,\frac{H}{2})=-\frac{\pi}{2} \\ \theta(0,z)=-\frac{\pi}{2} \\ \theta(R,z)=0 \end{cases} \tag{2.8}$$

where a is a variable. These boundary conditions are illustrated in Fig. 2.3.

Boundary Conditions (B)

A finite cut-off region is introduced which contains the defect core. Then another issue arises as to how to determine $\mathbf{n}$ on their boundaries. We address this issue by dealing with the following two cases.

(**1**) The vector field $\mathbf{n}$ on the toroidal surface surrounding a ring-like core: This case includes the ring-like cores at the mid-plane for radial ring or hyperbolic ring defects, as well as the ones at the top right corner for all types of defects. These ring-like cores are residing within tori of large major radii and small minor radii of length $b/2$. Because b is very small, so it is safe to assume that $\mathbf{n}$ on the surface of the toroid is essentially determined by the proximity of the defect (without regard to the bulk configuration), and that curvature of the defect line has a negligible effect. To determine the condition of $\mathbf{n}$ on the surface of the toroid, it is convenient to adopt Cartesian coordinates (x, y) centered on the defect as

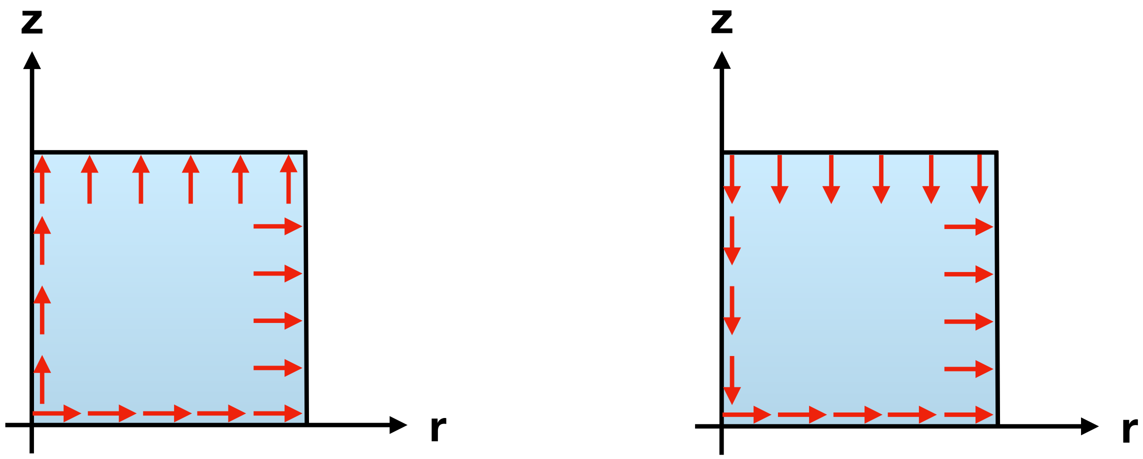

(a) Radial point (b) Hyperbolic point

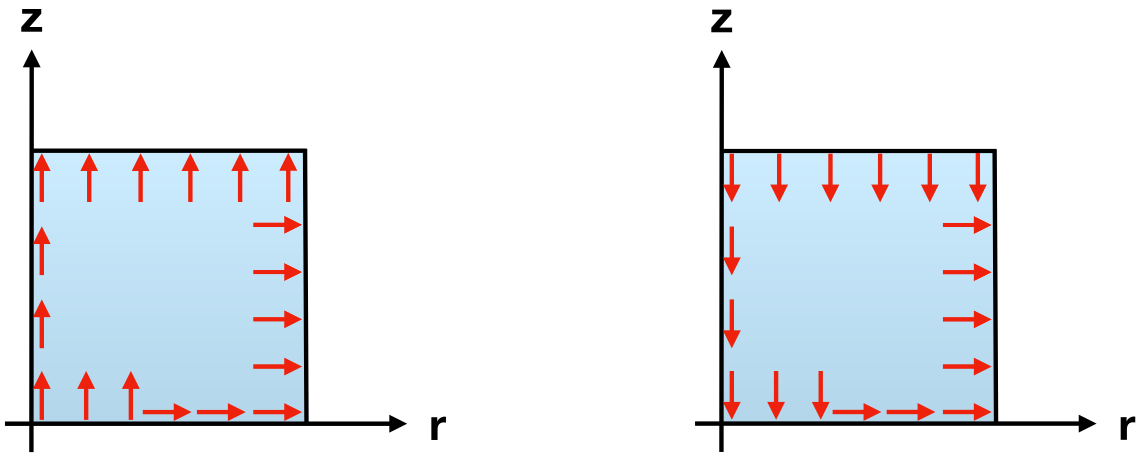

(c) Radial ring (d) Hyperbolic ring

Figure 2.3: Boundary conditions (A)

illustrated in Fig. 2.4. Thus, we write

$$\mathbf{n}(x, y) = \cos\theta(x, y)\,\hat{\mathbf{x}} + \sin\theta(x, y)\,\hat{\mathbf{y}}, \tag{2.9}$$

and, upon substituting this parametrization into Eq. (1.13), we arrive at the reduced free energy functional

$$F_d = L \int \frac{1}{2}\Big[(K_{11}\sin^2\theta + K_{33}\cos^2\theta)\Big(\frac{\partial\theta}{\partial x}\Big)^2 + (K_{11}\cos^2\theta + K_{33}\sin^2\theta)\Big(\frac{\partial\theta}{\partial y}\Big)^2$$

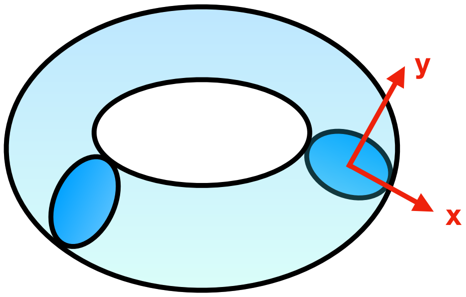

Figure 2.4: Cartesian coordinates on the cross-section of a ring-like defect core

$$- (K_{11} - K_{33}) \sin 2\theta \frac{\partial\theta}{\partial x}\frac{\partial\theta}{\partial y}\Big] \mathrm{d}x\mathrm{d}y, \tag{2.10}$$

where L is the length of the equivalent straight defect line. The associated Euler-Lagrange equation for $\theta(x, y)$ is then

$$\begin{aligned} &2(K_{11}\sin^2\theta + K_{33}\cos^2\theta)\frac{\partial^2\theta}{\partial x^2} + 2(K_{11}\cos^2\theta + K_{33}\sin^2\theta)\frac{\partial^2\theta}{\partial y^2} \\ &- (K_{11} - K_{33})\Big[- \sin 2\theta\Big(\frac{\partial\theta}{\partial x}\Big)^2 + \sin 2\theta\Big(\frac{\partial\theta}{\partial y}\Big)^2 \\ &+ 2\cos 2\theta\frac{\partial\theta}{\partial x}\frac{\partial\theta}{\partial y} + 2\sin 2\theta\frac{\partial^2\theta}{\partial x\partial y}\Big] = 0. \end{aligned} \tag{2.11}$$

We expect that the vector field $\mathbf{n}$ in the immediate vicinity of the defect core has cylindrical symmetry around it; therefore exchanging the independent variables (x, y) for (r, ϕ) via $(x, y) = r(\cos\phi, \sin\phi)$, and observing that $\theta = \theta(\phi)$, Equation (2.11) becomes the following nonlinear ordinary differential equation

$$\frac{\mathrm{d}^2\theta}{\mathrm{d}\phi^2} + \epsilon\Big[\cos(2\theta - 2\phi)\frac{\mathrm{d}^2\theta}{\mathrm{d}\phi^2} - \sin(2\theta - 2\phi)\Big(\frac{\mathrm{d}\theta}{\mathrm{d}\phi}\Big)^2 + 2\sin(2\theta - 2\phi)\frac{\mathrm{d}\theta}{\mathrm{d}\phi}\Big] = 0, \tag{2.12}$$

where $\epsilon \equiv (K_{11} - K_{33})/(K_{11} + K_{33})$, and the boundary condition is $\theta(2\pi) - \theta(0) = m\,\pi$ with m being an integer. Although Eq. (2.12) is nonlinear, some common liquid crystals usually have $|\epsilon| \ll 1$, therefore we may apply perturbation theory in ϵ [1]. To first order, the solution to Eq. (2.12) is

$$\theta(\phi) \approx \begin{cases} \frac{m}{2}\phi + C \text{ (for } m = 2\text{)}, \\ \\ \frac{m}{2}\phi + C + \epsilon\frac{m^2-4m}{4(m-2)^2}\Big[-\sin\left((m-2)\phi + 2C\right) + \sin(2C)\Big] \text{ (for } m \neq 2\text{)}, \end{cases} \tag{2.13}$$

where C is a constant of integration. With regard to the ring-like core at top right corner, we have $(m, C) = (-2, -\pi/2)$ for the radial defect and $(m, C) = (2, \pi/2)$ for the hyperbolic defect. With regard to the ring-like core at the mid-plane, we have $(m, C) = (1, 0)$ for the radial ring and $(m, C) = (-1, 0)$ for the hyperbolic ring.

(**2**) The vector field $\mathbf{n}$ on the spherical surface surrounding a point-like core: This case includes the point-like cores at the mid-planes for the radial point and the hyperbolic point. For convenience, we assume that the radius of the spherical surface surrounding the point equals the minor radius of the toroidal surface. Then we adopt the boundary conditions shown in Eq. (2.13), with $(m, C) = (2, 0)$ for the radial point and $(m, C) = (-2, 0)$ for the hyperbolic point.

To make it easier for numerical computations, we treat each boundary for the cut-off region as rectangular instead of circular; then the complete boundary conditions can be written as

Radial Point

$$\begin{cases} \theta(r < \frac{b}{2}, \frac{b}{2}) = \arctan \frac{b}{2r} \\ \\ \theta(r > \frac{b}{2}, 0) = 0 \\ \\ \theta(r < R - \frac{b}{2}, \frac{H}{2}) = \frac{\pi}{2} \\ \\ \theta(r > R - \frac{b}{2}, \frac{H}{2} - \frac{b}{2}) = -\arctan \frac{b}{2(R-r)} + \frac{\pi}{2} \\ \\ \theta(0, z) = \frac{\pi}{2} \\ \\ \theta(\frac{b}{2}, z < \frac{b}{2}) = \arctan \frac{2z}{b} \\ \\ \theta(R - \frac{b}{2}, z > \frac{H}{2} - \frac{b}{2}) = -\arctan \frac{H-2z}{2R-b} + \frac{\pi}{2} \\ \\ \theta(R, z) = 0 \end{cases} \tag{2.14}$$

Hyperbolic Point

$$\begin{cases} \theta(r < \frac{b}{2}, \frac{b}{2}) = -\arctan\frac{b}{2r} \\ \\ \theta(r > \frac{b}{2}, 0) = 0 \\ \\ \theta(r < R - \frac{b}{2}, \frac{H}{2}) = -\frac{\pi}{2} \\ \\ \theta(r > R - \frac{b}{2}, \frac{H}{2} - \frac{b}{2}) = \arctan\frac{b}{2(R-r)} - \frac{\pi}{2} \\ \\ \theta(0, z > \frac{b}{2}) = -\frac{\pi}{2} \\ \\ \theta(\frac{b}{2}, z < \frac{b}{2}) = -\arctan\frac{2z}{b} \\ \\ \theta(R - \frac{b}{2}, z > \frac{H}{2} - \frac{b}{2}) = \arctan\frac{H-2z}{2R-b} - \frac{\pi}{2} \\ \\ \theta(R, z) = 0 \end{cases} \tag{2.15}$$

Radial Ring

$$\begin{cases} \theta(r < a - \frac{b}{2}, 0) = \frac{\pi}{2} \\[2em] \theta(a - \frac{b}{2} < r < a, \frac{b}{2}) = \frac{1}{2}\left[\arctan\frac{b}{2(r-a)} + \pi\right] - \frac{3}{4}\epsilon\sin\left[\arctan\frac{b}{2(r-a)} + \pi\right] \\[2em] \theta(a < r < a + \frac{b}{2}, \frac{b}{2}) = \frac{1}{2}\arctan\frac{b}{2(r-a)} - \frac{3}{4}\epsilon\sin\left[\arctan\frac{b}{2(r-a)}\right] \\[2em] \theta(r > a + \frac{b}{2}, 0) = 0 \\[2em] \theta(r < R - \frac{b}{2}, \frac{H}{2}) = \frac{\pi}{2} \\[2em] \theta(r > R - \frac{b}{2}, \frac{H}{2} - \frac{b}{2}) = -\arctan\frac{b}{2(R-r)} + \frac{\pi}{2} \\[2em] \theta(0, z) = \frac{\pi}{2} \\[2em] \theta(a - \frac{b}{2}, z < \frac{b}{2}) = \frac{1}{2}(\pi - \arctan\frac{2z}{b}) - \frac{3}{4}\epsilon\sin(\pi - \arctan\frac{2z}{b}) \\[2em] \theta(a + \frac{b}{2}, z < \frac{b}{2}) = \frac{1}{2}\arctan\frac{2z}{b} - \frac{3}{4}\epsilon\sin(\arctan\frac{2z}{b}) \\[2em] \theta(R - \frac{b}{2}, z > \frac{H}{2} - \frac{b}{2}) = -\arctan\frac{H-2z}{2R-b} + \frac{\pi}{2} \\[2em] \theta(R, z) = 0 \end{cases} \tag{2.16}$$

Hyperbolic Ring

$$\begin{cases} \theta(r < a - \frac{b}{2}, 0) = -\frac{\pi}{2} \\ \theta(a - \frac{b}{2} < r < a, \frac{b}{2}) = -\frac{1}{2}\left[\arctan\frac{b}{2(r-a)} + \pi\right] + \frac{5}{4}\epsilon\sin\left[3\arctan\frac{b}{2(r-a)} + 3\pi\right] \\ \theta(a < r < a + \frac{b}{2}, \frac{b}{2}) = -\frac{1}{2}\arctan\frac{b}{2(r-a)} + \frac{5}{4}\epsilon\sin\left[3\arctan\frac{b}{2(r-a)}\right] \\ \theta(r > a + \frac{b}{2}, 0) = 0 \\ \theta(r < R - \frac{b}{2}, \frac{H}{2}) = -\frac{\pi}{2} \\ \theta(r > R - \frac{b}{2}, \frac{H}{2} - \frac{b}{2}) = \arctan\frac{b}{2(R-r)} - \frac{\pi}{2} \\ \theta(0, z) = -\frac{\pi}{2} \\ \theta(a - \frac{b}{2}, z < \frac{b}{2}) = -\frac{1}{2}(\pi - \arctan\frac{2z}{b}) + \frac{5}{4}\epsilon\sin(3\pi - 3\arctan\frac{2z}{b}) \\ \theta(a + \frac{b}{2}, z < \frac{b}{2}) = -\frac{1}{2}\arctan\frac{2z}{b} + \frac{5}{4}\epsilon\sin(3\arctan\frac{2z}{b}) \\ \theta(R - \frac{b}{2}, z > \frac{H}{2} - \frac{b}{2}) = \arctan\frac{H-2z}{2R-b} - \frac{\pi}{2} \\ \theta(R, z) = 0 \end{cases} \tag{2.17}$$

where a is a variable. These boundary conditions are illustrated in Fig. 2.5. Note that, strictly speaking, θ on the circular boundary of the cut-off region is asymmetric, and θ

on the rectangular boundary of the cut-off region is different from the one on the circular boundary. However, Eq. (2.13) is a good approximation if the cut-off region is small enough; and the errors can be treated as a change to the defect core energy, which is unlikely to affect the qualitatively features of the defect transitions.

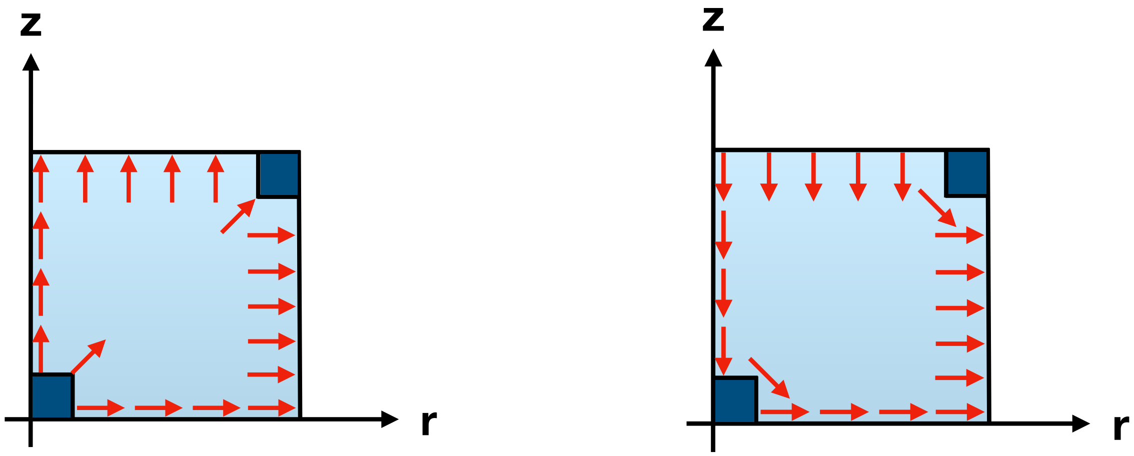

(a) Radial point

(b) Hyperbolic point

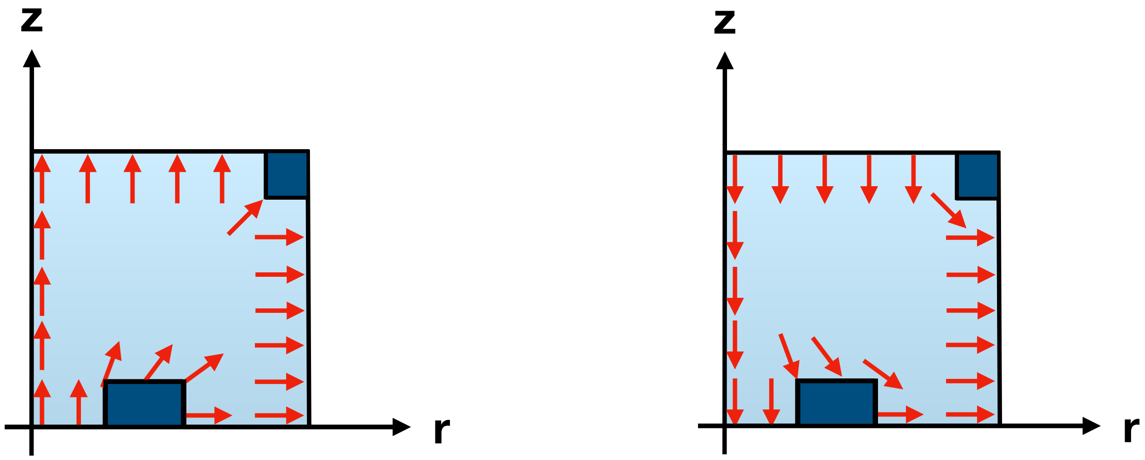

(c) Radial ring

(d) Hyperbolic ring

Figure 2.5: Boundary conditions (B)

2.1.3 Solving the Boundary Value Problem and Evaluating the Energy Functional

There are two kinds of boundary value problems: [a] solving Eq. (2.4) subject to boundary conditions (2.5) – (2.8), and [b] solving Eq. (2.4) subject to boundary conditions (2.14) – (2.17). The difference between the resulting solutions θ outside the cut-off regions (i.e., the regions which is of length b and contains the defect core) is minimal and can be ignored.

To determine the ground state, we need to substitute the solutions θ for different ring radii a into the energy functional Eq. (2.3) and search for the state which costs the lowest free energy. For both of the boundary value problems, the energy functional should not be evaluated on the cut-off regions, because: for boundary value problem (a), these regions can cost infinite free energy; for boundary value problem (b), θ is not defined on these regions.

To summarize, there are two equivalent methods based on Boundary Conditions (A) or (B). And the former is mentioned in Ref. [81]. In the numerical study conducted by Liang and Chen, it is not obvious that the cut-off length has been introduced [42]. And computing the energy difference between the ring defect and point defect at each Γ and K_{11}/K_{33} does not suffice to obtain a finite energy. Therefore, their results are not convincing, and we need to redo the numerical computations.

2.2 Numerical Strategy

To solve this problem numerically, we adopt finite difference method [82–86].

To start with, we choose a set of equally-spaced lattices on this rectangular domain of length R and width $H/2$. For all the defect structures we exhaust, we fix the value of $H/2$, and vary the value of R to achieve different values of aspect ratio Γ. For fixed $H/2$, we choose 33 lattice points; then for R, we choose $(2R/H) \cdot 32 + 1$ lattice points [note that, $(2R/H) \cdot 32 + 1$ is not necessarily an integer; but we define it to be of an integer type, therefore the number of the lattice points is the largest integer smaller than $(2R/H) \cdot 32 + 1$].

Secondly, we discretize Eq. (2.4) and the boundary conditions (2.5) – (2.8) or (2.14) – (2.17). For our study, we consider two different use of boundary conditions:

Case (1): Boundary Conditions (B) for both of the defect cores at the mid-planes and those at the top right corners;

Case (2): Boundary Conditions (A) for the defect cores at the top right corners and

Boundary Conditions (B) for those at the mid-planes.

Thirdly, we use the successive over-relaxation method to solve the difference equation resulting from the discretization of Eq. (2.4); see Ref. [82, 87, 88].

Finally, we evaluate the discretized version of the free energy functional Eq. (2.3). Note that for Case (2), when we evaluate this functional, we should leave out a thin layer of lattices (of thickness b) on the rightmost edge which contains the core at the top right corner as illustrated in Fig. 2.6. The reasons will be explained in Chapter 3.

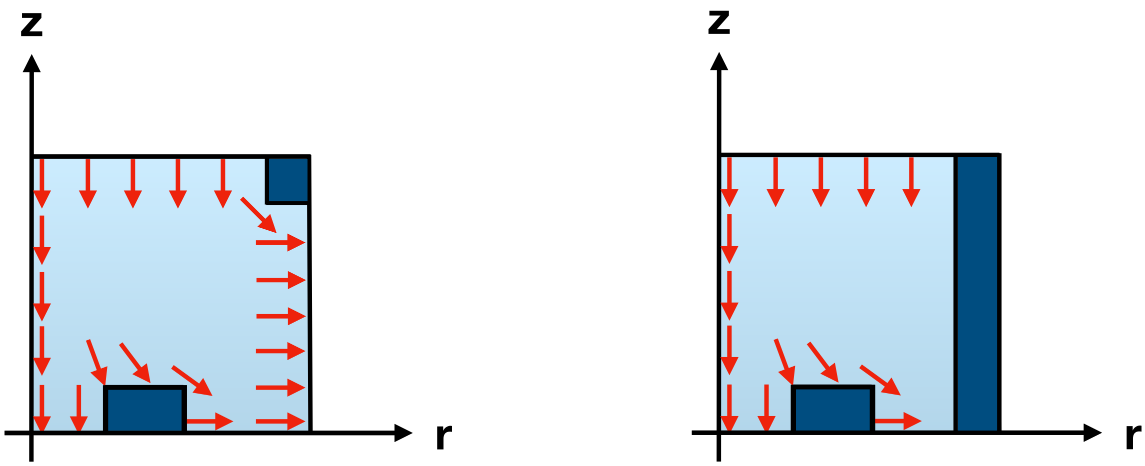

(a) Case (1): the defect cores (deep blue regions) are not in the domain of integration

(b) Case (2): the defect core and the thin layer (deep blue regions) are not in the domain of integration

Figure 2.6: The difference between Case (1) and Case (2) in the evaluation of energy functional

As mentioned before, we suspect that the original algorithm designed by Liang and Chen [42] does not converge, which leads to the possible problematic results. Here, we verify the convergence of our algorithm by plotting the energy landscapes of few examples as shown in Fig. 2.7.

For the source code, please visit our github repositories; see Ref. [89] for Case (1) and Ref. [90] for Case (2).

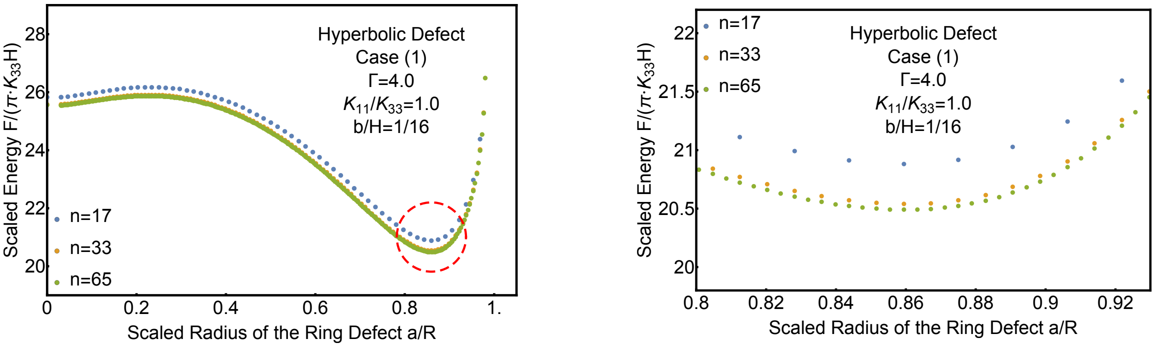

(a) The drawing of energy landscapes

(b) Enlarged drawing

Figure 2.7: Energy landscapes with different mesh densities. The difference between the landscapes with two neighboring mesh densities becomes smaller as the mesh densities increase

2.3 Results Part I – Equilibrium Defect Structures

As expected, by tuning the parameters Γ and K_{11}/K_{33}, we obtain four different equilibrium defect structures: hyperbolic point, hyperbolic ring, radial point (small ring) and radial ring, which are shown in Fig. 2.8. The point and ring defects are distinguished by whether the radius of the ring-like defect core is almost zero or nonzero. While it is easy to obtain the hyperbolic point defect, the radial defects usually have nonzero radii, so we consider those with very small radii as the radial point defects.

2.4 Results Part II – Free Energy Landscapes

For each Γ and K_{11}/K_{33}, there are two energy landscapes: one is for the hyperbolic defect and the other is for the radial defect, as shown in Fig. 2.9. The x-axis is for the scaled radius of the ring defect, denoted by a/R; the y-axis is for the scaled energy density, denoted by $F/(\pi K_{33} H \Gamma^2)$. Then the point defect is represented by the dot at $a/R = 0$, and the ring defect is represented by any dot at nonzero a/R. We can see that the landscapes have several local minima representing the equilibrium states, one of which is the global minimum representing the ground state. For the sake of simple exposition, we choose to show the landscape that contains the ground states.

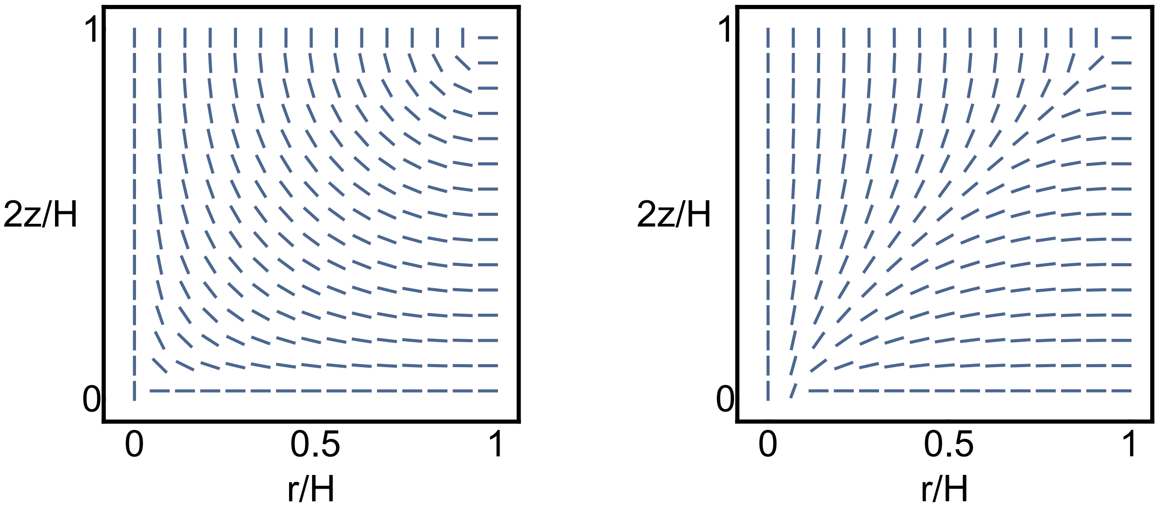

(a) Hyperbolic point ($\Gamma = 1$, $K_{11}/K_{33} = 1$) (b) Radial point ($\Gamma = 1$, $K_{11}/K_{33} = 0.1$)

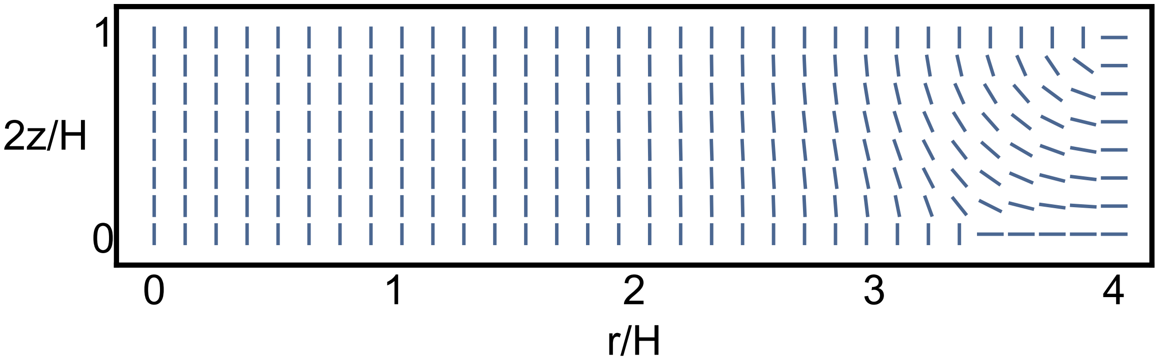

(c) Hyperbolic ring ($\Gamma = 4$, $K_{11}/K_{33} = 1$)

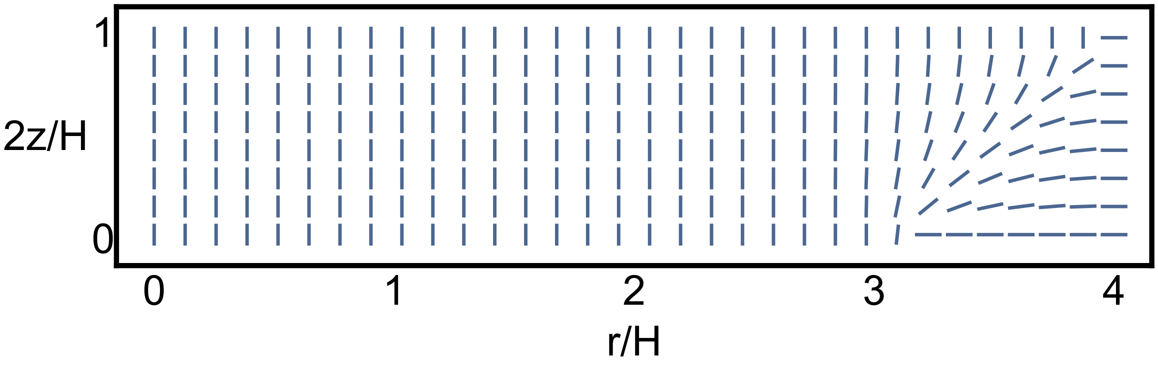

(d) Radial ring ($\Gamma = 4$, $K_{11}/K_{33} = 0.1$)

Figure 2.8: Examples of equilibrium defect structures (shown in one quarter of the axial plane)

To better understand the properties of the free energy landscapes, we consider three general categories: [a] Case (1) and cut-off length $b/H = 1/32$, [b] Case (1) and cut-off length $b/H = 1/16$, and [c] Case (2) and cut-off length $b/H = 1/32$. For each category, we consider hyperbolic types with $\Gamma = 1, 2, 3, 4$ and $K_{11}/K_{33} = 1, 2, 3, 4$ as well as radial types with $\Gamma = 1, 2, 3, 4$ and $K_{11}/K_{33} = 0.1, 0.2, 0.3, 0.4$; see Figs. 2.10 – 2.18.

Note that in Figs. 2.10 – 2.15, we choose scaled energy density $F/(\pi K_{33} H \Gamma^2)$. It may be a better quantity to characterize the energy costs by different defect structures than scaled energy $F/(\pi K_{33} H)$, because when H is fixed, the system with large Γ has a large volume and is surely expected to have a large total energy. Figures 2.10 – 2.15 show that, in general, the equilibrium ring defect has lower average energy density than equilibrium point defect, which is consistent with the fact that a larger portion of the ring defect structure is weakly distorted as shown in Fig. 2.8.

2.4.1 The Effects of Aspect Ratios

Hyperbolic Defects

For hyperbolic type of defects, Figures. 2.10, 2.12, 2.14, 3.11a, 3.12a and 2.18a show that: when Γ is small, there is only one minimum representing a point defect; when Γ increases, a second minimum which represents a ring defect appears, decreases its energy and slowly increases its radius. Therefore, we observe a hyperbolic point defect when Γ is small and a hyperbolic ring defect when Γ is large.

Radial Defects

For radial type of defects, Figures. 2.11, 2.13, 2.15, 3.11b, 3.12b and 2.18b show that: whatever the value of Γ is, there is always one minimum representing a ring defect; when Γ is very small, the radius of the equilibrium ring is so small that it may be treated as a point defect; and then, the radius increases as Γ increases. Therefore, we observe a radial point (small ring) defect when Γ is small and a radial ring defect when Γ is large.

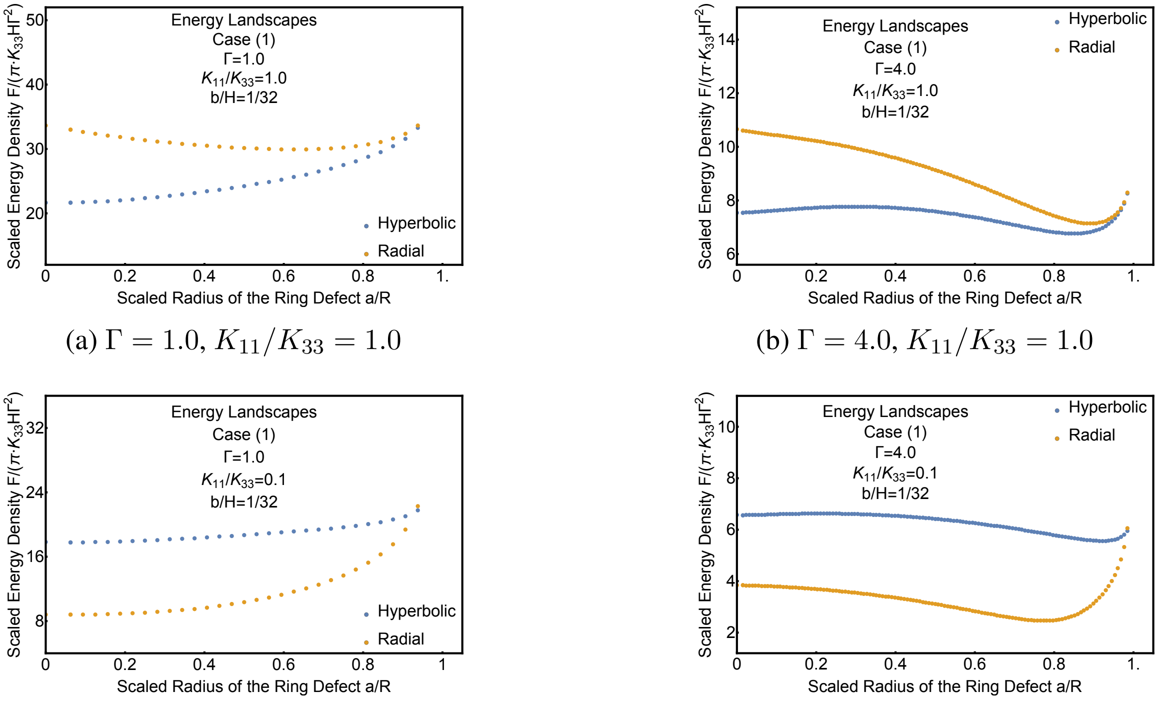

(a) $\Gamma = 1.0$, $K_{11}/K_{33} = 1.0$

(b) $\Gamma = 4.0$, $K_{11}/K_{33} = 1.0$

(c) $\Gamma = 1.0$, $K_{11}/K_{33} = 0.1$

(d) $\Gamma = 4.0$, $K_{11}/K_{33} = 0.1$

Figure 2.9: Energy landscapes for hyperbolic and radial types at the same Γ and K_{11}/K_{33}

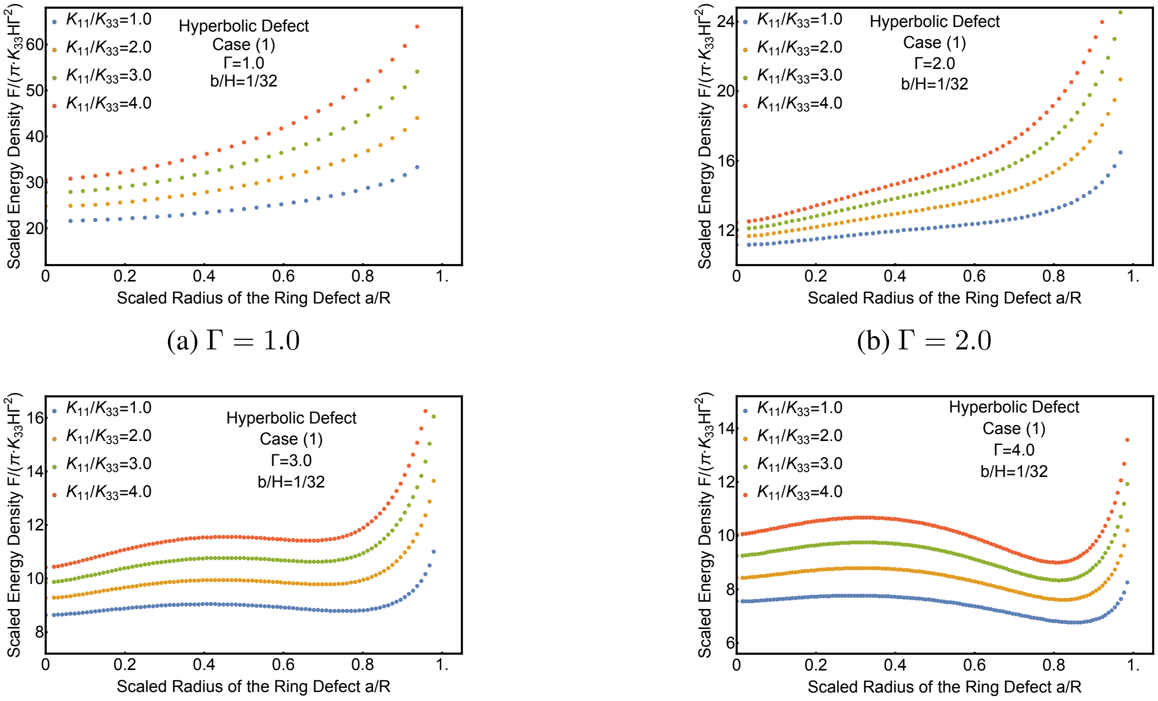

(a) $\Gamma = 1.0$

(b) $\Gamma = 2.0$

(c) $\Gamma = 3.0$

(d) $\Gamma = 4.0$

Figure 2.10: Energy landscapes for hyperbolic types of defects with Case (1) and $b/H = 1/32$

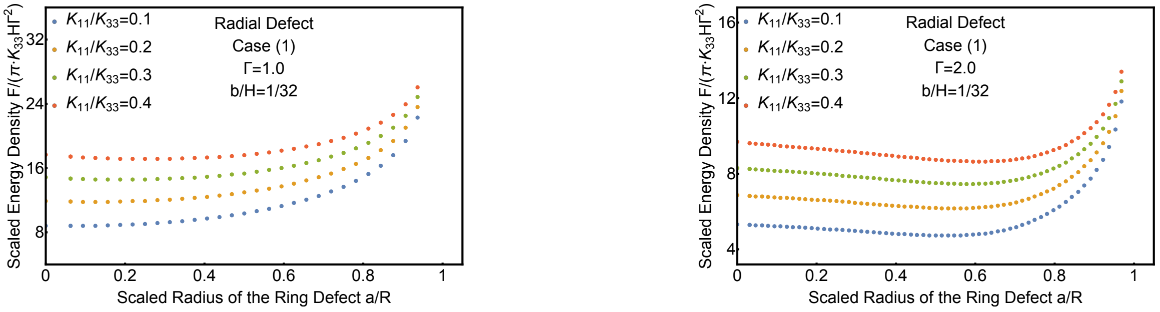

(a) $\Gamma = 1.0$ (b) $\Gamma = 2.0$

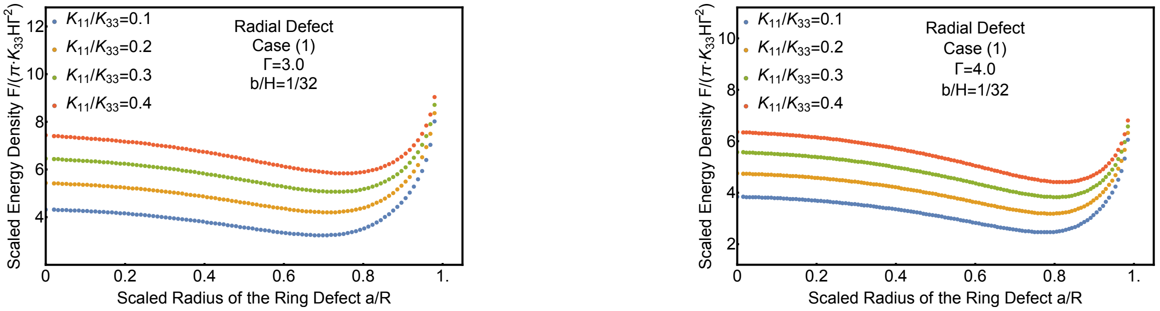

(c) $\Gamma = 3.0$ (d) $\Gamma = 4.0$

Figure 2.11: Energy landscapes for radial types of defects with Case (1) and $b/H = 1/32$

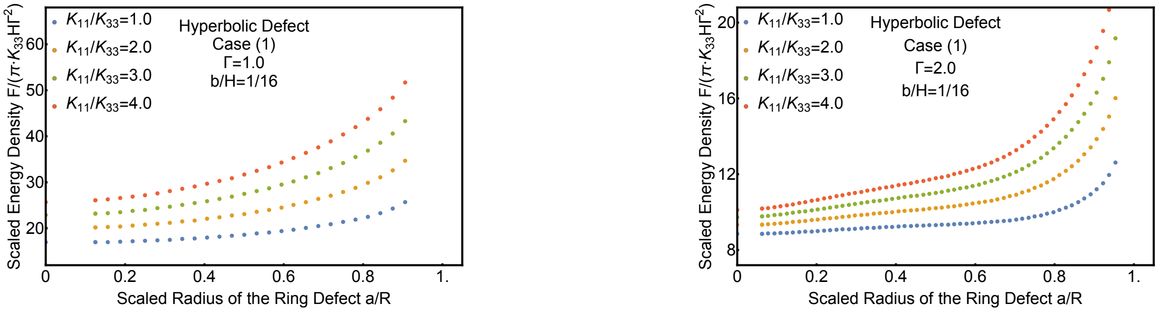

(a) $\Gamma = 1.0$ (b) $\Gamma = 2.0$

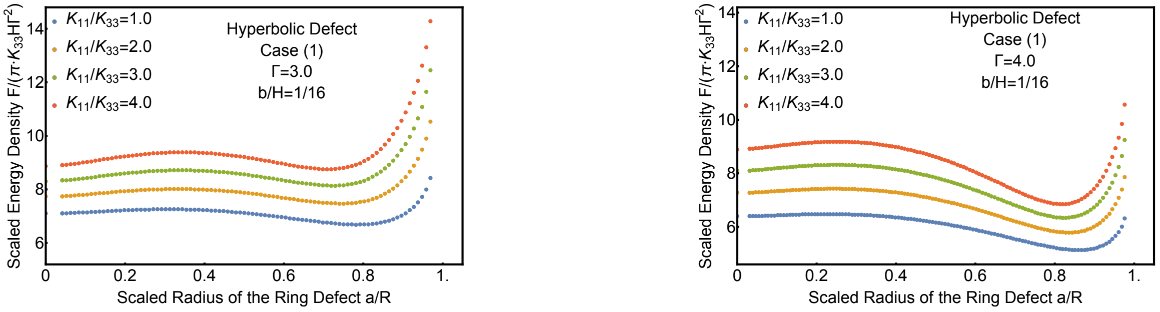

(c) $\Gamma = 3.0$ (d) $\Gamma = 4.0$

Figure 2.12: Energy landscapes for hyperbolic types of defects with Case (1) and $b/H = 1/16$

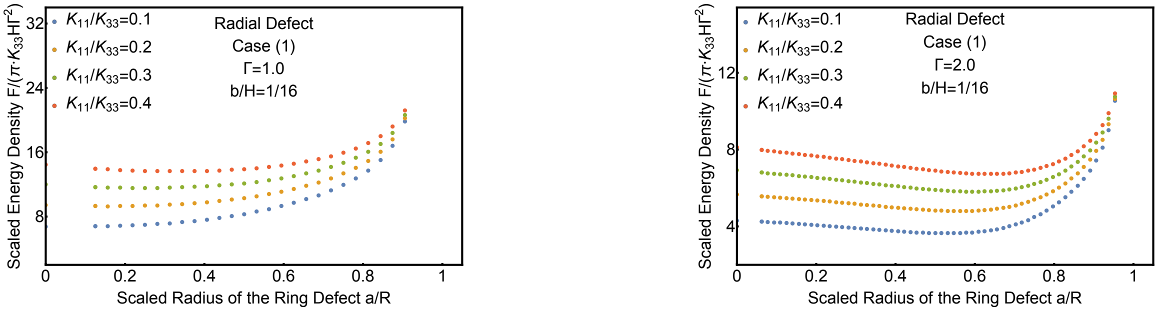

(a) $\Gamma = 1.0$ (b) $\Gamma = 2.0$

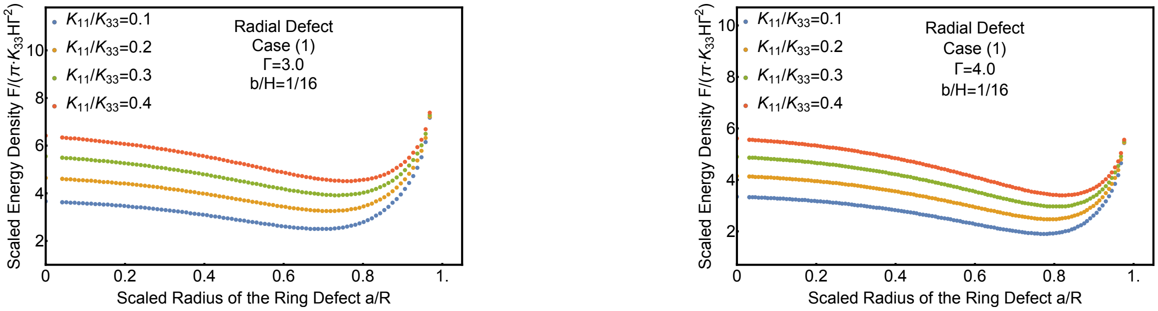

(c) $\Gamma = 3.0$ (d) $\Gamma = 4.0$

Figure 2.13: Energy landscapes for radial types of defects with Case (1) and $b/H = 1/16$

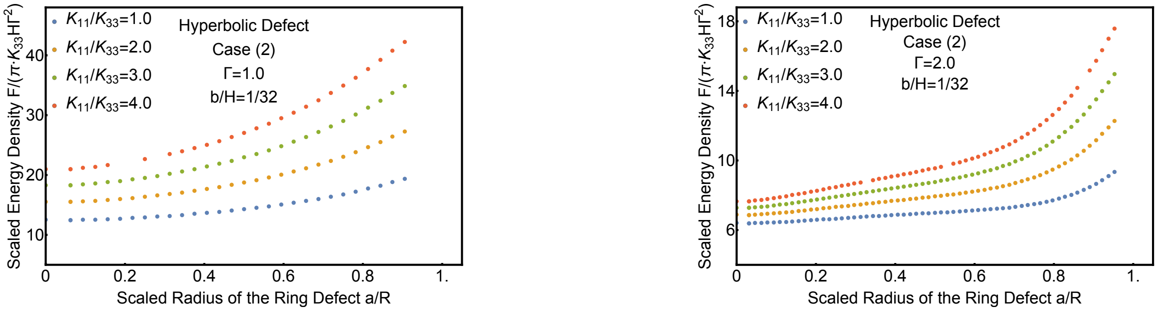

(a) $\Gamma = 1.0$ (b) $\Gamma = 2.0$

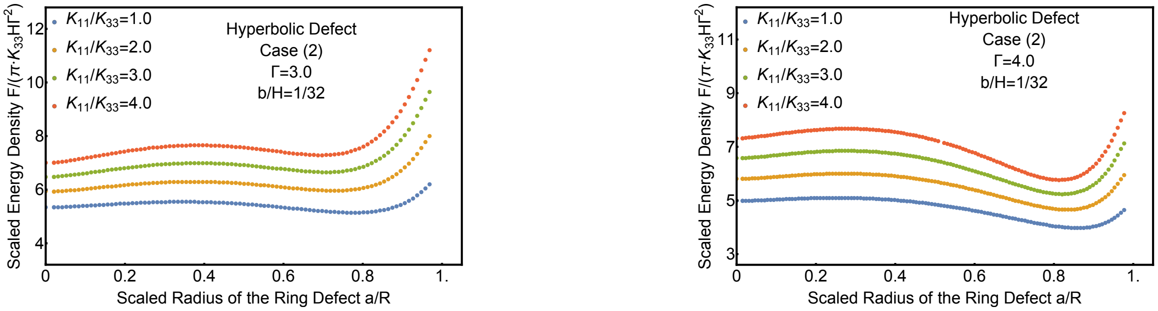

(c) $\Gamma = 3.0$ (d) $\Gamma = 4.0$

Figure 2.14: Energy landscapes for hyperbolic types of defects with Case (2) and $b/H = 1/32$

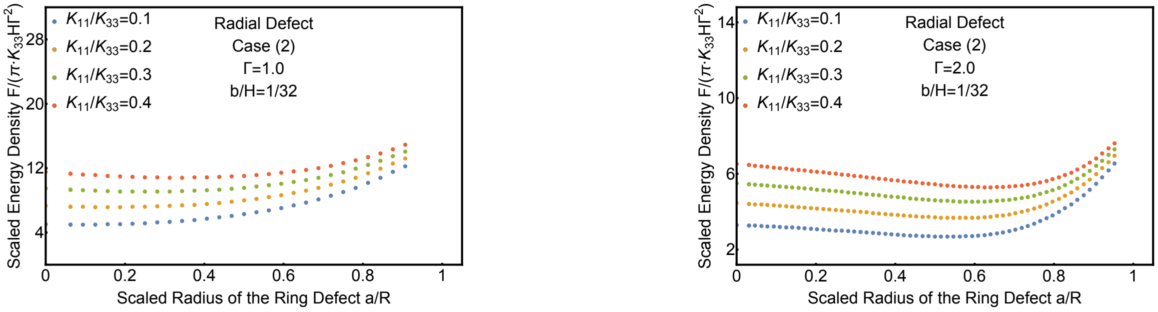

(a) $\Gamma = 1.0$ (b) $\Gamma = 2.0$

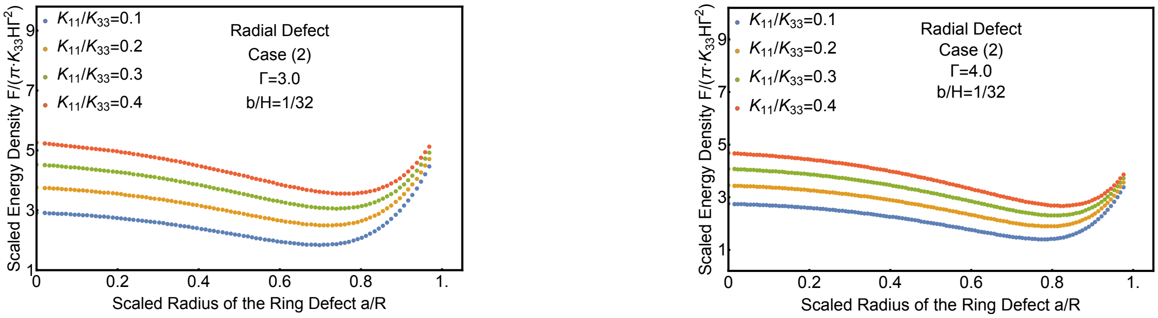

(c) $\Gamma = 3.0$ (d) $\Gamma = 4.0$

Figure 2.15: Energy landscapes for radial types of defects with Case (2) and $b/H = 1/32$

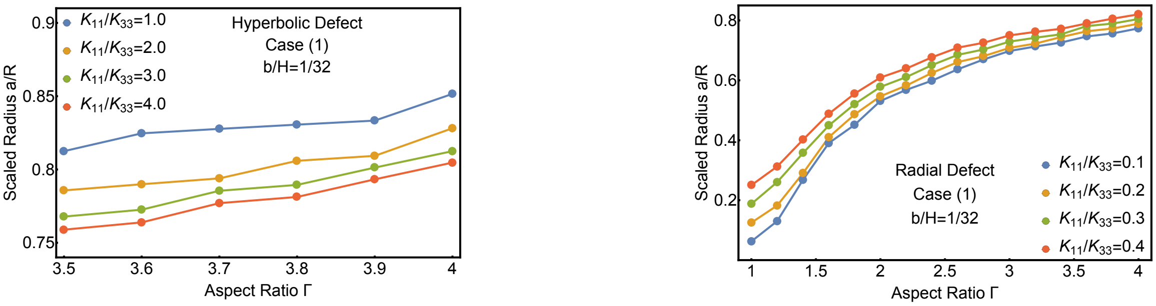

(a) Hyperbolic (b) Radial

Figure 2.16: Radii of the equilibrium ring defects with Case (1) and $b/H = 1/32$

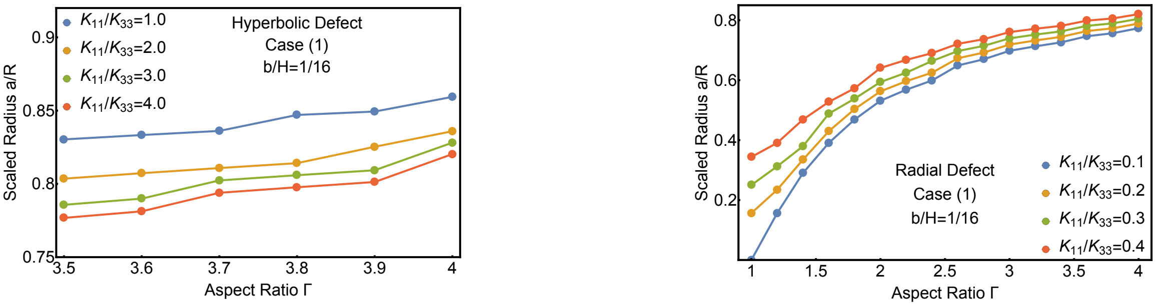

(a) Hyperbolic (b) Radial

Figure 2.17: Radii of the equilibrium ring defects with Case (1) and $b/H = 1/16$

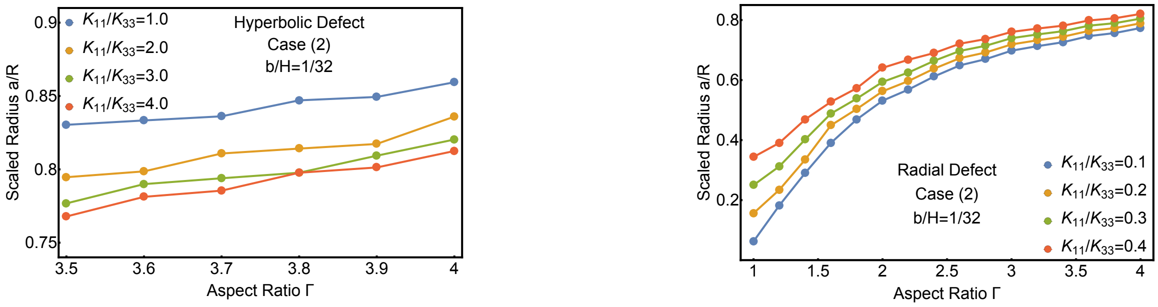

(a) Hyperbolic

(b) Radial

Figure 2.18: Radii of the equilibrium ring defects with Case (2) and $b/H = 1/32$

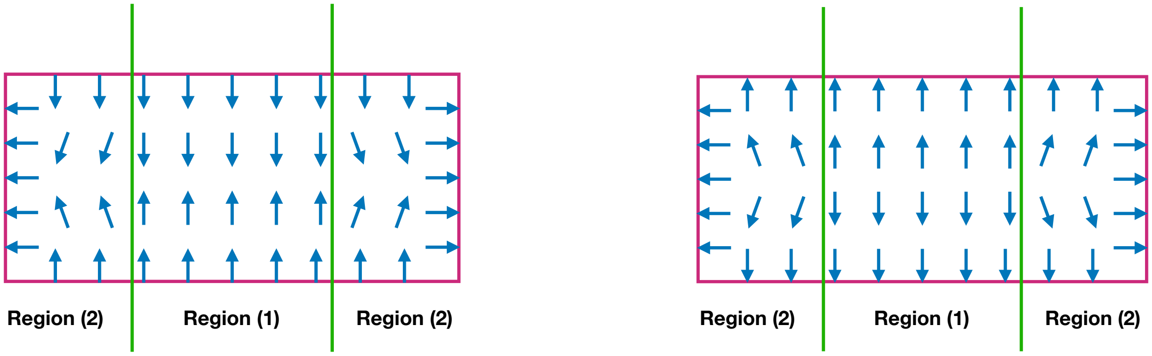

(a) Hyperbolic

(b) Radial

Figure 2.19: Regions in ring defects. Region (1) is weakly distorted; Region (2) is highly distorted

One may ask: why is the ring defect preferred over the point defect when Γ is large? A heuristic argument is in the following.

Let us first divide the cylinder into two regions as shown in Fig. 2.19: Region (1) is the cylinder bounded by the ring-like defect core with radius a and height H; and Region (2) is the remaining hollow cylinder. The vector field $\mathbf{n}$ is almost uniformly distributed in Region (1) while it is highly distorted in Region (2). Therefore the average energy density is almost zero in Region (1) while it is large in Region (2). In addition, the larger of the rescaled radius a/R of the ring-like core, the higher of the average energy density in Region (2).

We may imagine the competition between these two regions as follows: for fixed H and R, the system would like to increase Region (1) to reduce the total energy; however, if

Region (2) gets too small, its contribution to the total energy will increase due to its very high average energy density; as a result, Region (1) cannot be too large and Region (2) cannot be too small.

If the aspect ratio Γ is small, then in order not to make Region (2) too small, Region (1) may have to be zero, thus we may observe a point defect. If Γ is large, then there will be enough room for Region (1) to exist, therefore we may observe a ring defect.

2.4.2 The Effects of Frank Constant Ratios

Figures. 2.10 – 2.15 show that, when K_{33} is fixed, the defect structure with larger K_{11} has higher free energy. This is consistent with the fact that larger K_{11} results in larger splay distortion energy.

Moreover, by comparing the hyperbolic defects [i.e., Figs. 2.10, 2.12, 2.14, 3.11a, 3.12a and 2.18a] with the radial defects [i.e., Figs. 2.11, 2.13, 2.15, 3.11b, 3.12b and 2.18b], we observe that, even though the change of K_{11}/K_{33} in the radial defects is one order in magnitude less than the change in the hyperbolic defects, the changes of the energies are of the same order in both types. This can be explained by the fact that the splay distortion is more dominant in the radial defects and therefore the radial defects are more sensitive to the change of K_{11} when K_{33} is fixed.

2.4.3 The Effects of Cut-Off Lengths

In our numerical computations, we do not consider the energy inside the defect core with cut-off length b. By comparing landscapes of $b/H = 1/32$ [i.e., Figs. 2.10, 2.11] with those of $b/H = 1/16$ [i.e., Figs. 2.12, 2.13], we observe no obvious differences in the general shapes of the landscapes, and the energy difference should come from the hollow toroid (the difference of the two ring-like defect cores) with thickness $H/64$, major radius a and minor radius $H/32$ as illustrated in Fig. 2.20.

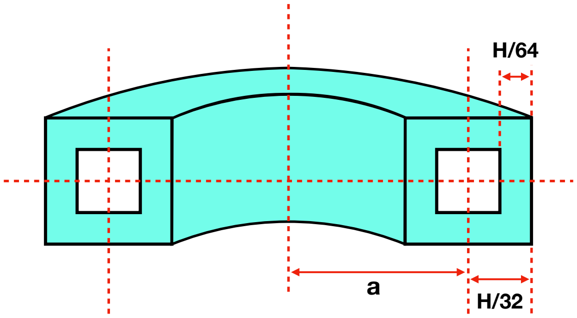

Figure 2.20: The difference between the two ring-like defect cores

Figures 2.21 and 2.22 illustrate the differences between landscapes of $b/H = 1/32$ and those of $b/H = 1/16$ [here, the scaled energy $F/(\pi K_{33}H)$ is a better choice than scaled energy density $F/(\pi K_{33}H\Gamma^2)$]. We observe that, the landscape differences are always linear functions, which is consistent with the fact that the energy difference of the two ring-like defect cores is proportional to the ring radius. Also, we notice that, the landscape differences have the same slopes for fixed K_{11}/K_{33} and have larger slopes for larger K_{11}/K_{33}, which implies that the energy density difference of the two ring-like defect cores is independent of Γ but is dependent of K_{11}/K_{33}.

Figure 2.23 illustrates the differences between the equilibrium ring radii of $b/H = 1/32$ and those of $b/H = 1/16$. We observe that the change of the cut-off length has small effect on large equilibrium rings, knowing that the accuracy of our algorithm is of order $\mathcal{O}(1/32)$. A tentative analytical justification follows.

Let b_1 and b_2 denote two cut-off lengths. And let $F = F(a)$ denote the free energy for cut-off length b_1, where a denotes the radius of the ring-like core. In another word, $F(a)$ is the total energy of the defect structure (inside the cylindrical bridge) with the radius of the ring-like core being a and the length of the cut-off region being b_1; and a can be the radius of an equilibrium ring or a non-equilibrium ring. Then the free energy for the cut-off length b_2 can be approximated by $F(a) + \Delta F(a) = F(a) + k(H) \cdot a$, where $\Delta F(a)$ represents the energy difference between the ring-like defect cores of these two states. Here we make an approximation that the field $\mathbf{n}$ is changed very little by different cut-off lengths,

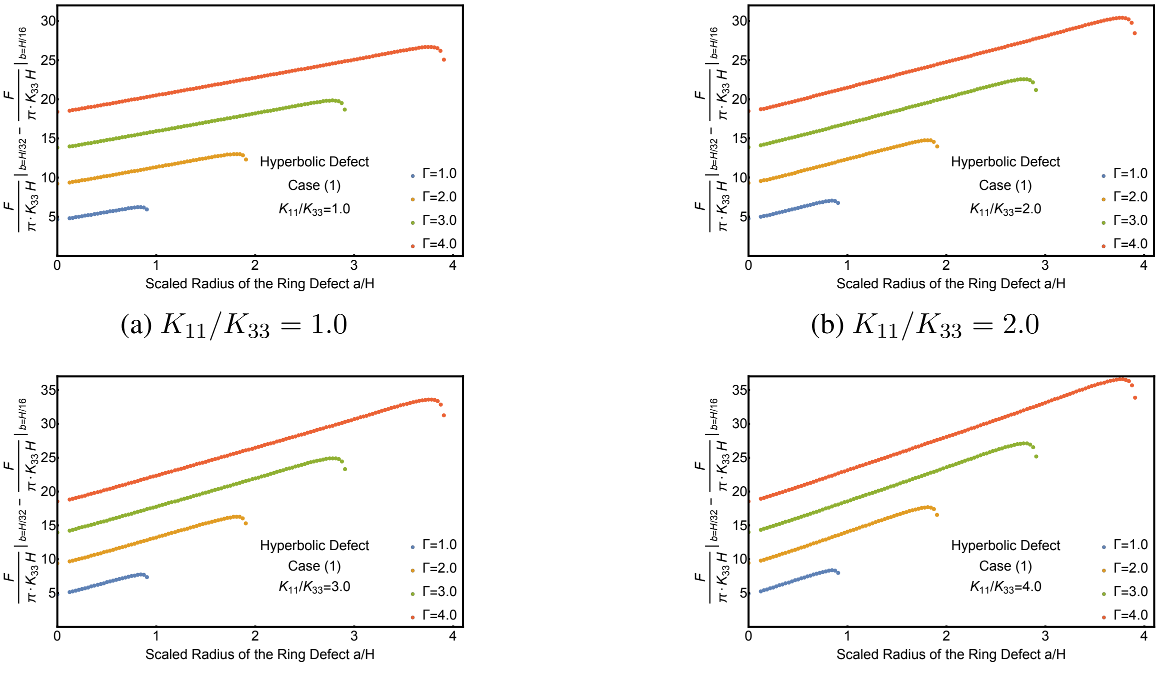

(a) $K_{11}/K_{33} = 1.0$

(b) $K_{11}/K_{33} = 2.0$

(c) $K_{11}/K_{33} = 3.0$

(d) $K_{11}/K_{33} = 4.0$

Figure 2.21: The differences between energy landscapes for hyperbolic defects between $b/H = 1/32$ and $b/H = 1/16$

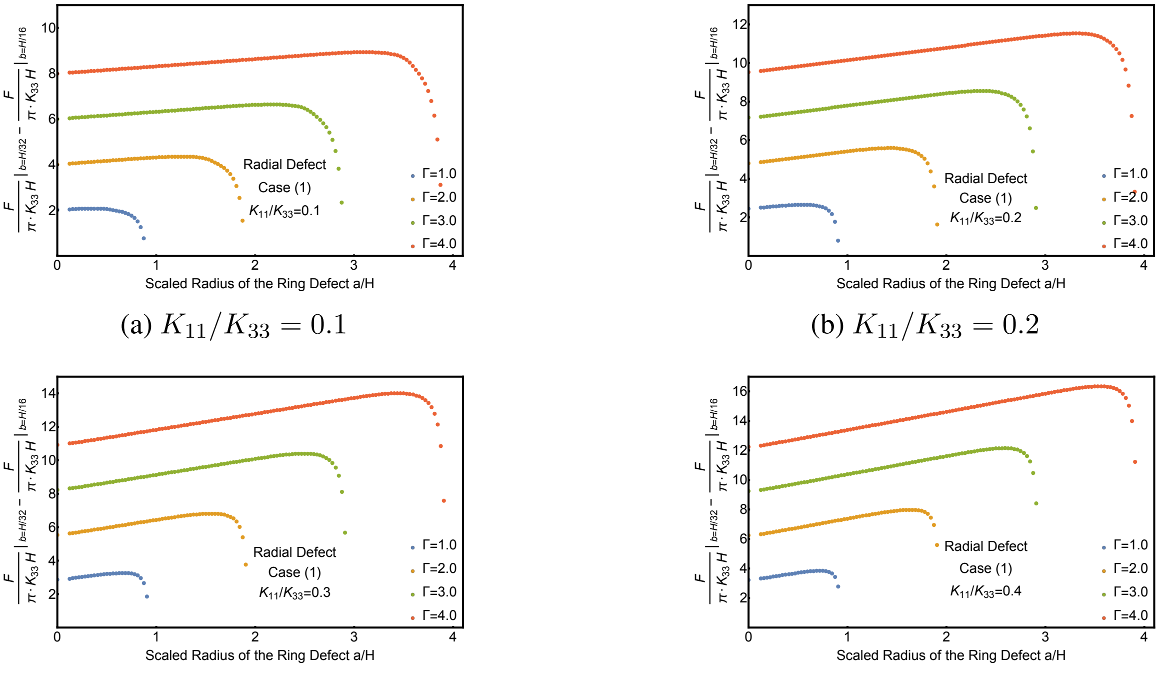

(a) $K_{11}/K_{33} = 0.1$

(b) $K_{11}/K_{33} = 0.2$

(c) $K_{11}/K_{33} = 0.3$

(d) $K_{11}/K_{33} = 0.4$

Figure 2.22: The differences between energy landscapes for radial defects between $b/H = 1/32$ and $b/H = 1/16$

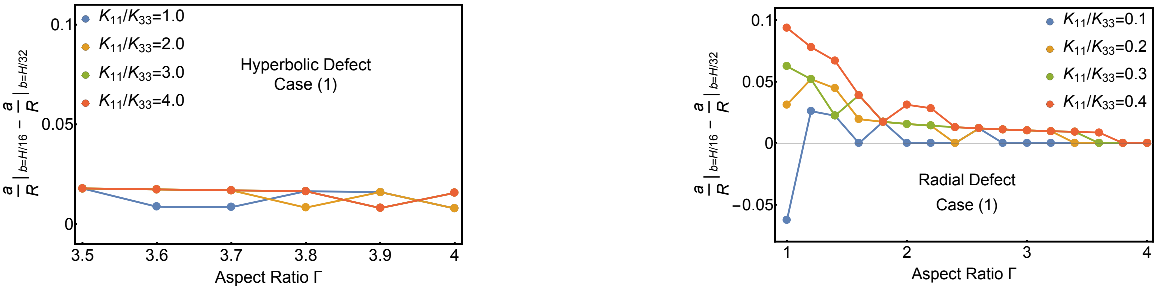

(a) Hyperbolic

(b) Radial

Figure 2.23: The differences between the equilibrium ring radii between different cut-off lengths

and the most important factor that affects the free energy is the change of the domain of integration, i.e., the change of the size of the cut-off region. The equilibrium conditions for defect structures with cut-off lengths b_1 and b_2 are written repectively as

$$F'(a) = 0, \tag{2.18}$$

$$F'(a) + k = 0. \tag{2.19}$$

Let a_1 and a_2 satisfy Eq. (2.18) and (2.19) respectively. And let $\Delta a = a_2 - a_1$ denote the difference between the two radii. If $|\Delta a/a_1| \ll 1$, then we can substitute $a_2 = a_1 + \Delta a$ into Eq. (2.19) and then we have

$$F'(a_1 + \Delta a) + k = 0 \Longrightarrow F'(a_1) + \Delta a \cdot F''(a_1) + k = 0 \tag{2.20}$$

$$\Longrightarrow \Delta a \cdot F''(a_1) + k = 0.$$

Therefore,

$$\left|\frac{\Delta a}{a_1}\right| \ll 1 \Longrightarrow \left|\frac{k}{a_1 \cdot F''(a_1)}\right| \ll 1. \tag{2.21}$$

Introducing the scaled quantities $\overline{a}_1 \equiv a_1/R$ and $\overline{F} \equiv F/\pi K_{33} H$, Condition (2.21) becomes

$$\left|\frac{k\Gamma}{\pi K_{33} \overline{F''}(\overline{a}_1)}\right| \ll 1 \Longrightarrow \overline{F''}(\overline{a}_1) \gg \left|\frac{k\Gamma}{\pi K_{33}}\right|. \tag{2.22}$$

A large equilibrium ring tends to have a very large $\overline{F''}$ and we suspect that it can richly satisfy Condition (2.22), therefore it is less sensitive to the change of the cut-off length.

2.4.4 The Effects of the Boundary Layer Near the Lateral Surface

We will see in Chapter 3 that, for our numerical method if the lateral surface is curved (e.g., waist-shaped or barrel-shaped), the boundary layer must be cut off in order to make sure the energy is finite. To understand the influence of this boundary layer and make sure the qualitative features of the energy landscapes do not change without this layer, we now focus our study on the energy landscapes in Case (1) and Case (2) with the same cut-off length $b = H/32$ as shown in Figs. 2.24 and 2.25. These figures show that the energy of the boundary layer has an *monotonic* dependence of Γ and K_{11}/K_{33}. So adding this energy or subtracting it from an energy landscape is unlikely to change the types and numbers of equilibrium states, and therefore we can say that the qualitative features of the energy landscapes do not change without the boundary layer.

Figure 2.26 illustrates the differences between the equilibrium ring radii from Case (1) and those from Case (2). We can conclude that this thin layer has small effect on large equilibrium rings. A tentative analytical justification follows.

First, we can write the energy of this thin layer as

$$\Delta F = h(a) \cdot H \cdot R \tag{2.23}$$

where $h(a)$ is the energy density with a being the ring radius, and the height H is fixed. Also, the radius R of the cylinder is a constant for a fixed Γ.

Then, let $F = F(a)$ denote the free energy of remaining region. For fixed Γ, the equilibrium conditions for Case (1) and (2) are written respectively as

$$F'(a) = 0, \tag{2.24}$$

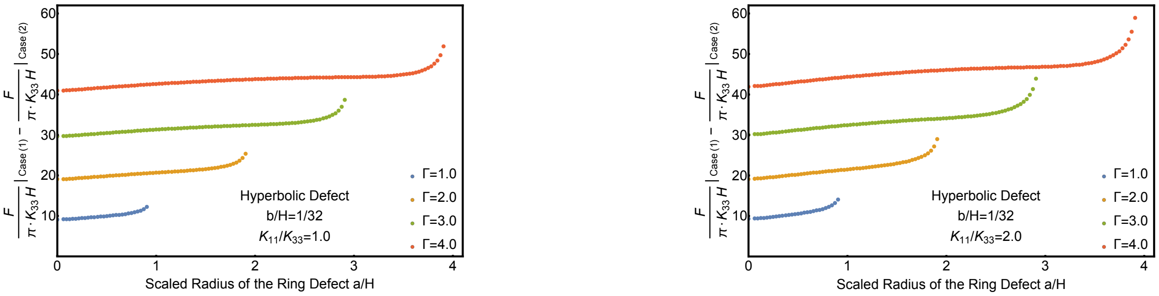

(a) $K_{11}/K_{33} = 1.0$ (b) $K_{11}/K_{33} = 2.0$

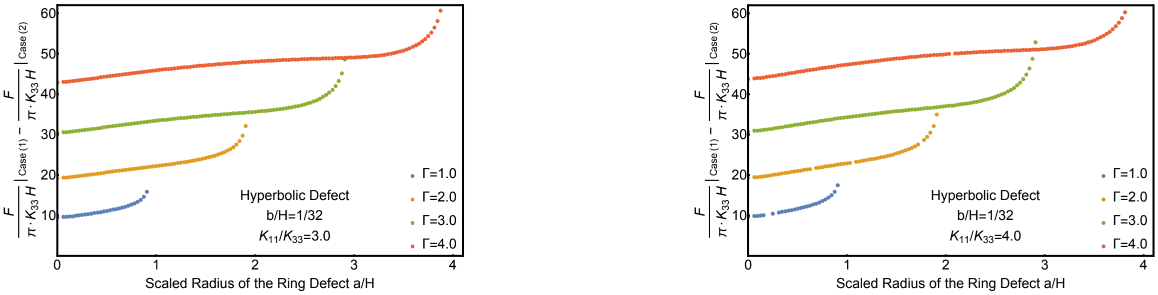

(c) $K_{11}/K_{33} = 3.0$ (d) $K_{11}/K_{33} = 4.0$

Figure 2.24: The differences between energy landscapes for hyperbolic defects between Case (1) and Case (2)

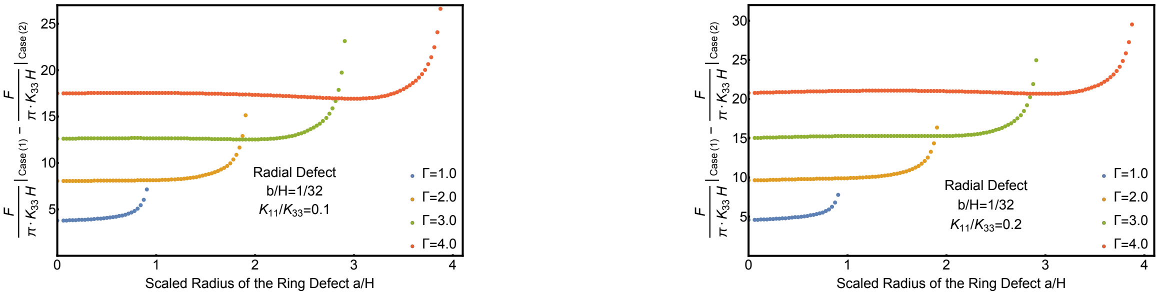

(a) $K_{11}/K_{33} = 0.1$ (b) $K_{11}/K_{33} = 0.2$

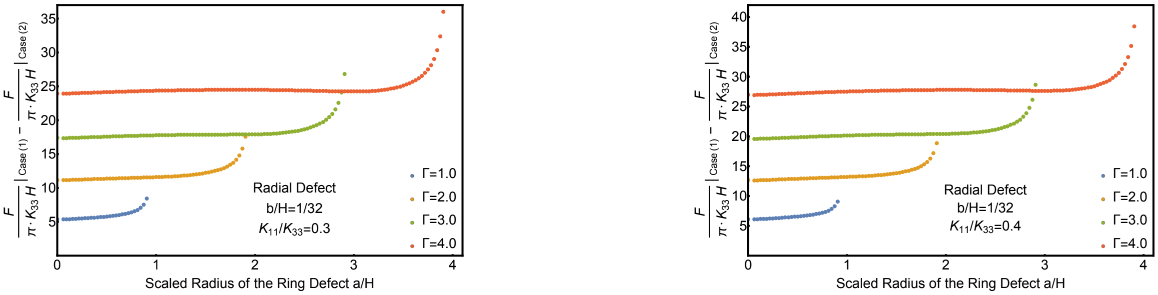

(c) $K_{11}/K_{33} = 0.3$ (d) $K_{11}/K_{33} = 0.4$

Figure 2.25: The differences between energy landscapes for radial defects between Case (1) and Case (2)

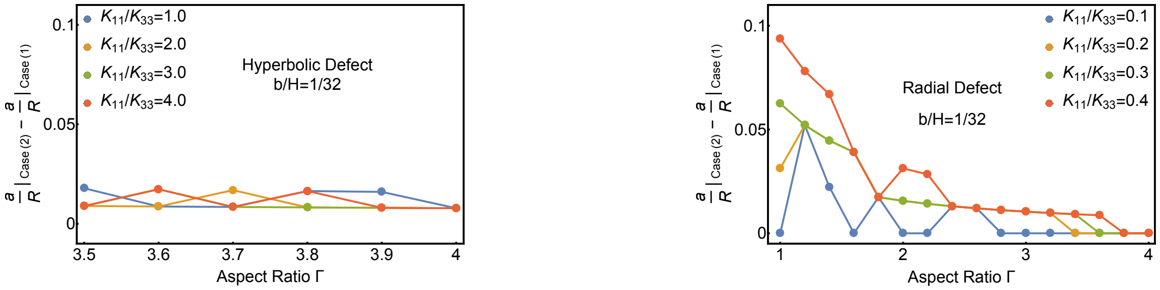

(a) Hyperbolic

(b) Radial

Figure 2.26: The differences between the equilibrium ring radii between Case (1) and Case (2)

$$F'(a) + h'HR = 0. \tag{2.25}$$

Let a_1 and a_2 satisfy Eq. (2.24) and (2.25) respectively; and let $\Delta a = a_2 - a_1$ denote the difference between the two radii. If $|\Delta a/a_1| \ll 1$, then we can substitute $a_2 = a_1 + \Delta a$ into Eq. (2.25) and we have

$$F'(a_1 + \Delta a) + h'HR = 0 \Longrightarrow F'(a_1) + \Delta a \cdot F''(a_1) + h'HR = 0 \tag{2.26}$$

$$\Longrightarrow \Delta a \cdot F''(a_1) + h'HR = 0.$$

Therefore we have

$$\left|\frac{\Delta a}{a_1}\right| \ll 1 \Longrightarrow \left|\frac{h'HR}{a_1 \cdot F''(a_1)}\right| \ll 1. \tag{2.27}$$

Introducing the scaled quantities $\overline{a}_1 \equiv a_1/R$ and $\overline{F} \equiv F/\pi K_{33} H$, the condition (2.27) becomes

$$\left|\frac{h'HR\Gamma}{\pi K_{33} \overline{F''}(\overline{a}_1)}\right| \ll 1 \Longrightarrow \overline{F''}(\overline{a}_1) \gg \left|\frac{h'HR\Gamma}{\pi K_{33}}\right| \tag{2.28}$$

We suspect that Condition (2.28) is richly satisfied by large equilibrium rings.

2.5 Results Part III – Defect Structure Diagrams

2.5.1 Common Features

Figure 2.27 shows the defect structure diagrams for Case (1) with $b/H = 1/32$, Case (1) with $b/H = 1/16$ and Case (2) with $b/H = 1/32$. These defect structure diagrams share some common features: (1) there exist hyperbolic point – hyperbolic ring; (2) there do not exist radial point – radial ring, and the radius of the radial ring gradually increases as Γ increases; (3) there exist radial defects – hyperbolic defects.

Feature (1) can be explained by the fact that two local minima (one represents the hyperbolic point, and the other represents the hyperbolic ring) are competing with each other. Feature (2) can be explained by the fact that there is only one local minima and the associate ring radius a is continuously changing with Γ. As for Feature (3), one may ask: why is the hyperbolic preferred over the radial when the Frank constant ratio K_{11}/K_{33} is large? The answer is that: the bend distortion free energy is dominant in the hyperbolic defect while the splay distortion free energy is dominant in the radial defect; when K_{33} is relatively small, then the hyperbolic defect (with bend distortion occupying more area) will cost less free energy.

2.5.2 The Effects of Cut-Off Lengths

By comparing Figs. 2.27a and 2.27b, we observe the effects of different cut-off lengths on the defect structure diagrams: the hyperbolic point – hyperbolic ring transition line for a greater cut-off length (i.e., $b/H = 1/16$) is to the left of the line for a shorter cut-off length (i.e., $b/H = 1/32$). The explanation is as follows.

As introduced before, let $F(a) + k \cdot a$ and $F(a)$ be the free energies for cut-off lengths b_1 and b_2 respectively with $b_1 < b_2$ (therefore $k \cdot a > 0$). For fixed K_{11}/K_{33}, let Γ_1 and Γ_2 denote the hyperbolic point – hyperbolic ring transition points for the two cases respectively. Then we know that at Γ_2, the two local minima for $F(a)$ have the same energy. However, at this same Γ_2, the local minimum representing the hyperbolic point defect has the lower energy for $F(a) + k \cdot a$ due to the fact that $k \cdot a$ is monotonically increasing with a. Thus, in order to reach the transition point Γ_1 for $F(a) + k \cdot a$, we need to further increase Γ to reduce the energy for the local minimum representing the hyperbolic ring defect. Therefore, we have $\Gamma_1 > \Gamma_2$.

2.5.3 The Effects of the Boundary Layer Near the Lateral Surface

By comparing Figs. 2.27a and 2.27c, we observe the effects of the boundary layer near the lateral surface on the phase diagrams: [a] the hyperbolic point – hyperbolic ring transition line for Case (2) is to the left of the line for Case (1); [b] the radial defect – hyperbolic defect transition line for Case (2) is slightly above the line for Case (1).

For [a], it can be explained as follows: as introduced before, let $F(a) + h(a) \cdot H \cdot R$ and $F(a)$ be the free energies for Case (1) and Case (2) respectively. For fixed K_{11}/K_{33}, let Γ_1 and Γ_2 denote the hyperbolic point – hyperbolic ring transition points respectively. Figure 2.24 shows that $h(a)$ has an increasing trend even though it may not be monotonically increasing, therefore it is reasonable to assume $h(a) \cdot H \cdot R$ to be larger for the hyperbolic ring than the hyperbolic point. Knowing that the two local minima for $F(a)$ have the same energy at Γ_2, in order to reach the transition point Γ_1 for $F(a) + h(a) \cdot H \cdot R$, we need to further increase Γ to reduce the energy for the local minimum representing the hyperbolic ring defect. Therefore, we have $\Gamma_1 > \Gamma_2$.

For [b], we do not have a good explanation so far. Also, notice that the difference is not large, so maybe a detailed calculation is necessary.

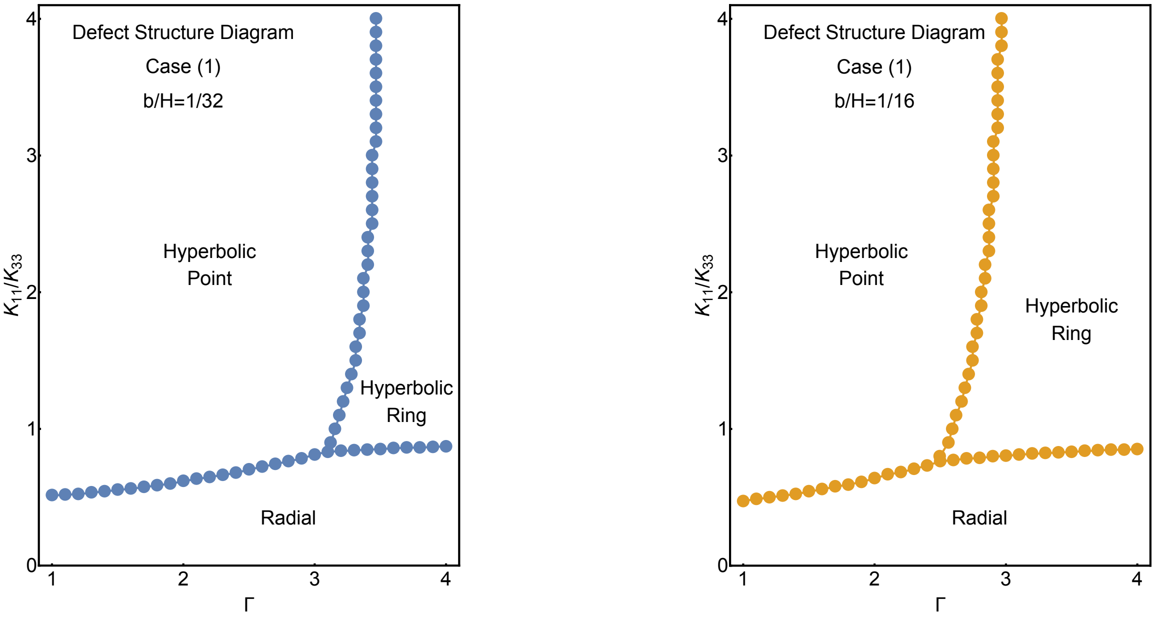

(a) Case (1), $b/H = 1/32$

(b) Case (1), $b/H = 1/16$

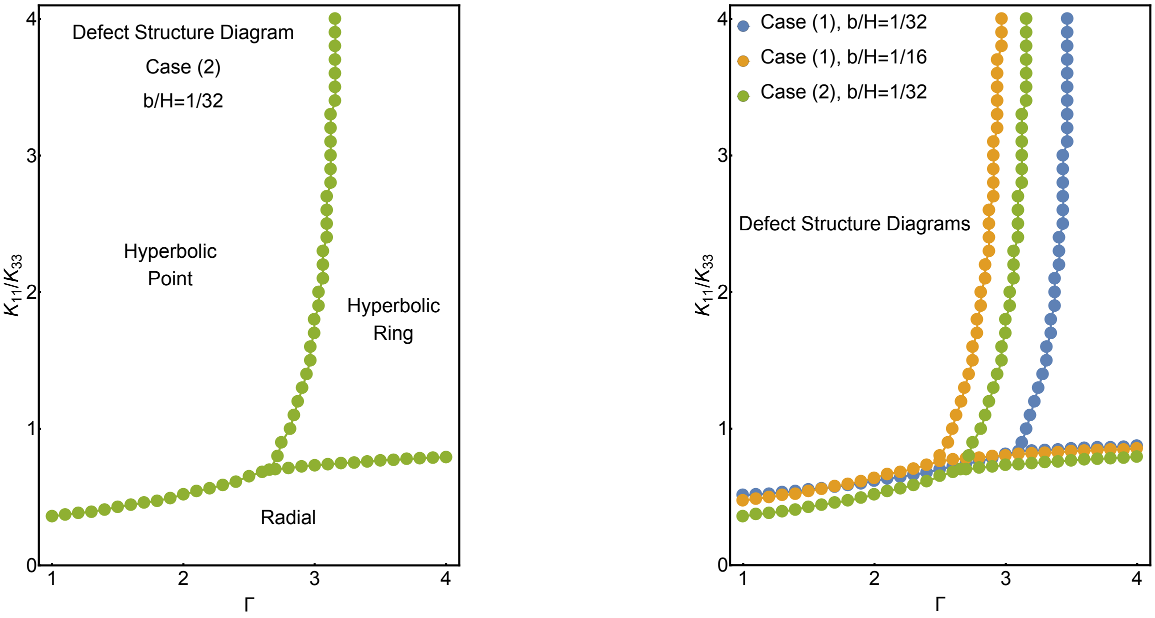

(c) Case (2), $b/H = 1/32$

(d) Comparison

Figure 2.27: Defect structure diagrams of cylindrical nematic bridges

CHAPTER 3

NUMERICAL STUDY OF NEMATIC LIQUID-CRYSTAL BRIDGES PART II – FINITE DIFFERENCE METHOD FOR WAIST-SHAPED AND BARREL-SHAPED NEMATIC BRIDGES

3.1 Introduction to the Experiments

The experiments were conducted in Prof. Fernandez Nieves' Lab by Ellis et al., and were performed on microscope stages; see Ref. [45]. The experimental setup is shown in Fig. 3.1, and three different shapes of bridges are illustrated in Fig. 3.2. For the experiments on waist-shaped bridges, the main procedure is as follows:

(1) To ensure homeotropic anchoring of the nematics on the glass microscope slides, they dip the slides into hexane (98.5% purity; BDH) with 0.1% w/w lecithin (granular; Acros).

(2) Place two microscope slides on top of each other on the microscope stage.

(3) In order to be capable of adjusting the distance between the slides, they connect the top slide to a micromanipulator.

(4) To create a waist-shaped bridge, they first raise the top slide and put a drop of 5CB (with the Frank constant ratio $K_{11}/K_{33} = 0.74$ and approximately 1 nL in volume) onto the bottom slide by the use of a glass capillary, then lower down the top slide until it touches the droplet (note that the outer medium is air).

(5) To determine whether there is a point or ring defect, they view the nematic bridge from the top by the use of polarized optical microscopy (POM).

(6) To determine whether it is a radial or hyperbolic type of defect, they view the nematic bridge from the side by the use of polarized epifluorescent microscopy (PFM).

For the experiments of barrel-shaped bridges, the procedure is almost the same except

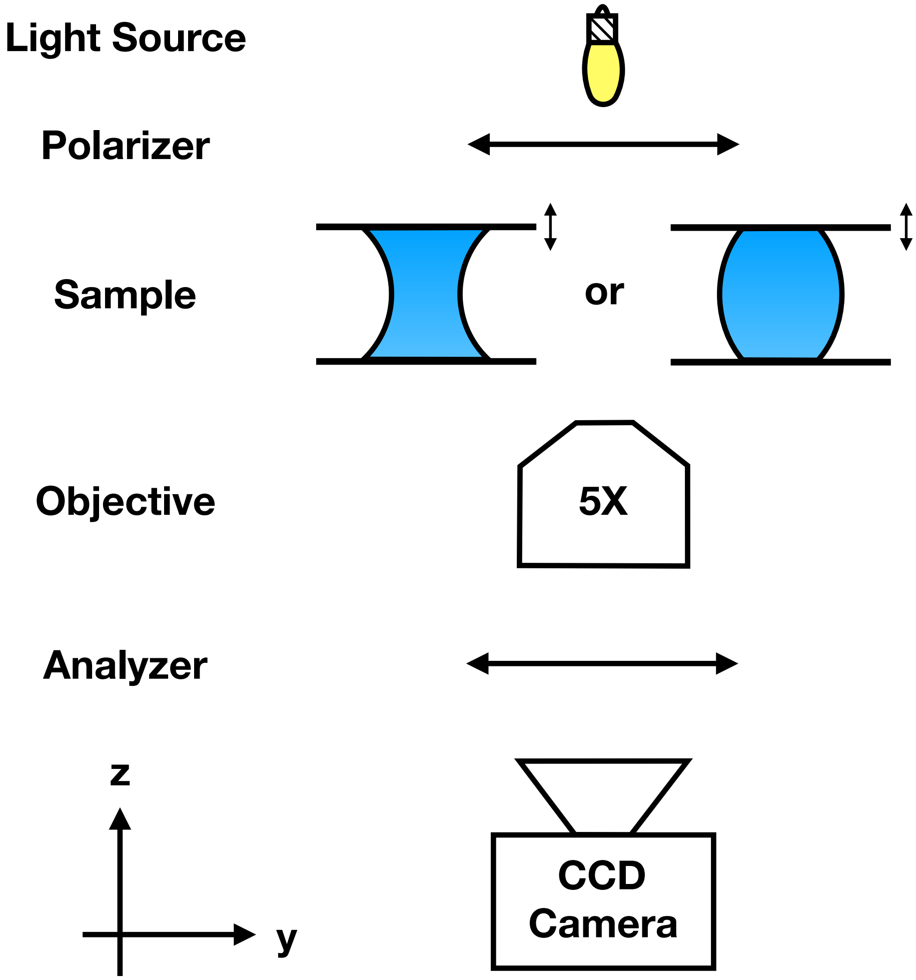

Figure 3.1: Experimental setup (based on Fig. 3(a) in Ref. [45])

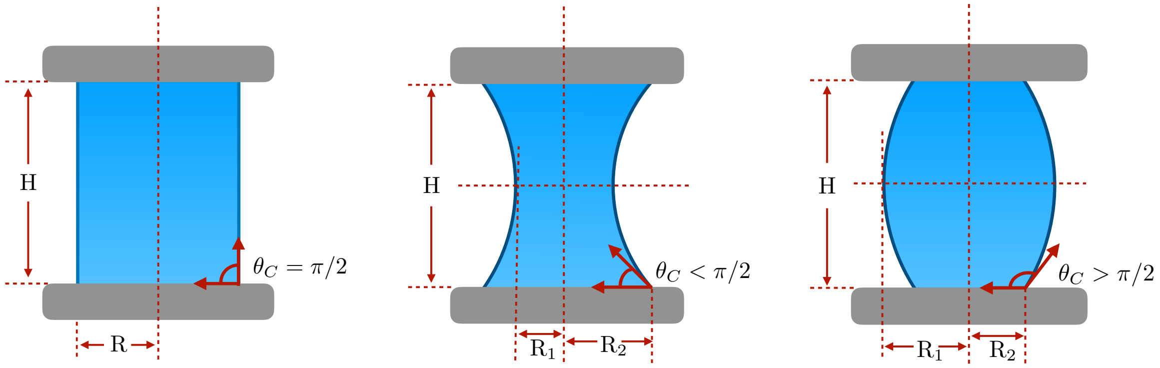

(a) Cylindrical bridge (b) Waist-shaped bridge (c) Barrel-shaped bridge

Figure 3.2: Nematic bridges

that we replace the Step (4) above by:

(4) To create a barrel-shaped bridge, they first raise the top slide and put a drop of 5CB onto the bottom slide by the use of a glass capillary, then lower down the top slide until it touches the droplet, and then submerge the nematic bridge in the water; to ensure homeotropic anchoring of the nematics on the nematics – water interface, they add 8 mM sodium dodecyl sulfate (Sigma Aldrich) into the water.

The main experimental results are:

(1) For waist-shaped bridges made of 5CB, there are only hyperbolic type of defects, and the hyperbolic point – hyperbolic ring transition occurs at $\Gamma_c = 2.7 \pm 0.3$; and for a bridge initially created with $\Gamma > \Gamma_c$, the hyperbolic ring is observed and therefore is the ground state; and for $\Gamma < \Gamma_c$, the hyperbolic point is the ground state. In addition, they have observed that: if the bridge starts at $\Gamma < \Gamma_c$ with a point defect, then the point defect never becomes a ring defect as Γ increases; however, for the bridge with $\Gamma > \Gamma_c$ which contains a point defect, the ring defect can always be recovered if they first melt the nematic phase in the bridge and then let this bridge cool back to the nematic phase. This implies that the point defect is metastable for $\Gamma > \Gamma_c$, i.e., the point defect is an equilibrium state but not a ground state for $\Gamma > \Gamma_c$. Note that in experiments, the aspect ratio Γ is defined to be $\Gamma = 2R/H$, where R is the radius of the mid-plane.

(2) For barrel-shaped bridges made of 5CB, there are only radial ring defects observed.

These experimental results are very interesting, and we would like to understand them through numerical computations, showing that the Oseen-Frank formalism for defects in nematics is effective in describing these phenomena. One tricky issue is that the actual process during which the bridge is undergoing defect transition is quite complex: when Γ is changed, the contact angle θ_C and K_{11}/K_{33} are unchanged but the shape of the lateral surface is deformed; although the shape of the boundary can be determined by Γ and θ_C, there will be more PDEs which make the computations much more expensive than those we did in Chapter 2. In addition, it is expected that some details of the boundary surface is not crucial to the defect transitions; rather, it is whether the surface is convex or concave that is most important. Therefore, in our numerical study, we aim at answering the following question:

What will the defect structure diagrams look like if the lateral surface of a cylindrical bridge slightly deviate so that the bridge becomes waist-shaped or barrel-shaped?

This simplifies our computations tremendously, because we can treat this deviation of lateral surface as a perturbation to the original cylinder. Although in principle our numerical computations will not be able to provide a great quantitative explanation to the experimental results, we can have a good qualitative or even semi-quantitative understanding.

3.2 Theoretical Preparations and Numerical Strategy

Similar to the cylindrical bridge, one quarter of the diametrical plane is sufficient for studying the defect structures of waist-shaped and barrel-shaped nematic bridges. We choose it to be the first quadrant of the Cartesian coordinate system in two dimensions, in which we need to solve boundary value problems. For the Euler-Lagrange equation, we use Eq. (2.4) as introduced in Chapter 2. For the boundary conditions, we choose Case (2), i.e., Boundary Conditions (A) for the defect cores at the top right corners and Boundary Conditions

(B) for those at the mid-planes, which are introduced in Sections 2.1.2 and 2.2. However, we are faced with some tricky issues shown as follows.

Issue (1)

In Fig. 3.2, there are two radii: the radius R_1 for the mid-plane, and the radius R_2 for the upper or lower plane. The question is: is the aspect ratio Γ defined to be $2R_1/H$ or $2R_2/H$?

Of course, these two definitions are equivalent. In our numerical study, we prefer $\Gamma = 2R_2/H$ to the one used in experiments. Our reasons are: (a) R_2 is the boundary for the boundary value problem, while R_1 can be the boundary only if the mid-plane is treated as a boundary by symmetry arguments; (b) R_2 is the radius of the ring-like defect cores located on the upper and lower planes, and the locations of the defect cores are supposed to be important information for studying defect structures. For convenience, we simply write R instead of R_2 for later discussions.

Issue (2)

We still choose the finite difference method to study the waist-shaped and barrel-shaped nematic bridges. However, one may ask: is it good to discretize the curved rightmost boundary with equally-spaced lattices, and why do we choose Case (2) instead of Case (1)?

If one wants to accurately describe the shape of the bridges created in the experiments so that the numerical results can match the experimental results with great precision, then the finite difference method is not good enough and the finite element method may be a better choice. However, our goal is to understand how convexity or concavity of the lateral surface affect the defect structure diagrams of the defect transitions, and we can understand it by small perturbations of the lateral surface of a cylinder; therefore, the finite difference method can be good enough if we can approximate the correct perturbations. A detailed exposition is in the following.

Assuming that the upper and lower boundaries are parallel to the x-axis when putting the axial plane in the $x-y$ plane, we choose the function

$$\frac{x}{H/2} = \Gamma - \frac{1}{5} + \frac{1}{5} \cdot \frac{y}{H/2} \tag{3.1}$$

as a phenomenological model of the shape of the lateral surface for the waist-shaped bridge; similarly, we choose

$$\frac{x}{H/2} = \Gamma + \frac{1}{5} - \frac{1}{5} \cdot \frac{y}{H/2} \tag{3.2}$$

to be the lateral surface for the barrel-shaped bridge. Then we discretize the boundaries of height $H/2$ with 33 lattice points; as a result, the discrete versions of the lateral boundaries are combinations of short line segments as shown in Fig. 3.3. Equations (3.1) and (3.2) are specially chosen such that the resulting discretized boundaries are close to the lateral boundary of a cylinder with the former being slightly concave and the latter being slightly convex.

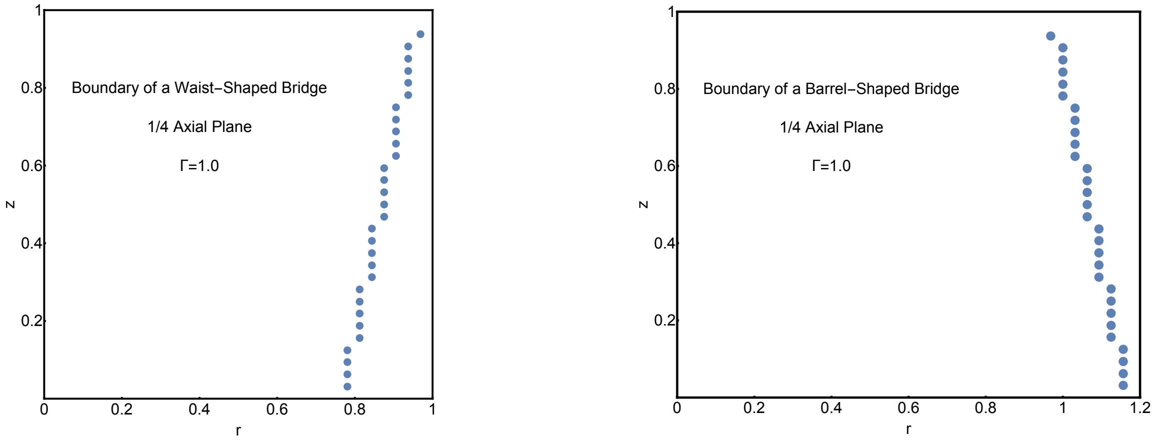

(a) Waist-shaped bridge

(b) Barrel-shaped bridge

Figure 3.3: Boundary of a nematic bridge

As we know, if the the vector field $\mathbf{n}$ does not change continuously along a path, then a defect core will come into being, for example, the defect core at the top right corner. Therefore the discontinuities on the discretized boundary are likely to be implanted by

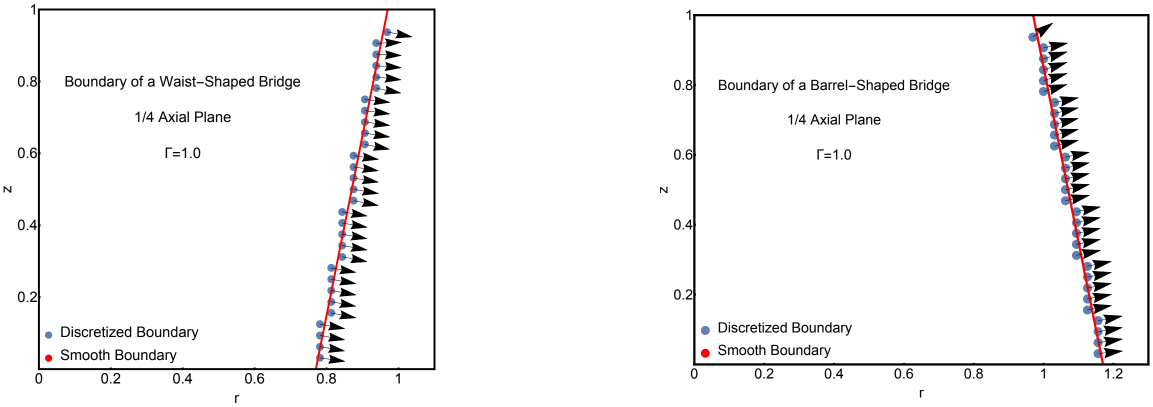

(a) Waist-shaped bridge

(b) Barrel-shaped bridge

Figure 3.4: Vectors on the lateral surface of a nematic bridge

defect cores, which should never occur to the actual smooth boundary. To cope with this issue, we use two tricks:

(a) For the homeotropic boundary condtions, we let $\mathbf{n}$ be perpendicular to the actual smooth boundary [i.e., Eqs. (3.1) and (3.2)] rather than the discretized boundary, which makes $\mathbf{n}$ on the lateral boundary to be as smooth as possible; see Fig. 3.4.

(b) When evaluating the energy functional, we leave out a layer of thickness b near the lateral boundary to avoid the infinite energy caused by the possible "fake" defects; this is also the reason why we should choose Case (2) for our study of waist-shaped and barrel-shaped nematic bridges.

Note that, even though Eqs. (3.1) [or (3.2)] make the lateral surfaces look like concave cones [or convex cones], the discretized surfaces are smooth at the midpoint. The two tricks mentioned above further make sure that the vector field $\mathbf{n}$ on the boundary has a general pattern of it perpendicular to a smooth concave (or convex) boundary.

For the source code, please visit our github repositories; see Ref. [91] for waist-shaped bridges and Ref. [92] for barrel-shaped bridges.

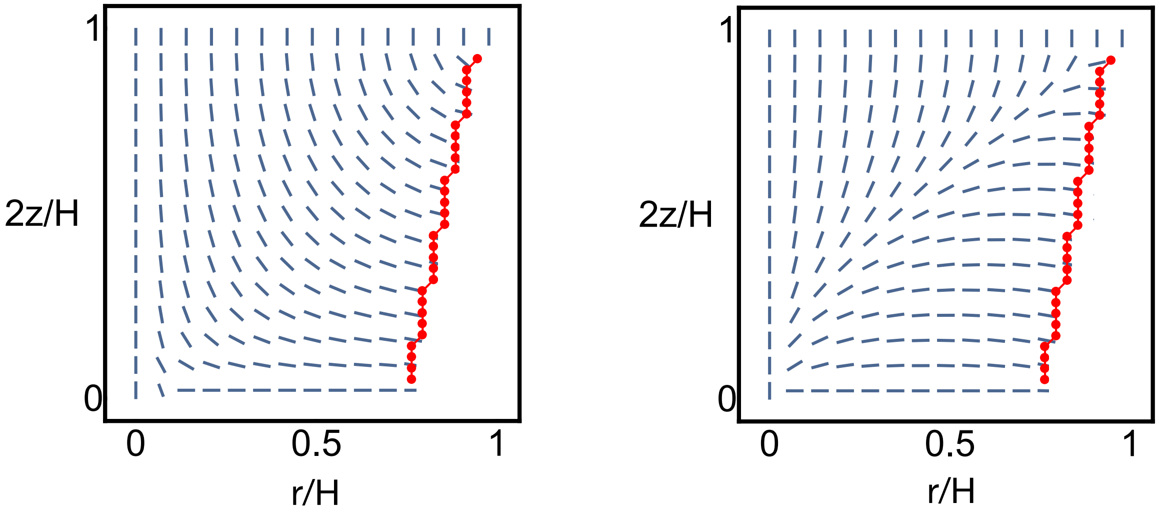

(a) Hyperbolic point ($\Gamma = 1$, $K_{11}/K_{33} = 4$)

(b) Radial point ($\Gamma = 1$, $K_{11}/K_{33} = 0.1$)

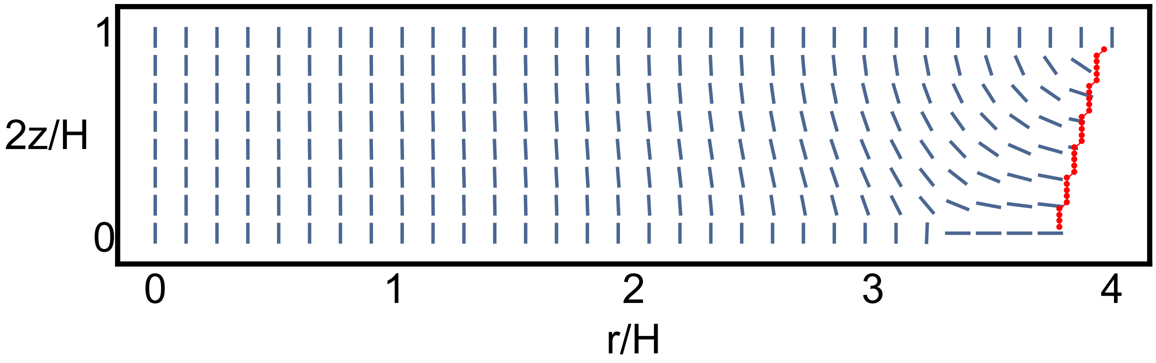

(c) Hyperbolic Ring ($\Gamma = 4$, $K_{11}/K_{33} = 4$)

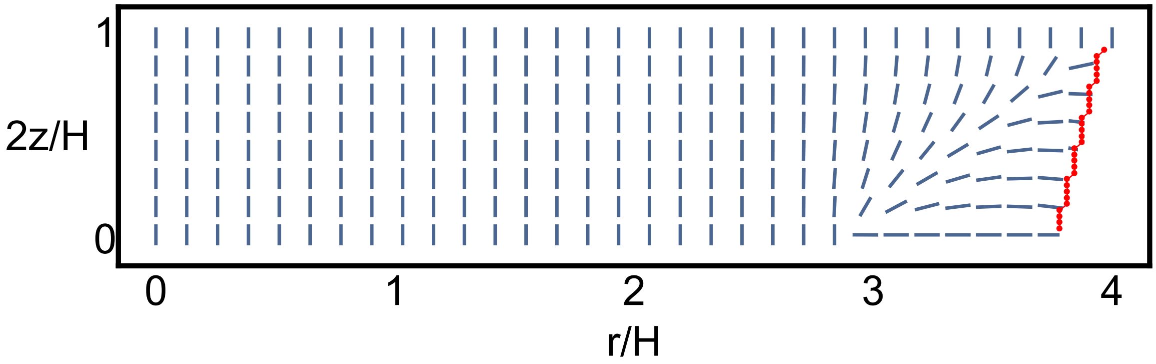

(d) Radial ring ($\Gamma = 4$, $K_{11}/K_{33} = 0.1$)

Figure 3.5: Equilibrium defect structures in waist-shaped bridges (shown in one quarter of the axial plane). The thickness of the boundary layer (which is not shown) is set to be the radius of the defect core, which is $b/2$, about the distance of two lattices in our algorithm

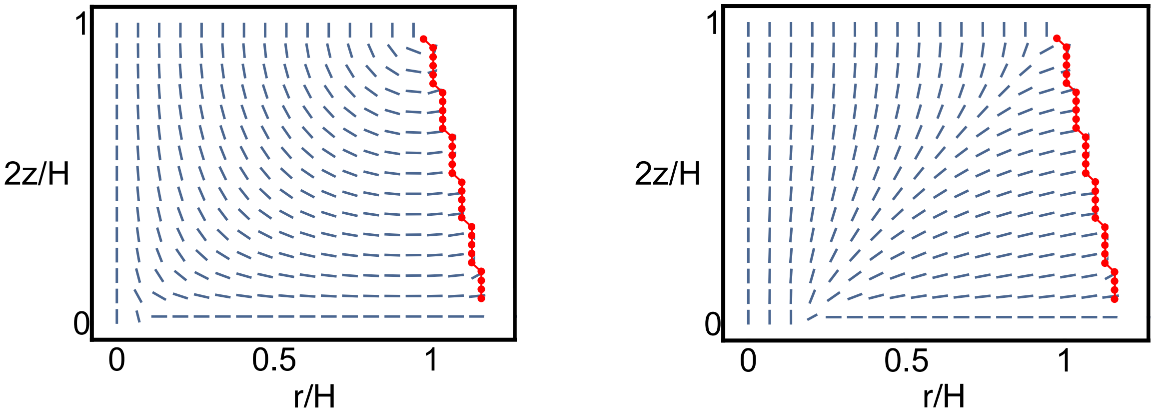

(a) Hyperbolic point ($\Gamma = 1$, $K_{11}/K_{33} = 4$)

(b) Radial point ($\Gamma = 1$, $K_{11}/K_{33} = 0.1$)

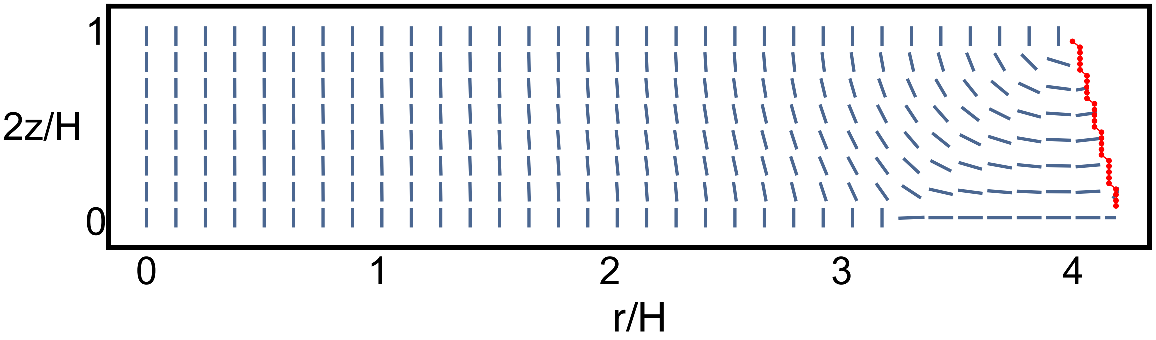

(c) Hyperbolic ring ($\Gamma = 4$, $K_{11}/K_{33} = 4$)

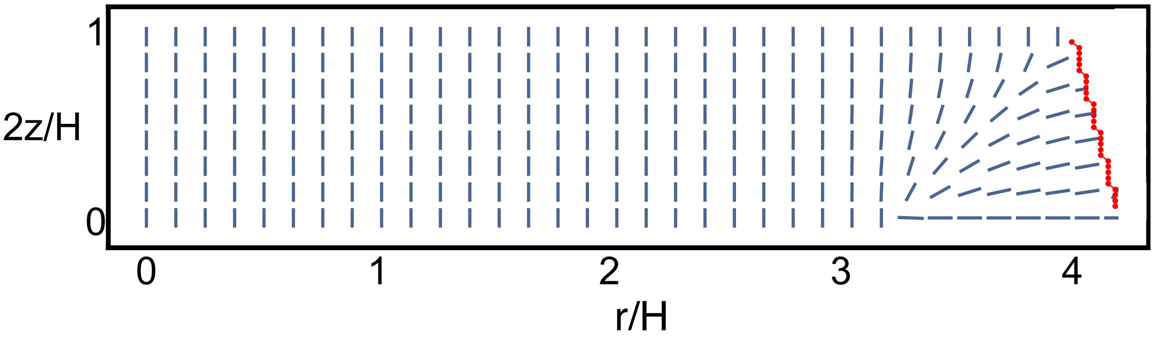

(d) Radial ring ($\Gamma = 4$, $K_{11}/K_{33} = 0.1$)

Figure 3.6: Equilibrium defect structures in barrel-shaped bridges (shown in one quarter of the axial plane). The thickness of the boundary layer (which is not shown) is set to be the radius of the defect core, which is $b/2$, about the distance of two lattices in our algorithm

3.3 Results Part I – Equilibrium Defect Structures

As with the case of cylindrical bridges, we observe four different types of equilibrium defect structures in both waist-shaped and barrel-shaped bridges, i.e., hyperbolic point, hyperbolic ring, radial point (small ring) and radial ring, which are shown in Figs. 3.5 and 3.6. However, same values of the parameters Γ and K_{11}/K_{33} can result in different equilibrium defect structures in a cylindrical, waist-shaped or barrel-shaped bridge, which implies that the convexity or concavity of the lateral surface affects the energy landscapes and defect structure diagrams.

3.4 Results Part II – Free Energy Landscapes

As mentioned in the Chapter 2, for each Γ and K_{11}/K_{33}, there are energy landscapes for both hyperbolic and radial defects. As usual, we choose to show the one that contains the ground state. In order to compare the energy landscapes, we consider Case (2) and $b/H = 1/32$ for all the three types of bridges. Moreover, concerning the fact that the region for hyperbolic defects in the defect structure diagram becomes larger for waist-shaped bridges and smaller for barrel-shaped bridges, we consider $\Gamma = 1, 2, 3, 4$ for all defect structures, and $K_{11}/K_{33} = 1, 2, 3, 4$ for hyperbolic defects in waist-shaped bridges, $K_{11}/K_{33} = 0.1$ for radial defects in waist-shaped bridges, $K_{11}/K_{33} = 4$ for hyperbolic defects in barrel-shaped bridges, $K_{11}/K_{33} = 0.1, 0.2, 0.3, 0.4$ for radial defects in barrel-shaped bridges; see Figs. 3.7 – 3.12.

Figures. 3.7 – 3.10 are the energy landscapes for waist-shaped and barrel-shaped bridges, which we need to compare with Figs. 2.14 – 2.15 shown in the Chapter 2. We observe that the effects of aspect ratios are the same in all three types of bridges: for hyperbolic defects, there is only one minimum representing a point defect when Γ is small and there appears another minimum representing a ring defect when Γ is large; for radial defects, there is only one minimum for whatever the value of Γ is. It is expected that the effects of Frank constant ratios and cut-off lengths should also be the same. Now, we focus on the analysis of the convexity and concavity of the lateral surface on the energy landscapes.

3.4.1 The Effects of Concavity of the Lateral Surface

By plotting the differences of energy landscapes between waist-shaped and cylindrical bridges, Figures. 3.13 and 3.14 show that:

(1) The energy for a hyperbolic type of defect is smaller in a waist-shaped bridge than a cylindrical bridge;

(2) The energy for a radial type of defect is greater in a waist-shaped bridge than a cylindrical bridge;

(3) When the ring radius is not too large, the difference of energy landscapes between the two types of bridges becomes flatter as Γ increases.

(1) and (2) imply that a concave lateral surface prefers a hyperbolic type of defect, therefore the radial defect – hyperbolic defect transition line moves downward along the K_{11}/K_{33} – axis. (3) implies that when Γ is large, the concavity results in almost the same amount of energy decrease for the two local energy minima near the hyperbolic point – hyperbolic ring transition, therefore the location of this transition line is nearly unaffected.

Figure 3.17 illustrates the differences between the equilibrium ring radii of waist-shaped bridges and those of cylindrical bridges. We observe that when Γ is large, the concavity does not change much of the radii of the hyperbolic or radial ring; however, when Γ is small, the concavity shrinks the radial ring (as a digression, the hyperbolic ring is not a ground state when Γ is small, so we do not consider it).

3.4.2 The Effects of Convexity of the Lateral Surface

By plotting the differences of energy landscapes between barrel-shaped and cylindrical bridges, Figures. 3.15 and 3.16 show that:

(1) The energy for a hyperbolic type of defect is greater in a barrel-shaped bridge than

a cylindrical bridge;

(2) The energy for a radial type of defect is smaller in a waist-shaped bridge than a cylindrical bridge;

(3) When the ring radius is not too large, the difference of energy landscapes between the two types of bridges becomes flatter as Γ increases.

(1) and (2) imply that a convex lateral surface prefers a radial type of defect, therefore the radial – hyperbolic transition line moves upward along the K_{11}/K_{33} – axis. (3) implies that when Γ is large, the concavity results in almost the same amount of energy decrease for the two local energy minima near the hyperbolic point – hyperbolic ring transition, therefore the location of this transition line is nearly unaffected.

Figure 3.18 illustrates the differences between the equilibrium ring radii of barrel-shaped bridges and those of cylindrical bridges. We observe that when Γ is large, the convexity does not change much of the radii of the hyperbolic or radial ring; however, when Γ is small, the convexity enlarge the radial ring.

3.5 Results Part III – Defect Structure Diagrams

Figures 3.19 and 3.20 are the defect structure diagrams of cylindrical, waist-shaped, and barrel-shaped bridges with Case (2) [as introduced in Section 3.2] and $b/H = 1/32$ based on two definitions of Γ: for the former, $\Gamma = 2R_2/H$ where R_2 is the radius of the upper or lower plane; for the latter, $\Gamma = 2R_1/H$ where R_1 is the radius of the mid-plane. A special note is that there are some outliers (which we ignore) in the defect structure diagrams of barrel-shaped bridges [i.e., Figs. 3.19c and 3.20c] which happen more frequently at the radial ring – hyperbolic ring transition line. For example, when plotting Fig. 3.19c, we observe that the radial ring – hyperbolic ring transition point at $\Gamma = 3.2$ has an abnormally large value of K_{11}/K_{33}, which is very likely due to our very crude numerical method. In order to get a better plot, we ignore this point and choose a nearby point instead. For the same example, we choose the transition point at $\Gamma = 3.22$ instead, which proves to be a

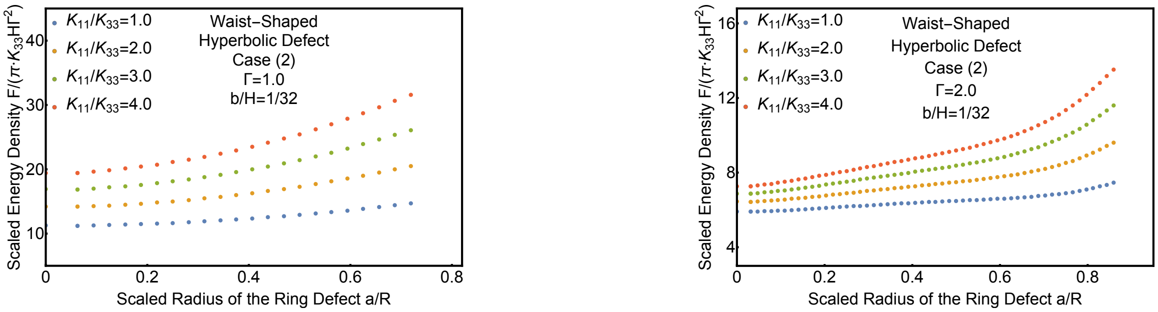

(a) $\Gamma = 1.0$ (b) $\Gamma = 2.0$

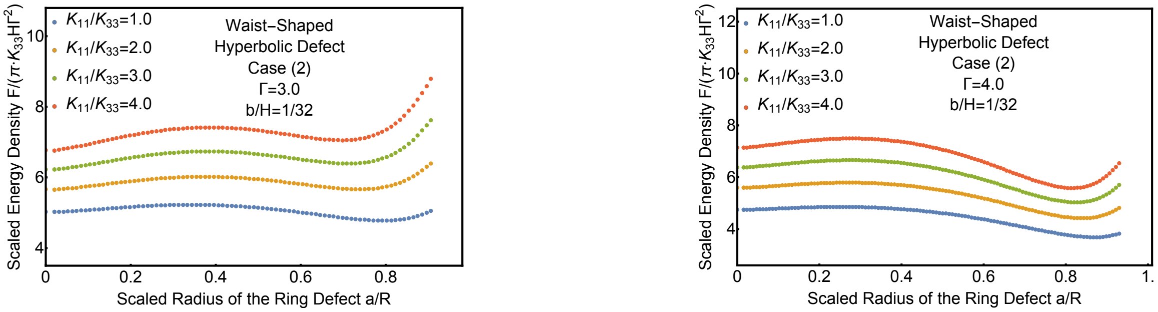

(c) $\Gamma = 3.0$ (d) $\Gamma = 4.0$

Figure 3.7: Energy landscapes for hyperbolic types of defects in waist-shaped bridges with Case (2) and $b/H = 1/32$

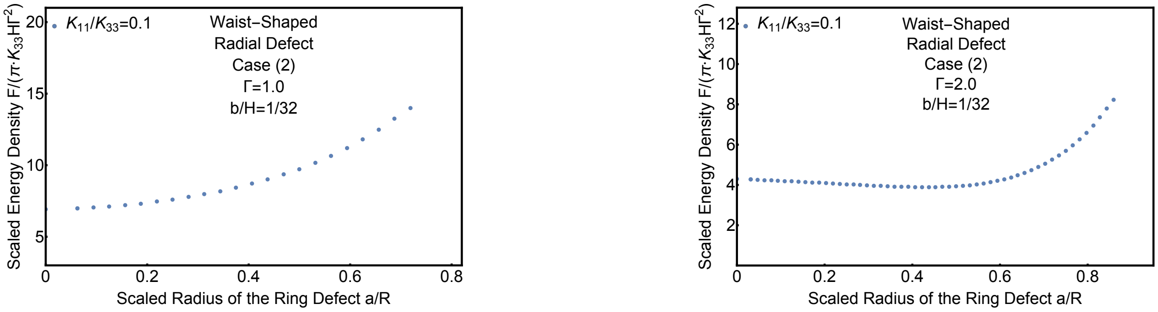

(a) $\Gamma = 1.0$ (b) $\Gamma = 2.0$

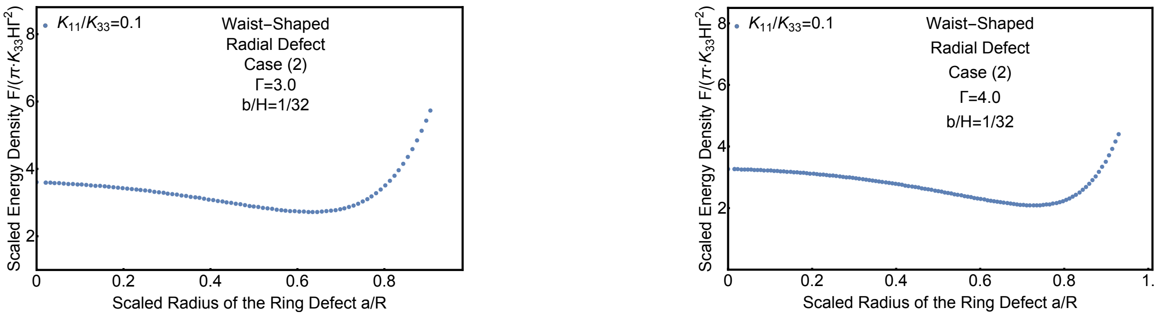

(c) $\Gamma = 3.0$ (d) $\Gamma = 4.0$

Figure 3.8: Energy landscapes for radial types of defects in waist-shaped bridges with Case (2) and $b/H = 1/32$

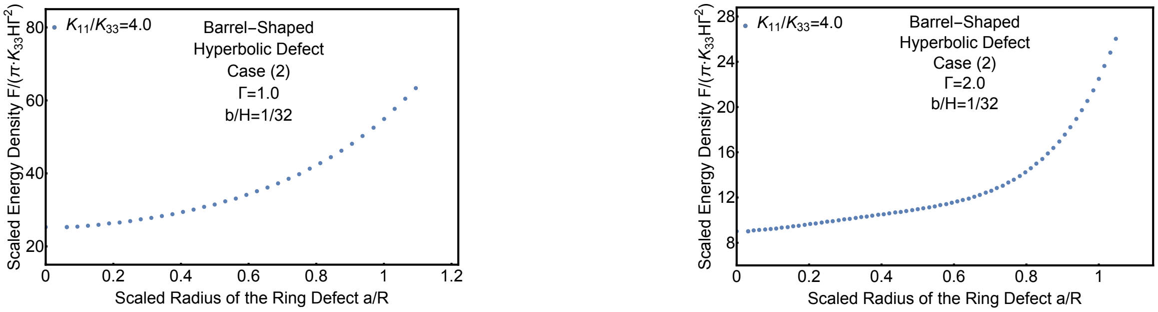

(a) $\Gamma = 1.0$ (b) $\Gamma = 2.0$

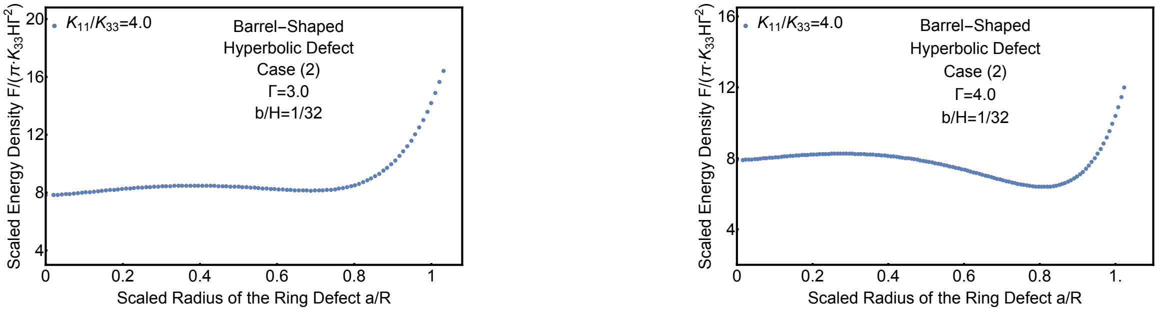

(c) $\Gamma = 3.0$ (d) $\Gamma = 4.0$

Figure 3.9: Energy landscapes for hyperbolic types of defects in barrel-shaped bridges with Case (2) and $b/H = 1/32$

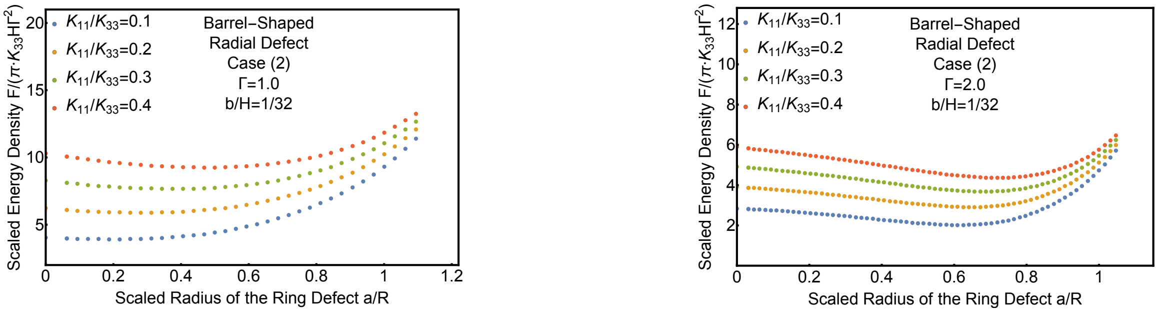

(a) $\Gamma = 1.0$ (b) $\Gamma = 2.0$

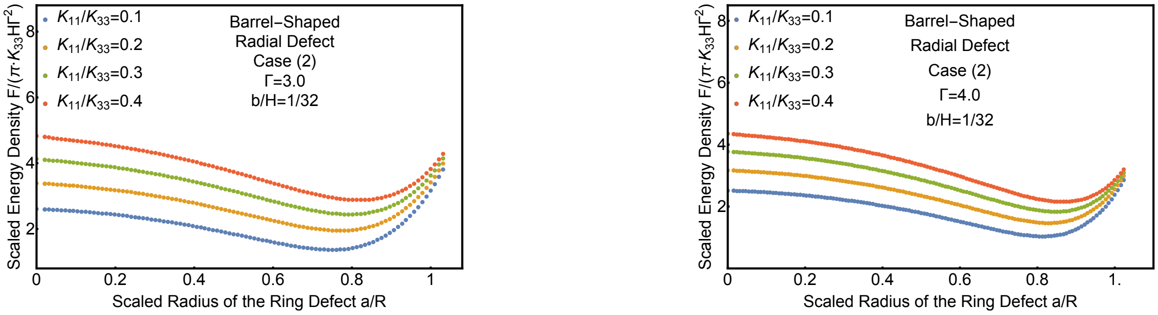

(c) $\Gamma = 3.0$ (d) $\Gamma = 4.0$

Figure 3.10: Energy landscapes for radial types of defects in barrel-shaped bridges with Case (2) and $b/H = 1/32$

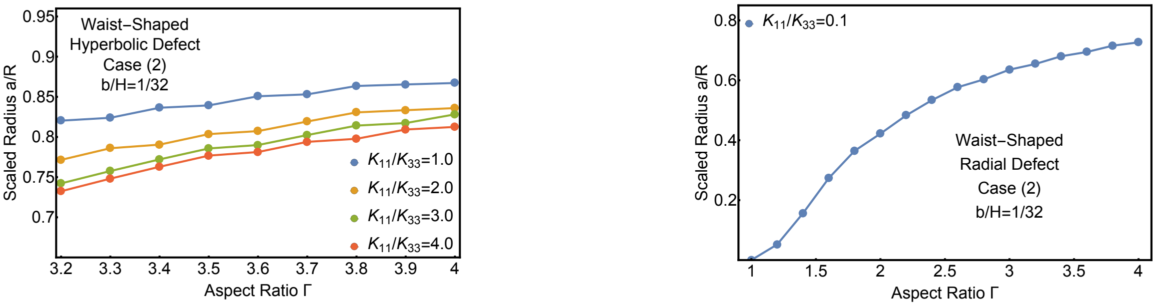

(a) Hyperbolic

(b) Radial

Figure 3.11: Radii of the ring defects in waist-shaped bridges with Case (2) and $b/H = 1/32$

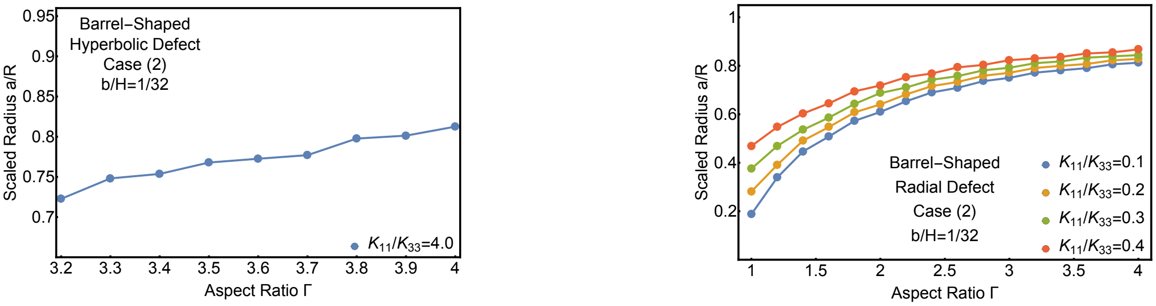

(a) Hyperbolic

(b) Radial

Figure 3.12: Radii of the ring defects in barrel-shaped bridges with Case (2) and $b/H = 1/32$

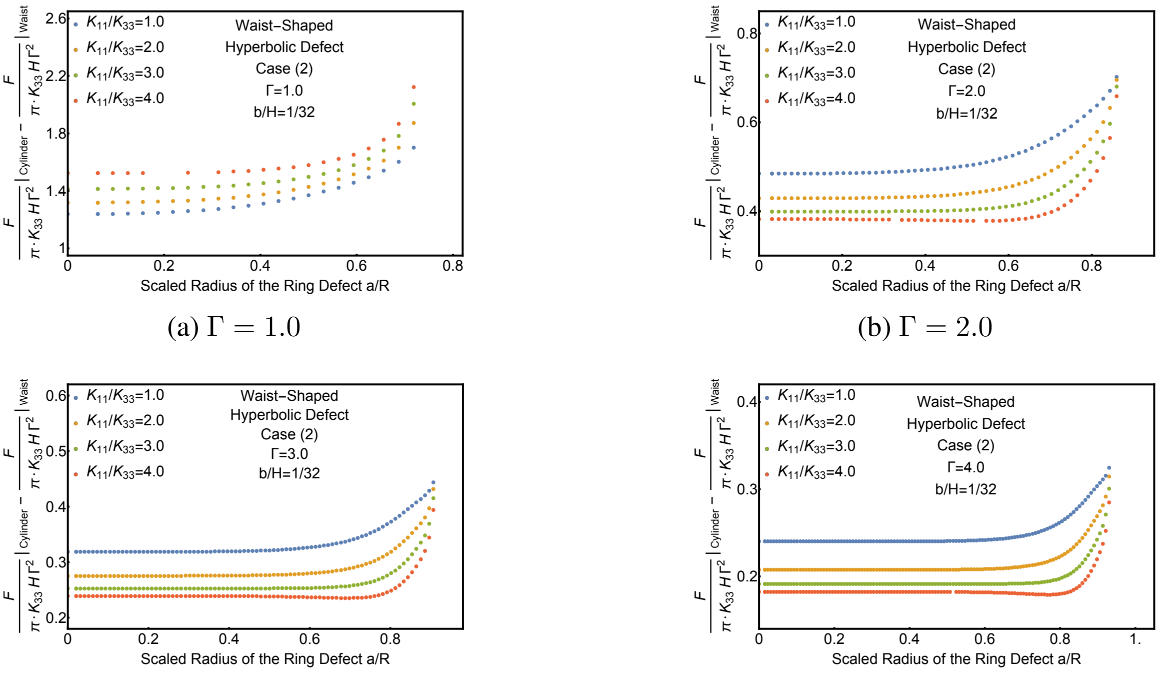

(a) $\Gamma = 1.0$

(b) $\Gamma = 2.0$

(c) $\Gamma = 3.0$

(d) $\Gamma = 4.0$

Figure 3.13: The differences between energy landscapes for hyperbolic defects between waist-shaped and cylindrical bridges with Case (2) and $b/H = 1/32$

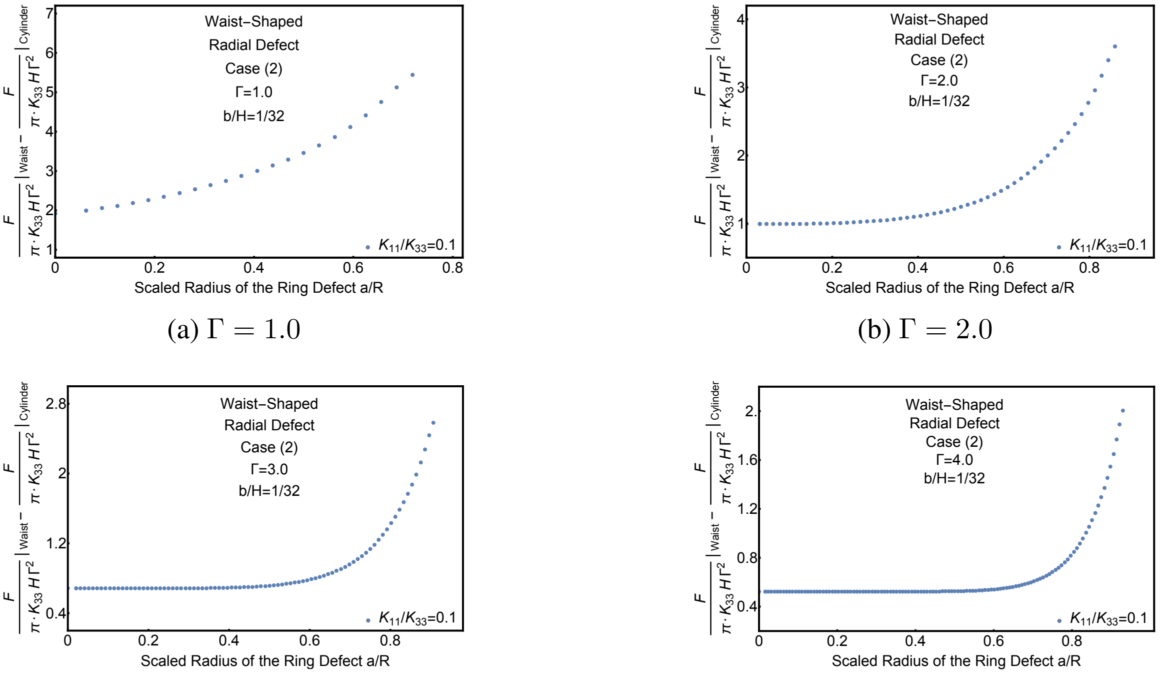

(a) $\Gamma = 1.0$

(b) $\Gamma = 2.0$

(c) $\Gamma = 3.0$

(d) $\Gamma = 4.0$

Figure 3.14: The differences between energy landscapes for radial defects between waist-shaped and cylindrical bridges with Case (2) and $b/H = 1/32$

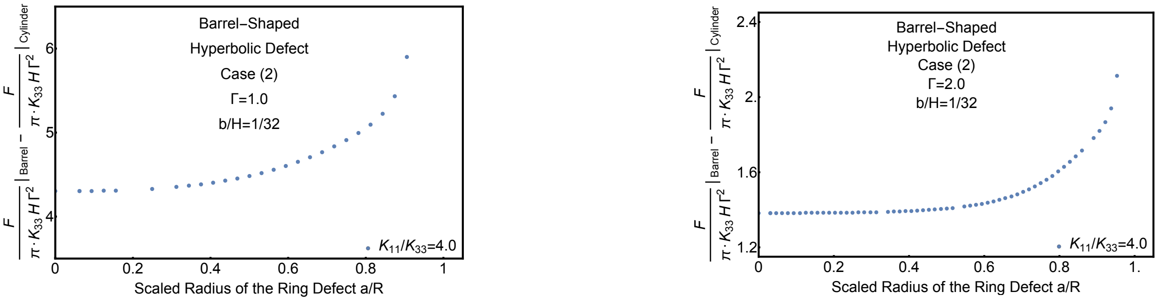

(a) $\Gamma = 1.0$ (b) $\Gamma = 2.0$

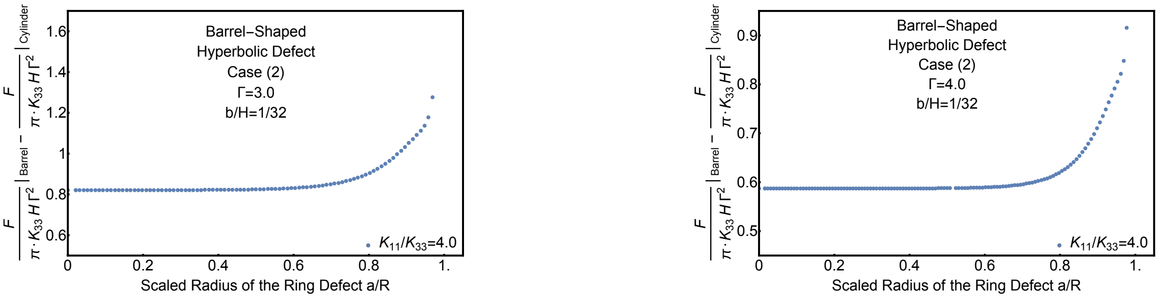

(c) $\Gamma = 3.0$ (d) $\Gamma = 4.0$

Figure 3.15: The differences between energy landscapes for hyperbolic defects between barrel-shaped and cylindrical bridges with Case (2) and $b/H = 1/32$

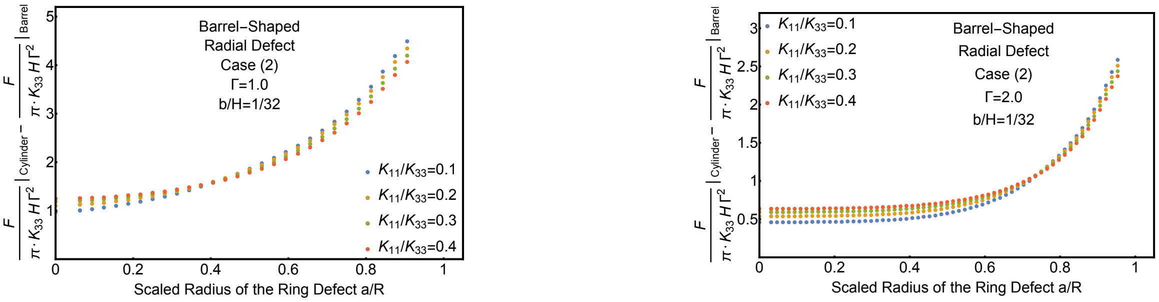

(a) $\Gamma = 1.0$ (b) $\Gamma = 2.0$

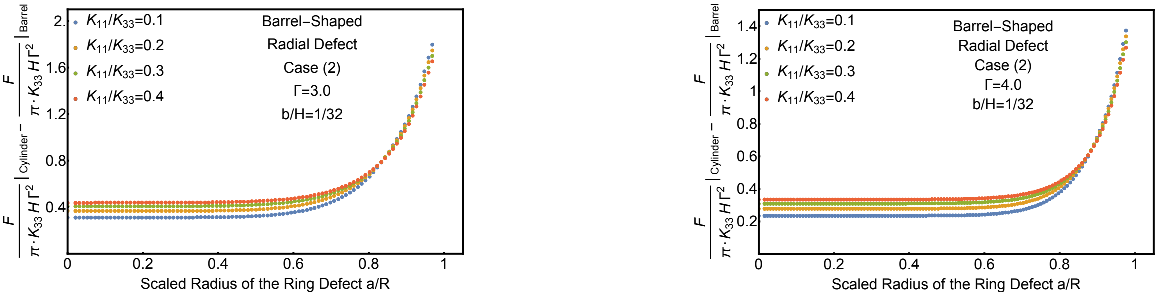

(c) $\Gamma = 3.0$ (d) $\Gamma = 4.0$

Figure 3.16: The differences between energy landscapes for radial defects between barrel-shaped and cylindrical bridges with Case (2) and $b/H = 1/32$

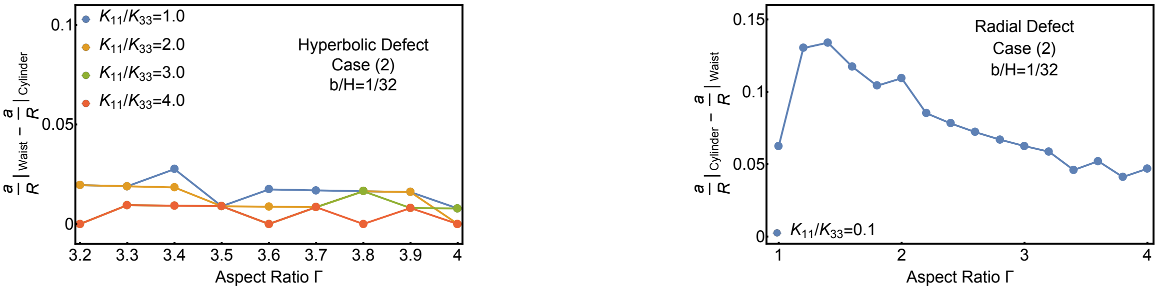

(a) Hyperbolic (b) Radial

Figure 3.17: The differences between the equilibrium ring radii between waist-shaped and cylindrical bridges with Case (2) and $b/H = 1/32$

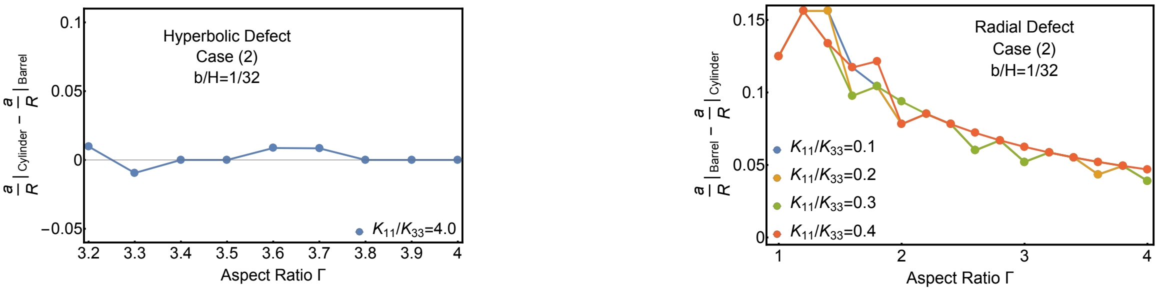

(a) Hyperbolic (b) Radial

Figure 3.18: The differences between the equilibrium ring radii between barrel-shaped and cylindrical bridges with Case (2) and $b/H = 1/32$

better choice with a decent value of K_{11}/K_{33}.

Common features

From Fig. 3.19, we observe that the concavity or the convexity of the lateral surface does not change some qualitative features of the defect structures in cylindrical bridges: in all three types of bridges (1) there exist hyperbolic point – hyperbolic ring transitions; (2) there do not exist radial point – radial ring transitions, and the radius of the radial ring gradually increases as Γ increases; (3) there exist radial defect – hyperbolic defect transitions.

The effects of concavity and convexity

Figure 3.19d is a comparison of the defect structure diagrams of the three types of bridges. We observe that the location of the hyperbolic point – hyperbolic ring transition line is not affected much (especially when Γ is large) by the concavity or convexity of the lateral surface, while the radial defect – hyperbolic defect transition line moves downward for the waist-shaped bridge and moves upward for the barrel-shaped bridge; and the reasons are provided in the last section.

The effects of the radii of the defect cores on the upper and lower planes

By comparing Figs. 3.19 with 3.20, we claim that the definition of the aspect ratio based on the radius of the upper or lower plane, i.e., $\Gamma = 2R_2/H$, is better, because the hyperbolic point – hyperbolic ring transition lines are almost overlapped. This curious phenomenon seems to suggest that the corners of the boundary, where defect cores are located, are more important to the defect transitions than the smooth part of the boundary.

3.6 Results Part IV – Comparing Numerical Results with Experiments

All the qualitative experimental results introduced before are consistent with our numerical results. Here we focus our discussion on the quantitative experimental result, i.e., the hyperbolic point – hyperbolic ring transition for a waist-shaped bridge made of 5CB ($K_{11}/K_{33} = 0.74$) occurs at $\Gamma_c = 2.7 \pm 0.3$.

The corresponding transition point $K_{11}/K_{33} = 0.74$ for the waist-shaped bridge used in our numerical computation is $\Gamma_2 = 2.60 \sim 2.63$ (where $\Gamma_2 = 2R_2/H$). Considering a different definition of Γ_1 is used in the experiments (where $\Gamma_1 = 2R_1/H$), the aspect ratio we need to compare with the experimental result should be $\Gamma_1 = 2.58 \sim 2.61$ which falls into the range 2.7 ± 0.3. The relevant energy landscapes are shown in Fig. 3.21.

There are some factors that contribute to the errors of our numerical approach:

(1) When measured in terms of Γ_2, the location of the hyperbolic point – hyperbolic ring transition line can be a little more affected by the actual shape of the lateral surface when Γ_2 is not large enough, which is indicated in Fig. 3.20d.

(2) Based on Fig. 3.19, we speculate that, whatever the shape of the lateral surface is, the location hyperbolic point – hyperbolic ring transition line is kept fixed when Γ_2 is large enough. Then the locations of the transition lines in terms of Γ_2 for our model [i.e., Eq. (3.1)] and the experiments [i.e., the lateral surface is of mean curvature] can be very close. However, since the radii of the mid-planes for these two cases are different, the locations of the transition lines in terms of Γ_1 may not be that close.

(3) The exclusion of the energy contribution from the thin layer near the lateral surface may tend to make our hyperbolic point – hyperbolic ring transition line located left to the actual transition line as indicated in Fig. 2.27d.

(4) In our model, the ratio of the cut-off length to the height is $b/H = 1/32$. In the experiments, H is on the order of 10^{-4}m, and the size of the defect core is on the order of 10^{-8}m, therefore the ratio is about 10^{-4}; see Ref. [6, 45]. As indicated in Fig. 2.27d, this also tends to make our hyperbolic point – hyperbolic ring transition line located left to the actual transition line.

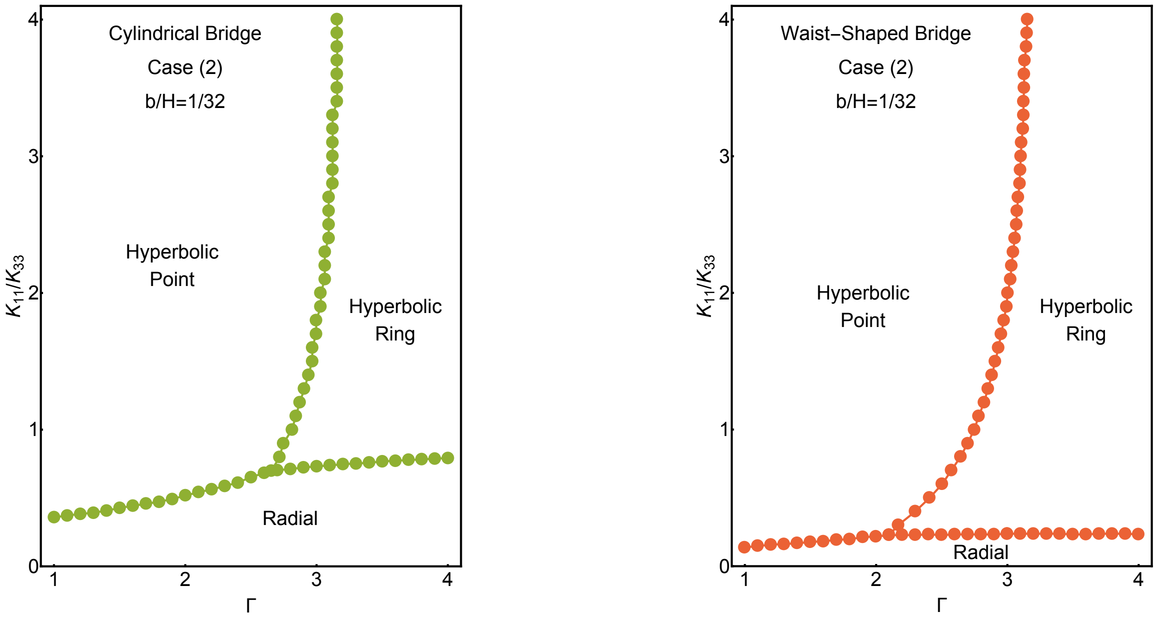

(a) Cylindrical bridge

(b) Waist-shaped bridge

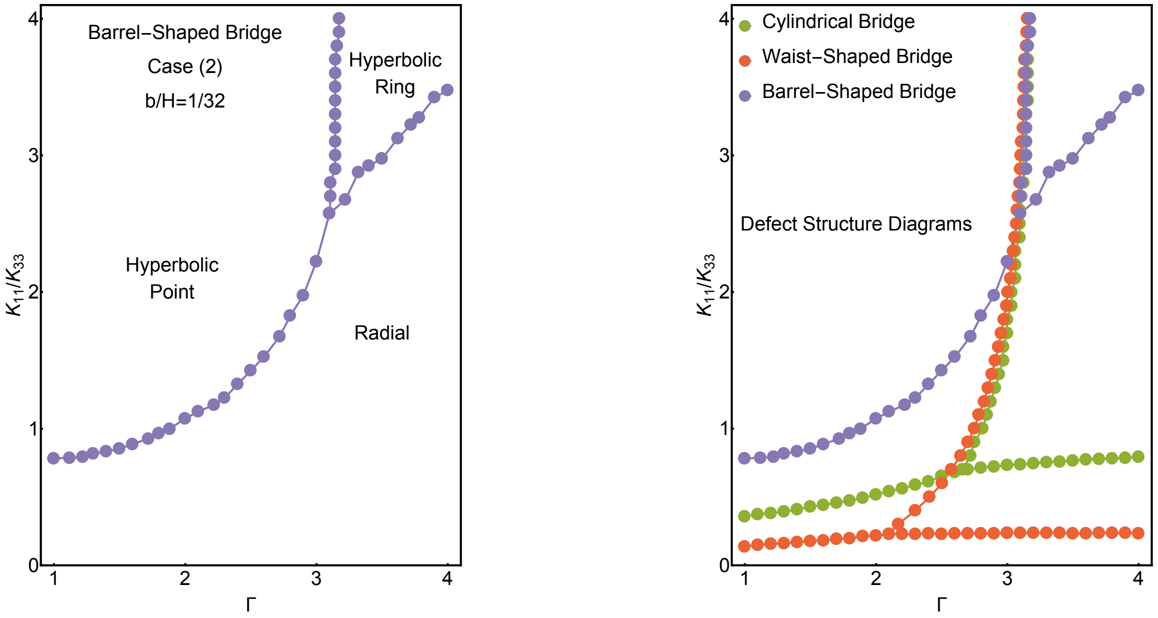

(c) Barrel-shaped bridge

(d) Comparison

Figure 3.19: Defect structure diagrams of cylindrical, waist-shaped and barrel-shaped bridges with aspect ratio defined to be $\Gamma = 2R_2/H$

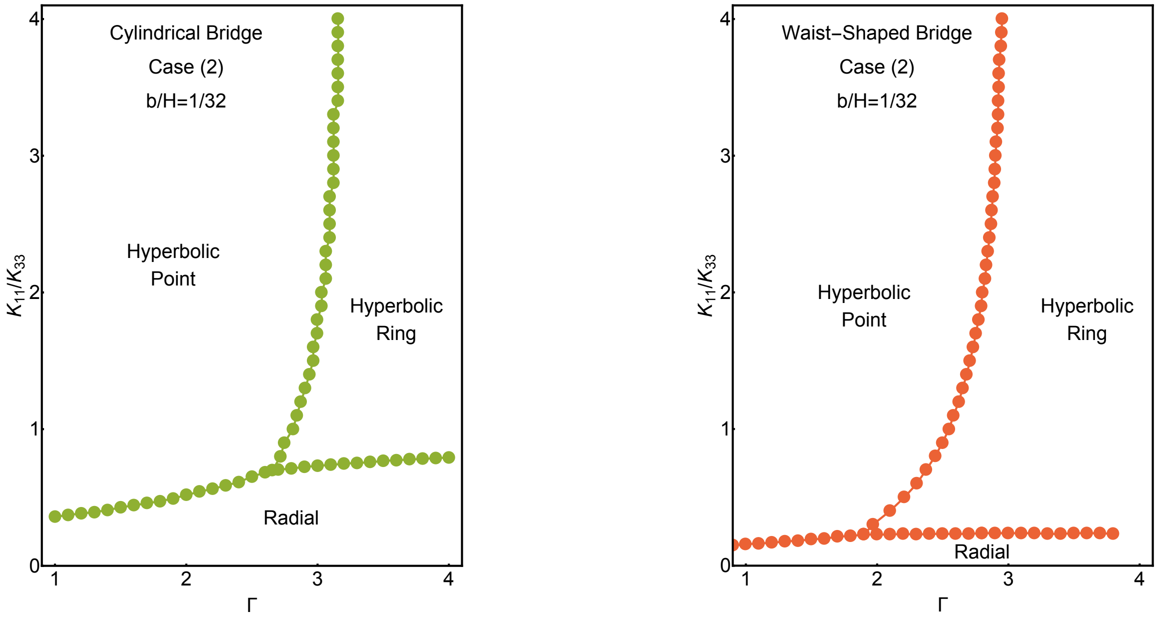

(a) Cylindrical bridge (b) Waist-shaped bridge

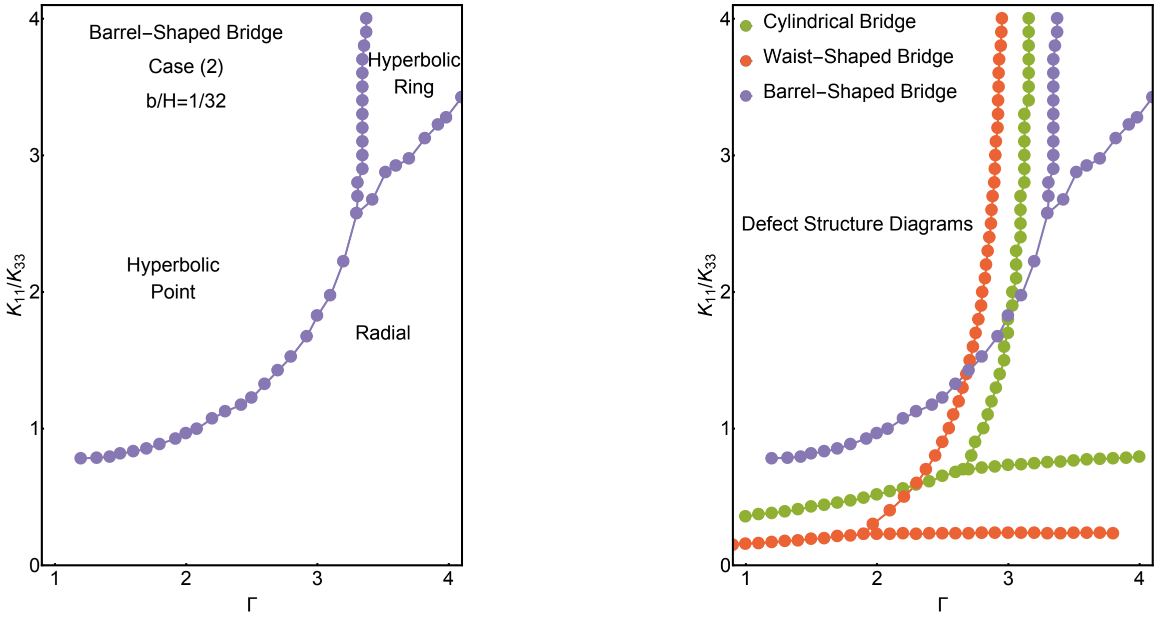

(c) Barrel-shaped bridge (d) Comparison

Figure 3.20: Defect structure diagrams of cylindrical, waist-shaped and barrel-shaped bridges with aspect ratio defined to be $\Gamma = 2R_1/H$. Compared with Fig. 3.19, the hyperbolic point – hyperbolic ring transition line remains unchanged for the cylindrical, and shifts to the left (or right) for the waist-shaped (or barrel-shaped)

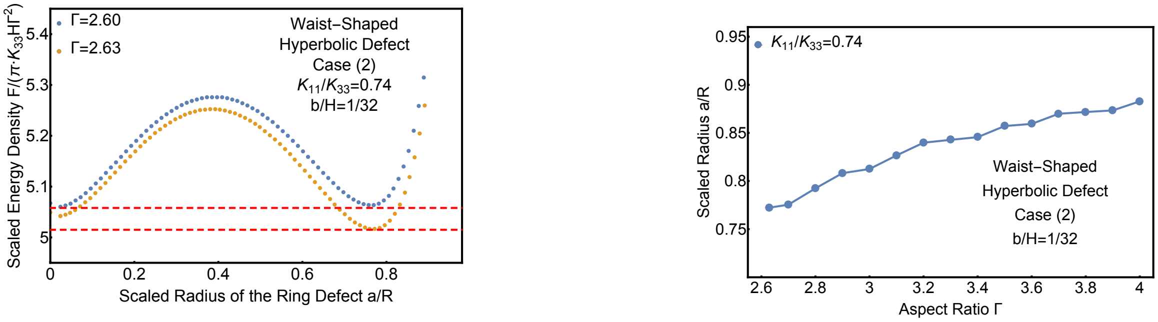

(a) Energy landscapes near the transition

(b) Radii of the ring defects

Figure 3.21: Energy landscapes and radii of the ring defects at $K_{11}/K_{33} = 0.74$ with Case (2) and $b/H = 1/32$

CHAPTER 4

NUMERICAL STUDY OF NEMATIC LIQUID-CRYSTAL BRIDGES PART II – MULTIGRID METHOD FOR CYLINDRICAL NEMATIC BRIDGES

From Chapter 2, we can see that for a fixed aspect ratio Γ and K_{11}/K_{33}, there are four equilibrium defect structures: hyperbolic point, hyperbolic ring, radial point (or small ring) and radial ring. Defects with ring radii other than the equilibrium ring radii are not in the equilibrium states. The finite difference method (with the use of successive over-relaxation method) introduced in Chapter 2 and 3 has to exhaust all the suspicious states most of which are in non-equilibrium. As mentioned in Chapter 1, this is due to the fact that the defect core is treated as an inner boundary in the Oseen-Frank formalism, therefore the Euler-Lagrange equation [i.e., Eq. (2.4)] cannot be satisfied in the whole region. By contrast, if we use Landau-de Gennes formalism, then its corresponding Euler-Lagrange equation will be satisfied in the whole region and the four equilibrium states will be its solutions. So our question is: can we stay within the context of the Oseen-Frank formalism and find solutions to only those four equilibrium states? This may require a new perspective, i.e., treating the inner boundaries as being created. In this section, we are experimenting with this new idea numerically.

4.1 Theoretical Preparations

Similar to Chapter 2, we neglect the energy contributions from the twist distortion and assume the unit vector field $\mathbf{n}$ has cylindrical symmetry. Therefore, we can focus our analysis on an arbitrary axial plane with length R and width H, and $\mathbf{n}$ can be parametrized as Eq. (2.1) which is rewritten here

$$\mathbf{n} = \cos\theta(r,z)\,\hat{\mathbf{r}} + \sin\theta(r,z)\,\hat{\mathbf{z}}. \tag{4.1}$$

However, different from Chapter 2, we do not assume $\mathbf{n}$ to be symmetric with respect to the mid-plane in the hope that our new algorithm may explore more equilibrium states.

Because no cut-off length is introduced in our numerical experiments, it is convenient to rescale R and H to be 1, and then let

$$\bar{r} = \frac{r}{R}, \tag{4.2}$$

$$\bar{z} = \frac{z}{H}, \tag{4.3}$$

$$\bar{\theta}(\bar{r}, \bar{z}) = \theta(r, z), \tag{4.4}$$

where $\bar{r}$, $\bar{z}$ and $\bar{\theta}(\bar{r}, \bar{z})$ are rescaled quantities. The Euler-Lagrange equation, i.e., Eq. (2.4), becomes

$$\begin{aligned} & K_{11}\frac{\sin 2\bar{\theta}}{\bar{r}} + \bar{r}\sin 2\bar{\theta}(K_{11} - K_{33})\Big(\Big(\frac{\partial\bar{\theta}}{\partial\bar{r}}\Big)^2 - \Big(\frac{\partial\bar{\theta}}{\partial\bar{z}}\Big)^2 \cdot \frac{\Gamma^2}{4}\Big) \\ & - \bar{r}\Gamma\cos 2\bar{\theta}(K_{11} - K_{33})\frac{\partial\bar{\theta}}{\partial\bar{r}}\frac{\partial\bar{\theta}}{\partial\bar{z}} + 2(K_{11}\sin^2\bar{\theta} + K_{33}\cos^2\bar{\theta})\frac{\partial\bar{\theta}}{\partial\bar{r}} \\ & - \frac{\Gamma}{2}\sin 2\bar{\theta}(K_{11} - K_{33})\frac{\partial\bar{\theta}}{\partial\bar{z}} + 2\bar{r}(K_{11}\sin^2\bar{\theta} + K_{33}\cos^2\bar{\theta})\frac{\partial^2\bar{\theta}}{\partial\bar{r}^2} \\ & + \frac{\Gamma^2}{2}\bar{r}(K_{11}\cos^2\bar{\theta} + K_{33}\sin^2\bar{\theta})\frac{\partial^2\bar{\theta}}{\partial\bar{z}^2} - \bar{r}\Gamma\sin 2\bar{\theta}(K_{11} - K_{33})\frac{\partial^2\bar{\theta}}{\partial\bar{r}\partial\bar{z}} = 0, \end{aligned} \tag{4.5}$$

where $\Gamma = 2R/H$ is the aspect ratio. The boundary conditions are

Radial Type

$$\begin{cases} \bar{\theta}(\bar{r},0) = -\frac{\pi}{2} \\ \bar{\theta}(\bar{r},1) = \frac{\pi}{2} \\ \bar{\theta}(0,\bar{z}) = \frac{\pi}{2} \text{ or } -\frac{\pi}{2} \\ \bar{\theta}(1,\bar{z}) = 0 \end{cases} \tag{4.6}$$

Hyperbolic Type

$$\begin{cases} \bar{\theta}(\bar{r},0) = \frac{\pi}{2} \\ \bar{\theta}(\bar{r},1) = -\frac{\pi}{2} \\ \bar{\theta}(0,\bar{z}) = \frac{\pi}{2} \text{ or } -\frac{\pi}{2} \\ \bar{\theta}(1,\bar{z}) = 0 \end{cases} \tag{4.7}$$

which are illustrated in Fig. 4.1. Note that $\bar{\theta}(0,\bar{z})$ in Eqs. (4.6) and (4.7) is not specified enough; and we will deal with this issue when constructing the initial conditions as introduced later.

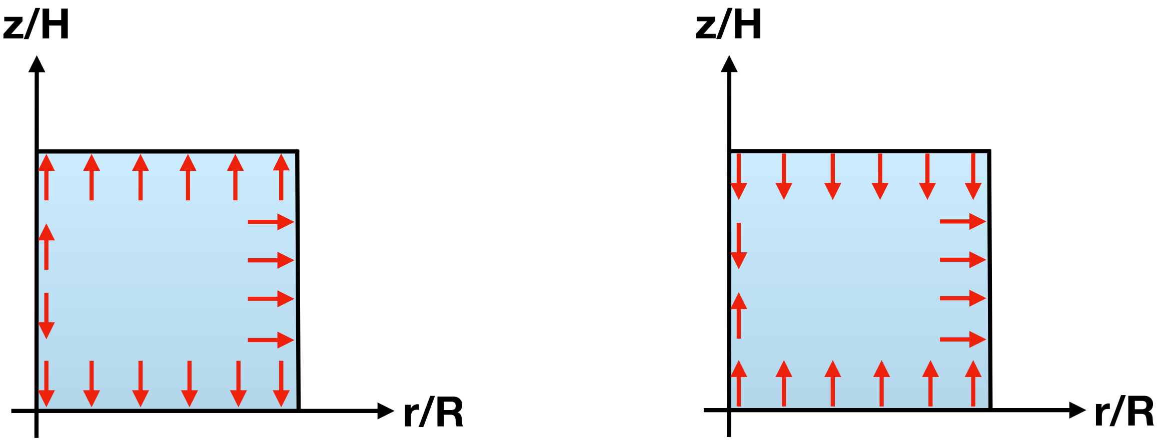

(a) Radial

(b) Hyperbolic

Figure 4.1: Boundary conditions on the one half of the axial plane

Then our job is to numerically solve the boundary value problem consisting of Eqs. (4.5)

– (4.7). However, Eqs. (4.6) and (4.7) are only the outer boundary conditions (the inner boundary conditions, i.e., the defect cores, are not specified), and Eq. (4.5) is only satisfied on a sub-domain (which does not contain the defect core) which has almost the same area as the whole region. Then a question arises: how can we create the inner boundary (i.e., the defect core) during the numerical process?

We suspect a "competition" between the Euler-Lagrange equation and the outer boundary condition: the Euler-Lagrange equation would like to be satisfied everywhere inside the domain bounded by the outer boundary; however, the outer boundary condition does not allow that to happen; therefore, there are some tiny regions, i.e., the defect cores, where the Euler-Lagrange equation is not satisfied. In short, we suspect that this "competition" leads to the formation of the defect structure.

4.2 Numerical Strategy

We suspect that this "competition" can be realized by the use of multigrid method. First, let me introduce the general ideas of multigrid method [82, 93–95].

Suppose we are aiming at solving the following PDE

$$\mathcal{L}(u) = f, \tag{4.8}$$

where $\mathcal{L}$ is the operator, f is the source term and u is the solution. After discretized on the grid with mesh size h, Equation (4.8) becomes

$$\mathcal{L}_h(u_h) = f_h, \tag{4.9}$$

where u_h is the exact solution on this grid. Let $\tilde{u}_h$ be an approximation of u_h, based on which we are aiming at obtaining a much better approximation. Let the residual d_h be

$$d_h = \mathcal{L}_h(\tilde{u}_h) - \mathcal{L}_h(u_h). \tag{4.10}$$

Then Eq. (4.9) is equivalent to

$$\mathcal{L}_h(\tilde{u}_h) = f_h + d_h. \tag{4.11}$$

Obviously, the smaller of d_h, the better of the approximation $\tilde{u}_h$.

For the relaxation method, we work on the same grid and decompose $\mathcal{L}_h$ as

$$\mathcal{L}_h = \mathcal{A}_h - \mathcal{B}_h, \tag{4.12}$$

where $\mathcal{A}_h$ is the part that is easy to be inversed, and the common methods include the Jacobi and Gauss-Seidel methods [82–84]. Then based on Eqs. (4.11) and (4.13), we arrive at following iterative equation

$$\tilde{u}_h^{(n)} = \mathcal{A}_h^{-1}(\mathcal{B}_h(\tilde{u}_h^{(n-1)}) + f_h), \tag{4.13}$$

where $\tilde{u}_h^{(n)}$ represents the approximated solution at the nth iterative step, which is expected to be closer to u_h than $\tilde{u}_h^{(n-1)}$. After enough iterative steps, we expect that d_h is very small and therefore $\tilde{u}_h$ is very close to u_h. For the study of defects in nematics, it is not obvious to us how to create a defect core during this relaxation process, because creating a defect core seems to imply a large change at that particular space point.

For the multigrid method, apart from the numerical process on the grid with mesh size h, i.e., Eqs. (4.9) and (4.11), we need to construct a numerical process on a coarser grid with mesh size H. The counterpart of Eq. (4.9) on this coarser grid is

$$\mathcal{L}_H(u_H) = \mathcal{L}_H(\mathcal{R}\tilde{u}_h) - \mathcal{R}d_h, \tag{4.14}$$

where $\mathcal{R}$ is the restriction operator. Let $\tilde{u}_H$ be an approximation of u_H, then the counterpart of Eq. (4.11) on this coarser grid is

$$\mathcal{L}_H(\tilde{u}_H) = \mathcal{L}_H(\mathcal{R}\tilde{u}_h) - \mathcal{R}d_h + d_H, \tag{4.15}$$

where d_H is the residual on this coarser grid. Then $\tilde{u}_h$ on the finer grid is updated by

$$\tilde{u}_h' = \tilde{u}_h + \mathcal{P}(\tilde{u}_H - \mathcal{R}\tilde{u}_h), \tag{4.16}$$

where $\mathcal{P}$ is the prolongation operator which interpolates the values on the coarser grid to the finer grid. We can also define the the relative truncation error by

$$\tau_h \equiv \mathcal{L}_H(\mathcal{R}u_h) - \mathcal{R}\mathcal{L}_h(u_h), \tag{4.17}$$

and its approximation by

$$\tilde{\tau}_h \equiv \mathcal{L}_H(\mathcal{R}\tilde{u}_h) - \mathcal{R}\mathcal{L}_h(\tilde{u}_h). \tag{4.18}$$

Then Eqs. (4.14) and (4.15) become, respectively,

$$\mathcal{L}_H(u_H) = f_H + \tau_h, \tag{4.19}$$

and

$$\mathcal{L}_H(\tilde{u}_H) = f_H + \tilde{\tau}_h + d_H. \tag{4.20}$$

Following the same procedures, we can construct numerical processes on many grids which have different mesh densities, hence the name multigrid method. Also on each grid, we can do a relaxation process such that d_h, $d_H \ldots$ are small enough.

We are optimistic that the multigrid method is able to create a defect core during the numerical process: first, after relaxation, the solution on the coarsest grid may contain the crudest information about the location of the defect core such as whether it is in the left half or right half of the whole region; then, by interpolating this solution to a finer grid and doing a relaxation process, we can obtain a solution that further fine down the location of the defect core; and finally, the solution on the finest grid may tell us the accurate location of the defect core. It is a rather unconventional use of the multigrid method, and the detailed description of our algorithm is as follows.

After rescaling, the whole domain (i.e., the one half of the axial plane) is a 1×1 square.

We choose six different grids with number of lattice points: 3×3, 5×5, 9×9, 17×17, 33×33 and 65×65, such that the mesh size of one grid is twice of the mesh size of the neighboring coarser grid. Let $\bar{\theta}^k_{i,j}$ denote the value on the k-th grid, i-th column and j-th row. Also, on the finest grid with 65×65 lattices, we assume that there is a horizontal line which cuts the whole region in halves. It is like a not fully formed inner boundary which contains the "branch cut" of the unit vector field $\mathbf{n}$. We expect it to induce the formation of a defect core during the numerical process, and we let it to be at the w-th row of the lattice points counting from the lower side of the square region.

The restriction operator $\mathcal{R}$ in our algorithm is defined by letting $\bar{\theta}^k_{i,j} = 0.5 \cdot \bar{\theta}^{k+1}_{2i-1,2j-1} + 0.125 \cdot (\bar{\theta}^{k+1}_{2i,2j-1} + \bar{\theta}^{k+1}_{2i-1,2j} + \bar{\theta}^{k+1}_{2i-2,2j-1} + \bar{\theta}^{k+1}_{2i-1,2j-2})$ [for $2 \le i \le n_k$], $\bar{\theta}^k_{i,1} = \bar{\theta}^{k+1}_{2i-1,1}$, $\bar{\theta}^k_{i,n_k} = \bar{\theta}^{k+1}_{2i-1,n_{k+1}}$ [for $1 \le i \le n_k$], and $\bar{\theta}^k_{1,j} = \bar{\theta}^{k+1}_{1,2j-1}$, $\bar{\theta}^k_{n_k,j} = \bar{\theta}^{k+1}_{n_{k+1},2j-1}$ [for $2 \le j \le n_k$]; where n_k is the number of lattice points along one side of the square in the k-th grid. The prolongation operator $\mathcal{P}$ is different for the coarsest grid and the rest of the grids due to the location of the above-mentioned horizontal line, and it will be introduced along with the numerical process shown as follows.

(a) Radial

(b) Hyperbolic

Figure 4.2: Vectors on the 3×3 grid

Step 1, start with the coarsest grid with 3×3 lattices. Of the total nine lattice points, eight are prescribed by the boundary condition. The value of the lattice point in the center can be calculated exactly by a nonlinear algebraic equation. For simplicity, we assign it to be the same as the one on its left side as shown in Fig. 4.2.

Step 2, work on the finer grid with 5×5 lattices. Firstly, there is an interpolation process: (a) copy the values on the coarsest grid with 3×3 lattices onto the grid with 5×5 lattices by letting $\bar{\theta}^2_{2i-1,2j-1}=\bar{\theta}^1_{i,j}$, where $i,j=1,2,3$; (b) make sure the grid with 5×5 lattices has the correct outer boundary conditions, i.e., $\bar{\theta}^2_{2i-1,2j}=\bar{\theta}^2_{2i-1,2j-1}$ (for $i=1,3$ and $j=1,2$) and $\bar{\theta}^2_{2i,2j-1}=\bar{\theta}^2_{3,2j-1}$ (for $i=1,2$ and $j=1,3$); (c) for the remaining lattice points, we let its value to be the upper boundary condition if $i>w\cdot5/65$ and let its value to be the lower boundary condition if $i\leq w\cdot5/65$, where $w\cdot5/65$ is the location of the horizontal line scaled on this grid (note that we define it to be an integer type when programming with C language). Secondly, there is a relaxation process by Eqs. (4.13) and (4.20) with a constraint specially designed to cope with the "branch cut" or head-tail symmetry of $\mathbf{n}$: when computing the difference equation, if the difference of the two neighboring $\bar{\theta}^2_{i,j}$, we add or subtract a π from it; in addition, if the updated $\bar{\theta}^2_{i,j}$ is less than 0, we force it to be 0; and if it is greater than π, we force it to be π. We hope that the resulting updated $\bar{\theta}^2_{i,j}$ can contain the crudest information about the location of the defect core. And finally, we compute the relative truncation error $\tilde{\tau}_{5\times5}$ and store it on the coarsest grid with 3×3 lattices.

Step 3, back to the coarsest grid with 3×3 lattices. Ideally, we should solve Eq. (4.20) with $\tilde{\tau}_{5\times5}$ given by Step 2 and d_H ignored. However, for simplicity, we just repeat Step 1, which may introduce some inaccuracies to our final numerical results.

Step 4, back to the grid with 5×5 lattices. We update $\bar{\theta}^2_{i,j}$ by Eq. (4.16), and then we do another round of relaxation process by Eq. (4.13).

Step 5, work on the grid with 9×9 lattices. Similar to Step 2, firstly, there is a an interpolation process with a slightly different prolongation operator: (a) copy the values on the 5×5 grid onto the corresponding lattice points on the 9×9 grid by letting $\bar{\theta}^3_{2i-1,2j-1}=\bar{\theta}^2_{i,j}$, where $i,j=1\sim5$; (b) make sure the 9×9 grid has the correct outer boundary conditions, i.e., $\bar{\theta}^3_{2i-1,2j}=\bar{\theta}^3_{2i-1,2j-1}$ [for $i=1,5$ and $j=1\sim4$] and $\bar{\theta}^3_{2i,2j-1}=\bar{\theta}^3_{5,2j-1}$

[for $i = 1 \sim 4$ and $j = 1, 5$]; (c) for the remaining lattice points, we let $\bar{\theta}^3_{2i,2j-1} = 0.5 \times (\bar{\theta}^3_{2i+1,2j-1} + \bar{\theta}^3_{2i-1,2j-1})$ [for $i = 1 \sim 4$, $j = 2 \sim 4$]; (d) if the location of the defect core $w \cdot 9/65$ (defined as integer type) is an even number, we let $\bar{\theta}^3_{2i-1,2j} = 0.5 \times (\bar{\theta}^3_{2i-1,2j-1} + \bar{\theta}^3_{2i-1,2j+1})$ [for $i, j = 2 \sim 4$, and $j \neq w \cdot 9/130$ or $1 + w \cdot 9/130$] and let $\bar{\theta}^3_{i,j} = \bar{\theta}^3_{i,j-1}$ [for $i = 1 \sim 9$ and $j = w \cdot 9/65$] as well as $\bar{\theta}^3_{i,j} = \bar{\theta}^3_{i,j+1}$ [for $i = 1 \sim 9$ and $j = 2 + w \cdot 9/65$]; (e) if the location of the defect core $w \cdot 9/65$ is an odd number, we let $\bar{\theta}^3_{2i-1,2j} = 0.5 \times (\bar{\theta}^3_{2i-1,2j-1} + \bar{\theta}^3_{2i-1,2j+1})$ [for $i, j = 2 \sim 4$, and $j \neq 0.5 \times (-1 + w \cdot 9/65)$ or $0.5 \times (1 + w \cdot 9/65)$] and let $\bar{\theta}^3_{i,j} = \bar{\theta}^3_{i,j-1}$ [for $i = 1 \sim 9$ and $j = -1 + w \cdot 9/65$] as well as $\bar{\theta}^3_{i,j} = \bar{\theta}^3_{i,j+1}$ [for $i = 1 \sim 9$ and $j = 1 + w \cdot 9/65$]. Secondly, there is a relaxation process by Eq. (4.13) and (4.20) with the same constraint as introduced in Step 2. We hope that the resulting updated $\bar{\theta}^3_{i,j}$ can fine down the location of the defect core. And finally, we compute $\tilde{\tau}_{9\times 9}$ and store it on the grid with 5×5 lattices.

Step 6, back to the grid with 5×5 lattices. There is the same relaxation process with updated $\tilde{\tau}_{9\times 9}$. Then we compute a new $\tilde{\tau}_{5\times 5}$ and store it on the coarsest grid with 3×3 lattices.

Step 7, back to the coarsest grid with 3×3 lattices, where we just repeat Step 1 or 3.

Step 8, back to the grid with 5×5 lattices, where we update $\bar{\theta}^2_{i,j}$ by Eq. (4.16) and do another round of relaxation process.

Step 9, back to the grid with 9×9 lattices, where we update $\bar{\theta}^3_{i,j}$ and do another round of relaxation process.

The remaining steps follow the same pattern: we work on the grid with 17×17 lattices, then go down to the coarsest grid with 3×3 lattices, then bounce back to the finer grid, and eventually obtain our numerical solution on the finest grid with 65×65 lattices, where the accurate location of the defect core is expected to be determined. The diagram of the complete numerical process is shown in Fig. 4.3.

Compared with the numerical method introduced in Chapter 2 and 3 which requires

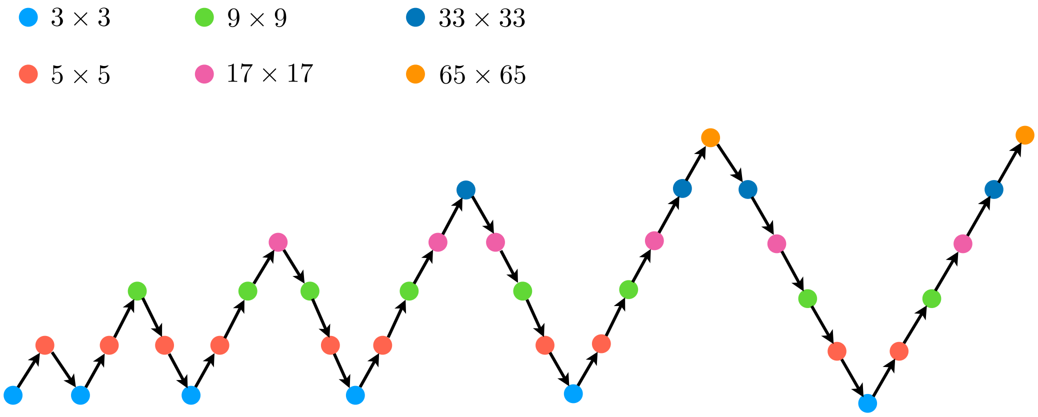

Figure 4.3: Diagram of the numerical process of the multigrid method used in our study

an energy landscape to determine the ground state, the multigrid method is expected to directly show us the equilibrium states, nevertheless a more theoretical justification is lacking. The most worrisome fact about our algorithm is that Eq. (4.5) is only satisfied outside the defect core (i.e., inner boundary), not everywhere inside the domain bounded by the outer boundary. This leads to the fact that we do not know for sure when we should stop the iterative process, and our temporary treatment is to wait until the solution stabilizes, i.e., the resulting unit vector field $\mathbf{n}$ does not change its pattern. This problem also makes the evaluation of the energy functional impossible. As a result, we are unable to determine which one of the equilibrium states is the ground state.

This algorithm has the ability to "create" defect cores: initially, we only specify that the defect core is at the w-row of the lattice points; then after running the algorithm, we observe the defect core is formed at a fixed column, and the defect core is characterized by a tiny region where the the direction of the vector field $\mathbf{n}$ looks undefined. A different algorithm which also "creates" defect cores is introduced in Ref. [96], where the relaxation and gradient methods are used. The main difference is that: for our algorithm, the seemingly equilibrium defect structures are obtained without the evaluation of energy functional. There may be two possible explanations: (1) there is a deficiency in our algorithm so that the resulting defect structures are not guaranteed to be in equilibrium; (2) there may be some differences in finding equilibrium ring defects (for our algorithm) and equilibrium point defects (for the algorithm introduced in Ref. [96]). Here I must confess that I am unable to provide a more theoretical justification of our numerical idea and algorithm. What I can show are some interesting results which may guide our future study and induce other researchers' interest.

For the source code, please visit our github repository; see Ref. [97].

4.3 Results

4.3.1 Qualitative Study of Defect Structures

The most interesting fact about this algorithm is that it can efficiently produce the four types of equilibrium defect structures as shown in Fig. 4.4, which we can compare with Fig. 2.8 in Chapter 2. For specified Γ and K_{11}/K_{33}, the hyperbolic or radial point defect can be obtained by setting $w = 36$ (or a few of other values, where recall that we let the defect core to be at the w-row of the lattices) and using the boundary condition Eq. (4.7) or (4.6); and the hyperbolic or radial ring defect can be obtained by setting $w = 33$ (or a few of other values) and using the boundary condition Eq. (4.7) or (4.6).

However, there is an inconsistency between the results here and the ones in Chapter 2: here, it seems that the four defect structures are the equilibrium states; nevertheless, the results in Chapter 2 show that there is only one local minimum for the radial type of defects. In addition, our algorithm works well for K_{11}/K_{33} being close to one when Eq. (4.5) is close to being a semi-linear PDE; otherwise, we may obtain some bizarre-looking solutions which are obviously not the equilibrium states. That implies that our algorithm does not cope with nonlinearity very well.

If the resulting four defect structures, where the defect cores are located at the midplane, are proved to be the equilibrium states, then our next question is: can we prove these are the only equilibrium states, or can we produce other equilibrium states? We observe that, in most cases, the resulting defect cores are located close to the horizontal line prescribed in our algorithm. We suspect that the question can be answered after our

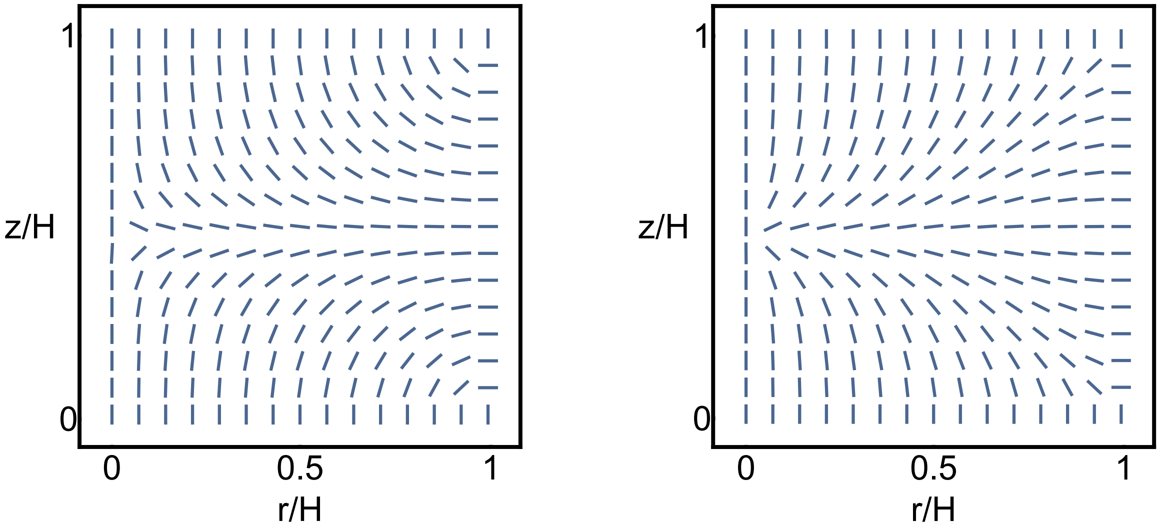

(a) Hyperbolic point

(b) Radial point

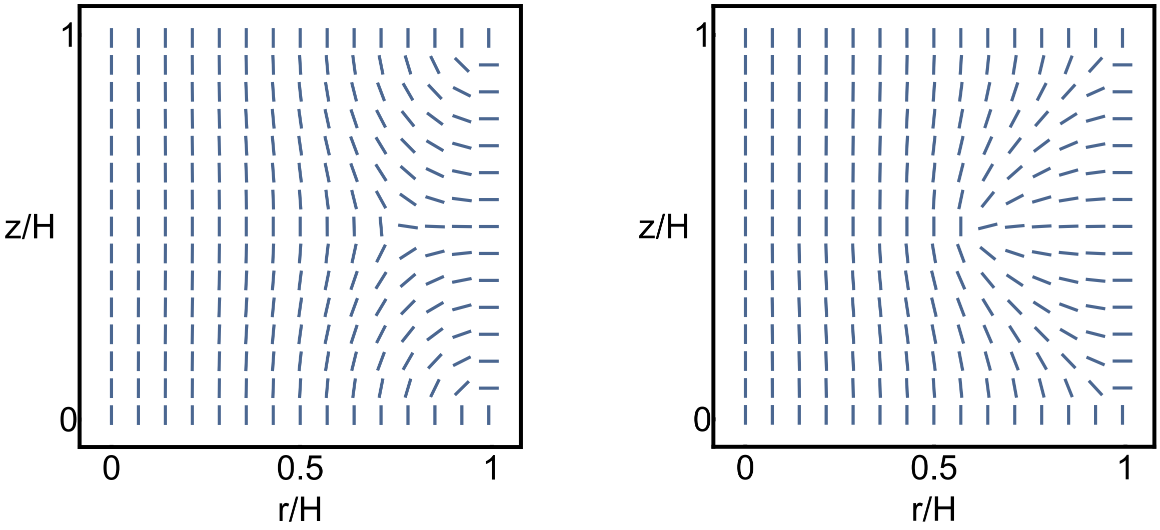

(c) Hyperbolic ring

(d) Radial ring

Figure 4.4: Defect structures at $\Gamma = 1.0$, $K_{11}/K_{33} = 2.0$ (shown in one half of the diametrical plane)

algorithm is modified such that the defect core not only moves freely on the prescribed horizontal line but also moves freely away from it.

4.3.2 Quantitative Study of Ring Radii

One attempt of showing the effectiveness of this algorithm in producing equilibrium defect structures is to compare the radii of the ring defects obtained by this algorithm with the results from Chapter 2.

Figures. 4.5 and 4.6 provide the comparisons of the ring radii calculated by the multigrid method with the equilibrium ring radii calculated by the successive over-relaxation method introduced in Chapter 2. Although the lines representing the multigrid method is highly nonsmooth, they are not far from the lines representing the equilibrium defect structures; in addition, they show the correct relation between the equilibrium ring radii and Γ, i.e., the scaled equilibrium ring radii increase with the increase of Γ. The reason why these lines do not always show the correct relation between the equilibrium ring radii and K_{11}/K_{33} is likely due to the fact that our algorithm does not have a good treatment for the nonlinearity.

By comparing the defect structures obtained by the multigrid method and those obtained in Chapter 2, Figs. 4.7 and 4.8 further confirm that the defect structures (obtained by the multigrid method) with almost same radii as the equilibrium defect structures do look like the equilibrium states. One may say that the defect core in Fig. 4.7a is nicely formed while the defect core in Fig. 4.8a is awfully formed; however, this intuition needs to be justified at a higher level of lattice refinement.

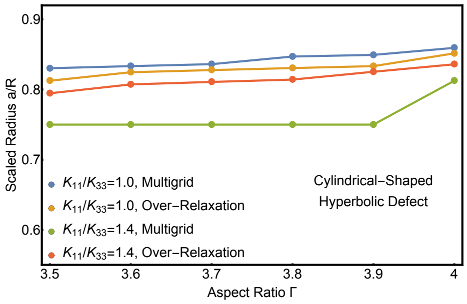

Figure 4.5: Comparison of the equilibrium hyperbolic – ring radii calculated by the multigrid method and the successive over-relaxation method at $K_{11}/K_{33} = 1.0$ and 1.4

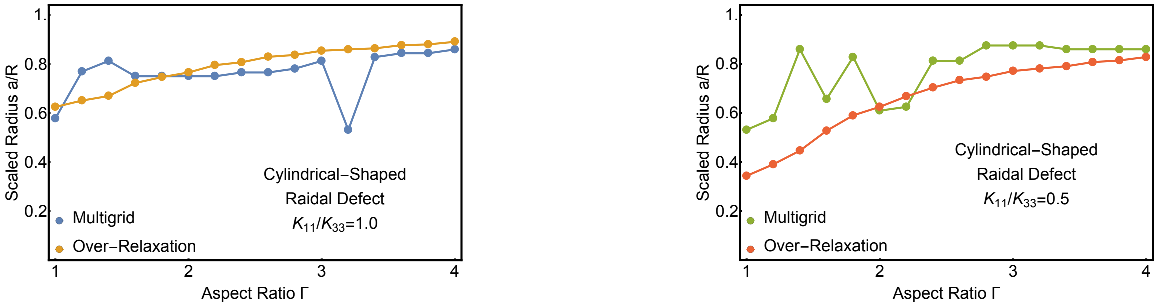

(a) Equilibrium radial – ring radii calculated by the multigrid method and the successive over-relaxation method at $K_{11}/K_{33} = 1.0$

(b) Equilibrium radial – ring radii calculated by the multigrid method and the successive over-relaxation method at $K_{11}/K_{33} = 0.5$

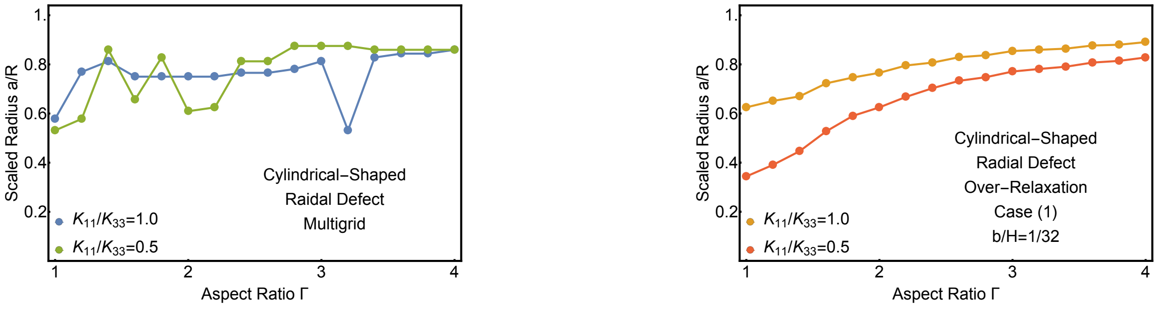

(c) Equilibrium radial – ring radii calculated by the multigrid method at $K_{11}/K_{33} = 1.0$ and 0.5

(d) Equilibrium radial – ring radii calculated by the successive over-relaxation method at $K_{11}/K_{33} = 1.0$ and 0.5

Figure 4.6: Comparison of the equilibrium radial – ring radii calculated by the multigrid method and the successive over-relaxation method at $K_{11}/K_{33} = 1.0$ and 0.5

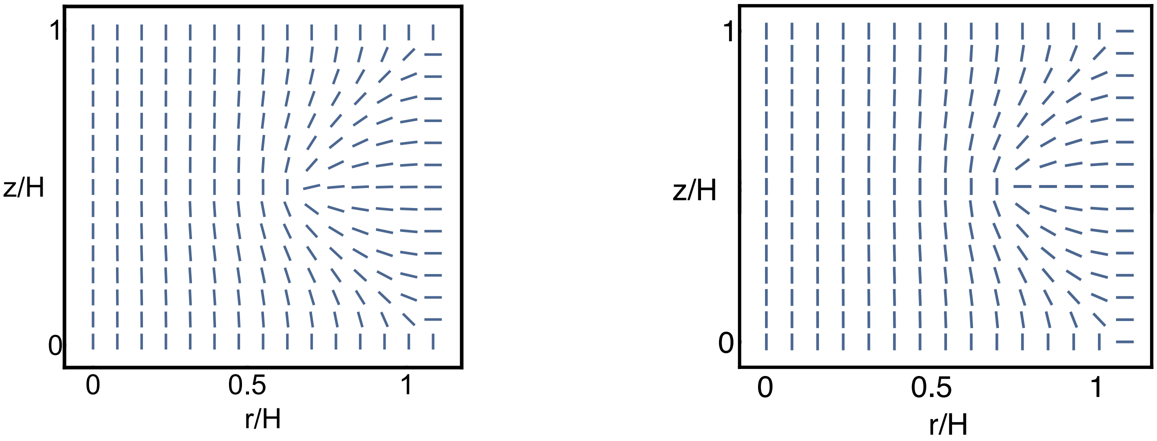

(a) Defect structure by the multigrid method

(b) Defect structure by the successive over-relaxation method

Figure 4.7: Comparison of the defect structures calculated by the multigrid method and the successive over-relaxation method at $\Gamma = 2.2$, $K_{11}/K_{33} = 0.5$

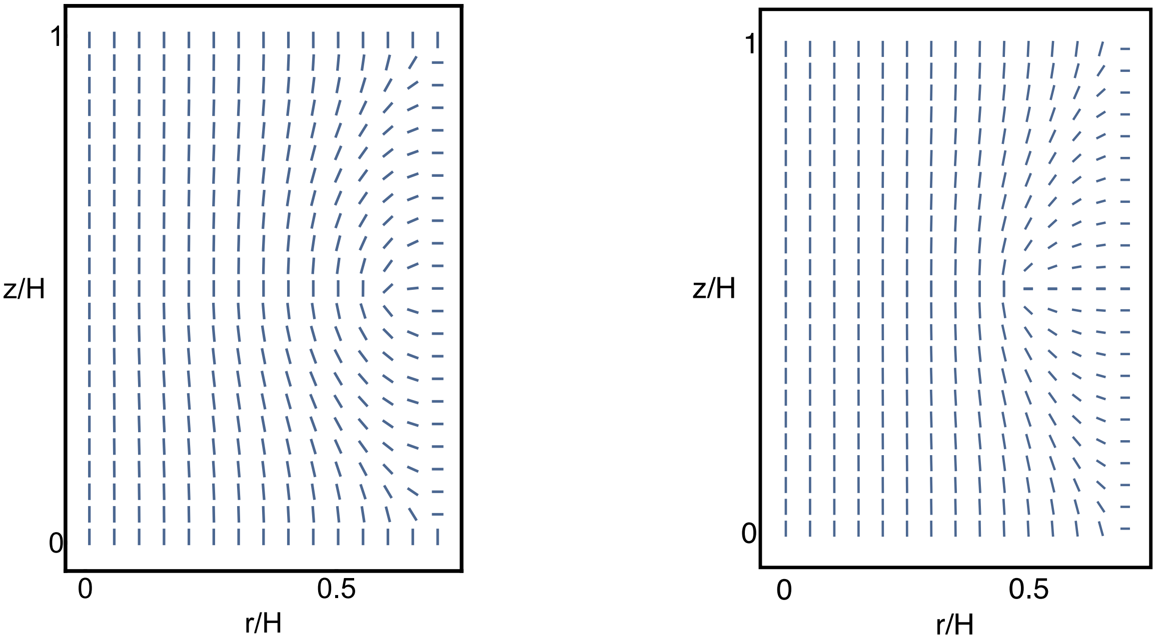

(a) Defect structure by the multigrid method

(b) Defect structure by the successive over-relaxation method

Figure 4.8: Comparison of the defect structures calculated by the multigrid method and the successive over-relaxation method at $\Gamma = 1.4$, $K_{11}/K_{33} = 0.5$

CHAPTER 5

ANALYTICAL STUDY OF NEMATIC DEFECTS PART I – CALCULUS OF VARIATIONS FOR ONE-DIMENSIONAL DISCONTINUOUS FUNCTIONS

The multigrid method introduced in Chapter 4 provides numerical evidence that the defect cores (inner boundaries) can be created in the process of solving the Euler-Lagrange equation. However its methodology does not apply to analytical calculations. To construct an analytical theory, we first choose to believe that this is still a problem of calculus of variations (may be a weird one). Then the next step is to figure out the domain of the function space.

For many examples of calculus of variations we encounter, the domain is fixed and the functional derivative is conducted on this fixed domain; see Refs. [79, 80, 98]. However, in the Oseen-Frank formalism of defects in nematics, the domain is divided by the emergent defect cores and branch cuts into many patches. The solution is nicely smooth on each patch, but can be wildly discontinuous on the whole domain [11, 19–22]. That means, the function space for the whole domain can be a very large Sobolev space, while the function space for each patch is a space of smooth functions. To resolve this issue, first we need to figure out whether (1) the energy comes from the differentiation and integration of the function over the whole domain, or (2) it comes from the differentiation and integration over each patch and then sum them up. According to the discussions in Chapter 1, the differentiation and integration over the defect cores and branch cuts leads to an unphysical energy. Therefore, (2) is physically correct. We classify this type of problems as the calculus of variations for discontinuous functions. In this chapter, we focus our discussions on some special one-dimensional examples.

5.1 The Principle – Method (A)

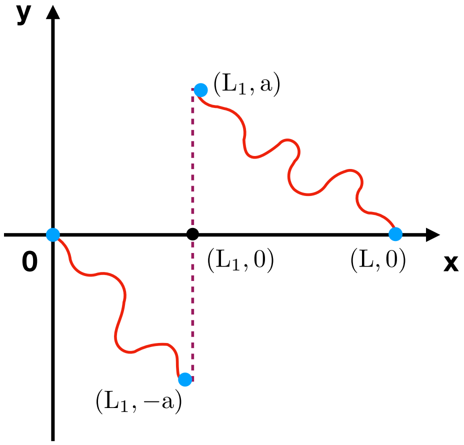

Figure 5.1: Calculus of variations

Let us start with the functional

$$F[f(x), f'(x)] = \int_U \mathrm{d}x\, \mathcal{F}(f(x), f'(x)), \tag{5.1}$$

subject to the outer boundary conditions

$$f(0) = f(L) = 0, \tag{5.2}$$

and inner boundary conditions

$$f(L_1^-) = -f(L_1^+) = -a, \tag{5.3}$$

with a being a fixed parameter, which is illustrated in Fig. 5.1. The domain U is defined to be the union of two disjoint sets, i.e., $U = [0, L_1) \cup (L_1, L]$, where the variable L_1 is the location of the discontinuity. This makes sure that the differentiation and integration processes do not cross the discontinuity, therefore there will be no “unphysical” infinite energy. A detailed procedure is in the following.

To find its first functional derivative, let $f_b(x), f_c(x)$ denote the functions $f(x)$ with discontinuities being at $L_1 = b, c$ [i.e., $f_b(b^-) = -f_b(b^+) = -a$, $f_c(c^-) = -f_c(c^+) = -a$], and let $\delta f_b(x), \delta f_c(x)$ denote the variations on $f_b(x), f_c(x)$ with $\delta f_b(b^-) = \delta f_b(b^+) = 0$, $\delta f_c(c^-) = \delta f_c(c^+) = 0$. Assume $\delta f_b(x), \delta f_c(x)$ are small, and $|c - b| \ll 1$. Then,

$$0 = F[f_c + \delta f_c] - F[f_b] = (F[f_c + \delta f_c] - F[f_c]) + (F[f_c] - F[f_b]), \tag{5.4}$$

which is

$$\int_U \left(\frac{\partial \mathcal{F}}{\partial f_c} - \frac{\mathrm{d}}{\mathrm{d}x} \left(\frac{\partial \mathcal{F}}{\partial f_c'} \right) \right) \delta f_c = F[f_b] - F[f_c] = F(L_1 = b) - F(L_1 = c) = \left. \frac{\mathrm{d}F}{\mathrm{d}L_1} \right|_{L_1 = c} \cdot (b - c). \tag{5.5}$$

Note that we do not consider $F[f_c + \delta f_b]$, because $f_c + \delta f_b$ does not satisfy the boundary conditions thus it is not in the function space we are working on. Because b, c, and δf_c are independent, so we have

$$\frac{\partial \mathcal{F}}{\partial f} - \frac{\mathrm{d}}{\mathrm{d}x} \left(\frac{\partial \mathcal{F}}{\partial f'} \right) = 0, \tag{5.6}$$

$$\frac{\mathrm{d}F}{\mathrm{d}L_1} = 0. \tag{5.7}$$

Equations (5.4) – (5.7) implies that the small variations of the functional F around an equilibrium state can be decomposed into two parts: (1) the small variations due to the change of the function f with the location of discontinuity fixed, and (2) the small variations due to the change of the locations of discontinuities.

Now in order to determine whether Eqs. (5.6) and (5.7) are a local minimizer, we need to compute the second functional derivatives:

$$F[f_c + \delta f_c] - F[f_b] = (F[f_c + \delta f_c] - F[f_c]) + (F[f_c] - F[f_b]) \tag{5.8}$$

$$= 0 + \int \mathrm{d}x_1 \int \mathrm{d}x_2 \, \frac{\delta^2 \mathcal{F}}{\delta f_c(x_1) \delta f_c(x_2)} \delta f_c(x_1) \delta f_c(x_2)$$

$$+ \frac{1}{2} \left. \frac{\mathrm{d}^2 F}{\mathrm{d}L_1^2} \right|_{L_1 = c} \cdot (b - c)^2.$$

The local energy minimizer requires Eqs. (5.6) and (5.7) as well as

$$\frac{\delta^2 \mathcal{F}}{\delta f(x_1)\delta f(x_2)} \geq 0, \tag{5.9}$$

and

$$\frac{\mathrm{d}^2 F}{\mathrm{d}L_1^2} \geq 0. \tag{5.10}$$

The above procedure is equivalent to doing calculus of variations for two separate patches divided by the discontinuity and determine the ground states by comparing the total energies contributed from these two patches. It is actually the theoretical foundation for the numerical work in Chapter 2 and 3. Following this procedure which we call **Method (A)**, we consider the following two simple examples.

5.2 Example 1 – Solved by Method (A)

Consider a more specific energy functional

$$F[f(x), f'(x)] = \int_U \left(\frac{\mathrm{d}f}{\mathrm{d}x}\right)^2 \mathrm{d}x, \tag{5.11}$$

with Eqs. (5.2) and (5.3) as boundary conditions, and $U = [0, L_1) \cup (L_1, L]$. The question is: what is the ground state?

Now by Method (A), we start with the Euler-Lagrange equation

$$\frac{\mathrm{d}^2 f}{\mathrm{d}x^2} = 0, \tag{5.12}$$

which is satisfied on U. The solution is

$$f(x) = \begin{cases} -\frac{a}{L_1}x, x \in [0, L_1), \\ \\ -\frac{a}{L-L_1}x + \frac{L}{L-L_1}a, x \in (L_1, L]; \end{cases} \tag{5.13}$$

which is shown in Fig. 5.2.

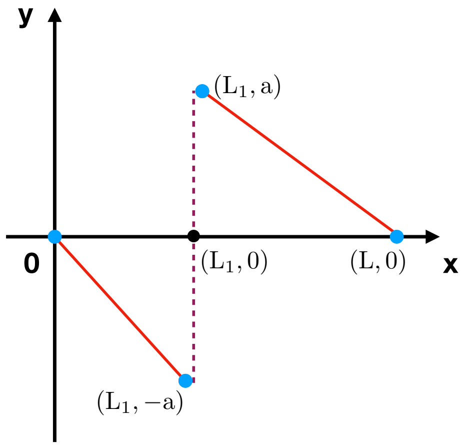

Figure 5.2: Solution to Equation (5.13)

Then substitute Eq. (5.13) into Eq. (5.11), and we arrive at the following energy landscape

$$F(L_1) = \frac{a^2}{L_1} + \frac{a^2}{L - L_1}, \tag{5.14}$$

and the ground state is $L_1 = L/2$.

5.3 Example 2 – Solved by Method (A)

Consider a similar but slightly more difficult example with the energy functional

$$F[f(x), f'(x)] = \int_U \left[\left(\frac{\mathrm{d}f}{\mathrm{d}x} \right)^2 + A^2 f^2 \right] \mathrm{d}x, \tag{5.15}$$

Equations (5.2) and (5.3) are the boundary conditions, and the domain is $U = [0, L_1) \cup (L_1, L]$. The question is the same: what is the ground state?

Similarly, the Euler-Lagrange equation is

$$\frac{\mathrm{d}^2 f}{\mathrm{d}x^2} - A^2 f = 0, \tag{5.16}$$

and its solution is

$$f(x) = \begin{cases} -\frac{a}{e^{AL_1}-e^{-AL_1}}e^{Ax} + \frac{a}{e^{AL_1}-e^{-AL_1}}e^{-Ax}, x \in [0, L_1), \\ \\ \frac{a}{e^{AL_1}-e^{2AL-AL_1}}e^{Ax} - \frac{a}{e^{-2AL+AL_1}-e^{-AL_1}}e^{-Ax}, x \in (L_1, L]. \end{cases} \tag{5.17}$$

Then substitute Eq. (5.17) into Eq. (5.16), and we have the following energy landscape

$$F(L_1) = a^2A \cdot \frac{e^{AL_1} + e^{-AL_1}}{e^{AL_1} - e^{-AL_1}} + a^2A \cdot \frac{e^{2AL-AL_1} + e^{AL_1}}{e^{2AL-AL_1} - e^{AL_1}}. \tag{5.18}$$

The ground state is still $L_1 = L/2$.

Compared with Example 1, there is only a slight modification for Example 2. The ground state is shown to be unchanged but the calculation is much more involved. It is expected that for the problem of defects in nematics, Method (A) can sometimes become impossible for an analytical study. The reason is that it requires solving a boundary value problem on each patch, which is computationally expensive. Since the ground state is only characterized by the locations of the inner boundaries, we expect to find a method that is able to extract only the information of inner boundaries without struggling for the exact solutions. To work in this direction, we "glue" all the patches by Fourier series, and call it **Method (B)** to distinguish it from Method (A). Below are our experiments with this new idea on the above two examples.

5.4 Example 1 – Solved by Method (B)

We write f as Fourier series of sine functions

$$f(x) = \sum_{k=1}^{\infty} b_k \sin \frac{k\pi x}{L}, \tag{5.19}$$

where b_k is unknown. The we write its first derivative as

$$\frac{\mathrm{d}f}{\mathrm{d}x} = \sum_{k=1}^{\infty} \frac{k\pi b_k}{L} \cos\frac{k\pi x}{L}. \tag{5.20}$$

Written in terms of Fourier series, $f(x)$ and $f'(x)$ are assigned certain values at the discontinuous $x = L_1$, hence the patches are glued together. Here, the energy functional is still denoted by $F[f(x), f'(x)]$ while we should keep in mind that $f(x)$ and $f'(x)$ are expressed as Eqs. (5.19) and (5.20) and are defined on the whole domain, i.e., $[0, L]$ or $U \cup \{L_1\}$.

Now the next step is to construct an energy function of which the small variations only include the change of the location of the discontinuity. We start by deriving the expression for b_k.

On $[0, L_1)$ by Eq. (5.12), we have

$$0 = \int_0^{L_1^-} \frac{\mathrm{d}^2 f}{\mathrm{d}x^2} \sin\frac{k\pi x}{L} \mathrm{d}x = \int_0^{L_1^-} \sin\frac{k\pi x}{L} \mathrm{d}\Big(\frac{\mathrm{d}f}{\mathrm{d}x}\Big) \tag{5.21}$$

$$= \sin\frac{k\pi L_1}{L} \cdot \frac{\mathrm{d}f}{\mathrm{d}x}\Big|_{L_1} + \frac{k\pi a}{L} \cos\frac{k\pi L_1}{L} - \Big(\frac{k\pi}{L}\Big)^2 \int_0^{L_1^-} f \sin\frac{k\pi x}{L} \mathrm{d}x.$$

Therefore,

$$\int_0^{L_1} f \sin\frac{k\pi x}{L} \mathrm{d}x = \frac{aL}{k\pi} \cos\frac{k\pi L_1}{L} + \Big(\frac{L}{k\pi}\Big)^2 \sin\frac{k\pi L_1}{L} \cdot \frac{\mathrm{d}f}{\mathrm{d}x}\Big|_{L_1^-}. \tag{5.22}$$

Similarly on $(L_1, L]$, we have

$$\int_{L_1^+}^{L} f \sin\frac{k\pi x}{L} \mathrm{d}x = \frac{aL}{k\pi} \cos\frac{k\pi L_1}{L} - \Big(\frac{L}{k\pi}\Big)^2 \sin\frac{k\pi L_1}{L} \cdot \frac{\mathrm{d}f}{\mathrm{d}x}\Big|_{L_1^+}. \tag{5.23}$$

Therefore,

$$b_k = \frac{2}{L} \int_0^{L} f \sin\frac{k\pi x}{L} \mathrm{d}x = \frac{2}{L}\Big(\int_0^{L_1^-} f \sin\frac{k\pi x}{L} \mathrm{d}x + \int_{L_1^+}^{L} f \sin\frac{k\pi x}{L} \mathrm{d}x\Big) \tag{5.24}$$

$$= \frac{4a}{k\pi} \cos\frac{k\pi L_1}{L} + \frac{2L}{(k\pi)^2} B \sin\frac{k\pi L_1}{L},$$

where

$$B = \frac{\mathrm{d}f}{\mathrm{d}x}\Big|_{L_1^+} - \frac{\mathrm{d}f}{\mathrm{d}x}\Big|_{L_1^-}.$$

Note that the second equality of Eq. (5.24) is due to the fact that f is a bounded function.

To determine the unknown B in Eq. (5.24), we use Dirichlet's theorem, which is, in our example, the fact that f, when written in terms of Fourier series as shown in Eq. (5.19), is zero at the discontinuity; see Ref. [99–101]. Therefore we have

$$\sum_{k=1}^{\infty}\Big(\frac{4a}{k\pi}\cos\frac{k\pi L_1}{L} + \frac{2L}{(k\pi)^2}B\sin\frac{k\pi L_1}{L}\Big)\sin\frac{k\pi L_1}{L} = 0 \tag{5.25}$$

$$\Longrightarrow \sum_{k=1}^{\infty}\frac{4a}{k\pi}\cos\frac{k\pi L_1}{L}\sin\frac{k\pi L_1}{L} = -B\cdot\sum_{k=1}^{\infty}\frac{2L}{(k\pi)^2}\sin\frac{k\pi L_1}{L}\sin\frac{k\pi L_1}{L}.$$

To determine B, we make use of the following identity

$$\sum_{k=1}^{\infty}\frac{1}{k\pi}\sin(k\pi x) = \frac{1}{2} - \frac{x}{2}. \tag{5.26}$$

Then the LHS of Eq. (5.26) becomes

$$\sum_{k=1}^{\infty}\frac{4a}{k\pi}\cos\frac{k\pi L_1}{L}\sin\frac{k\pi L_1}{L} = 2a\Big(\frac{1}{2} - \frac{L_1}{L}\Big), \tag{5.27}$$

which is monotonically decreasing. For the summation part in the RHS of Eq. (5.26), we have the following relation

$$\frac{\mathrm{d}}{\mathrm{d}L_1}\Big(\sum_{k=1}^{\infty}\frac{2L}{(k\pi)^2}\sin\frac{k\pi L_1}{L}\sin\frac{k\pi L_1}{L}\Big) = \sum_{k=1}^{\infty}\frac{2}{k\pi}\sin\frac{2k\pi L_1}{L} = 2\Big(\frac{1}{2} - \frac{L_1}{L}\Big). \tag{5.28}$$

Knowing that this part is zero at the two end points $L_1 = 0$ or L, then we can obtain the solution to Eq. (5.28), which is written as

$$\sum_{k=1}^{\infty}\frac{2L}{(k\pi)^2}\sin\frac{k\pi L_1}{L}\sin\frac{k\pi L_1}{L} = L_1 - \frac{L_1^2}{L}. \tag{5.29}$$

Then substitute Eqs. (5.27) and (5.29) into Eq. (5.25), and we have

$$B = a\Big(\frac{1}{L-L_1} - \frac{1}{L_1}\Big). \tag{5.30}$$

Substitute Eq. (5.30) into Eq. (5.24) and then substitute Eq. (5.24) into Eq. (5.19) and (5.20), we have

$$f(x) = f_1(x) + f_2(x), \tag{5.31}$$

where

$$f_1(x) = \sum_{k=1}^{\infty} \frac{4a}{k\pi} \cos\frac{k\pi L_1}{L} \sin\frac{k\pi x}{L}, \tag{5.32}$$

$$f_2(x) = \sum_{k=1}^{\infty} \frac{2L\cdot B}{(k\pi)^2} \sin\frac{k\pi L_1}{L} \sin\frac{k\pi x}{L} = \sum_{k=1}^{\infty} \frac{2aL}{(k\pi)^2}\Big(\frac{1}{L-L_1} - \frac{1}{L_1}\Big) \sin\frac{k\pi L_1}{L} \sin\frac{k\pi x}{L}; \tag{5.33}$$

and

$$\frac{\mathrm{d}f}{\mathrm{d}x} = \sum_{k=1}^{\infty} \Big[4a\cos\frac{k\pi L_1}{L} + \frac{2L\cdot B}{k\pi}\sin\frac{k\pi L_1}{L}\Big]\cdot\frac{1}{L}\cos\frac{k\pi x}{L} \tag{5.34}$$

$$= \sum_{k=1}^{\infty} \Big[4a\cos\frac{k\pi L_1}{L} + \frac{2aL}{k\pi}\Big(\frac{1}{L-L_1} - \frac{1}{L_1}\Big)\sin\frac{k\pi L_1}{L}\Big]\cdot\frac{1}{L}\cos\frac{k\pi x}{L}.$$

Then we substitute Eqs. (5.31) and (5.34) into the energy functional

$$F[f(x), f'(x)] = \int_0^L \Big(\frac{\mathrm{d}f}{\mathrm{d}x}\Big)^2 \mathrm{d}x, \tag{5.35}$$

and the resulting energy function is

$$F(L_1) = \sum_{k=1}^{\infty} \frac{(b_k k\pi)^2}{2L} = F_1(L_1) + F_2(L_1) + F_3(L_1), \tag{5.36}$$

where

$$F_1(L_1) = \frac{1}{2L}\cdot\sum_{k=1}^{\infty}\Big(4a\cos\frac{k\pi L_1}{L}\Big)^2, \tag{5.37}$$

$$F_2(L_1) = \frac{1}{2L} \cdot \sum_{k=1}^{\infty} \Big(\frac{2L \cdot B}{k\pi} \sin \frac{k\pi L_1}{L}\Big)^2 = \frac{1}{2L} \cdot \sum_{k=1}^{\infty} \Big[\frac{2aL}{k\pi}\Big(\frac{1}{L-L_1} - \frac{1}{L_1}\Big) \sin \frac{k\pi L_1}{L}\Big]^2, \tag{5.38}$$

$$F_3(L_1) = \frac{1}{L} \cdot \sum_{k=1}^{\infty} \Big(4a \cos \frac{k\pi L_1}{L}\Big) \cdot \Big(\frac{2L \cdot B}{k\pi} \sin \frac{k\pi L_1}{L}\Big) \tag{5.39}$$

$$= \frac{1}{L} \cdot \sum_{k=1}^{\infty} \Big(4a \cos \frac{k\pi L_1}{L}\Big) \cdot \Big[\frac{2aL}{k\pi}\Big(\frac{1}{L-L_1} - \frac{1}{L_1}\Big) \sin \frac{k\pi L_1}{L}\Big].$$

F_1 is insanely divergent, while interestingly for F_2, Eq. (5.38) is equal to

$$F_2(L_1) = \frac{a^2}{L_1} + \frac{a^2}{L-L_1} - \frac{4a^2}{L}. \tag{5.40}$$

We can see that Eqs. (5.41) and (5.14) are equally effective in determining the ground state. But can we throw away $F_1(L_1)$ and $F_3(L_1)$, and keep only $F_2(L_1)$? Now it is time to figure out what $F_1(L_1)$ and $F_3(L_1)$ represent.

For $F_3(L_1)$, Eq. (5.39) is equal to

$$F_3(L_1) = -2 \cdot \Big(\frac{a^2}{L_1} + \frac{a^2}{L-L_1} - \frac{4a^2}{L}\Big), \tag{5.41}$$

which is finite except at two extreme points, i.e., $L_1 = 0$ or L, therefore it does not contain the fictitious core energy.

For $F_1(L_1)$, let us first consider the following energy functional

$$F(y, L_1) = \int_0^y \Big(\frac{\mathrm{d}f}{\mathrm{d}x}\Big)^2 \mathrm{d}x = F_1(y, L_1) + F_2(y, L_1) + F_3(y, L_1), \tag{5.42}$$

where $F(L, L_1) = F(L_1)$, $F_1(L, L_1) = F_1(L_1)$, $F_2(L, L_1) = F_2(L_1)$, and $F_3(L, L_1) = F_3(L_1)$. Then after tedious calculations, we have

$$F_1(y, L_1) = \int_0^L \Big(\frac{\mathrm{d}f_1}{\mathrm{d}x}\Big)^2 \mathrm{d}x \tag{5.43}$$

$$= \frac{4a^2}{L^2} \cdot \lim_{N\to\infty} \sum_{k=1}^{N} \Big(y + y \cdot \cos \frac{2k\pi L_1}{L} \Big)$$

$$+ \frac{4a^2}{L^2} \cdot \lim_{N\to\infty} \sum_{k_1,k_2=1,k_1\neq k_2,}^{N} \Big[\frac{L}{(k_1-k_2)\pi} \cos \frac{(k_1-k_2)\pi L_1}{L} \sin \frac{(k_1-k_2)\pi y}{L}$$

$$+ \frac{L}{(k_1-k_2)\pi} \cos \frac{(k_1+k_2)\pi L_1}{L} \sin \frac{(k_1-k_2)\pi y}{L} \Big]$$

$$+ \frac{4a^2}{L^2} \cdot \lim_{N\to\infty} \sum_{k_1,k_2=1}^{N} \Big[\frac{L}{(k_1+k_2)\pi} \cos \frac{(k_1-k_2)\pi L_1}{L} \sin \frac{(k_1+k_2)\pi y}{L}$$

$$+ \frac{L}{(k_1+k_2)\pi} \cos \frac{(k_1+k_2)\pi L_1}{L} \sin \frac{(k_1+k_2)\pi y}{L} \Big]$$

$$= -\frac{2a^2}{\pi L} \cdot \frac{\sin \frac{\pi y}{L}}{\cos \frac{\pi L_1}{L} - \cos \frac{\pi y}{L}} + \frac{a^2}{\pi L} \cdot \frac{\cos \frac{(2N+1)\pi L_1}{L}}{\sin \frac{\pi L_1}{L}} \ln \left(\frac{1 - \cos \frac{\pi (y-L_1)}{L}}{1 - \cos \frac{\pi (y+L_1)}{L}} \right)$$

$$+ \frac{4a^2 y}{L^2} + \begin{cases} 0, & \text{if } 0 < y < L_1 \\ \frac{4(N-1)a^2}{L} + \frac{2a^2}{L} \Big(-1 + \frac{\sin \frac{(2N+1)\pi L_1}{L}}{\sin \frac{\pi L_1}{L}} \Big), & \text{if } L_1 < y < L \end{cases}$$

see Appendix A.

Equation (5.43) implies that $F_1(L_1)$ contains the fictitious core energy because there is an infinite energy jump at $y = L_1$. However, for some fixed large value of N, two values of L_1 with a tiny difference can result in two values of $F_1(L_1)$ with a large difference, which contradicts our intuition that the energy function $F_1(L_1)$ should be a differentiable function. To resolve this issue, we speculate that N should depend on L_1 and satisfies the following condition:

$$(N - s) \cdot \frac{L_1}{L} \in \mathbb{Z}, \tag{5.44}$$

where s is a fixed integer. Equation (5.44) implies that, when N is fixed, $F_1(L_1)$ works for only finite number of states characterized by different values of L_1, and only when $N \to \infty$ can it be effective for comparing all the states and determining the ground state.

Now we need to show that (5.44) is both a sufficient and necessary condition for $F_1(L_1)$ being differentiable.

Proof. **Part I:** Prove that (5.44) is a sufficient condition.

If L_1/L is a rational number, then obviously we can choose an integer N_1 that satisfies (5.44). For many different rational values of L_1/L, we can choose $(N-s)$ to be the least common multiple of all the (N_1-s)s. If L_1/L is an irrational number, then for any arbitrary small number δ_1, there exists an integer N_1, such that

$$(N_1 - s) \cdot \frac{L_1}{L} - \delta_1 \in \mathbb{Z}. \tag{5.45}$$

For many different irrational values of L_1/L, we can choose $(N-s)$ to be the least common multiple of all the (N_1-s)s, and each δ_1 to be replace by $\delta/(N-s)$, where δ is arbitrarily small. Therefore, Condition (5.44) can be satisfied by L_1/L being any real number. Then we substitute Eq. (5.44) into Eq. (5.43), and the resulting $F_1(y, L_1)$ is written as

$$\begin{aligned} F_1(y, L_1) = &-\frac{2a^2}{\pi L} \cdot \frac{\sin\frac{\pi y}{L}}{\cos\frac{\pi L_1}{L} - \cos\frac{\pi y}{L}} \\ &+ \frac{a^2}{\pi L} \cdot \frac{\cos\frac{(2s+1)\pi L_1}{L}}{\sin\frac{\pi L_1}{L}} \ln\left(\frac{1-\cos\frac{\pi(y-L_1)}{L}}{1-\cos\frac{\pi(y+L_1)}{L}}\right) \\ &+ \frac{4a^2 y}{L^2} + \begin{cases} 0, & \text{if } 0 < y < L_1 \\ \frac{4(N-1)a^2}{L} + \frac{2a^2}{L}\Big(-1 + \frac{\sin\frac{(2s+1)\pi L_1}{L}}{\sin\frac{\pi L_1}{L}}\Big), & \text{if } L_1 < y < L \end{cases} \end{aligned} \tag{5.46}$$

Then let $y = L$, and we have

$$F_1(L_1) = \frac{4a^2}{L} + \frac{4(N-1)a^2}{L} + \frac{2a^2}{L}\Big(-1 + \frac{\sin\frac{(2s+1)\pi L_1}{L}}{\sin\frac{\pi L_1}{L}}\Big), \tag{5.47}$$

which is differentiable.

Part II: Prove that Condition (5.44) is a necessary condition.

If $F_1(L_1)$ is differentiable, then

$$\frac{\sin\frac{(2N+1)\pi L_1}{L}}{\sin\frac{\pi L_1}{L}} \tag{5.48}$$

is differentiable. We can write (5.48) as

$$\frac{\sin\left(\pi h + \frac{\pi L_1}{L}\right)}{\sin\frac{\pi L_1}{L}}, \tag{5.49}$$

where h is a differentiable function of L_1/L. Then N must satisfy the following condition

$$N \cdot \frac{L_1}{L} - \frac{1}{2} \cdot h\Big(\frac{L_1}{L}\Big) \in \mathbb{Z}. \tag{5.50}$$

If h is a constant function, then without loss of generality, we assume $h \in [0, 2)$. And we can check that only $h = 0$ can make sure that Condition (5.50) is satisfied for all values of L_1/L. If h is not a constant function, then we need to make sure

$$\frac{L}{2L_1} \cdot h\Big(\frac{L_1}{L}\Big) \in \mathbb{Z}. \tag{5.51}$$

Therefore we have

$$h\Big(\frac{L_1}{L}\Big) = 2s \cdot \frac{L_1}{L}, \tag{5.52}$$

where s is an integer. Substitute Eq. (5.52) into Condition (5.50), and we arrive at Condition (5.44). $\square$

Among the many possible values of s, we find that $s = 0$ is the best option, because $F_1(L_1)$ becomes

$$F_1(L_1) = \frac{4a^2}{L} + \frac{4(N-1)a^2}{L}, \tag{5.53}$$

which is independent of L_1 (i.e., the location of the discontinuity). With this choice, $F_1(L_1)$ is the part of the energy that contains the infinite core energy but it does not change when the core moves. To have an idea of the importance of Condition (5.44) [in this case with $s = 0$] in determining $F_1(L_1)$, please see Figure 5.3a which shows that, when $N = 50$, $F_1(L_1)$ has same values for L_1 being 0.04, 0.3, 0.6 and 0.96, while $F_1(L_1 = 0.61)$ has a different value.

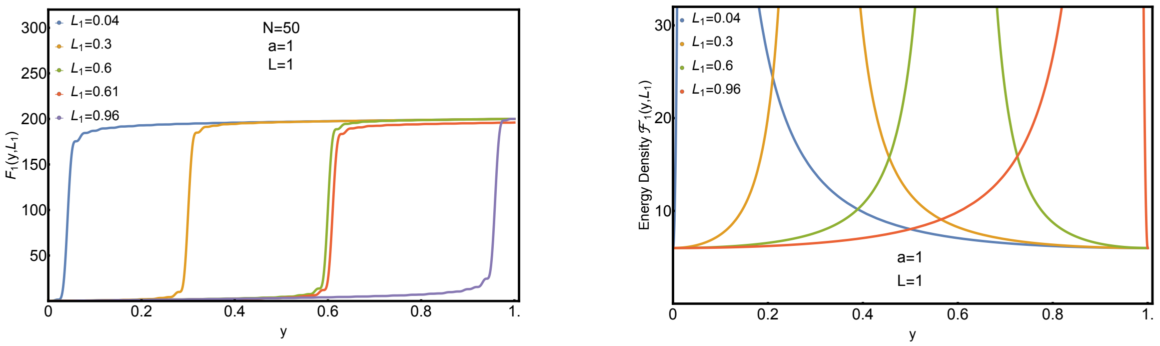

(a) $F_1(y, L_1)$

(b) $\mathcal{F}_1(y, L_1)$

Figure 5.3: Background energy and its energy density

In order to better understand the fictitious core energy, we need Eq. (5.46) as well as its density profile

$$\mathcal{F}_1(y, L_1) = \frac{4a^2}{L^2} + \frac{a^2}{2L^2} \cdot \left[\csc^2 \frac{\pi(y - L_1)}{2L} + \left(\cos \frac{\pi(y - 3L_1)}{2L} - \cos \frac{\pi(y + L_1)}{2L} \right) \right.$$

$$\left. \cdot \cot \frac{\pi L_1}{L} \csc^2 \frac{\pi(y - L_1)}{2L} \csc \frac{\pi(y + L_1)}{2L} + \csc^2 \frac{\pi(y + L_1)}{2L} \right], \tag{5.54}$$

as illustrated in Fig. 5.3b. From Eqs. (5.53) and (5.54), we have two observations:

(1) The fictitious core energy spans over a large region which contains the zero-sized core (i.e., the discontinuity) at $y = L_1$; in another word, the core has a nonzero size from an energy point of view. We attribute it to Gibbs phenomenon: the Fourier series of the discontinuous function f [i.e., Eq. (5.19)] has large oscillations and the size of the region where these oscillations occur is almost zero; however when we substitute Eqs. (5.19) and (5.20) into Eq. (5.35), the effect of these oscillations magnifies.

(2) There is a "base" energy $4a^2/L$ in Eq. (5.47); and if we add it to Eq. (5.35), the

resulting energy is equal to Eq. (5.14).

To make it convenient for later discussions, let us redefine the above concepts, and name $F_1(L_1)$ as the background energy (since it is independent of L_1) which consists of three parts:

(a) The fictitious core free energy (new) which is the infinite energy jump right at the discontinuity;

(b) The fictitious fluctuation energy which is the energy caused by large oscillations near the discontinuity (i.e., Gibbs phenomenon);

(c) The base energy which is $4a^2/L$ in this example.

Now in order to legally throw away the core and fluctuation energies in $F_1(L_1)$ together with $F_3(L_1)$, let us make a deep comparison between Method (A) and (B) in solving Example 1.

For clarity, let us denote the function and energy in Method (A) by g and G respectively instead of f and F, while we keep the notations in Method (B) unchanged. The domains of f and g are $U \cup \{L_1\}$ and U respectively. We observe that when the location of the discontinuity is fixed at $x = L_1$, the only differences between f and g are that f has an (almost) perpendicular line at $x = L_1$ and large oscillations near it. Let η and ξ denote these two effects respectively, thus the relation between f and g is written as

$$f = g + \eta + \xi. \tag{5.55}$$

g can be further decomposed as

$$g = (g - g_2) + g_2, \tag{5.56}$$

where $g_2 = f_2|_U$ and f_2 being Eq. (6.48).

Compare the energy functions Eqs. (5.14), (5.36) – (5.41) and (5.47), and we have the

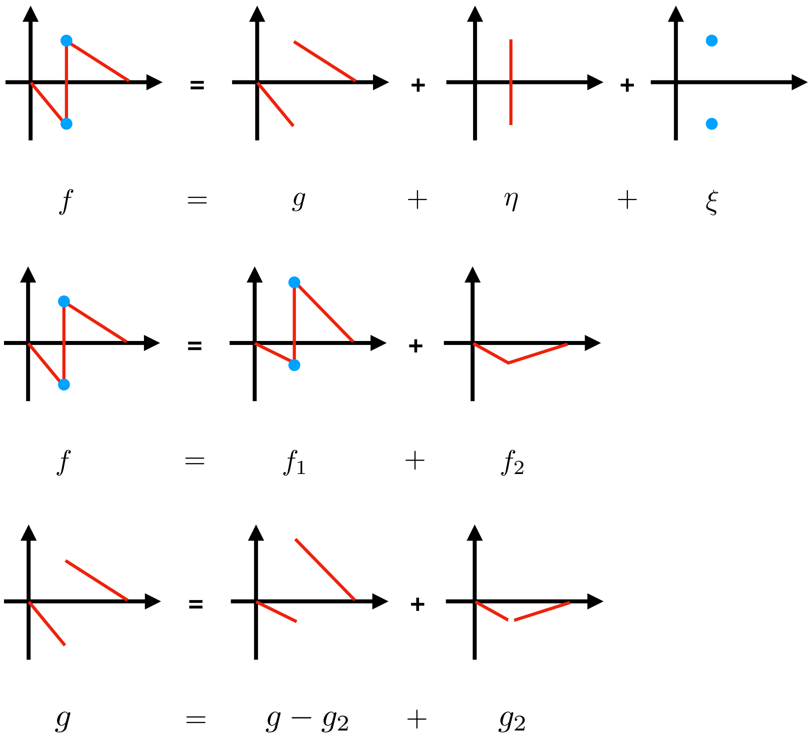

Figure 5.4: Comparisons between f [the solution by using Method (B)] and g [the solution by using Method (A)]

following observations:

(a) $g = (g - g_2) + g_2$ contributes to the real energy $G(L_1)$, where $g - g_2$ contributes to the base energy (i.e., $4a^2/L$);

(b) $f_1 = (g - g_2) + \eta + \xi$ contributes to the background energy $F_1(L_1)$;

(c) $F_2(L_1)$ is equal to $G(L_1)$ minus the base energy;

(d) $F_3(L_1)$ can be seen as the interaction energy between f_2 and $\eta + \xi$. [We can see that Eq. (5.39) is the interaction energy between $f_1 = (g - g_2) + \eta + \xi$ and f_2; then we observe that the interaction energy between $g - g_2$ and f_2 is zero because the first derivatives of the former is a constant on U.]; see Fig. 5.4.

According to the discussion before, the physical free energy functional does not contain any contribution from the differentiation and integration of the function f across the defect core, so any part of the energy involving η or ξ should be thrown away and that includes the core and fluctuation energies in $F_1(L_1)$ as well as $F_3(L_1)$. The resulting regularized energy calculated by Method (B) is the sum of $F_2(L_1)$ and the base energy, i.e.,

$$F(L_1) = F_2(L_1) + \frac{4a^2}{L} = \frac{a^2}{L_1} + \frac{a^2}{L - L_1} \tag{5.57}$$

which is equal to Eq. (5.14). Therefore, Method (A) and (B) are equivalent, at least for Example 1.

So far, Method (B) seems much more difficult than Method (A) with lots of efforts on how to throw away unphysical energies. Is there a criterion that tells us which part of the Fourier series of f [i.e., Eq. (5.19)] is related to these unphysical energies and should be thrown away? Two common features for this part of Fourier series are: (a) its first derivative is extremely divergent, and (b) its corresponding free energy is independent of the location of the discontinuity (i.e., independent of L_1). That is all we know and we lack a complete criterion in the general context to specify this part of Fourier series. Fortunately, in this example, we know we should throw away f_1 and keep only f_2.

However, even though we know the criterion for this example, the computation leading to Eq. (5.30) is still not simple enough. Our next question is: do we have to get the exact solution for f_2 [i.e., the second equality of Eq. (6.48) instead of the first equality] in order to determine the ground state? It is about how to extract the necessary information, and the answer is a no for this example. Our reasons are as follows.

Firstly, we observe that the procedure from Eq. (5.19) to (5.24) makes sure that the variable L_1 in the Fourier series of f [i.e., Eqs. (5.31) – (6.48)] is either in a trigonometric function or in B, and both the numerator and denominator of B are Fourier series with L_1 as the variable.

Secondly, we realize that: in order to show that a finite number of Fourier modes determine the ground state, we need to show that $F_2(L_1)$ can be replaced by a finite number of trigonometric functions; and therefore we need to show that B can be replaced by a rational function of trigonometric functions.

Thirdly, we observe that by keeping only the first terms of the summations in Eq. (5.25), the resulting

$$B = -\frac{2\pi a}{L}\cot\frac{\pi L_1}{L}, \tag{5.58}$$

has the same zero point and monotonicity with Eq. (5.30).

Lastly, we observe that the part in $F_2(L_1)$, i.e.,

$$\sum_{k=1}^{\infty}\left(\frac{1}{k\pi}\sin\frac{k\pi L_1}{L}\right)^2$$

has the property that its first term has the same monotonicity and zero points with the whole sequence; therefore we substitute Eq. (5.58) into the first Fourier mode of the first equality of Eq. (5.38), and the result is

$$F_2(L_1) = \frac{8a^2}{L}\cos^2\frac{\pi L_1}{L}; \tag{5.59}$$

interestingly but unsurprisingly, Eqs. (5.14) and (5.59) have the same ground states, thus are equally effective. Figure 5.5 shows the comparisons between Method (A) and (B) for this example by plotting the energy landscapes and the function B.

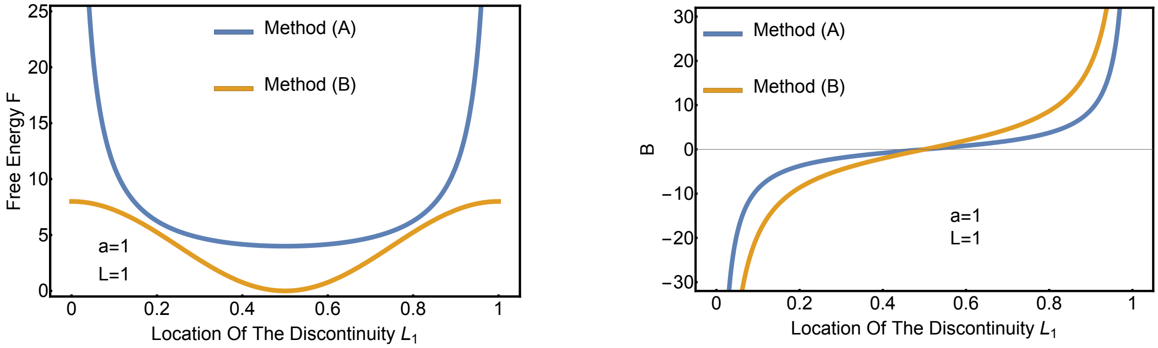

(a) The comparison of energy landscapes [i.e., Equations (5.14) and (5.59)]

(b) The comparison of B [i.e., Equations (5.30) and (5.58)]

Figure 5.5: Comparisons between Methods (A) and (B) in Example 1

5.5 Example 2 – Solved by Method (B)

By the same procedure, the function f can be decomposed as

$$f(x) = f_1(x) + f_2(x), \tag{5.60}$$

where

$$f_1(x) = \sum_{k=1}^{\infty} \frac{4a}{k\pi} \cos\frac{k\pi L_1}{L} \sin\frac{k\pi x}{L}, \tag{5.61}$$

$$f_2(x) = \sum_{k=1}^{\infty} \left[\frac{\frac{4k\pi a}{L^2}}{A^2 + (\frac{k\pi}{L})^2} \cos\frac{k\pi L_1}{L} + \frac{2C}{L} \cdot \frac{1}{A^2 + (\frac{k\pi}{L})^2} \cdot \sin\frac{k\pi L_1}{L} \right. \tag{5.62}$$

$$\left. - \frac{4a}{k\pi} \cos\frac{k\pi L_1}{L} \right] \sin\frac{k\pi x}{L}. \tag{5.63}$$

By using Dirichlet's theorem, C satisfies

$$\sum_{k=1}^{\infty} \left[\frac{\frac{4k\pi a}{L^2}}{A^2 + (\frac{k\pi}{L})^2} \cos\frac{k\pi L_1}{L} + \frac{2C}{L} \cdot \frac{1}{A^2 + (\frac{k\pi}{L})^2} \cdot \sin\frac{k\pi L_1}{L} \right] \sin\frac{k\pi L_1}{L} = 0 \tag{5.64}$$

$$\Longrightarrow$$

$$\sum_{k=1}^{\infty} \frac{\frac{4k\pi a}{L^2}}{A^2 + (\frac{k\pi}{L})^2} \cos\frac{k\pi L_1}{L} \sin\frac{k\pi L_1}{L} = -\frac{2C}{L} \cdot \sum_{k=1}^{\infty} \frac{1}{A^2 + (\frac{k\pi}{L})^2} \cdot \sin\frac{k\pi L_1}{L} \sin\frac{k\pi L_1}{L}.$$

The LHS of Eq. (5.64) satisfies

$$\sum_{k=1}^{\infty} \frac{2a}{k\pi} \sin\frac{2k\pi L_1}{L} - \sum_{k=1}^{\infty} \frac{\frac{4k\pi a}{L^2}}{A^2 + (\frac{k\pi}{L})^2} \cos\frac{k\pi L_1}{L} \sin\frac{k\pi L_1}{L} \tag{5.65}$$

$$= \sum_{k=1}^{\infty} \frac{2a}{k\pi} \frac{A^2}{A^2 + (\frac{k\pi}{L})^2} \sin\frac{2k\pi L_1}{L}$$

$$\Longrightarrow$$

$$\frac{\mathrm{d}^2}{\mathrm{d}L_1^2}\sum_{k=1}^{\infty}\frac{2a}{k\pi}\sin\frac{2k\pi L_1}{L}-\frac{\mathrm{d}^2}{\mathrm{d}L_1^2}\sum_{k=1}^{\infty}\frac{\frac{4k\pi a}{L^2}}{A^2+(\frac{k\pi}{L})^2}\cos\frac{k\pi L_1}{L}\sin\frac{k\pi L_1}{L}$$

$$=-\sum_{k=1}^{\infty}\frac{2aA^2}{A^2+(\frac{k\pi}{L})^2}\frac{2k\pi}{L}\sin\frac{2k\pi L_1}{L}$$

$$\Longrightarrow$$

$$\frac{\mathrm{d}^2}{\mathrm{d}L_1^2}\sum_{k=1}^{\infty}\frac{\frac{4k\pi a}{L^2}}{A^2+(\frac{k\pi}{L})^2}\cos\frac{k\pi L_1}{L}\sin\frac{k\pi L_1}{L}-4A^2\cdot\sum_{k=1}^{\infty}\frac{\frac{4k\pi a}{L^2}}{A^2+(\frac{k\pi}{L})^2}\cos\frac{k\pi L_1}{L}\sin\frac{k\pi L_1}{L}=0.$$

Therefore, we have

$$\sum_{k=1}^{\infty}\frac{\frac{4k\pi a}{L^2}}{A^2+(\frac{k\pi}{L})^2}\cos\frac{k\pi L_1}{L}\sin\frac{k\pi L_1}{L}=D\cdot(e^{2AL_1}-e^{2AL-2AL_1}), \tag{5.66}$$

where D is a constant. For the summation part in the RHS of Eq. (5.64), we have

$$\frac{\mathrm{d}}{\mathrm{d}L_1}\sum_{k=1}^{\infty}\frac{1}{A^2+(\frac{k\pi}{L})^2}\cdot\sin\frac{k\pi L_1}{L}\sin\frac{k\pi L_1}{L}=\frac{L}{2a}\cdot\sum_{k=1}^{\infty}\frac{\frac{4k\pi a}{L^2}}{A^2+(\frac{k\pi}{L})^2}\cos\frac{k\pi L_1}{L}\sin\frac{k\pi L_1}{L}. \tag{5.67}$$

Therefore,

$$\sum_{k=1}^{\infty}\frac{1}{A^2+(\frac{k\pi}{L})^2}\cdot\sin\frac{k\pi L_1}{L}\sin\frac{k\pi L_1}{L}=\frac{L\cdot D}{4Aa}\cdot(e^{2AL_1}+e^{2AL-2AL_1}-1-e^{2AL}). \tag{5.68}$$

Then substitute Eqs. (5.66) and (5.68) into Eq. (5.64), and we have

$$C=-Aa\cdot\frac{e^{AL_1}+e^{-AL_1}}{e^{AL_1}-e^{-AL_1}}+Aa\cdot\frac{e^{2AL-AL_1}+e^{AL_1}}{e^{2AL-AL_1}-e^{AL_1}}. \tag{5.69}$$

We can decompose the energy function $F(L_1)$ as

$$F(L_1)=F_1(L_1)+F_2(L_1)+F_3(L_1)+F_4(L_1), \tag{5.70}$$

where

$$F_1(L_1) = \int_0^L \Big(\frac{\mathrm{d}f_1}{\mathrm{d}x}\Big)^2 \mathrm{d}x \tag{5.71}$$

$$= \frac{1}{2L} \cdot \sum_{k=1}^{\infty} \Big(4a \cos \frac{k\pi L_1}{L}\Big)^2,$$

$$F_2(L_1) = \int_0^L \Big(\frac{\mathrm{d}f_2}{\mathrm{d}x}\Big)^2 \mathrm{d}x \tag{5.72}$$

$$= \frac{1}{2L} \cdot \sum_{k=1}^{\infty} \Bigg[\frac{\frac{4(k\pi)^2 a}{L^2}}{A^2 + (\frac{k\pi}{L})^2} \cos \frac{k\pi L_1}{L} - 4a \cos \frac{k\pi L_1}{L} + \frac{2C}{L} \cdot \frac{k\pi}{A^2 + (\frac{k\pi}{L})^2} \cdot \sin \frac{k\pi L_1}{L}\Bigg]^2$$

$$= \frac{1}{2L} \cdot \sum_{k=1}^{\infty} \Bigg[\frac{\frac{4(k\pi)^2 a}{L^2}}{A^2 + (\frac{k\pi}{L})^2} \cos \frac{k\pi L_1}{L} - 4a \cos \frac{k\pi L_1}{L} + \frac{2}{L}$$

$$\cdot \frac{k\pi \cdot \sin \frac{k\pi L_1}{L}}{A^2 + (\frac{k\pi}{L})^2} \Big(- Aa \cdot \frac{e^{AL_1} + e^{-AL_1}}{e^{AL_1} - e^{-AL_1}} + Aa \cdot \frac{e^{2AL - AL_1} + e^{AL_1}}{e^{2AL - AL_1} - e^{AL_1}}\Big)\Bigg]^2,$$

$$F_3(L_1) = 2 \int_0^L \Big(\frac{\mathrm{d}f_1}{\mathrm{d}x}\Big) \cdot \Big(\frac{\mathrm{d}f_2}{\mathrm{d}x}\Big) \mathrm{d}x \tag{5.73}$$

$$= \frac{1}{L} \cdot \sum_{k=1}^{\infty} \Big(4a \cos \frac{k\pi L_1}{L}\Big) \cdot \Bigg[\frac{\frac{4(k\pi)^2 a}{L^2}}{A^2 + (\frac{k\pi}{L})^2} \cos \frac{k\pi L_1}{L} - 4a \cos \frac{k\pi L_1}{L}$$

$$+ \frac{2C}{L} \cdot \frac{k\pi}{A^2 + (\frac{k\pi}{L})^2} \cdot \sin \frac{k\pi L_1}{L}\Bigg]$$

$$= \frac{1}{L} \cdot \sum_{k=1}^{\infty} \Big(4a \cos \frac{k\pi L_1}{L}\Big) \cdot \Bigg[\frac{\frac{4(k\pi)^2 a}{L^2}}{A^2 + (\frac{k\pi}{L})^2} \cos \frac{k\pi L_1}{L} - 4a \cos \frac{k\pi L_1}{L} + \frac{2}{L}$$

$$\cdot \frac{k\pi \cdot \sin \frac{k\pi L_1}{L}}{A^2 + (\frac{k\pi}{L})^2} \Bigg(- Aa \cdot \frac{e^{AL_1} + e^{-AL_1}}{e^{AL_1} - e^{-AL_1}} + Aa \cdot \frac{e^{2AL - AL_1} + e^{AL_1}}{e^{2AL - AL_1} - e^{AL_1}}\Bigg)\Bigg],$$

$$\begin{aligned} F_4(L_1) &= \int_0^L (A^2 f^2)\mathrm{d}x \qquad (5.74) \\ &= \frac{A^2 L}{2} \cdot \sum_{k=1}^{\infty} \left[\frac{\frac{4k\pi a}{L^2}}{A^2 + (\frac{k\pi}{L})^2} \cos\frac{k\pi L_1}{L} + \frac{2C}{L} \cdot \frac{1}{A^2 + (\frac{k\pi}{L})^2} \sin\frac{k\pi L_1}{L} \right]^2 \\ &= \frac{A^2 L}{2} \cdot \sum_{k=1}^{\infty} \left[\frac{\frac{4k\pi a}{L^2}}{A^2 + (\frac{k\pi}{L})^2} \cos\frac{k\pi L_1}{L} + \frac{2}{L} \cdot \frac{\sin\frac{k\pi L_1}{L}}{A^2 + (\frac{k\pi}{L})^2} \cdot \right. \\ &\left. \left(- Aa \cdot \frac{e^{AL_1} + e^{-AL_1}}{e^{AL_1} - e^{-AL_1}} + Aa \cdot \frac{e^{2AL - AL_1} + e^{AL_1}}{e^{2AL - AL_1} - e^{AL_1}} \right) \right]^2 . \end{aligned}$$

The above decompositions, i.e., Eqs (5.60) – (5.63) and (5.70) – (5.74) are not arbitrary, because we need to make sure:

(a) $F_1(L_1)$ is the background energy, which is independent of L_1;

(b) $F_3(L_1)$ is the fictitious interaction energy;

(c) $F_2(L_1) + F_4(L_1)$ is the same as Eq. (5.18) up to a constant, therefore is equally effective in determining the ground state; and in this case, we have

$$\begin{aligned} F_2(L_1) + F_4(L_1) &= \frac{8A^2 a^2}{L^3} \sum_{k=1}^{\infty} \left[\frac{k\pi}{A^2 + (\frac{k\pi}{L})^2} \right]^2 \cos^2\frac{k\pi L_1}{L} \qquad (5.75) \\ &+ \frac{8A^4 a^2}{L} \sum_{k=1}^{\infty} \left[\frac{1}{A^2 + (\frac{k\pi}{L})^2} \right]^2 \cos^2\frac{k\pi L_1}{L} \\ &+ \frac{2A^2 C^2}{L} \sum_{k=1}^{\infty} \left[\frac{1}{A^2 + (\frac{k\pi}{L})^2} \right]^2 \sin^2\frac{k\pi L_1}{L} \\ &+ \frac{2C^2}{L^3} \sum_{k=1}^{\infty} \left[\frac{k\pi}{A^2 + (\frac{k\pi}{L})^2} \right]^2 \sin^2\frac{k\pi L_1}{L} \\ &= a^2 A \cdot \frac{e^{AL_1} + e^{-AL_1}}{e^{AL_1} - e^{-AL_1}} + a^2 A \cdot \frac{e^{2AL - AL_1} + e^{AL_1}}{e^{2AL - AL_1} - e^{AL_1}} - \frac{4a^2}{L}. \end{aligned}$$

(d) $F_1(L_1)$ and $F_3(L_1)$ are contributed by f_1.

Now similar to the last section, we can replace the old expression for $F_2(L_1) + F_4(L_1)$ [i.e., Eq. (5.75)] by a finite number of trigonometric functions. By keeping only the first terms of the summation terms in Eq. (5.64), we have

$$C = -\frac{2\pi a}{L} \cot \frac{\pi L_1}{L}, \tag{5.76}$$

which has the same zero point and monotonicity with Eq. (5.69). For the same reason as discussed in the last section, we substitute Eq. (5.76) into the first term of Eq. (5.75), then we have

$$F_2(L_1) + F_4(L_1) = \frac{8a^2}{L} \cos^2 \frac{\pi L_1}{L}, \tag{5.77}$$

which has the same ground state with Eq. (5.18), thus is equally effective. Surprisingly, Eqs. (5.59) and (5.77) are the same. Figure 5.6 shows the comparisons between Method (A) and (B) for this example by plotting the energy landscapes.

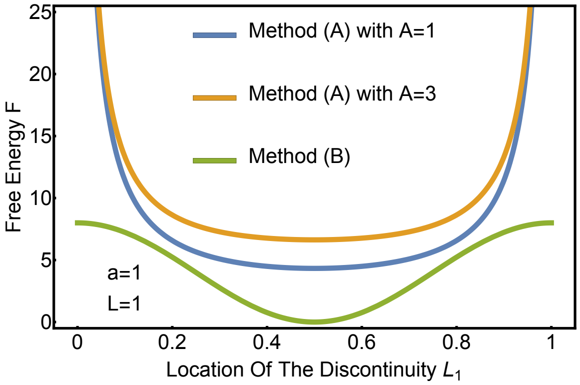

Figure 5.6: Comparison between Methods (A) and (B) in Example 2 for energy landscapes [i.e., Equations (5.18) and (5.77)]

We observe that $F_2(L_1) + F_4(L_1)$ has an energy minimum at $L_1 = L/2$. However, the cross term shown in the expression for $F_4(L_1)$ [i.e., Eq. (5.74)] has an energy maximum at $L_1 = L/2$. Fortunately, this term is canceled out by the cross term in $F_2(L_1)$; otherwise the energy landscape may have the shape of a Mexican hat. It is thus interesting to consider what will happen if A is a function of x instead of being a constant.

5.6 Example 3 – Solved by Method (A) and (B)

Now let us consider M discontinuities located at $x = L_1, L_1 + L_2, \dots, L_1 + L_2 + \cdots + L_M$ with the same energy functional as shown in Example 1 [i.e., Eq. (5.11)]. Our goal is, still, to find the ground state when $L_1, L_2, \dots, L_M$ can vary. The outer boundary conditions are Eq. (5.2); and the inner boundary conditions are $f = -a$ (or a) on the left (or right) side of each discontinuity.

5.6.1 Method (A)

By solving the Euler-Lagrange equation [i.e., Eq. (5.12)] on each patch, we have the following solution

$$f(x) = \begin{cases} -\frac{a}{L_1}x, \ x \in [0, L_1), \\ \\ -\frac{2a}{L_2}x + \frac{2aL_1}{L_2} + a, \ x \in (L_1, L_2), \\ \\ \vdots \\ -\frac{2a}{L_i}x + \frac{2a}{L_i}(L_1 + L_2 + \cdots + L_{i-1}) + a, \ x \in (L_1 + \cdots + L_{i-1}, L_1 + \cdots + L_{i-1} + L_i), \\ \\ \vdots \\ -\frac{a}{L-(L_1+L_2+\cdots+L_M)}x + \frac{aL}{L-(L_1+L_2+\cdots+L_M)}, \ x \in (L_1 + \cdots + L_M, L]; \end{cases} \tag{5.78}$$

which is illustrated in Fig. 5.7.

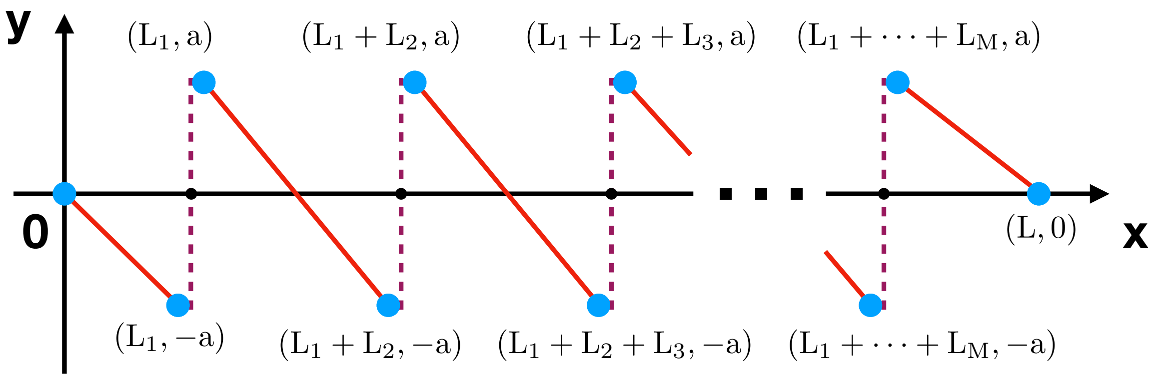

Figure 5.7: Solution to Equation (5.12) on the domain $[0, L]$ with M discontinuities [i.e., Equation (5.78)]

Therefore the energy landscape is

$$F(L_1, L_2, \ldots, L_M) = \frac{a^2}{L_1} + \frac{4a^2}{L_2} + \cdots + \frac{4a^2}{L_i} + \cdots + \frac{4a^2}{L_M} + \frac{a^2}{L - (L_1 + L_2 + \cdots + L_M)}. \tag{5.79}$$

To find the ground state, we solve the following equations

$$\frac{\partial F}{\partial L_i} = 0,\ i \in \{1, 2, \ldots, M\}, \tag{5.80}$$

which are written explicitly as

$$-\frac{1}{L_1^2} + \frac{1}{[L - (L_1 + L_2 + \cdots + L_M)]^2} = 0, \tag{5.81}$$

$$-\frac{4}{L_i^2} + \frac{1}{[L - (L_1 + L_2 + \cdots + L_M)]^2} = 0,\ i \in \{2, 3, \ldots, M\} \tag{5.82}$$

By solving Eqs. (5.81) and (5.82), we obtain the following ground state

$$L_1 = \frac{L}{2M}, L_2 = L_3 = \cdots = L_M = \frac{L}{M}. \tag{5.83}$$

5.6.2 Method (B)

We have

$$f(x) = f_1(x) + f_2(x), \tag{5.84}$$

where

$$f_1(x) = \sum_{k=1}^{\infty} \Big[\frac{4a}{k\pi}\cos\frac{k\pi L_1}{L} + \frac{4a}{k\pi}\cos\frac{k\pi(L_1+L_2)}{L} + \cdots \tag{5.85}$$

$$+ \frac{4a}{k\pi}\cos\frac{k\pi(L_1+L_2+\cdots+L_M)}{L}\Big]\sin\frac{k\pi x}{L},$$

$$f(x) = \sum_{k=1}^{\infty} \Big[\frac{2L}{(k\pi)^2}B_1\sin\frac{k\pi L_1}{L} + \frac{2L}{(k\pi)^2}B_2\sin\frac{k\pi(L_1+L_2)}{L} \tag{5.86}$$

$$+ \cdots + \frac{2L}{(k\pi)^2}B_M\sin\frac{k\pi(L_1+L_2+\cdots+L_M)}{L}\Big]\sin\frac{k\pi x}{L};$$

and the energy function

$$F(L_1, L_2, \ldots, L_M) = F_1(L_1, L_2, \ldots, L_M) + F_2(L_1, L_2, \ldots, L_M) + F_3(L_1, L_2, \ldots, L_M), \tag{5.87}$$

where

$$F_1(L_1, L_2, \cdots, L_M) = \sum_{k=1}^{\infty} \frac{2}{L}\Big[2a\cos\frac{k\pi L_1}{L} + 2a\cos\frac{k\pi(L_1+L_2)}{L} \tag{5.88}$$

$$+ \cdots + 2a\cos\frac{k\pi(L_1+L_2+\cdots+L_M)}{L}\Big]^2,$$

$$F_2(L_1, L_2, \cdots, L_M) = \sum_{k=1}^{\infty} \frac{2}{L}\Big[\frac{L}{k\pi}B_1\sin\frac{k\pi L_1}{L} + \frac{L}{k\pi}B_2\sin\frac{k\pi(L_1+L_2)}{L} \tag{5.89}$$

$$+ \cdots + \frac{L}{k\pi}B_M\sin\frac{k\pi(L_1+L_2+\cdots+L_M)}{L}\Big]^2,$$

$$
\begin{aligned}
F_3(L_1, L_2, \cdots, L_M) = \sum_{k=1}^{\infty} \frac{4}{L} \Big[& 2a\cos\frac{k\pi L_1}{L} + 2a\cos\frac{k\pi(L_1+L_2)}{L} \\
& + \cdots + 2a\cos\frac{k\pi(L_1+L_2+\cdots+L_M)}{L} \Big] \\
& \cdot \Big[\frac{L}{k\pi} B_1 \sin\frac{k\pi L_1}{L} + \frac{L}{k\pi} B_2 \sin\frac{k\pi(L_1+L_2)}{L} \\
& + \cdots + \frac{L}{k\pi} B_M \sin\frac{k\pi(L_1+L_2+\cdots+L_M)}{L} \Big]^2 .
\end{aligned}
\tag{5.90}
$$

$B_1, B_2, \cdots, B_M$ are functions of $L_1, L_2, \cdots, L_M$. By the Dirichlet's theorem, we have

$$
f(L_1) = f(L_1+L_2) = \cdots = f(L_1+L_2+\cdots+L_M) = 0, \tag{5.91}
$$

which gives

$$
B_1 = \frac{2}{L_2} - \frac{1}{L_1}, B_2 = \frac{2}{L_3} - \frac{2}{L_2}, \ldots, B_M = \frac{1}{L-(L_1+L_2+\cdots+L_M)} - \frac{2}{L_M}. \tag{5.92}
$$

We can check that the above decompositions are indeed correct, therefore we can use $F_2(L_1, L_2, \cdots, L_M)$ to determine the ground state. Following the same steps as described in the last two sections, we can replace the old expressions for $B_1, B_2, \ldots, B_M$ by a finite number of trigonometric functions. Although for the time being we are unable to justify our choice, we do find good replacements by letting $B_1, B_2, \ldots, B_M$ satisfy the following equations

$$
\begin{aligned}
& 2a\cos\frac{\pi L_1}{L} + 2a\cos\frac{\pi(L_1+L_2)}{L} + 2a\cos\frac{\pi(L_1+L_2+\cdots+L_M)}{L} \\
& + \cdots + \frac{L}{\pi} B_1 \sin\frac{\pi L_1}{L} + \frac{L}{\pi} B_2 \sin\frac{\pi(L_1+L_2)}{L} \\
& + \cdots + \frac{L}{\pi} B_M \sin\frac{\pi(L_1+L_2+\cdots+L_M)}{L} = 0,
\end{aligned}
\tag{5.93}
$$

$$2a\cos\frac{2\pi L_1}{L} + 2a\cos\frac{2\pi(L_1+L_2)}{L} + 2a\cos\frac{2\pi(L_1+L_2+\cdots+L_M)}{L}$$

$$+\cdots+\frac{L}{2\pi}B_1\sin\frac{2\pi L_1}{L} + \frac{L}{2\pi}B_2\sin\frac{2\pi(L_1+L_2)}{L}$$

$$+\cdots+\frac{L}{2\pi}B_M\sin\frac{2\pi(L_1+L_2+\cdots+L_M)}{L} = 0,$$

$$\cdots\cdots$$

$$2a\cos\frac{M\pi L_1}{L} + 2a\cos\frac{M\pi(L_1+L_2)}{L} + 2a\cos\frac{M\pi(L_1+L_2+\cdots+L_M)}{L}$$

$$+\cdots+\frac{L}{M\pi}B_1\sin\frac{M\pi L_1}{L} + \frac{L}{M\pi}B_2\sin\frac{M\pi(L_1+L_2)}{L}$$

$$+\cdots+\frac{L}{M\pi}B_M\sin\frac{M\pi(L_1+L_2+\cdots+L_M)}{L} = 0.$$

Then a good replacement for Eq. (5.89) is written as

$$F_2(L_1,L_2,\ldots,L_M) = \sum_{k=1}^{M}\frac{8a^2}{L}\Big[\cos\frac{k\pi L_1}{L} + \cos\frac{k\pi(L_1+L_2)}{L} + \cdots + \cos\frac{k\pi(L_1+L_2+\cdots+L_M)}{L}\Big]^2, \tag{5.94}$$

Thus the ground state is given by

$$\cos\frac{k\pi L_1}{L} + \cos\frac{k\pi(L_1+L_2)}{L} + \cdots + \cos\frac{k\pi(L_1+L_2+\cdots+L_M)}{L} = 0,\ \forall k\in\{1,2,\ldots,M\}, \tag{5.95}$$

and is exactly Eq. (5.83). Again, we can see that the largest few Fourier modes determine the ground state.

5.7 The Principle – Method (B)

There are three major parts of Method (B): the use of Fourier series, the regularization of the free energy, and the preservation of finite Fourier modes.

5.7.1 The Use of Fourier Series

First of all, we have an Euler-Lagrange equation that is satisfied locally but not globally. In another word, it is satisfied on each patch but not on the whole domain. Then we insert the LHS of the equation (suppose the RHS is zero) into integrals as shown in Eq. (5.21), and the information of the inner boundaries is encoded in the domain of the integrals. Then we do integration by parts as well as glue all the integrals on each patch into one integral on the whole domain, thus we get the Fourier coefficients of the function. Finally, the function can be written as Fourier series, and the energy function can be expressed in terms of the Fourier coefficients.

One interesting feature is that there is no need for the type of Fourier basis being determined by the outer boundary conditions. If the basis requires the function to be zero at the boundary (e.g., the sine series), then there will be Gibbs phenomenon for the resulting Fourier series at the boundary, and the points extremely close to the boundary will have the boundary values.

5.7.2 The Regularization of the Free Energy

When computing the physical free energy, we should not do the differentiation and integration across the inner boundaries (i.e., the defect core). To take care of that, Method (A) does the differentiation and integration on each patch, and then sum up the values of all the integrals. By contrast, Method (B) does the differentiation and integration on the whole domain, and then subtract all the unphysical contributions which include the fictitious core energy, the fictitious fluctuation energy and the fictitious interaction energy. This is similar to the Hadamard regularization [102, 103]. For an effective use of Method (B), we need a general criterion to determine which part in the Fourier series of the function contributes to the unphysical energy, and therefore use the remaining part of the Fourier series for all the later discussions. From the three examples we have shown, we see some properties of this part of the Fourier series: (1) its first derivative is an extremely divergent sequence; (2) it alone contributes to the background energy which is infinitely large but is independent of the locations of the inner boundaries. Since the these examples are too specific, we are currently unable to foresee a criterion that is suitable for a wider class of examples.

5.7.3 The Preservation of Finite Fourier Modes

The first two parts help to show that Method (B) is equivalent to Method (A). This part establishes the fact that Method (B) has the computational advantage since it does not require a complete solution to the Euler-Lagrange equation. The first part makes sure that the variables representing the locations of the inner boundaries are either contained in some trigonometric functions or some unknown functions that need to be determined by the Dirichlet's theorem [i.e., Eqs. (5.25), (5.64) and (5.91)]. This part implies that those unknown functions can be replaced by a rational function of trigonometric functions [i.e., Eqs. (5.58), (5.76) and (5.93)], and therefore the effective free energy is related to only finite number of Fourier modes.

So far, this is mainly an observation, because we haven't found a general scheme to prove this argument and it is actually not too difficult to determine the unknown functions for simple examples such as Example 1 and 2.

In short, Method (B) has a much different perspective compared to Method (A). It is promising that it can solve some difficult problems which Method (A) cannot do.

CHAPTER 6

ANALYTICAL STUDY OF NEMATIC DEFECTS PART II – DEFECTS IN TWO-DIMENSIONAL NEMATICS

For a two-dimensional nematics, the unit vector field $\mathbf{n}$ can be decomposed as

$$\mathbf{n} = n_x\,\hat{\mathbf{x}} + n_y\,\hat{\mathbf{y}}. \tag{6.1}$$

Consider a rectangular region with length L_1 and width L_2, the energy functional (with one-constant approximation) is written as

$$F = \frac{K}{2}\int_0^{L_1} \mathrm{d}x \int_0^{L_2} \mathrm{d}y \,\Big[\Big(\frac{\partial n_x}{\partial x}\Big)^2 + \Big(\frac{\partial n_x}{\partial y}\Big)^2 + \Big(\frac{\partial n_y}{\partial x}\Big)^2 + \Big(\frac{\partial n_y}{\partial y}\Big)^2\Big], \tag{6.2}$$

subject to the constraints

$$n_x^2 + n_y^2 = 1, \tag{6.3}$$

and $\mathbf{n} \equiv -\mathbf{n}$ (head-tail symmetry) [1, 98]. Thus we have the following Euler-Lagrange Equations

$$\frac{\partial^2 n_x}{\partial x^2} + \frac{\partial^2 n_x}{\partial y^2} + \Big[\Big(\frac{\partial n_x}{\partial x}\Big)^2 + \Big(\frac{\partial n_x}{\partial y}\Big)^2 + \Big(\frac{\partial n_y}{\partial x}\Big)^2 + \Big(\frac{\partial n_y}{\partial y}\Big)^2\Big] n_x = 0, \tag{6.4}$$

$$\frac{\partial^2 n_y}{\partial x^2} + \frac{\partial^2 n_y}{\partial y^2} + \Big[\Big(\frac{\partial n_x}{\partial x}\Big)^2 + \Big(\frac{\partial n_x}{\partial y}\Big)^2 + \Big(\frac{\partial n_y}{\partial x}\Big)^2 + \Big(\frac{\partial n_y}{\partial y}\Big)^2\Big] n_y = 0. \tag{6.5}$$

In addition, we consider a particular set of homeotropic boundary conditions shown as follows

$$n_x(0,y) = -1 \qquad (6.6) \qquad\qquad n_y(0,y) = 0 \qquad (6.10)$$

$$n_x(L_1,y) = 1 \qquad (6.7) \qquad\qquad n_y(L_1,y) = 0 \qquad (6.11)$$

$$n_x(x,0) = 0 \qquad (6.8) \qquad\qquad n_y(x,0) = -1 \qquad (6.12)$$

$$n_x(x,L_2) = 0 \qquad (6.9) \qquad\qquad n_y(x,L_2) = 1 \qquad (6.13)$$

which are illustrated in in Fig. 6.1. The aspect ratio is defined to be $\Gamma = L_1/L_2$.

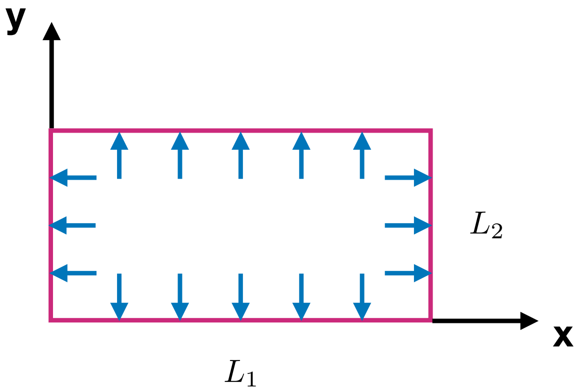

Figure 6.1: Boundary conditions for two-dimensional nematics confined in a rectangle

The most tricky issue about this boundary value problem is that Eqs. (6.4) and (6.5) are not satisfied on the whole domain because the outer boundary conditions (6.6) – (6.13) force the formation of inner boundaries. As introduced in Chapter 1, the inner boundaries include: (a) the defect core, which is characterized by $|\mathbf{n}|= 0$; and (b) the branch cut, which is due to the multi-valuedness of $\mathbf{n}$ caused by the head-tail symmetry. For the time being, we are focusing solely on defects with winding number ± 1 to avoid the difficulties related to the branch cuts. There are similar studies done by Bethuel et al.; see Ref.[104]. But here we are trying to develop a different strategy: discussing the energy functional on the whole domain and creating the inner boundaries during the calculation.

6.1 A Failed Attempt

One natural idea of creating the inner boundaries is to make them part of the solutions to the boundary value problem [i.e., Eqs. (6.4) – (6.13)], however the solutions can be too discontinuous. To resolve this issue, we are inspired by the fact that for a Heaviside function, the location of its discontinuity is the same as the location of the zero point for its first few Fourier modes; and zero points are very natural to be contained inside a function. Therefore, instead of solving Eqs. (6.4) and (6.5), we are looking for solving simpler PDEs with the locations of the zero points of its solutions coinciding with the locations of the defect cores; and we guess the solutions to the new PDEs and the solutions to Eqs. (6.4) and (6.5) may have the first few Fourier modes in common.

To find the new PDEs, we observe that the free energy density

$$\mathcal{F}_d = \frac{K}{2}\Big[\Big(\frac{\partial n_x}{\partial x}\Big)^2 + \Big(\frac{\partial n_x}{\partial y}\Big)^2 + \Big(\frac{\partial n_y}{\partial x}\Big)^2 + \Big(\frac{\partial n_y}{\partial y}\Big)^2\Big], \tag{6.14}$$

shows up in Eqs. (6.4) and (6.5). In addition, we expect an energy "jump" when the number of defect cores increase. Therefore we may approximate Eqs. (6.4) and (6.5) by

$$\frac{\partial^2 m_x}{\partial x^2} + \frac{\partial^2 m_x}{\partial y^2} + \lambda m_x = 0, \tag{6.15}$$

$$\frac{\partial^2 m_y}{\partial x^2} + \frac{\partial^2 m_y}{\partial y^2} + \lambda m_y = 0; \tag{6.16}$$

where $\lambda = 2\overline{\mathcal{F}_d}/K$ with $\overline{\mathcal{F}_d}$ being interpreted as the mean energy density; and $\mathbf{m} = (m_x, m_y)$ is expected to share the first few Fourier modes with $\mathbf{n}$.

We use separation of variables to solve Eqs. (6.15) and (6.16) subject to the boundary conditions (6.6) – (6.13) by letting

$$m_x(x,y) = \sum_i A_i(x)B_i(y), \tag{6.17}$$

$$m_y(x,y) = \sum_j C_j(x)D_j(y). \tag{6.18}$$

Then substitute Eqs. (6.17) – (6.18) into Eqs. (6.15) – (6.16), and we have

$$\frac{1}{A}\frac{\mathrm{d}^2 A}{\mathrm{d}x^2} + \frac{1}{B}\frac{\mathrm{d}^2 B}{\mathrm{d}y^2} = -\lambda, \tag{6.19}$$

$$\frac{1}{C}\frac{\mathrm{d}^2 C}{\mathrm{d}x^2} + \frac{1}{D}\frac{\mathrm{d}^2 D}{\mathrm{d}y^2} = -\lambda. \tag{6.20}$$

The boundary conditions Eqs. (6.6) – (6.13) become

$$\sum_i A_i(0)B_i(y) = -1 \tag{6.21}$$

$$\sum_i A_i(L_1)B_i(y) = 1 \tag{6.22}$$

$$B_i(0) = 0 \tag{6.23}$$

$$B_i(L_2) = 0 \tag{6.24}$$

$$C_j(0) = 0 \tag{6.25}$$

$$C_j(L_1) = 0 \tag{6.26}$$

$$\sum_j C_j(x)D_j(0) = -1 \tag{6.27}$$

$$\sum_j C_j(x)D_j(L_2) = 1 \tag{6.28}$$

We expect that zero points are isolated, therefore $A_i(x)$, $B_i(y)$, $C_j(x)$ and $D_j(y)$ are all trigonometric functions. Thus m_x and m_y can be written as

$$m_x(x,y) = \sum_i \left[a_i \sin\left(\sqrt{\lambda - \left(\frac{i\pi}{L_2}\right)^2}\cdot x\right) + b_i \cos\left(\sqrt{\lambda - \left(\frac{i\pi}{L_2}\right)^2}\cdot x\right)\right] \sin\left(\frac{i\pi y}{L_2}\right), \tag{6.29}$$

$$m_y(x,y) = \sum_j \Big[c_j \sin\Big(\sqrt{\lambda - \Big(\frac{j\pi}{L_1}\Big)^2}\cdot y\Big) + d_j \cos\Big(\sqrt{\lambda - \Big(\frac{j\pi}{L_1}\Big)^2}\cdot y\Big)\Big] \sin\Big(\frac{j\pi x}{L_1}\Big), \tag{6.30}$$

where a_i, b_i, c_j, d_j are constants and they satisfy

$$\sum_i b_i \sin\Big(\frac{i\pi y}{L_2}\Big) = -1, \tag{6.31}$$

$$\sum_i \Big[a_i \sin\Big(\sqrt{\lambda - \Big(\frac{i\pi}{L_2}\Big)^2}\cdot L_1\Big) + b_i \cos\Big(\sqrt{\lambda - \Big(\frac{i\pi}{L_2}\Big)^2}\cdot L_1\Big)\Big] \sin\Big(\frac{i\pi y}{L_2}\Big) = 1, \tag{6.32}$$

$$\sum_j d_j \sin\Big(\frac{j\pi x}{L_1}\Big) = -1, \tag{6.33}$$

$$\sum_j \Big[c_j \sin\Big(\sqrt{\lambda - \Big(\frac{j\pi}{L_1}\Big)^2}\cdot L_2\Big) + d_j \cos\Big(\sqrt{\lambda - \Big(\frac{j\pi}{L_1}\Big)^2}\cdot L_2\Big)\Big] \sin\Big(\frac{j\pi x}{L_1}\Big) = 1. \tag{6.34}$$

Therefore we have the following solutions

$$m_x(x,y) = \sum_{p=0}^{\infty} \frac{4}{(2p+1)\pi}\left[\frac{1+\cos\Big(\sqrt{\lambda - \Big(\frac{(2p+1)\pi}{L_2}\Big)^2}\cdot L_1\Big)}{\sin\Big(\sqrt{\lambda - \Big(\frac{(2p+1)\pi}{L_2}\Big)^2}\cdot L_1\Big)} \cdot \sin\Big(\sqrt{\lambda - \Big(\frac{(2p+1)\pi}{L_2}\Big)^2}\right.$$

$$\left.\cdot x\Big) - \cos\Big(\sqrt{\lambda - \Big(\frac{(2p+1)\pi}{L_2}\Big)^2}\cdot x\Big)\right] \cdot \sin\frac{(2p+1)\pi y}{L_2}, \tag{6.35}$$

$$m_y(x,y) = \sum_{q=0}^{\infty} \frac{4}{(2q+1)\pi}\left[\frac{1+\cos\Big(\sqrt{\lambda - \Big(\frac{(2q+1)\pi}{L_1}\Big)^2}\cdot L_2\Big)}{\sin\Big(\sqrt{\lambda - \Big(\frac{(2q+1)\pi}{L_1}\Big)^2}\cdot L_2\Big)} \cdot \sin\Big(\sqrt{\lambda - \Big(\frac{(2q+1)\pi}{L_1}\Big)^2}\right.$$

$$\cdot\, y\Big) - \cos\left(\sqrt{\lambda - \Big(\frac{(2q+1)\pi}{L_1}\Big)^2}\cdot y\right)\Bigg] \cdot \sin\frac{(2q+1)\pi x}{L_1}. \tag{6.36}$$

It is further shown that the number of zero points to Eqs. (6.35) and (6.36) depends on the ranges of λ, and their locations depend on the specific values of λ. Some examples are shown in Fig. 6.2.

To verify if this method is correct, we run a finite difference algorithm (with over-relaxation) for this rectangular domain, and consider one hyperbolic point fixed at the center, together with two radial points located at the line $y = L_2/2$, symmetric with respect to the center, which is illustrated in Fig. 6.3a. Figure 6.3b shows that they tend to collapse into a single radial point located at the center, and the only other suspicious equilibrium state is a saddle point (possibly happens when Γ is large) with the radial point being at the center and the two hyperbolic points being at $(L_1/4, L_2/2)$ and $(3L_1/4, L_2/2)$, which does not seem to be captured by our theory after being compared with Figs. 6.2c and 6.2d.

The problem about this method is that there are many unjustified assumptions: (a) we are not sure that boundary conditions (6.6) – (6.13) should be the same for both $\mathbf{n}$ and $\mathbf{m}$; (b) we do not have evidence showing that zero points of $\mathbf{m}$ coincide with the defect cores of $\mathbf{n}$; and (c) we are unable to justify that $\mathbf{n}$ and $\mathbf{m}$ have the first few Fourier modes in common. The nice thing about this method is that we can watch the topology change with the change of the values of the parameter λ, and we hope to see similar results from a correct theory of defects in nematics. We realize that such a theory needs to be derived more rigorously and systematically.

6.2 A Promising Attempt

The defects in a two-dimensional nematics is like a two-dimensional analogue of the examples introduced in Chapter 5. While Method (A) can only be used for numerical computations, Method (B) seems quite promising for this two-dimensional example.

First, we need a local analysis for each defect core to show that all the defect cores have

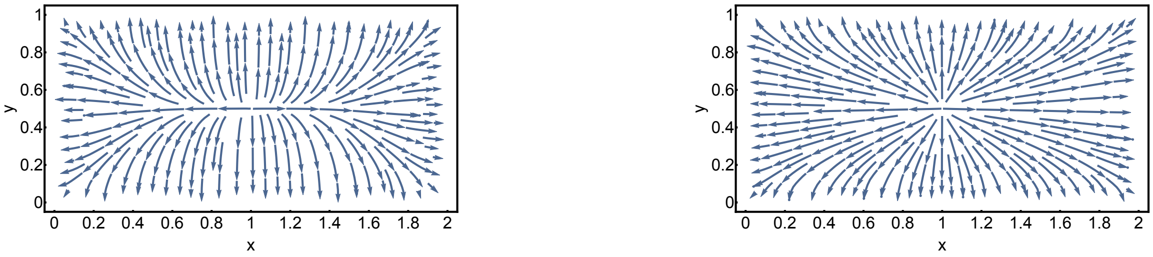

(a) $\lambda = 3$ (b) $\lambda = 16$

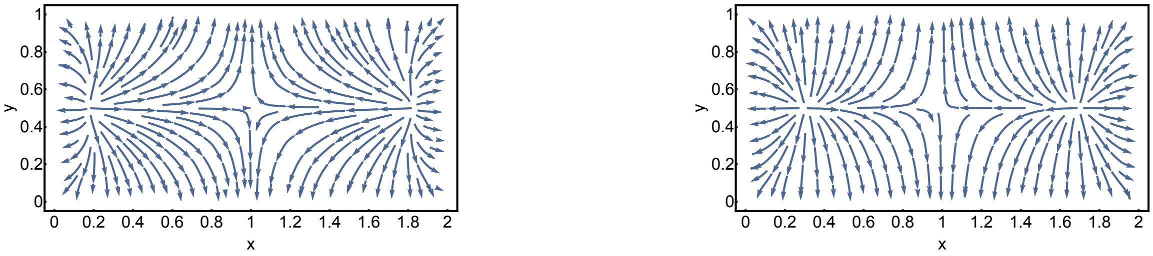

(c) $\lambda = 25$ (d) $\lambda = 31$

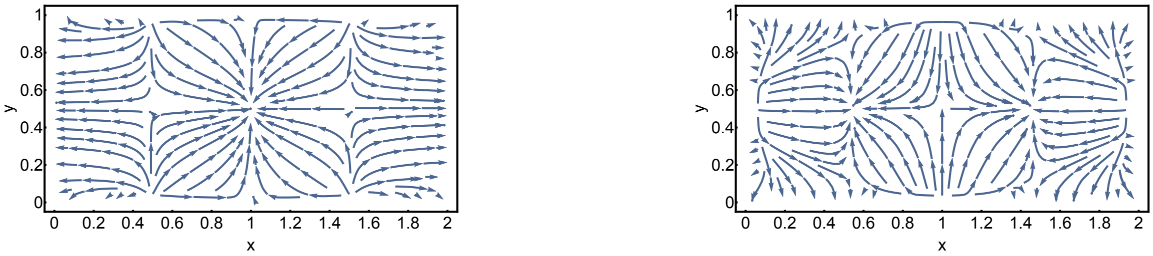

(e) $\lambda = 48$ (f) $\lambda = 56$

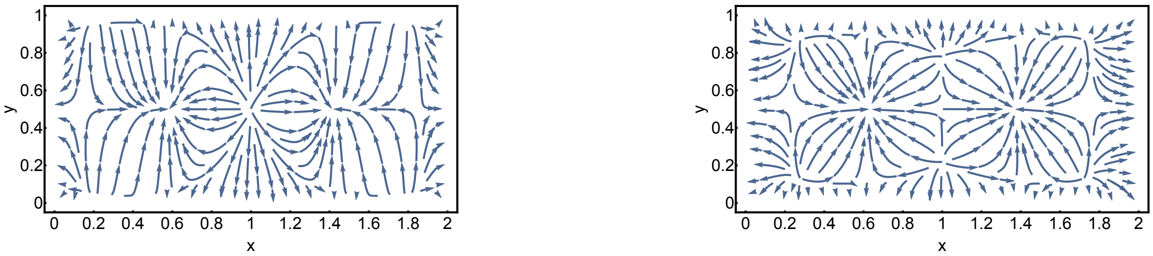

(g) $\lambda = 65$ (h) $\lambda = 79$

Figure 6.2: Vector field $\mathbf{m}$ for different values of λ

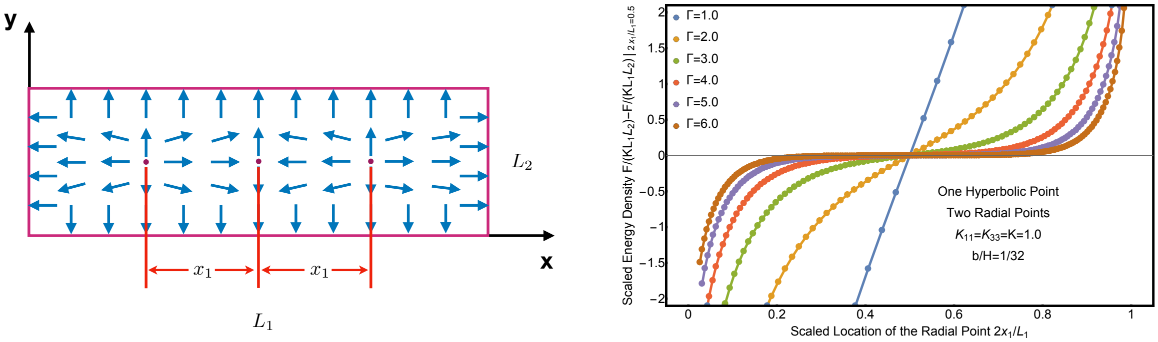

(a) Defect structures

(b) Energy landscapes

Figure 6.3: One hyperbolic point and two radial points in two-dimensional nematics

similar properties.

6.2.1 Local Analysis

For an arbitrary defect core, we choose a polar coordinate system with its coordinate singularity coinciding with it. Parametrize the unit vector field $\mathbf{n}$ as

$$\mathbf{n} = \cos\theta(\rho, \phi)\ \hat{\mathbf{x}} + \sin\theta(\rho, \phi)\ \hat{\mathbf{y}}, \tag{6.37}$$

which satisfies Eqs. (6.4) and (6.5) in the polar coordinates

$$\frac{\partial^2\theta}{\partial\rho^2} + \frac{1}{\rho}\frac{\partial\theta}{\partial\rho} + \frac{1}{\rho^2}\frac{\partial^2\theta}{\partial\phi^2} = 0. \tag{6.38}$$

To determine $\mathbf{n}$ in the vicinity of defect core, we expand $\theta(\rho, \phi)$ as

$$\theta(\rho, \phi) = \theta_0(\phi) + \rho\theta_1(\phi) + \rho^2\theta_2(\phi) + \ldots, \tag{6.39}$$

assuming ρ is small. Then substitute Eq. (6.39) into Eq. (6.38), and we have the equation for $\theta_0(\phi)$

$$\frac{\partial^2\theta_0}{\partial\phi^2} = 0. \tag{6.40}$$

Its solution is

$$\theta_0 = m\phi + D, \tag{6.41}$$

where D is a constant, and m is an integer or half-integer. Equation (6.41) describes a local property: $\mathbf{n}$ is symmetric near the defect core, independent of its location. This local property is similar to the properties shared in the examples introduced in Chapter 5 where each discontinuity jumps from $-a$ to a, therefore we may use the same techniques from Method (B) for a global treatment.

6.2.2 Global Treatment

Since $\mathbf{n}$ is a function confined in a finite rectangle, it can be expanded as sums of trigonometric functions shown as follows

$$\begin{aligned} n_x &= \sum_{j_1,k_1=1}^{\infty} a_{j_1,k_1} \sin\frac{j_1\pi x}{L_1} \sin\frac{k_1\pi y}{L_2} \\ &= \sum_{j_1=1}^{\infty} c_{j_1,0} \sin\frac{j_1\pi x}{L_1} + \sum_{j_1,k_1=1}^{\infty} c_{j_1,k_1} \sin\frac{j_1\pi x}{L_1} \cos\frac{k_1\pi y}{L_2} \\ &= \sum_{k_1=1}^{\infty} e_{0,k_1} \sin\frac{k_1\pi y}{L_2} + \sum_{j_1,k_1=1}^{\infty} e_{j_1,k_1} \cos\frac{j_1\pi x}{L_1} \sin\frac{k_1\pi y}{L_2}, \end{aligned} \tag{6.42}$$

$$\begin{aligned} n_y &= \sum_{j_2,k_2=1}^{\infty} b_{j_2,k_2} \sin\frac{j_2\pi x}{L_1} \sin\frac{k_2\pi y}{L_2} \\ &= \sum_{j_2=1}^{\infty} d_{j_2,0} \sin\frac{j_2\pi x}{L_1} + \sum_{j_2,k_2=1}^{\infty} d_{j_2,k_2} \sin\frac{j_2\pi x}{L_1} \cos\frac{k_2\pi y}{L_2} \\ &= \sum_{k_2=1}^{\infty} f_{0,k_2} \sin\frac{k_2\pi y}{L_2} + \sum_{j_2,k_2=1}^{\infty} f_{j_2,k_2} \cos\frac{j_2\pi x}{L_1} \sin\frac{k_2\pi y}{L_2}. \end{aligned} \tag{6.43}$$

Note that n_x and n_y have more than one representation. This method of Fourier series has the ability of describing the profile of $\mathbf{n}$, however there can be jump discontinuities at the outer and inner boundaries, causing an unphysical energy. Therefore, an effective use of this method should always be accompanied with a proper regularization.

The next step is to derive a set of algebraic equations by substituting Eqs. (6.42) – (6.43) into Eqs. (6.4) – (6.13). It turns out that we need only two representations. For convenience, we choose the representations involving c_{j_1,k_1}, d_{j_2,k_2}, e_{j_1,k_1} and f_{j_2,k_2}. The resulting equations are as follows:

$$\begin{aligned}
&-(j_1\pi)\frac{L_2}{L_1}\cos(j_1\pi) - (j_1\pi)\frac{L_2}{L_1} - \frac{(j_1\pi)^2}{2}\frac{L_2}{L_1}c_{j_1,0} + \int_0^{L_1} \mathrm{d}x\ \sin\frac{j_1\pi x}{L_1}\frac{\partial n_x}{\partial y}\Big|_{L_2} \\
&- \int_0^{L_1} \mathrm{d}x\ \sin\frac{j_1\pi x}{L_1}\frac{\partial n_x}{\partial y}\Big|_0 + \frac{\pi^2}{32}\sum_{m_1,m_2,n_1,n_2=1}^{\infty}(c_{j_1-n_1+n_2,m_1-m_2} - c_{j_1-n_1+n_2,m_1+m_2} \\
&-c_{j_1-n_1-n_2,m_1-m_2} + c_{j_1-n_1-n_2,m_1+m_2} - c_{j_1+n_1+n_2,m_1-m_2} + c_{j_1+n_1+n_2,m_1+m_2} \\
&+c_{j_1+n_1-n_2,m_1-m_2} - c_{j_1+n_1-n_2,m_1+m_2}) \times \Big(n_1n_2\frac{L_2}{L_1}e_{n_1,m_1}e_{n_2,m_2} \\
&+ m_1m_2\frac{L_1}{L_2}c_{n_1,m_1}c_{n_2,m_2} + n_1n_2\frac{L_2}{L_1}f_{n_1,m_1}f_{n_2,m_2} + m_1m_2\frac{L_1}{L_2}d_{n_1,m_1}d_{n_2,m_2}\Big) = 0,
\end{aligned} \tag{6.44}$$

$$\begin{aligned}
&-(k_2\pi)\frac{L_1}{L_2}\cos(k_2\pi) - (k_2\pi)\frac{L_1}{L_2} - \frac{(k_2\pi)^2}{2}\frac{L_1}{L_2}f_{0,k_2} + \int_0^{L_2} \mathrm{d}y\ \sin\frac{k_2\pi y}{L_2}\frac{\partial n_y}{\partial x}\Big|_{L_1} \\
&- \int_0^{L_2} \mathrm{d}y\ \sin\frac{k_2\pi y}{L_2}\frac{\partial n_y}{\partial x}\Big|_0 + \frac{\pi^2}{32}\sum_{m_1,m_2,n_1,n_2=1}^{\infty}(f_{n_1-n_2,k_2-m_1+m_2} - f_{n_1-n_2,k_2-m_1-m_2} \\
&-f_{n_1-n_2,k_2+m_1+m_2} + f_{n_1-n_2,k_2+m_1-m_2} - f_{n_1+n_2,k_2-m_1+m_2} + f_{n_1+n_2,k_2-m_1-m_2} \\
&+f_{n_1+n_2,k_2+m_1+m_2} - f_{n_1-n_2,k_2+m_1-m_2}) \times \Big(n_1n_2\frac{L_2}{L_1}e_{n_1,m_1}e_{n_2,m_2} \\
&+ m_1m_2\frac{L_1}{L_2}c_{n_1,m_1}c_{n_2,m_2} + n_1n_2\frac{L_2}{L_1}f_{n_1,m_1}f_{n_2,m_2} + m_1m_2\frac{L_1}{L_2}d_{n_1,m_1}d_{n_2,m_2}\Big) = 0,
\end{aligned} \tag{6.45}$$

$$\int_0^{L_2} \mathrm{d}y\ \sin\frac{k_1\pi y}{L_2}\frac{\partial n_x}{\partial x}\Big|_{L_1} - \int_0^{L_2} \mathrm{d}y\ \sin\frac{k_1\pi y}{L_2}\frac{\partial n_x}{\partial x}\Big|_0 - \frac{(k_1\pi)^2}{2}\frac{L_1}{L_2}e_{0,k_1} \tag{6.46}$$

$$+\frac{\pi^2}{32}\sum_{m_1,m_2,n_1,n_2=1}^{\infty}(e_{n_1-n_2,k_1-m_1+m_2} - e_{n_1-n_2,k_1-m_1-m_2} - e_{n_1-n_2,k_1+m_1+m_2}$$

$$+e_{n_1-n_2,k_1+m_1-m_2} - e_{n_1+n_2,k_1-m_1+m_2} + e_{n_1+n_2,k_1-m_1-m_2} + e_{n_1+n_2,k_1+m_1+m_2}$$

$$-e_{n_1-n_2,k_1+m_1-m_2}) \times \Big(n_1n_2\frac{L_2}{L_1}e_{n_1,m_1}e_{n_2,m_2} + m_1m_2\frac{L_1}{L_2}c_{n_1,m_1}c_{n_2,m_2}$$

$$+ n_1n_2\frac{L_2}{L_1}f_{n_1,m_1}f_{n_2,m_2} + m_1m_2\frac{L_1}{L_2}d_{n_1,m_1}d_{n_2,m_2}\Big) = 0,$$

$$-\frac{(j_2\pi)^2}{2}\frac{L_2}{L_1}d_{j_2,0} + \int_0^{L_1} \mathrm{d}x\ \sin\frac{j_2\pi x}{L_1}\frac{\partial n_y}{\partial y}\Big|_{L_2} - \int_0^{L_1} \mathrm{d}x\ \sin\frac{j_2\pi x}{L_1}\frac{\partial n_y}{\partial y}\Big|_0 \tag{6.47}$$

$$+\frac{\pi^2}{32}\sum_{m_1,m_2,n_1,n_2=1}^{\infty}(d_{j_2-n_1+n_2,m_1-m_2} - d_{j_2-n_1+n_2,m_1+m_2} - d_{j_2-n_1-n_2,m_1-m_2}$$

$$+d_{j_2-n_1-n_2,m_1+m_2} - d_{j_2+n_1+n_2,m_1-m_2} + d_{j_2+n_1+n_2,m_1+m_2} + d_{j_2+n_1-n_2,m_1-m_2}$$

$$-d_{j_2+n_1-n_2,m_1+m_2}) \times \Big(n_1n_2\frac{L_2}{L_1}e_{n_1,m_1}e_{n_2,m_2} + m_1m_2\frac{L_1}{L_2}c_{n_1,m_1}c_{n_2,m_2}$$

$$+ n_1n_2\frac{L_2}{L_1}f_{n_1,m_1}f_{n_2,m_2} + m_1m_2\frac{L_1}{L_2}d_{n_1,m_1}d_{n_2,m_2}\Big) = 0,$$

$$\cos(k_1\pi)\int_0^{L_1} \mathrm{d}x\ \sin\frac{j_1\pi x}{L_1}\frac{\partial n_x}{\partial y}\Big|_{L_2} - \int_0^{L_1} \mathrm{d}x\ \sin\frac{j_1\pi x}{L_1}\frac{\partial n_x}{\partial y}\Big|_0 \tag{6.48}$$

$$-\Big[\Big(\frac{j_1\pi}{L_1}\Big)^2 + \Big(\frac{k_1\pi}{L_2}\Big)^2\Big]\frac{L_1L_2}{4}c_{j_1,k_1} + \frac{\pi^2}{64}\sum_{m_1,m_2,n_1,n_2=1}^{\infty}\big(c_{j_1-n_1+n_2,k_1+m_1-m_2}$$

$$+c_{j_1-n_1+n_2,k_1-m_1+m_2} - c_{j_1-n_1+n_2,k_1+m_1+m_2} - c_{j_1-n_1+n_2,k_1-m_1-m_2}$$

$$-c_{j_1-n_1-n_2,k_1+m_1-m_2} - c_{j_1-n_1-n_2,k_1-m_1+m_2} + c_{j_1-n_1-n_2,k_1+m_1+m_2}$$

$$+c_{j_1-n_1-n_2,k_1-m_1-m_2} - c_{j_1+n_1+n_2,k_1+m_1-m_2} - c_{j_1+n_1+n_2,k_1+m_1-m_2}$$

$$+c_{j_1+n_1+n_2,k_1+m_1+m_2} + c_{j_1+n_1+n_2,k_1-m_1-m_2} + c_{j_1+n_1-n_2,k_1+m_1-m_2}$$

$$+ c_{j_1+n_1-n_2,k_1-m_1+m_2} - c_{j_1+n_1-n_2,k_1+m_1+m_2} - c_{j_1+n_1-n_2,k_1-m_1-m_2}\big)$$

$$\times\Big(n_1n_2\frac{L_2}{L_1}e_{n_1,m_1}e_{n_2,m_2} + m_1m_2\frac{L_1}{L_2}c_{n_1,m_1}c_{n_2,m_2} + n_1n_2\frac{L_2}{L_1}f_{n_1,m_1}f_{n_2,m_2}$$

$$+ m_1m_2\frac{L_1}{L_2}d_{n_1,m_1}d_{n_2,m_2}\Big) = 0,$$

$$\cos(j_2\pi)\int_0^{L_2}\mathrm{d}y\ \sin\frac{k_2\pi y}{L_2}\frac{\partial n_y}{\partial x}\Big|_{L_1} - \int_0^{L_2}\mathrm{d}y\ \sin\frac{k_2\pi y}{L_2}\frac{\partial n_y}{\partial x}\Big|_0 \tag{6.49}$$

$$-\Big[\Big(\frac{j_2\pi}{L_1}\Big)^2 + \Big(\frac{k_2\pi}{L_2}\Big)^2\Big]\frac{L_1L_2}{4}f_{j_2,k_2} + \frac{\pi^2}{64}\sum_{m_1,m_2,n_1,n_2=1}^{\infty}\big(f_{j_2+n_1-n_2,k_2-m_1+m_2}$$

$$-f_{j_2+n_1-n_2,k_2-m_1-m_2} - f_{j_2+n_1-n_2,k_2+m_1+m_2} + f_{j_2+n_1-n_2,k_2+m_1-m_2}$$

$$+f_{j_2-n_1+n_2,k_2-m_1+m_2} - f_{j_2-n_1+n_2,k_2-m_1-m_2} - f_{j_2-n_1+n_2,k_2+m_1+m_2}$$

$$+f_{j_2-n_1+n_2,k_2+m_1-m_2} - f_{j_2+n_1+n_2,k_2-m_1+m_2} + f_{j_2+n_1+n_2,k_2-m_1-m_2}$$

$$+f_{j_2+n_1+n_2,k_2+m_1+m_2} - f_{j_2+n_1+n_2,k_2+m_1-m_2} - f_{j_2-n_1-n_2,k_2-m_1+m_2}$$

$$+f_{j_2-n_1-n_2,k_2-m_1-m_2} + f_{j_2-n_1-n_2,k_2+m_1+m_2} - f_{j_2-n_1-n_2,k_2+m_1-m_2})$$

$$\times\Big(n_1 n_2 \frac{L_2}{L_1} e_{n_1,m_1} e_{n_2,m_2} + m_1 m_2 \frac{L_1}{L_2} c_{n_1,m_1} c_{n_2,m_2} + n_1 n_2 \frac{L_2}{L_1} f_{n_1,m_1} f_{n_2,m_2}$$

$$+ m_1 m_2 \frac{L_1}{L_2} d_{n_1,m_1} d_{n_2,m_2}\Big) = 0,$$

$$\cos(j_1\pi) \int_0^{L_2} \mathrm{d}y \ \sin\frac{k_1 \pi y}{L_2} \frac{\partial n_x}{\partial x}\Big|_{L_1} - \int_0^{L_2} \mathrm{d}y \ \sin\frac{k_1 \pi y}{L_2} \frac{\partial n_x}{\partial x}\Big|_0 \tag{6.50}$$

$$-\Big[\Big(\frac{j_1\pi}{L_1}\Big)^2 + \Big(\frac{k_1\pi}{L_2}\Big)^2\Big] \frac{L_1 L_2}{4} e_{j_1,k_1} + \frac{\pi^2}{64} \sum_{m_1,m_2,n_1,n_2=1}^{\infty} (e_{j_1+n_1-n_2,k_1-m_1+m_2}$$

$$-e_{j_1+n_1-n_2,k_1-m_1-m_2} - e_{j_1+n_1-n_2,k_1+m_1+m_2} + e_{j_1+n_1-n_2,k_1+m_1-m_2}$$

$$+e_{j_1-n_1+n_2,k_1-m_1+m_2} - e_{j_1-n_1+n_2,k_1-m_1-m_2} - e_{j_1-n_1+n_2,k_1+m_1+m_2}$$

$$+e_{j_1-n_1+n_2,k_1+m_1-m_2} - e_{j_1+n_1+n_2,k_2-m_1+m_2} + e_{j_1+n_1+n_2,k_1-m_1-m_2}$$

$$+e_{j_1+n_1+n_2,k_1+m_1+m_2} - e_{j_1+n_1+n_2,k_1+m_1-m_2} - e_{j_1-n_1-n_2,k_2-m_1+m_2}$$

$$+e_{j_1-n_1-n_2,k_1-m_1-m_2} + e_{j_1-n_1-n_2,k_1+m_1+m_2} - e_{j_1-n_1-n_2,k_1+m_1-m_2})$$

$$\times\Big(n_1 n_2 \frac{L_2}{L_1} e_{n_1,m_1} e_{n_2,m_2} + m_1 m_2 \frac{L_1}{L_2} c_{n_1,m_1} c_{n_2,m_2} + n_1 n_2 \frac{L_2}{L_1} f_{n_1,m_1} f_{n_2,m_2}$$

$$+ m_1 m_2 \frac{L_1}{L_2} d_{n_1,m_1} d_{n_2,m_2}\Big) = 0,$$

$$\cos(k_2\pi)\int_0^{L_1} \mathrm{d}x\ \sin\frac{j_2\pi x}{L_1}\frac{\partial n_y}{\partial y}\Big|_{L_2} - \int_0^{L_1} \mathrm{d}x\ \sin\frac{j_2\pi x}{L_1}\frac{\partial n_y}{\partial y}\Big|_0 \tag{6.51}$$

$$-\Big[\Big(\frac{j_2\pi}{L_1}\Big)^2 + \Big(\frac{k_2\pi}{L_2}\Big)^2\Big]\frac{L_1L_2}{4}d_{j_2,k_2} + \frac{\pi^2}{64}\sum_{m_1,m_2,n_1,n_2=1}^{\infty}(d_{j_2-n_1+n_2,k_2+m_1-m_2}$$

$$+d_{j_2-n_1+n_2,k_2-m_1+m_2} - d_{j_2-n_1+n_2,k_2+m_1+m_2} - d_{j_2-n_1+n_2,k_2-m_1-m_2}$$

$$-d_{j_2-n_1-n_2,k_2+m_1-m_2} - d_{j_2-n_1-n_2,k_1-m_1+m_2} + d_{j_2-n_1-n_2,k_2+m_1+m_2}$$

$$+d_{j_2-n_1-n_2,k_2-m_1-m_2} - d_{j_2+n_1+n_2,k_2+m_1-m_2} - d_{j_2+n_1+n_2,k_1+m_1-m_2}$$

$$+d_{j_2+n_1+n_2,k_2+m_1+m_2} + d_{j_2+n_1+n_2,k_2-m_1-m_2} + d_{j_2+n_1-n_2,k_2+m_1-m_2}$$

$$+d_{j_2+n_1-n_2,k_1-m_1+m_2} - d_{j_2+n_1-n_2,k_2+m_1+m_2} - d_{j_2+n_1-n_2,k_2-m_1-m_2})$$

$$\times\Big(n_1n_2\frac{L_2}{L_1}e_{n_1,m_1}e_{n_2,m_2} + m_1m_2\frac{L_1}{L_2}c_{n_1,m_1}c_{n_2,m_2} + n_1n_2\frac{L_2}{L_1}f_{n_1,m_1}f_{n_2,m_2}$$

$$+ m_1m_2\frac{L_1}{L_2}d_{n_1,m_1}d_{n_2,m_2}\Big) = 0,$$

$$\sum_{j_1=0}^{\infty} e_{j_1,k_1} = \frac{2}{k_1\pi}[(-1)^{k_1} - 1] \tag{6.52}$$

$$\sum_{j_1=0}^{\infty} (-1)^{j_1} e_{j_1,k_1} = \frac{2}{k_1\pi}[1 - (-1)^{k_1}] \tag{6.53}$$

$$\sum_{k_1=0}^{\infty} c_{j_1,k_1} = 0 \tag{6.54}$$

$$\sum_{k_1=0}^{\infty} (-1)^{k_1} c_{j_1,k_1} = 0 \tag{6.55}$$

$$\sum_{j_2=0}^{\infty} f_{j_2,k_2} = 0 \tag{6.56}$$

$$\sum_{j_2=0}^{\infty} (-1)^{j_2} f_{j_1,k_1} = 0 \tag{6.57}$$

$$\sum_{k_2=0}^{\infty} d_{j_2,k_2} = \frac{2}{j_2\pi}[(-1)^{j_2} - 1] \tag{6.58}$$

$$\sum_{k_2=0}^{\infty} (-1)^{k_2} d_{j_2,k_2} = \frac{2}{j_2\pi}[1 - (-1)^{j_2}] \tag{6.59}$$

see Appendix B for a detailed derivation.

By counting arguments, Eqs. (6.44) – (6.59) have infinite solutions (each has infinite terms), each of which corresponds to a defect structure. Also note that if Eqs. (6.44) – (6.51) do not have the nonlinear terms, then there is only one solution, which is consistent with the fact that the boundary value problem of the Laplace equation has a unique solution; see Appendix E for an example.

Next, in order to obtain the energy function, we need to substitute Eqs. (6.42) – (6.43) into Eq. (6.2). However, first we need to figure out which representation of n_x corresponds to which representation of n_y. By a calculation of Eqs. (6.44) – (6.59) involving only the Fourier modes with $0 \leq j_1, j_2, k_1, k_2 \leq 2$, we suspect that $\sin(j\pi x/L_1)\cos(k\pi y/L_2)$ – representation for n_x corresponds to $\cos(j\pi x/L_1)\sin(k\pi y/L_2)$ – representation for n_y, and $\cos(j\pi x/L_1)\sin(k\pi y/L_2)$ – representation for n_x corresponds to $\sin(j\pi x/L_1)\cos(k\pi y/L_2)$ – representation for n_y; see Appendix D. Therefore, we obtain the energy function which is written as

$$F = \frac{K}{4} L_1 L_2 \cdot \Bigg\{ \sum_{j_1=1}^{\infty} c_{j_1,0}^2 \Big(\frac{j_1\pi}{L_1}\Big)^2 + \frac{1}{2} \sum_{j_1,k_1=1}^{\infty} c_{j_1,k_1}^2 \Big[\Big(\frac{j_1\pi}{L_1}\Big)^2 + \Big(\frac{k_1\pi}{L_2}\Big)^2\Big]$$

$$+\sum_{k_2=1}^{\infty} f_{0,k_2}^2\Big(\frac{k_2\pi}{L_2}\Big)^2+\frac{1}{2}\sum_{j_2,k_2=1}^{\infty} f_{j_2,k_2}^2\Big[\Big(\frac{j_2\pi}{L_1}\Big)^2+\Big(\frac{k_2\pi}{L_2}\Big)^2\Big]\Big\}; \tag{6.60}$$

or

$$F=\frac{K}{4}L_1L_2\cdot\Big\{\sum_{j_1=1}^{\infty} d_{j_2,0}^2\Big(\frac{j_2\pi}{L_1}\Big)^2+\frac{1}{2}\sum_{j_2,k_2=1}^{\infty} d_{j_2,k_2}^2\Big[\Big(\frac{j_2\pi}{L_1}\Big)^2+\Big(\frac{k_2\pi}{L_2}\Big)^2\Big]$$

$$+\sum_{k_1=1}^{\infty} e_{0,k_1}^2\Big(\frac{k_1\pi}{L_2}\Big)^2+\frac{1}{2}\sum_{j_1,k_1=1}^{\infty} e_{j_1,k_1}^2\Big[\Big(\frac{j_1\pi}{L_1}\Big)^2+\Big(\frac{k_1\pi}{L_2}\Big)^2\Big]\Big\}. \tag{6.61}$$

Equations. (6.60) and (6.61) should have the same values, therefore we are actually considering two copies of the same system.

So far we have completed Step 1 of Method (B), which is to write the vector field $\mathbf{n}$ and energy function in terms of Fourier series. Two important observations from this step are: (a) finite number of algebraic equations (6.44) – (6.59) represent infinite number of defect structures from which we can pick up the ground state in the later work; (b) two copies of energy functions (6.60) – (6.61) should be obtained simultaneously.

For Step 2: the regularization of the free energy, and Step 3: the preservation of finite fourier modes, the difficulties still remain with regard to how to deal with Eqs. (6.44) – (6.59). Just like its one-dimensional analogues introduced in the last chapter, we guess that the largest few Fourier modes in this two-dimensional system can determine the ground state.

CHAPTER 7

CONCLUSIONS

The major theme of this work is the treatment of the defect core in the Oseen-Frank formalism of uniaxial nematics. Mostly, the defect core is treated as either a boundary or a coordinate singularity. We have adopted the first treatment in the numerical study of defect transitions in the nematic bridges with cylindrical, waist-like and barrel-like shapes, with the use of finite difference method (with the successive over-relaxation method).

(1) For the cylindrical bridge, our results confirm the existence of different types of equilibrium defect structures: hyperbolic point, hyperbolic ring, radial point (small ring) and radial ring, originally discovered in the work by Liang and Chen [42], with a clarification that the radial point is difficult to obtain and a radial small ring may be considered as a radial point in experimental observations. Moreover, the phase diagram we have obtained, which has a better accuracy, confirms the existence of three out of four defect transitions mentioned in their original work, which are: hyperbolic point – hyperbolic ring, radial defect – hyperbolic point and radial defect – hyperbolic ring transitions; yet it misses the radial point – radial ring transition. This is explained by our analysis of the energy landscapes: there are two equilibrium states representing point and ring respectively for the hyperbolic defects, however there is only one equilibrium state representing either point (small ring) or ring for the radial defects.

(2) For the waist-shaped and barrel-shaped bridges, we have constructed one example for each and have observed that some qualitative features in the cylindrical bridge, such as the types of the equilibrium defect structures and defect transitions, are still maintained regardless of the shapes. As for the quantitative features, we have observed that the convexity and concavity of the shapes have a great influence on the position of the radial defect – hyperbolic defect transition line, however the position of the hyperbolic

point – hyperbolic ring transition line is affected much less obviously. We have further compared our numerical results with the experimental data provided by Ellis et al. (see Ref. [45]) on the hyperbolic point – hyperbolic ring transition for the waist-shaped bridge made of 5CB. Our numerical computation shows that the transition happens at the aspect ratio $\Gamma = 2.58 \sim 2.61$ which falls into the 2.7 ± 0.3 range observed from the experiments.

However, the two treatments mentioned above impede a general analytical theory of defects in nematics. We wonder if a defect core can be created within the Oseen-Frank formalism during the calculation of Euler-Lagrange equation or the energy functional, which is one of the advantages of the Landau-de Gennes formalism where the defect core can be created as the emergence of biaxial nematic state in a tiny region. To test the feasibility of this idea, we have conducted a numerical experiment by using a special multigrid method on the study of equilibrium defect structures in the cylindrical bridge. Instead of merely increasing the efficiency as the multigrid method usually does, the modified version is expected to contain the crudest information of the defect core to on the coarsest grid and fine down the location of the defect core on a finer grid. Without exhaustive search, this algorithm directly produces the four equilibrium defect structures.

To construct an analytical theory, we have first experimented on the one-dimensional analogue where the defect cores are represented by the jump discontinuities. Method (A), which corresponds to the first treatment mentioned before, treats the jump discontinuities as inner boundaries and solves the boundary value problem in each patch. We regard the results obtained by Method (A) as physically correct and use them to test the correctness of new methods. Then we have developed Method (B), which expands the solutions in terms of Fourier series with unknown coefficients, treats the jump discontinuities as part of the solutions we need to obtain. We have observed that the correct energy function from Method (B) can be obtained by properly throwing away an infinitely large part. We have also noticed that the resulting regularized energy function is equally effective with a finite number of its Fourier modes for the purpose of determining the ground state, and the number of Fourier modes is equal to the number of discontinuities. Then we have applied Method (B) to study two-dimensional nematics confined in a rectangle. Considering one-constant approximation, we have derived a finite set of equations which can represent an infinite number of defect structures with the winding number for each defect core to be ± 1. Further work involves how to select the ground states from these defect structures, how to prove our speculation that a finite number of Fourier modes may determine the equilibrium defect structures, and how to include the defect cores with winding number $\pm 1/2$. We hope that our attempts can provide a new perspective for the analytical study of defects in nematics.

Appendices

APPENDIX A

DERIVATION OF EQUATION (5.43)

$F_1(y, L_1)$ can be written as

$$F_1(y, L_1) = \int_0^y \Big(\frac{\mathrm{d}f_1}{\mathrm{d}x}\Big)^2 \mathrm{d}x \tag{A.1}$$

$$= \int_0^y \Big(\sum_{k=1}^{\infty} \frac{4a}{L} \cos\frac{k\pi L_1}{L} \cos\frac{k\pi x}{L}\Big)^2 \mathrm{d}x$$

$$= \frac{4a^2}{L^2} \sum_{k_1,k_2=1}^{\infty} \Big[\frac{L}{(k_1-k_2)\pi} \cos\frac{(k_1-k_2)\pi L_1}{L} \sin\frac{(k_1-k_2)\pi y}{L}$$

$$+ \frac{L}{(k_1-k_2)\pi} \cos\frac{(k_1+k_2)\pi L_1}{L} \sin\frac{(k_1-k_2)\pi y}{L}$$

$$+ \frac{L}{(k_1+k_2)\pi} \cos\frac{(k_1-k_2)\pi L_1}{L} \sin\frac{(k_1+k_2)\pi y}{L}$$

$$+ \frac{L}{(k_1+k_2)\pi} \cos\frac{(k_1+k_2)\pi L_1}{L} \sin\frac{(k_1+k_2)\pi y}{L}\Big].$$

The first summation term in Eq. (A.1) can be further written as

$$\sum_{k_1,k_2=1}^{\infty} \frac{L}{(k_1-k_2)\pi} \cos\frac{(k_1-k_2)\pi L_1}{L} \sin\frac{(k_1-k_2)\pi y}{L} \tag{A.2}$$

$$= \lim_{N\to\infty} \sum_{k_1=k_2=1}^{N} \frac{L}{(k_1-k_2)\pi} \cos\frac{(k_1-k_2)\pi L_1}{L} \sin\frac{(k_1-k_2)\pi y}{L}$$

$$+ 2\lim_{N\to\infty} \sum_{k_1>k_2=1}^{N} \frac{L}{(k_1-k_2)\pi} \cos\frac{(k_1-k_2)\pi L_1}{L} \sin\frac{(k_1-k_2)\pi y}{L};$$

where

$$\sum_{k_1=k_2=1}^{N} \frac{L}{(k_1-k_2)\pi} \cos\frac{(k_1-k_2)\pi L_1}{L} \sin\frac{(k_1-k_2)\pi y}{L} = N\cdot y, \tag{A.3}$$

and

$$\sum_{k_1>k_2=1}^{N} \frac{L}{(k_1-k_2)\pi} \cos\frac{(k_1-k_2)\pi L_1}{L} \sin\frac{(k_1-k_2)\pi y}{L} \tag{A.4}$$

$$= \sum_{k_1=2}^{N}\sum_{k_2=1}^{k_1-1} \frac{L}{(k_1-k_2)\pi} \cos\frac{(k_1-k_2)\pi L_1}{L} \sin\frac{(k_1-k_2)\pi y}{L}$$

$$= \sum_{k_1=2}^{N}\sum_{k_2=1}^{k_1-1} \int_0^\infty \mathrm{d}v\, e^{-\frac{k_1-k_2}{L}\pi v} \cdot \frac{1}{2}\Big(e^{i\frac{k_1-k_2}{L}\pi L_1} + e^{-i\frac{k_1-k_2}{L}\pi L_1}\Big) \cdot \frac{1}{2i}\Big(e^{i\frac{k_1-k_2}{L}\pi y} - e^{-i\frac{k_1-k_2}{L}\pi y}\Big)$$

$$= \frac{L}{2\pi}\int_1^\infty \mathrm{d}x \Bigg\{ -\frac{1}{x(x^2-2x\cos\frac{\pi(L_1+y)}{L}+1)^2}\Big[x^2\sin\frac{\pi(2L_1+2y)}{L}$$

$$-2x\sin\frac{\pi(L_1+y)}{L} - x^{-N+3}\sin\frac{\pi(N+1)(L_1+y)}{L} + 2x^{-N+2}\sin\frac{\pi N(L_1+y)}{L}$$

$$-x^{-N+1}\sin\frac{\pi(N-1)(L_1+y)}{L}\Big] - \frac{1}{x(x^2-2x\cos\frac{\pi(y-L_1)}{L}+1)^2}\Big[x^2\sin\frac{\pi(2y-2L_1)}{L}$$

$$-2x\sin\frac{\pi(y-L_1)}{L} - x^{-N+3}\sin\frac{\pi(N+1)(y-L_1)}{L} + 2x^{-N+2}\sin\frac{\pi N(y-L_1)}{L}$$

$$-x^{-N+1}\sin\frac{\pi(N-1)(y-L_1)}{L}\Big] + (N-1)\frac{\sin\frac{\pi(L_1+y)}{L}}{1-2x\cos\frac{\pi(L_1+y)}{L}+x^2}$$

$$+(N-1)\frac{\sin\frac{\pi(y-L_1)}{L}}{1-2x\cos\frac{\pi(y-L_1)}{L}+x^2}\Bigg\}$$

$$\xrightarrow{N\to\infty} \frac{L}{2\pi}\int_1^\infty \mathrm{d}x \Bigg\{ -\frac{1}{x(x^2-2x\cos\frac{\pi(L_1+y)}{L}+1)^2}\Big[x^2\sin\frac{\pi(2L_1+2y)}{L}$$

$$-2x\sin\frac{\pi(L_1+y)}{L}\Big]-\frac{1}{x(x^2-2x\cos\frac{\pi(y-L_1)}{L}+1)^2}\Big[x^2\sin\frac{\pi(2y-2L_1)}{L}$$

$$-2x\sin\frac{\pi(y-L_1)}{L}\Big]+(N-1)\frac{\sin\frac{\pi(L_1+y)}{L}}{1-2x\cos\frac{\pi(L_1+y)}{L}+x^2}$$

$$+(N-1)\frac{\sin\frac{\pi(y-L_1)}{L}}{1-2x\cos\frac{\pi(y-L_1)}{L}+x^2}\Bigg\}$$

$$=\frac{L}{2\pi}\Bigg\{-\Bigg[\frac{\sin\frac{\pi(L_1+y)}{L}\cos\frac{\pi(L_1+y)}{L}}{4\sin^2\frac{\pi(L_1+y)}{2L}}-\frac{\cos^2\frac{\pi(L_1+y)}{L}}{\sin\frac{\pi(L_1+y)}{L}}+\frac{\pi}{2}\cdot\frac{\sin\frac{\pi(L_1+y)}{L}\cos^2\frac{\pi(L_1+y)}{L}}{|\sin\frac{\pi(L_1+y)}{L}|^3}$$

$$-\arctan\left(\frac{\sin^2\frac{\pi(L_1+y)}{2L}}{|\sin\frac{\pi(L_1+y)}{2L}\cos\frac{\pi(L_1+y)}{2L}|}\right)\cdot\frac{\sin\frac{\pi(L_1+y)}{L}\cos^2\frac{\pi(L_1+y)}{L}}{|\sin\frac{\pi(L_1+y)}{L}|^3}\Bigg]$$

$$+\Bigg[-\frac{1}{2\sin\frac{\pi(L_1+y)}{L}}+\frac{\pi}{2|\sin\frac{\pi(L_1+y)}{L}|\sin\frac{\pi(L_1+y)}{L}}-\arctan\left(\tan\frac{\pi(L_1+y)}{2L}\right)\cdot\frac{1}{\sin^2\frac{\pi(L_1+y)}{L}}\Bigg]$$

$$-\Bigg[\frac{\sin\frac{\pi(y-L_1)}{L}\cos\frac{\pi(y-L_1)}{L}}{4\sin^2\frac{\pi(y-L_1)}{2L}}-\frac{\cos^2\frac{\pi(y-L_1)}{L}}{\sin\frac{\pi(y-L_1)}{L}}+\frac{\pi}{2}\cdot\frac{\sin\frac{\pi(y-L_1)}{L}\cos^2\frac{\pi(y-L_1)}{L}}{|\sin\frac{\pi(y-L_1)}{L}|^3}$$

$$-\arctan\left(\tan\frac{\pi(y-L_1)}{2L}\right)\cdot\frac{\cos^2\frac{\pi(y-L_1)}{L}}{\sin^2\frac{\pi(y-L_1)}{L}}\Bigg]+\Bigg[-\frac{1}{2\sin\frac{\pi(y-L_1)}{L}}$$

$$+\frac{\pi}{2|\sin\frac{\pi(y-L_1)}{L}|\sin\frac{\pi(y-L_1)}{L}}-\arctan\left(\tan\frac{\pi(y-L_1)}{2L}\right)\cdot\frac{1}{\sin^2\frac{\pi(y-L_1)}{L}}\Bigg]$$

$$+(N-1)\times\Bigg[\frac{\pi}{2}\cdot\frac{\sin\frac{\pi(L_1+y)}{L}}{|\sin\frac{\pi(L_1+y)}{L}|}-\arctan\left(\tan\frac{\pi(L_1+y)}{2L}\right)\Bigg]$$

$$+(N-1)\times\Bigg[\frac{\pi}{2}\cdot\frac{\sin\frac{\pi(y-L_1)}{L}}{|\sin\frac{\pi(y-L_1)}{L}|}-\arctan\left(\tan\frac{\pi(y-L_1)}{2L}\right)\Bigg]\Bigg\}$$

$$
= \frac{L}{2\pi} \times \begin{cases} \Big[- N \cdot \frac{\pi y}{L} - \frac{\cos \frac{\pi(L_1+y)}{2L}}{2\sin \frac{\pi(L_1+y)}{2L}} - \frac{\cos \frac{\pi(y-L_1)}{2L}}{2\sin \frac{\pi(y-L_1)}{2L}} \Big], & \text{if } 0 < y < L_1 \\ \\ \Big[N\pi - N \cdot \frac{\pi y}{L} - \frac{\cos \frac{\pi(L_1+y)}{2L}}{2\sin \frac{\pi(L_1+y)}{2L}} - \frac{\cos \frac{\pi(y-L_1)}{2L}}{2\sin \frac{\pi(y-L_1)}{2L}} \Big], & \text{if } L_1 < y < L \end{cases}
$$

The second summation term in Eq. (A.1) can be further written as

$$
\sum_{k_1,k_2=1}^{\infty} \frac{L}{(k_1-k_2)\pi} \cos \frac{(k_1+k_2)\pi L_1}{L} \sin \frac{(k_1-k_2)\pi y}{L} \tag{A.5}
$$

$$
= \lim_{N\to\infty} \sum_{k_1=k_2=1}^{N} \frac{L}{(k_1-k_2)\pi} \cos \frac{(k_1+k_2)\pi L_1}{L} \sin \frac{(k_1-k_2)\pi y}{L}
$$

$$
+ 2 \lim_{N\to\infty} \sum_{k_1>k_2=1}^{N} \frac{L}{(k_1-k_2)\pi} \cos \frac{(k_1+k_2)\pi L_1}{L} \sin \frac{(k_1-k_2)\pi y}{L}
$$

where

$$
\sum_{k_1=k_2=1}^{N} \frac{L}{(k_1-k_2)\pi} \cos \frac{(k_1+k_2)\pi L_1}{L} \sin \frac{(k_1-k_2)\pi y}{L} \tag{A.6}
$$

$$
= \sum_{k=1}^{N} y \cdot \cos \frac{2k\pi L_1}{L} = \frac{y}{2} \cdot \frac{\cos \frac{2N\pi L_1}{L} - \cos \frac{2(N+1)\pi L_1}{L}}{1 - \cos \frac{2\pi L_1}{L}} - \frac{y}{2}
$$

and

$$
\sum_{k_1>k_2=1}^{N} \frac{L}{(k_1-k_2)\pi} \cos \frac{(k_1+k_2)\pi L_1}{L} \sin \frac{(k_1-k_2)\pi y}{L} \tag{A.7}
$$

$$
= \sum_{k_1=2}^{N} \sum_{k_2=1}^{k_1-1} \frac{L}{(k_1-k_2)\pi} \cos \frac{(k_1+k_2)\pi L_1}{L} \sin \frac{(k_1-k_2)\pi y}{L}
$$

$$
= \sum_{k_1=2}^{N} \sum_{k_2=1}^{k_1-1} \int_0^{\infty} \mathrm{d}v \, e^{-\frac{k_1-k_2}{L}\pi v} \cdot \frac{1}{2}\Big(e^{i\frac{k_1+k_2}{L}\pi L_1} + e^{-i\frac{k_1+k_2}{L}\pi L_1} \Big) \cdot \frac{1}{2i} \Big(e^{i\frac{k_1-k_2}{L}\pi y} - e^{-i\frac{k_1-k_2}{L}\pi y} \Big)
$$

$$= \frac{L}{2\pi}\int_1^\infty \mathrm{d}x \Bigg\{ -\frac{1}{x\Big(x^2-2\cos\frac{\pi(y-L_1)}{L}+1\Big)\Big(x^2-2\cos\frac{\pi(y+L_1)}{L}+1\Big)}\Bigg[x^2\sin\frac{2\pi(y+L_1)}{L}$$

$$-x\sin\frac{\pi(y+3L_1)}{L}-x\sin\frac{\pi(y+L_1)}{L}+\sin\frac{2\pi L_1}{L}$$

$$-x^{-N+3}\sin\frac{(N+1)\pi(y+L_1)}{L}+x^{-N+2}\sin\frac{(N+1)\pi(y+L_1)-\pi(y-L_1)}{L}$$

$$+x^{-N+2}\sin\frac{N\pi(y+L_1)}{L}-x^{-N+1}\sin\frac{N\pi(y+L_1)-\pi(y-L_1)}{L}\Bigg]$$

$$-\frac{1}{x\Big(x^2-2\cos\frac{\pi(y-L_1)}{L}+1\Big)\Big(x^2-2\cos\frac{\pi(y+L_1)}{L}+1\Big)}\Bigg[x^2\sin\frac{2\pi(y-L_1)}{L}$$

$$+x\sin\frac{\pi(3L_1-y)}{L}-x\sin\frac{\pi(y-L_1)}{L}-\sin\frac{2\pi L_1}{L}$$

$$-x^{-N+3}\sin\frac{(N+1)\pi(y-L_1)}{L}+x^{-N+2}\sin\frac{(N+1)\pi(y-L_1)-\pi(y+L_1)}{L}$$

$$+x^{-N+2}\sin\frac{N\pi(y-L_1)}{L}-x^{-N+1}\sin\frac{N\pi(y-L_1)-\pi(y+L_1)}{L}\Bigg]$$

$$-\frac{1}{2x\Big(x^2-2\cos\frac{\pi(y-L_1)}{L}+1\Big)\Big(1-\cos\frac{2\pi L_1}{L}\Big)}\Bigg[-x\sin\frac{\pi(y+3L_1)}{L}$$

$$+x\sin\frac{\pi(y+L_1)}{L}+\sin\frac{4\pi L_1}{L}-\sin\frac{2\pi L_1}{L}+x\sin\frac{\pi(y-L_1)+2(N+1)\pi L_1}{L}$$

$$-x\sin\frac{\pi(y-L_1)+2N\pi L_1}{L}-\sin\frac{2(N+1)\pi L_1}{L}+\sin\frac{2N\pi L_1}{L}\Bigg]$$

$$-\frac{1}{2x\Big(x^2-2\cos\frac{\pi(y+L_1)}{L}+1\Big)\Big(1-\cos\frac{2\pi L_1}{L}\Big)}\Bigg[x\sin\frac{\pi(3L_1-y)}{L}$$

$$+ x\sin\frac{\pi(y-L_1)}{L} - \sin\frac{4\pi L_1}{L} + \sin\frac{2\pi L_1}{L} + x\sin\frac{\pi(y+L_1)-2(N+1)\pi L_1}{L}$$

$$- x\sin\frac{\pi(y+L_1)-2N\pi L_1}{L} + \sin\frac{2(N+1)\pi L_1}{L} - \sin\frac{2N\pi L_1}{L}\Bigg]\Bigg\}$$

$$\xrightarrow{N\to\infty} \frac{L}{2\pi}\int_1^\infty \mathrm{d}x \Bigg\{ - \frac{1}{x\Big(x^2-2\cos\frac{\pi(y-L_1)}{L}+1\Big)\Big(x^2-2\cos\frac{\pi(y+L_1)}{L}+1\Big)}$$

$$\cdot\Bigg[x^2\sin\frac{2\pi(y+L_1)}{L} - x\sin\frac{\pi(y+3L_1)}{L} - x\sin\frac{\pi(y+L_1)}{L} + \sin\frac{2\pi L_1}{L}\Bigg]$$

$$- \frac{1}{x\Big(x^2-2\cos\frac{\pi(y-L_1)}{L}+1\Big)\Big(x^2-2\cos\frac{\pi(y+L_1)}{L}+1\Big)}\Bigg[x^2\sin\frac{2\pi(y-L_1)}{L}$$

$$+ x\sin\frac{\pi(3L_1-y)}{L} - x\sin\frac{\pi(y-L_1)}{L} - \sin\frac{2\pi L_1}{L}\Bigg]$$

$$- \frac{1}{2x\Big(x^2-2\cos\frac{\pi(y-L_1)}{L}+1\Big)\Big(1-\cos\frac{2\pi L_1}{L}\Big)}\Bigg[-x\sin\frac{\pi(y+3L_1)}{L}$$

$$+ x\sin\frac{\pi(y+L_1)}{L} + \sin\frac{4\pi L_1}{L} - \sin\frac{2\pi L_1}{L} + x\sin\frac{\pi(y-L_1)+2(N+1)\pi L_1}{L}$$

$$- x\sin\frac{\pi(y-L_1)+2N\pi L_1}{L} - \sin\frac{2(N+1)\pi L_1}{L} + \sin\frac{2N\pi L_1}{L}\Bigg]$$

$$- \frac{1}{2x\Big(x^2-2\cos\frac{\pi(y+L_1)}{L}+1\Big)\Big(1-\cos\frac{2\pi L_1}{L}\Big)}\Bigg[x\sin\frac{\pi(3L_1-y)}{L}$$

$$+ x\sin\frac{\pi(y-L_1)}{L} - \sin\frac{4\pi L_1}{L} + \sin\frac{2\pi L_1}{L} + x\sin\frac{\pi(y+L_1)-2(N+1)\pi L_1}{L}$$

$$- x \sin \frac{\pi(y + L_1) - 2N\pi L_1}{L} + \sin \frac{2(N+1)\pi L_1}{L} - \sin \frac{2N\pi L_1}{L} \Bigg] \Bigg\}$$

$$= \frac{L}{2\pi} \times$$

$$\begin{cases} \left[\frac{\pi}{2} \cdot \frac{y}{L} - \frac{\pi}{2} \cdot \frac{y}{L} \cdot \frac{\sin \frac{(2N+1)\pi L_1}{L}}{\sin \frac{\pi L_1}{L}} + \frac{\cos \frac{(2N+1)\pi L_1}{L} + \cos \frac{\pi L_1}{L}}{4 \sin \frac{\pi L_1}{L}} \ln \left(\frac{1 - \cos \frac{\pi(y-L_1)}{L}}{1 - \cos \frac{\pi(y+L_1)}{L}} \right) \right], & \text{if } 0 < y < L_1 \\ \left[\frac{\pi}{2} \left(1 - \frac{y}{L} \right) \cdot \left(-1 + \frac{\sin \frac{(2N+1)\pi L_1}{L}}{\sin \frac{\pi L_1}{L}} \right) + \frac{\cos \frac{(2N+1)\pi L_1}{L} + \cos \frac{\pi L_1}{L}}{4 \sin \frac{\pi L_1}{L}} \ln \left(\frac{1 - \cos \frac{\pi(y-L_1)}{L}}{1 - \cos \frac{\pi(y+L_1)}{L}} \right) \right], & \text{if } L_1 < y < L \end{cases}$$

The third summation term in Eq. (A.1) can be further written as

$$\sum_{k_1,k_2=1}^{N} \frac{L}{(k_1+k_2)\pi} \cos \frac{(k_1-k_2)\pi L_1}{L} \sin \frac{(k_1+k_2)\pi y}{L} \tag{A.8}$$

$$= \sum_{k_1,k_2=1}^{N} \int_0^{\infty} \mathrm{d}v \, e^{-\frac{k_1+k_2}{L}\pi v} \cdot \frac{1}{2} \left(e^{i\frac{k_1-k_2}{L}\pi L_1} + e^{-i\frac{k_1-k_2}{L}\pi L_1} \right) \cdot \frac{1}{2i} \left(e^{i\frac{k_1+k_2}{L}\pi y} - e^{-i\frac{k_1+k_2}{L}\pi y} \right)$$

$$= \frac{L}{\pi} \int_1^{\infty} \mathrm{d}x \, \frac{1}{x\left(x^2 - 2x \cos \frac{\pi(y+L_1)}{L} + 1 \right)\left(x^2 - 2x \cos \frac{\pi(y-L_1)}{L} + 1 \right)} \cdot \Bigg[x^2 \sin \frac{2\pi y}{L}$$

$$- x \sin \frac{\pi(y+L_1)}{L} - x \sin \frac{\pi(y-L_1)}{L} - x^{-N+2} \sin \frac{(N+1)\pi(y+L_1) + \pi(y-L_1)}{L}$$

$$- x^{-N+2} \sin \frac{N\pi(y-L_1) + 2\pi y}{L} + x^{-N+1} \sin \frac{(N+1)\pi(y+L_1)}{L}$$

$$+ x^{-N+1} \sin \frac{N\pi(y+L_1) + \pi(y-L_1)}{L} - x^{-N} \sin \frac{N\pi(y+L_1)}{L}$$

$$+ x^{-N+1} \sin \frac{N\pi(y-L_1) + \pi(y+L_1)}{L} + x^{-N+1} \sin \frac{(N+1)\pi(y-L_1)}{L}$$

$$- x^{-N}\sin\frac{N\pi(y-L_1)}{L} + x^{-2N+2}\sin\frac{2(N+1)\pi y}{L}$$

$$- x^{-2N+1}\sin\frac{2(N+1)\pi y-\pi(y-L_1)}{L} + x^{-2N}\sin\frac{2N\pi y}{L} - x^{-2N+1}\sin\frac{2N\pi y+\pi(y-L_1)}{L}\Bigg]$$

$$\xrightarrow{N\to\infty} \frac{L}{\pi}\int_1^{\infty}\mathrm{d}x\,\frac{1}{x\Big(x^2-2x\cos\frac{\pi(y+L_1)}{L}+1\Big)\Big(x^2-2x\cos\frac{\pi(y-L_1)}{L}+1\Big)}\cdot\Bigg[x^2\sin\frac{2\pi y}{L}$$

$$- x\sin\frac{\pi(y+L_1)}{L} - x\sin\frac{\pi(y-L_1)}{L}\Bigg]$$

$$= -\frac{L}{4\pi}\cdot\frac{\cos\frac{\pi L_1}{L}}{\sin\frac{\pi L_1}{L}}\ln\left(\frac{1-\cos\frac{\pi(y-L_1)}{L}}{1-\cos\frac{\pi(y+L_1)}{L}}\right) + \begin{cases}\frac{y}{2}, & \text{if } 0<y<L_1\\[2em] \frac{y-L}{2}, & \text{if } L_1<y<L\end{cases}$$

The fourth summation term in Eq. (A.1) can be further written as

$$\sum_{k_1,k_2=1}^{N}\frac{L}{(k_1+k_2)\pi}\cos\frac{(k_1+k_2)\pi L_1}{L}\sin\frac{(k_1+k_2)\pi y}{L} \tag{A.9}$$

$$= \sum_{k_1,k_2=1}^{\infty}\int_0^{\infty}\mathrm{d}v\,e^{-\frac{k_1+k_2}{L}\pi v}\cdot\frac{1}{2}\Big(e^{i\frac{k_1+k_2}{L}\pi L_1}+e^{-i\frac{k_1+k_2}{L}\pi L_1}\Big)\cdot\frac{1}{2i}\Big(e^{i\frac{k_1+k_2}{L}\pi y}-e^{-i\frac{k_1+k_2}{L}\pi y}\Big)$$

$$= \frac{L}{2\pi}\int_1^{\infty}\mathrm{d}x\Bigg\{\frac{1}{x\Big(x^2-2x\cos\frac{\pi(y+L_1)}{L}+1\Big)^2}\Bigg[x^2\sin\frac{2\pi(y+L_1)}{L} - 2x\sin\frac{\pi(y+L_1)}{L}$$

$$- 2x^{-N+2}\sin\frac{(N+2)\pi(y+L_1)}{L} + 4x^{-N+1}\sin\frac{(N+1)\pi(y+L_1)}{L}$$

$$- 2x^{-N}\sin\frac{N\pi(y+L_1)}{L} + x^{-2N+2}\sin\frac{(2N+2)\pi(y+L_1)}{L}$$

$$- 2x^{-2N+1}\sin\frac{(2N+1)\pi(y+L_1)}{L} + x^{-2N}\sin\frac{2N\pi(y+L_1)}{L}\Bigg]$$

$$+ \frac{1}{x\Big(x^2 - 2x\cos\frac{\pi(y-L_1)}{L}+1\Big)^2}\Bigg[x^2\sin\frac{2\pi(y-L_1)}{L} - 2x\sin\frac{\pi(y-L_1)}{L}$$

$$- 2x^{-N+2}\sin\frac{(N+2)\pi(y-L_1)}{L} + 4x^{-N+1}\sin\frac{(N+1)\pi(y-L_1)}{L}$$

$$- 2x^{-N}\sin\frac{N\pi(y-L_1)}{L} + x^{-2N+2}\sin\frac{(2N+2)\pi(y-L_1)}{L}$$

$$- 2x^{-2N+1}\sin\frac{(2N+1)\pi(y-L_1)}{L} + x^{-2N}\sin\frac{2N\pi(y-L_1)}{L}\Bigg]\Bigg\}$$

$$\xrightarrow{N\to\infty} \frac{L}{2\pi}\int_1^\infty \mathrm{d}x\Bigg\{\frac{1}{x\Big(x^2 - 2x\cos\frac{\pi(y+L_1)}{L}+1\Big)^2}\Bigg[x^2\sin\frac{2\pi(y+L_1)}{L}$$

$$- 2x\sin\frac{\pi(y+L_1)}{L}\Bigg] + \frac{1}{x\Big(x^2 - 2x\cos\frac{\pi(y-L_1)}{L}+1\Big)^2}\Bigg[x^2\sin\frac{2\pi(y-L_1)}{L}$$

$$- 2x\sin\frac{\pi(y-L_1)}{L}\Bigg]\Bigg\}$$

$$= \frac{L}{2\pi}\times\begin{cases}\left[\frac{\pi y}{L} + \frac{\cos\frac{\pi(y+L_1)}{2L}}{2\sin\frac{\pi(y+L_1)}{2L}} + \frac{\cos\frac{\pi(y-L_1)}{2L}}{2\sin\frac{\pi(y-L_1)}{2L}}\right], & \text{if } 0<y<L_1\\ \\ \left[\frac{\pi y}{L} - \pi + \frac{\cos\frac{\pi(y+L_1)}{2L}}{2\sin\frac{\pi(y+L_1)}{2L}} + \frac{\cos\frac{\pi(y-L_1)}{2L}}{2\sin\frac{\pi(y-L_1)}{2L}}\right], & \text{if } L_1<y<L\end{cases}$$

Then we substitute Eqs. (A.3) and (A.4) into Eqs. (A.2), and substitute Eqs. (A.6) and (A.7) into Eq. (A.5). And then we substitute Eqs. (A.2), (A.5), (A.8) and (A.9) into

Eq. (A.1), and we can finally obtain Eq. (5.41).

APPENDIX B

DERIVATION OF EQUATIONS (6.44) – (6.51)

Assume there is one point defect with winding number 1 located at the point $(L_1^{(1)}, L_2^{(1)})$ in the rectangle $[0, L_1] \times [0, L_2]$ as illustrated in Fig. B.1. Then consider n_x on the patch $(0, L_1^{(1)}) \times (0, L_2^{(1)})$, we have

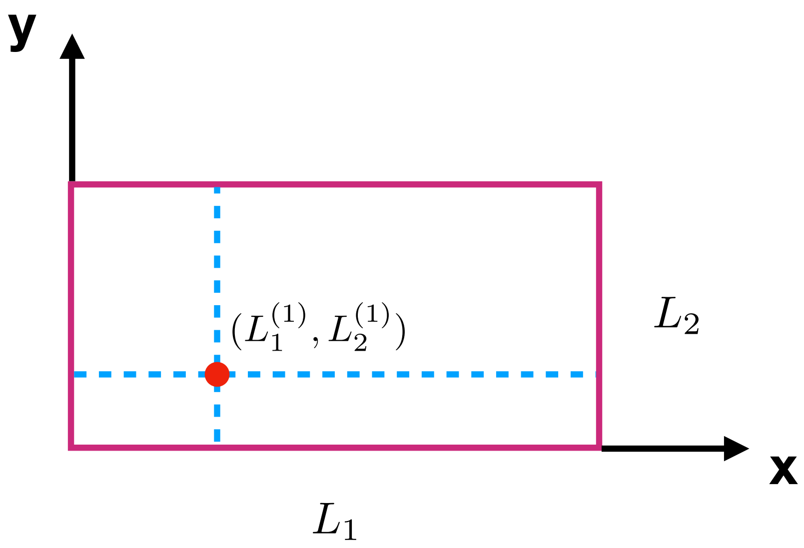

Figure B.1: The four patches and one defect core

$$\begin{aligned}
&\int_0^{L_1^{(1)}} \mathrm{d}x \int_0^{L_2^{(1)}} \mathrm{d}y \left(\frac{\partial^2 n_x}{\partial x^2} + \frac{\partial^2 n_x}{\partial y^2}\right) \sin\frac{j_1 \pi x}{L_1} \sin\frac{k_1 \pi y}{L_2} \\
&= \sin\frac{j_1 \pi L_1^{(1)}}{L_1} \int_0^{L_2^{(1)}} \mathrm{d}y \; \sin\frac{k_1 \pi y}{L_2} \cdot \frac{\partial n_x}{\partial x}\Big|_{L_1^{(1)}} + \sin\frac{k_1 \pi L_2^{(1)}}{L_2} \int_0^{L_1^{(1)}} \mathrm{d}x \; \sin\frac{j \pi x}{L_1} \\
&\cdot \frac{\partial n_x}{\partial y}\Big|_{L_2^{(1)}} - \frac{j_1 \pi}{L_1} \cos\frac{j_1 \pi L_1^{(1)}}{L_1} \int_0^{L_2^{(1)}} \mathrm{d}y \; \sin\frac{k_1 \pi y}{L_2} \cdot n_x(L_1^{(1)}, y)
\end{aligned} \tag{B.1}$$

$$- \frac{k_1\pi}{L_2} \cos\frac{k_1\pi L_2^{(1)}}{L_2} \int_0^{L_1^{(1)}} \mathrm{d}x \ \sin\frac{j_1\pi x}{L_1} \cdot n_x(x, L_2^{(1)}) + \frac{L_2}{L_1} \cdot \frac{j_1}{k_1} \cos\frac{k_1\pi L_2^{(1)}}{L_2}$$

$$- \frac{L_2}{L_1} \cdot \frac{j_1}{k_1} - \Big(\frac{j_1\pi}{L_1}\Big)^2 \int_0^{L_1^{(1)}} \mathrm{d}x \int_0^{L_2^{(1)}} \mathrm{d}y \ n_x \sin\frac{j_1\pi x}{L_1} \sin\frac{k_1\pi y}{L_2}$$

$$- \Big(\frac{k_1\pi}{L_2}\Big)^2 \int_0^{L_1^{(1)}} \mathrm{d}x \int_0^{L_2^{(1)}} \mathrm{d}y \ n_x \sin\frac{j_1\pi x}{L_1} \sin\frac{k_1\pi y}{L_2};$$

and,

$$\int_0^{L_1^{(1)}} \mathrm{d}x \int_0^{L_2^{(1)}} \mathrm{d}y \ n_x \Big[\Big(\frac{\partial n_x}{\partial x}\Big)^2 + \Big(\frac{\partial n_x}{\partial y}\Big)^2 + \Big(\frac{\partial n_y}{\partial x}\Big)^2 + \Big(\frac{\partial n_y}{\partial y}\Big)^2\Big] \sin\frac{j_1\pi x}{L_1} \sin\frac{k_1\pi y}{L_2}$$

$$= \sum_{m_1,m_2,n_1,n_2} \Big(\frac{4}{L_1L_2}\Big)^2 \Big[\int_0^{L_1^{(1)}} \mathrm{d}x \int_0^{L_2^{(1)}} \mathrm{d}y \tag{B.2}$$

$$\cdot\, n_x \sin\frac{j_1\pi x}{L_1} \sin\frac{n_1\pi x}{L_1} \sin\frac{n_2\pi x}{L_1} \sin\frac{k_1\pi y}{L_2} \sin\frac{m_1\pi y}{L_2} \sin\frac{m_2\pi y}{L_2}\Big]$$

$$\cdot \Big[n_1n_2\Big(\frac{\pi}{L_1}\Big)^2 \cdot \Big(\int_0^{L_1} \mathrm{d}x_1 \int_0^{L_2} \mathrm{d}y_1 \ n_x \cos\frac{n_1\pi x_1}{L_1} \sin\frac{m_1\pi y_1}{L_2}\Big)$$

$$\cdot \Big(\int_0^{L_1} \mathrm{d}x_1 \int_0^{L_2} \mathrm{d}y_1 \ n_x \cos\frac{n_2\pi x_2}{L_1} \sin\frac{m_2\pi y_1}{L_2}\Big)$$

$$+ m_1m_2\Big(\frac{\pi}{L_2}\Big)^2 \cdot \Big(\int_0^{L_1} \mathrm{d}x_1 \int_0^{L_2} \mathrm{d}y_1 \ n_x \sin\frac{n_1\pi x_1}{L_1} \cos\frac{m_1\pi y_1}{L_2}\Big)$$

$$\cdot \Big(\int_0^{L_1} \mathrm{d}x_1 \int_0^{L_2} \mathrm{d}y_1 \ n_x \sin\frac{n_2\pi x_2}{L_1} \cos\frac{m_2\pi y_1}{L_2}\Big)$$

$$+ n_1n_2\Big(\frac{\pi}{L_1}\Big)^2 \cdot \Big(\int_0^{L_1} \mathrm{d}x_1 \int_0^{L_2} \mathrm{d}y_1 \ n_y \cos\frac{n_1\pi x_1}{L_1} \sin\frac{m_1\pi y_1}{L_2}\Big)$$

$$\cdot \Big(\int_0^{L_1} \mathrm{d}x_1 \int_0^{L_2} \mathrm{d}y_1 \ n_y \cos\frac{n_2\pi x_2}{L_1} \sin\frac{m_2\pi y_1}{L_2}\Big)$$

$$+\, m_1 m_2 \Big(\frac{\pi}{L_2}\Big)^2 \cdot \Big(\int_0^{L_1} \mathrm{d}x_1 \int_0^{L_2} \mathrm{d}y_1 \; n_y \sin\frac{n_1 \pi x_1}{L_1} \cos\frac{m_1 \pi y_1}{L_2} \Big)$$

$$\cdot \Big(\int_0^{L_1} \mathrm{d}x_1 \int_0^{L_2} \mathrm{d}y_1 \; n_y \sin\frac{n_2 \pi x_2}{L_1} \cos\frac{m_2 \pi y_1}{L_2} \Big) \Big].$$

On the patch $(0, L_1^{(1)}) \times (L_2^{(1)}, L_2)$, we have

$$\int_0^{L_1^{(1)}} \mathrm{d}x \int_{L_2^{(1)}}^{L_2} \mathrm{d}y \, \Big(\frac{\partial^2 n_x}{\partial x^2} + \frac{\partial^2 n_x}{\partial y^2} \Big) \sin\frac{j_1 \pi x}{L_1} \sin\frac{k_1 \pi y}{L_2} \tag{B.3}$$

$$= \sin\frac{j_1 \pi L_1^{(1)}}{L_1} \int_{L_2^{(1)}}^{L_2} \mathrm{d}y \; \sin\frac{k_1 \pi y}{L_2} \cdot \frac{\partial n_x}{\partial x}\Big|_{L_1^{(1)}} + \sin(k_1 \pi) \int_0^{L_1^{(1)}} \mathrm{d}x \; \sin\frac{j_1 \pi x}{L_1} \cdot \frac{\partial n_x}{\partial y}\Big|_{L_2}$$

$$- \sin\frac{k_1 \pi L_2^{(1)}}{L_2} \int_0^{L_1^{(1)}} \mathrm{d}x \; \sin\frac{j_1 \pi x}{L_1} \cdot \frac{\partial n_x}{\partial y}\Big|_{L_2^{(1)}} - \frac{j_1 \pi}{L_1} \cos\frac{j_1 \pi L_1^{(1)}}{L_1} \int_{L_2^{(1)}}^{L_2} \mathrm{d}y \; \sin\frac{k_1 \pi y}{L_2}$$

$$\cdot\, n_x(L_1^{(1)}, y) + \frac{k_1 \pi}{L_2} \cos\frac{k_1 \pi L_2^{(1)}}{L_2} \int_0^{L_1^{(1)}} \mathrm{d}x \; \sin\frac{j_1 \pi x}{L_1} \cdot n_x(x, L_2^{(1)}) - \frac{L_2}{L_1} \cdot \frac{j_1}{k_1} \cos\frac{k_1 \pi L_2^{(1)}}{L_2}$$

$$- \Big(\frac{j_1 \pi}{L_1}\Big)^2 \int_0^{L_1^{(1)}} \mathrm{d}x \int_{L_2^{(1)}}^{L_2} \mathrm{d}y \; n_x \sin\frac{j_1 \pi x}{L_1} \sin\frac{k_1 \pi y}{L_2}$$

$$- \Big(\frac{k_1 \pi}{L_2}\Big)^2 \int_0^{L_1^{(1)}} \mathrm{d}x \int_{L_2^{(1)}}^{L_2} \mathrm{d}y \; n_x \sin\frac{j_1 \pi x}{L_1} \sin\frac{k_1 \pi y}{L_2};$$

and,

$$\int_0^{L_1^{(1)}} \mathrm{d}x \int_{L_2^{(1)}}^{L_2} \mathrm{d}y \; n_x \Big[\Big(\frac{\partial n_x}{\partial x}\Big)^2 + \Big(\frac{\partial n_x}{\partial y}\Big)^2 + \Big(\frac{\partial n_y}{\partial x}\Big)^2 + \Big(\frac{\partial n_y}{\partial y}\Big)^2 \Big] \sin\frac{j_1 \pi x}{L_1} \sin\frac{k_1 \pi y}{L_2}$$

$$= \sum_{m_1, m_2, n_1, n_2} \Big(\frac{4}{L_1 L_2}\Big)^2 \Big[\int_0^{L_1^{(1)}} \mathrm{d}x \int_{L_2^{(1)}}^{L_2} \mathrm{d}y \tag{B.4}$$

$$\cdot\, n_x \sin\frac{j_1\pi x}{L_1}\sin\frac{n_1\pi x}{L_1}\sin\frac{n_2\pi x}{L_1}\sin\frac{k_1\pi y}{L_2}\sin\frac{m_1\pi y}{L_2}\sin\frac{m_2\pi y}{L_2}\Big]$$

$$\cdot\Big[n_1 n_2\Big(\frac{\pi}{L_1}\Big)^2\cdot\Big(\int_0^{L_1}\mathrm{d}x_1\int_0^{L_2}\mathrm{d}y_1\; n_x\cos\frac{n_1\pi x_1}{L_1}\sin\frac{m_1\pi y_1}{L_2}\Big)$$

$$\cdot\Big(\int_0^{L_1}\mathrm{d}x_1\int_0^{L_2}\mathrm{d}y_1\; n_x\cos\frac{n_2\pi x_2}{L_1}\sin\frac{m_2\pi y_1}{L_2}\Big)$$

$$+\, m_1 m_2\Big(\frac{\pi}{L_2}\Big)^2\cdot\Big(\int_0^{L_1}\mathrm{d}x_1\int_0^{L_2}\mathrm{d}y_1\; n_x\sin\frac{n_1\pi x_1}{L_1}\cos\frac{m_1\pi y_1}{L_2}\Big)$$

$$\cdot\Big(\int_0^{L_1}\mathrm{d}x_1\int_0^{L_2}\mathrm{d}y_1\; n_x\sin\frac{n_2\pi x_2}{L_1}\cos\frac{m_2\pi y_1}{L_2}\Big)$$

$$+\, n_1 n_2\Big(\frac{\pi}{L_1}\Big)^2\cdot\Big(\int_0^{L_1}\mathrm{d}x_1\int_0^{L_2}\mathrm{d}y_1\; n_y\cos\frac{n_1\pi x_1}{L_1}\sin\frac{m_1\pi y_1}{L_2}\Big)$$

$$\cdot\Big(\int_0^{L_1}\mathrm{d}x_1\int_0^{L_2}\mathrm{d}y_1\; n_y\cos\frac{n_2\pi x_2}{L_1}\sin\frac{m_2\pi y_1}{L_2}\Big)$$

$$+\, m_1 m_2\Big(\frac{\pi}{L_2}\Big)^2\cdot\Big(\int_0^{L_1}\mathrm{d}x_1\int_0^{L_2}\mathrm{d}y_1\; n_y\sin\frac{n_1\pi x_1}{L_1}\cos\frac{m_1\pi y_1}{L_2}\Big)$$

$$\cdot\Big(\int_0^{L_1}\mathrm{d}x_1\int_0^{L_2}\mathrm{d}y_1\; n_y\sin\frac{n_2\pi x_2}{L_1}\cos\frac{m_2\pi y_1}{L_2}\Big)\Big].$$

On the patch $(0, L_1^{(1)}) \times (L_2^{(1)}, L_2)$, we have

$$\int_{L_1^{(1)}}^{L_1}\mathrm{d}x\int_0^{L_2^{(1)}}\mathrm{d}y\;\Big(\frac{\partial^2 n_x}{\partial x^2}+\frac{\partial^2 n_x}{\partial y^2}\Big)\sin\frac{j_1\pi x}{L_1}\sin\frac{k_1\pi y}{L_2} \tag{B.5}$$

$$=\sin(j_1\pi)\int_0^{L_2^{(1)}}\mathrm{d}y\;\sin\frac{k_1\pi y}{L_2}\cdot\frac{\partial n_x}{\partial x}\Big|_{L_1}-\sin\frac{j_1\pi L_1^{(1)}}{L_1}\int_0^{L_2^{(1)}}\mathrm{d}y\;\sin\frac{k_1\pi y}{L_2}$$

$$\cdot \frac{\partial n_x}{\partial x}\Big|_{L_1^{(1)}} - \frac{L_2}{L_1}\cdot\frac{j_1}{k_1}\cos(j_1\pi) + \frac{L_2}{L_1}\cdot\frac{j_1}{k_1}\cos(j_1\pi)\cos\frac{k_1\pi L_2^{(1)}}{L_2}$$

$$+\sin\frac{k_1\pi L_2^{(1)}}{L_2}\int_{L_1^{(1)}}^{L_1}\mathrm{d}x\ \sin\frac{j_1\pi x}{L_1}\cdot\frac{\partial n_x}{\partial y}\Big|_{L_2^{(1)}} + \frac{j_1\pi}{L_1}\cos\frac{j_1\pi L_1^{(1)}}{L_1}\int_0^{L_2^{(1)}}\mathrm{d}y\ \sin\frac{k_1\pi y}{L_2}$$

$$\cdot\, n_x(L_1^{(1)},y) - \frac{k_1\pi}{L_2}\cos\frac{k_1\pi L_2^{(1)}}{L_2}\int_{L_1^{(1)}}^{L_1}\mathrm{d}x\ \sin\frac{j_1\pi x}{L_1}\cdot n_x(x,L_2^{(1)})$$

$$-\Big(\frac{j_1\pi}{L_1}\Big)^2\int_{L_1^{(1)}}^{L_1}\mathrm{d}x\int_0^{L_2^{(1)}}\mathrm{d}y\ n_x\sin\frac{j_1\pi x}{L_1}\sin\frac{k_1\pi y}{L_2}$$

$$-\Big(\frac{k_1\pi}{L_2}\Big)^2\int_{L_1^{(1)}}^{L_1}\mathrm{d}x\int_0^{L_2^{(1)}}\mathrm{d}y\ n_x\sin\frac{j_1\pi x}{L_1}\sin\frac{k_1\pi y}{L_2};$$

and

$$\int_{L_1^{(1)}}^{L_1}\mathrm{d}x\int_0^{L_2^{(1)}}\mathrm{d}y\ n_x\Big[\Big(\frac{\partial n_x}{\partial x}\Big)^2+\Big(\frac{\partial n_x}{\partial y}\Big)^2+\Big(\frac{\partial n_y}{\partial x}\Big)^2+\Big(\frac{\partial n_y}{\partial y}\Big)^2\Big]\sin\frac{j_1\pi x}{L_1}\sin\frac{k_1\pi y}{L_2}$$

$$=\sum_{m_1,m_2,n_1,n_2}\Big(\frac{4}{L_1L_2}\Big)^2\Big[\int_{L_1^{(1)}}^{L_1}\mathrm{d}x\int_0^{L_2^{(1)}}\mathrm{d}y \tag{B.6}$$

$$\cdot\, n_x\sin\frac{j_1\pi x}{L_1}\sin\frac{n_1\pi x}{L_1}\sin\frac{n_2\pi x}{L_1}\sin\frac{k_1\pi y}{L_2}\sin\frac{m_1\pi y}{L_2}\sin\frac{m_2\pi y}{L_2}\Big]$$

$$\cdot\Big[n_1n_2\Big(\frac{\pi}{L_1}\Big)^2\cdot\Big(\int_0^{L_1}\mathrm{d}x_1\int_0^{L_2}\mathrm{d}y_1\ n_x\cos\frac{n_1\pi x_1}{L_1}\sin\frac{m_1\pi y_1}{L_2}\Big)$$

$$\cdot\Big(\int_0^{L_1}\mathrm{d}x_1\int_0^{L_2}\mathrm{d}y_1\ n_x\cos\frac{n_2\pi x_2}{L_1}\sin\frac{m_2\pi y_1}{L_2}\Big)$$

$$+\,m_1m_2\Big(\frac{\pi}{L_2}\Big)^2\cdot\Big(\int_0^{L_1}\mathrm{d}x_1\int_0^{L_2}\mathrm{d}y_1\ n_x\sin\frac{n_1\pi x_1}{L_1}\cos\frac{m_1\pi y_1}{L_2}\Big)$$

$$\cdot\Big(\int_0^{L_1}\mathrm{d}x_1\int_0^{L_2}\mathrm{d}y_1\ n_x\sin\frac{n_2\pi x_2}{L_1}\cos\frac{m_2\pi y_1}{L_2}\Big)$$

$$+ n_1 n_2 \Big(\frac{\pi}{L_1}\Big)^2 \cdot \Big(\int_0^{L_1} \mathrm{d}x_1 \int_0^{L_2} \mathrm{d}y_1 \; n_y \cos\frac{n_1 \pi x_1}{L_1} \sin\frac{m_1 \pi y_1}{L_2}\Big)$$

$$\cdot \Big(\int_0^{L_1} \mathrm{d}x_1 \int_0^{L_2} \mathrm{d}y_1 \; n_y \cos\frac{n_2 \pi x_2}{L_1} \sin\frac{m_2 \pi y_1}{L_2}\Big)$$

$$+ m_1 m_2 \Big(\frac{\pi}{L_2}\Big)^2 \cdot \Big(\int_0^{L_1} \mathrm{d}x_1 \int_0^{L_2} \mathrm{d}y_1 \; n_y \sin\frac{n_1 \pi x_1}{L_1} \cos\frac{m_1 \pi y_1}{L_2}\Big)$$

$$\cdot \Big(\int_0^{L_1} \mathrm{d}x_1 \int_0^{L_2} \mathrm{d}y_1 \; n_y \sin\frac{n_2 \pi x_2}{L_1} \cos\frac{m_2 \pi y_1}{L_2}\Big)\Big].$$

On the patch $(L_1^{(1)}, L_1) \times (L_2^{(1)}, L_2)$, we have

$$\int_{L_1^{(1)}}^{L_1} \mathrm{d}x \int_{L_2^{(1)}}^{L_2} \mathrm{d}y \, \Big(\frac{\partial^2 n_x}{\partial x^2} + \frac{\partial^2 n_x}{\partial y^2}\Big) \sin\frac{j_1 \pi x}{L_1} \sin\frac{k_1 \pi y}{L_2} \tag{B.7}$$

$$= \sin(j_1 \pi) \int_{L_2^{(1)}}^{L_2} \mathrm{d}y \; \sin\frac{k_1 \pi y}{L_2} \cdot \frac{\partial n_x}{\partial x}\Big|_{L_1} - \sin\frac{j_1 \pi L_1^{(1)}}{L_1} \int_{L_2^{(1)}}^{L_2} \mathrm{d}y \; \sin\frac{k_1 \pi y}{L_2} \cdot \frac{\partial n_x}{\partial x}\Big|_{L_1^{(1)}}$$

$$+ \sin(k_1 \pi) \int_{L_1^{(1)}}^{L_1} \mathrm{d}x \; \sin\frac{j_1 \pi x}{L_1} \cdot \frac{\partial n_x}{\partial y}\Big|_{L_2} - \sin\frac{k_1 \pi L_2^{(1)}}{L_2} \int_{L_1^{(1)}}^{L_1} \mathrm{d}x \; \sin\frac{j_1 \pi x}{L_1}$$

$$\cdot \frac{\partial n_x}{\partial y}\Big|_{L_2^{(1)}} - \frac{L_2}{L_1} \cdot \frac{j_1}{k_1} \cos(j_1 \pi) \cos\frac{k_1 \pi L_2^{(1)}}{L_2} + \frac{L_2}{L_1} \cdot \frac{j_1}{k_1} \cos(j_1 \pi) \cos(k_1 \pi)$$

$$+ \frac{j_1 \pi}{L_1} \cos\frac{j_1 \pi L_1^{(1)}}{L_1} \int_{L_2^{(1)}}^{L_2} \mathrm{d}y \; \sin\frac{k_1 \pi y}{L_2} \cdot n_x(L_1^{(1)}, y) + \frac{k_1 \pi}{L_2} \cos\frac{k_1 \pi L_2^{(1)}}{L_2}$$

$$\cdot \int_{L_1^{(1)}}^{L_1} \mathrm{d}x \; \sin\frac{j_1 \pi x}{L_1} \cdot n_x(x, L_2^{(1)}) - \Big(\frac{j_1 \pi}{L_1}\Big)^2 \int_{L_1^{(1)}}^{L_1} \mathrm{d}x \int_{L_2^{(1)}}^{L_2} \mathrm{d}y \, n_x \sin\frac{j_1 \pi x}{L_1} \sin\frac{k_1 \pi y}{L_2}$$

$$- \Big(\frac{k_1 \pi}{L_2}\Big)^2 \int_{L_1^{(1)}}^{L_1} \mathrm{d}x \int_{L_2^{(1)}}^{L_2} \mathrm{d}y \, n_x \sin\frac{j_1 \pi x}{L_1} \sin\frac{k_1 \pi y}{L_2};$$

and,

$$
\begin{aligned}
&\int_{L_1^{(1)}}^{L_1} \mathrm{d}x \int_{L_2^{(1)}}^{L_2} \mathrm{d}y\; n_x \Big[\Big(\frac{\partial n_x}{\partial x}\Big)^2 + \Big(\frac{\partial n_x}{\partial y}\Big)^2 + \Big(\frac{\partial n_y}{\partial x}\Big)^2 + \Big(\frac{\partial n_y}{\partial y}\Big)^2\Big] \sin\frac{j_1\pi x}{L_1} \sin\frac{k_1\pi y}{L_2} \\
&= \sum_{m_1,m_2,n_1,n_2} \Big(\frac{4}{L_1L_2}\Big)^2 \Big[\int_{L_1^{(1)}}^{L_1} \mathrm{d}x \int_{L_2^{(1)}}^{L_2} \mathrm{d}y \qquad\qquad \text{(B.8)} \\
&\cdot n_x \sin\frac{j_1\pi x}{L_1} \sin\frac{n_1\pi x}{L_1} \sin\frac{n_2\pi x}{L_1} \sin\frac{k_1\pi y}{L_2} \sin\frac{m_1\pi y}{L_2} \sin\frac{m_2\pi y}{L_2}\Big] \\
&\cdot \Big[n_1n_2\Big(\frac{\pi}{L_1}\Big)^2 \cdot \Big(\int_0^{L_1} \mathrm{d}x_1 \int_0^{L_2} \mathrm{d}y_1\; n_x \cos\frac{n_1\pi x_1}{L_1} \sin\frac{m_1\pi y_1}{L_2}\Big) \\
&\cdot \Big(\int_0^{L_1} \mathrm{d}x_1 \int_0^{L_2} \mathrm{d}y_1\; n_x \cos\frac{n_2\pi x_2}{L_1} \sin\frac{m_2\pi y_1}{L_2}\Big) \\
&+ m_1m_2\Big(\frac{\pi}{L_2}\Big)^2 \cdot \Big(\int_0^{L_1} \mathrm{d}x_1 \int_0^{L_2} \mathrm{d}y_1\; n_x \sin\frac{n_1\pi x_1}{L_1} \cos\frac{m_1\pi y_1}{L_2}\Big) \\
&\cdot \Big(\int_0^{L_1} \mathrm{d}x_1 \int_0^{L_2} \mathrm{d}y_1\; n_x \sin\frac{n_2\pi x_2}{L_1} \cos\frac{m_2\pi y_1}{L_2}\Big) \\
&+ n_1n_2\Big(\frac{\pi}{L_1}\Big)^2 \cdot \Big(\int_0^{L_1} \mathrm{d}x_1 \int_0^{L_2} \mathrm{d}y_1\; n_y \cos\frac{n_1\pi x_1}{L_1} \sin\frac{m_1\pi y_1}{L_2}\Big) \\
&\cdot \Big(\int_0^{L_1} \mathrm{d}x_1 \int_0^{L_2} \mathrm{d}y_1\; n_y \cos\frac{n_2\pi x_2}{L_1} \sin\frac{m_2\pi y_1}{L_2}\Big) \\
&+ m_1m_2\Big(\frac{\pi}{L_2}\Big)^2 \cdot \Big(\int_0^{L_1} \mathrm{d}x_1 \int_0^{L_2} \mathrm{d}y_1\; n_y \sin\frac{n_1\pi x_1}{L_1} \cos\frac{m_1\pi y_1}{L_2}\Big) \\
&\cdot \Big(\int_0^{L_1} \mathrm{d}x_1 \int_0^{L_2} \mathrm{d}y_1\; n_y \sin\frac{n_2\pi x_2}{L_1} \cos\frac{m_2\pi y_1}{L_2}\Big)\Big].
\end{aligned}
$$

Then on the whole rectangle $[0, L_1] \times [0, L_2]$, we sum up Eqs. (B.1), (B.3), (B.5), (B.7), and the result is

$$\int_0^{L_1} \mathrm{d}x \int_0^{L_2} \mathrm{d}y \,\Big(\frac{\partial^2 n_x}{\partial x^2} + \frac{\partial^2 n_x}{\partial y^2}\Big) \sin\frac{j_1 \pi x}{L_1} \sin\frac{k_1 \pi y}{L_2} \tag{B.9}$$

$$= \frac{L_2}{L_1} \cdot \frac{j_1}{k_1} \cdot [-1 - \cos(j_1\pi) + \cos(k_1\pi) + \cos(j_1\pi) \cdot \cos(k_1\pi)]$$

$$- \Big[\Big(\frac{j_1\pi}{L_1}\Big)^2 + \Big(\frac{k_1\pi}{L_2}\Big)^2\Big] \cdot \int_0^{L_1} \mathrm{d}x \int_0^{L_2} \mathrm{d}y \; n_x \sin\frac{j_1\pi x}{L_1} \sin\frac{k_1 \pi x}{L_2}.$$

We sum up Eqs. (B.2), (B.4), (B.6), (B.8), and the result is

$$\int_0^{L_1} \mathrm{d}x \int_0^{L_2} \mathrm{d}y \; n_x \Big[\Big(\frac{\partial n_x}{\partial x}\Big)^2 + \Big(\frac{\partial n_x}{\partial y}\Big)^2 + \Big(\frac{\partial n_y}{\partial x}\Big)^2 + \Big(\frac{\partial n_y}{\partial y}\Big)^2\Big] \sin\frac{j_1\pi x}{L_1} \sin\frac{k_1\pi y}{L_2}$$

$$= \sum_{m_1,m_2,n_1,n_2} \Big(\frac{4}{L_1 L_2}\Big)^2 \Big[\int_0^{L_1} \mathrm{d}x \int_0^{L_2} \mathrm{d}y \tag{B.10}$$

$$\cdot\, n_x \sin\frac{j_1\pi x}{L_1} \sin\frac{n_1\pi x}{L_1} \sin\frac{n_2\pi x}{L_1} \sin\frac{k_1\pi y}{L_2} \sin\frac{m_1\pi y}{L_2} \sin\frac{m_2\pi y}{L_2}\Big]$$

$$\cdot \Big[n_1 n_2 \Big(\frac{\pi}{L_1}\Big)^2 \cdot \Big(\int_0^{L_1} \mathrm{d}x_1 \int_0^{L_2} \mathrm{d}y_1 \; n_x \cos\frac{n_1\pi x_1}{L_1} \sin\frac{m_1\pi y_1}{L_2}\Big)$$

$$\cdot \Big(\int_0^{L_1} \mathrm{d}x_1 \int_0^{L_2} \mathrm{d}y_1 \; n_x \cos\frac{n_2\pi x_2}{L_1} \sin\frac{m_2\pi y_1}{L_2}\Big)$$

$$+ m_1 m_2 \Big(\frac{\pi}{L_2}\Big)^2 \cdot \Big(\int_0^{L_1} \mathrm{d}x_1 \int_0^{L_2} \mathrm{d}y_1 \; n_x \sin\frac{n_1\pi x_1}{L_1} \cos\frac{m_1\pi y_1}{L_2}\Big)$$

$$\cdot \Big(\int_0^{L_1} \mathrm{d}x_1 \int_0^{L_2} \mathrm{d}y_1 \; n_x \sin\frac{n_2\pi x_2}{L_1} \cos\frac{m_2\pi y_1}{L_2}\Big)$$

$$+ n_1 n_2 \Big(\frac{\pi}{L_1}\Big)^2 \cdot \Big(\int_0^{L_1} \mathrm{d}x_1 \int_0^{L_2} \mathrm{d}y_1 \; n_y \cos\frac{n_1\pi x_1}{L_1} \sin\frac{m_1\pi y_1}{L_2}\Big)$$

$$\cdot \Big(\int_0^{L_1} \mathrm{d}x_1 \int_0^{L_2} \mathrm{d}y_1 \; n_y \cos\frac{n_2\pi x_2}{L_1} \sin\frac{m_2\pi y_1}{L_2}\Big)$$

$$+ m_1 m_2 \Big(\frac{\pi}{L_2}\Big)^2 \cdot \Big(\int_0^{L_1} \mathrm{d}x_1 \int_0^{L_2} \mathrm{d}y_1 \; n_y \sin\frac{n_1 \pi x_1}{L_1} \cos\frac{m_1 \pi y_1}{L_2}\Big)$$

$$\cdot \Big(\int_0^{L_1} \mathrm{d}x_1 \int_0^{L_2} \mathrm{d}y_1 \; n_y \sin\frac{n_2 \pi x_2}{L_1} \cos\frac{m_2 \pi y_1}{L_2}\Big)\Big].$$

Similarly, consider n_y on the whole rectangle $[0, L_1] \times [0, L_2]$, and we have

$$\int_0^{L_1} \mathrm{d}x \int_0^{L_2} \mathrm{d}y \,\Big(\frac{\partial^2 n_y}{\partial x^2} + \frac{\partial^2 n_y}{\partial y^2}\Big) \sin\frac{j_2 \pi x}{L_1} \sin\frac{k_2 \pi y}{L_2} \tag{B.11}$$

$$= \frac{L_1}{L_2} \cdot \frac{k_2}{j_2} \cdot [-1 + \cos(j_2\pi) - \cos(k_2\pi) + \cos(j_2\pi) \cdot \cos(k_2\pi)]$$

$$- \Big[\Big(\frac{j_2\pi}{L_1}\Big)^2 + \Big(\frac{k_2\pi}{L_2}\Big)^2\Big] \cdot \int_0^{L_1} \mathrm{d}x \int_0^{L_2} \mathrm{d}y \; n_x \sin\frac{j_2 \pi x}{L_1} \sin\frac{k_2 \pi x}{L_2};$$

and,

$$\int_0^{L_1} \mathrm{d}x \int_0^{L_2} \mathrm{d}y \; n_y \Big[\Big(\frac{\partial n_x}{\partial x}\Big)^2 + \Big(\frac{\partial n_x}{\partial y}\Big)^2 + \Big(\frac{\partial n_y}{\partial x}\Big)^2 + \Big(\frac{\partial n_y}{\partial y}\Big)^2\Big] \sin\frac{j_2 \pi x}{L_1} \sin\frac{k_2 \pi y}{L_2}$$

$$= \sum_{m_1, m_2, n_1, n_2} \Big(\frac{4}{L_1 L_2}\Big)^2 \Big[\int_0^{L_1} \mathrm{d}x \int_0^{L_2} \mathrm{d}y \tag{B.12}$$

$$\cdot\, n_y \sin\frac{j_2 \pi x}{L_1} \sin\frac{n_1 \pi x}{L_1} \sin\frac{n_2 \pi x}{L_1} \sin\frac{k_2 \pi y}{L_2} \sin\frac{m_1 \pi y}{L_2} \sin\frac{m_2 \pi y}{L_2}\Big]$$

$$\cdot \Big[n_1 n_2 \Big(\frac{\pi}{L_1}\Big)^2 \cdot \Big(\int_0^{L_1} \mathrm{d}x_1 \int_0^{L_2} \mathrm{d}y_1 \; n_x \cos\frac{n_1 \pi x_1}{L_1} \sin\frac{m_1 \pi y_1}{L_2}\Big)$$

$$\cdot \Big(\int_0^{L_1} \mathrm{d}x_1 \int_0^{L_2} \mathrm{d}y_1 \; n_x \cos\frac{n_2 \pi x_2}{L_1} \sin\frac{m_2 \pi y_1}{L_2}\Big)$$

$$+ m_1 m_2 \Big(\frac{\pi}{L_2}\Big)^2 \cdot \Big(\int_0^{L_1} \mathrm{d}x_1 \int_0^{L_2} \mathrm{d}y_1 \; n_x \sin\frac{n_1 \pi x_1}{L_1} \cos\frac{m_1 \pi y_1}{L_2}\Big)$$

$$
\begin{aligned}
&\cdot \Big(\int_0^{L_1} \mathrm{d}x_1 \int_0^{L_2} \mathrm{d}y_1 \; n_x \sin\frac{n_2 \pi x_2}{L_1} \cos\frac{m_2 \pi y_1}{L_2}\Big) \\
&+ n_1 n_2 \Big(\frac{\pi}{L_1}\Big)^2 \cdot \Big(\int_0^{L_1} \mathrm{d}x_1 \int_0^{L_2} \mathrm{d}y_1 \; n_y \cos\frac{n_1 \pi x_1}{L_1} \sin\frac{m_1 \pi y_1}{L_2}\Big) \\
&\cdot \Big(\int_0^{L_1} \mathrm{d}x_1 \int_0^{L_2} \mathrm{d}y_1 \; n_y \cos\frac{n_2 \pi x_2}{L_1} \sin\frac{m_2 \pi y_1}{L_2}\Big) \\
&+ m_1 m_2 \Big(\frac{\pi}{L_2}\Big)^2 \cdot \Big(\int_0^{L_1} \mathrm{d}x_1 \int_0^{L_2} \mathrm{d}y_1 \; n_y \sin\frac{n_1 \pi x_1}{L_1} \cos\frac{m_1 \pi y_1}{L_2}\Big) \\
&\cdot \Big(\int_0^{L_1} \mathrm{d}x_1 \int_0^{L_2} \mathrm{d}y_1 \; n_y \sin\frac{n_2 \pi x_2}{L_1} \cos\frac{m_2 \pi y_1}{L_2}\Big)\Big].
\end{aligned}
$$

Equations (6.4) and (6.5) imply that Eq. (B.9) $+$ Eq. (B.10) $= 0$ and Eq. (B.11) $+$ Eq. (B.12) $= 0$. Then by Eqs. (6.42) and (6.43), we obtain two algebraic equations in terms of a_{j_1,k_1}, b_{j_2,k_2}, c_{j_1,k_1}, d_{j_2,k_2}, e_{j_1,k_1} and f_{j_2,k_2}. To get more algebraic equations, we follow the above procedures for the bases $\sin(j\pi x/L_1)\cos(k\pi y/L_2)$ and $\cos(j\pi x/L_1)\sin(k\pi y/L_2)$. Eventually, we obtain Eqs. (6.44) – (6.51). Also, note that these algebraic equations do not contain L_1^1 and L_2^1, and the above derivation does not depend on the number and locations of defect cores.

APPENDIX C

SOME THOUGHTS ON THE SOLUTIONS OF EQUATIONS (6.44) – (6.59)

Equations. (6.42) and (6.43) imply that n_x and n_y have more than one representation. However, we are unsure of which representation of n_x corresponds to which representation of n_y in the decomposition of the unit vector field $\mathbf{n}$. Because it is a rather qualitative feature, some "bold" moves on Eqs. (6.44) – (6.59) may be expected. We experiment with these algebraic equations and restrict the number of Fourier modes by letting $0 \leq j_1, j_2, k_1, k_2 \leq 2$ (assuming other Fourier modes are vanishingly small), then Eqs. (6.44) – (6.59) simplify to

$$\begin{aligned}
&-\frac{\pi^2}{2}\frac{L_2}{L_1}c_{1,0} + \left[\left(\frac{\pi}{L_1}\right)^2 + \left(\frac{2\pi}{L_2}\right)^2\right]\frac{L_1 L_2}{4}c_{1,2} \qquad \text{(C.1)}\\
&+\frac{\pi^2}{64}(9c_{1,0} - 12c_{1,2})\Big(\frac{L_2}{L_1}e_{1,1}e_{1,1} + \frac{L_1}{L_2}c_{1,1}c_{1,1} + \frac{L_2}{L_1}f_{1,1}f_{1,1} + \frac{L_1}{L_2}d_{1,1}d_{1,1}\Big)\\
&+\frac{\pi^2}{32}(6c_{1,1})\Big(\frac{L_2}{L_1}e_{1,2}e_{1,1} + 2\frac{L_1}{L_2}c_{1,2}c_{1,1} + \frac{L_2}{L_1}f_{1,2}f_{1,1} + 2\frac{L_1}{L_2}d_{1,2}d_{1,1}\Big)\\
&+\frac{\pi^2}{64}(12c_{2,0} - 16c_{2,2})\Big(2\frac{L_2}{L_1}e_{2,1}e_{1,1} + \frac{L_1}{L_2}c_{2,1}c_{1,1} + 2\frac{L_2}{L_1}f_{2,1}f_{1,1} + \frac{L_1}{L_2}d_{2,1}d_{1,1}\Big)\\
&+\frac{\pi^2}{64}(6c_{1,0} - 3c_{1,2})\Big(\frac{L_2}{L_1}e_{1,2}e_{1,2} + 4\frac{L_1}{L_2}c_{1,2}c_{1,2} + \frac{L_2}{L_1}f_{1,2}f_{1,2} + 4\frac{L_1}{L_2}d_{1,2}d_{1,2}\Big)\\
&+\frac{\pi^2}{32}(4c_{2,1})\Big(2\frac{L_2}{L_1}e_{2,2}e_{1,1} + 2\frac{L_1}{L_2}c_{2,2}c_{1,1} + 2\frac{L_2}{L_1}f_{2,2}f_{1,1} + 2\frac{L_1}{L_2}d_{2,2}d_{1,1}\Big)\\
&+\frac{\pi^2}{32}(4c_{2,1})\Big(2\frac{L_2}{L_1}e_{1,2}e_{2,1} + 2\frac{L_1}{L_2}c_{1,2}c_{2,1} + 2\frac{L_2}{L_1}f_{1,2}f_{2,1} + 2\frac{L_1}{L_2}d_{1,2}d_{2,1}\Big)\\
&+\frac{\pi^2}{64}(6c_{1,0} - 8c_{1,2})\Big(4\frac{L_2}{L_1}e_{2,1}e_{2,1} + \frac{L_1}{L_2}c_{2,1}c_{2,1} + 4\frac{L_2}{L_1}f_{2,1}f_{2,1} + \frac{L_1}{L_2}d_{2,1}d_{2,1}\Big)
\end{aligned}$$

$$+\frac{\pi^2}{32}(4c_{1,1})\Big(4\frac{L_2}{L_1}e_{2,1}e_{2,2}+2\frac{L_1}{L_2}c_{2,1}c_{2,2}+4\frac{L_2}{L_1}f_{2,1}f_{2,2}+2\frac{L_1}{L_2}d_{2,1}d_{2,2}\Big)$$

$$+\frac{\pi^2}{64}(8c_{2,0}-4c_{2,2})\Big(2\frac{L_2}{L_1}e_{1,2}e_{2,2}+4\frac{L_1}{L_2}c_{1,2}c_{2,2}+2\frac{L_2}{L_1}f_{1,2}f_{2,2}+4\frac{L_1}{L_2}d_{1,2}d_{2,2}\Big)$$

$$+\frac{\pi^2}{64}(4c_{1,0}-2c_{1,2})\Big(4\frac{L_2}{L_1}e_{2,2}e_{2,2}+4\frac{L_1}{L_2}c_{2,2}c_{2,2}+4\frac{L_2}{L_1}f_{2,2}f_{2,2}+4\frac{L_1}{L_2}d_{2,2}d_{2,2}\Big)=0;$$

$$-4\pi\frac{L_2}{L_1}-2\pi^2\frac{L_2}{L_1}c_{2,0}+\Big[\Big(\frac{2\pi}{L_1}\Big)^2+\Big(\frac{2\pi}{L_2}\Big)^2\Big]\frac{L_1L_2}{4}c_{2,2} \tag{C.2}$$

$$+\frac{\pi^2}{64}(6c_{2,0}-8c_{2,2})\Big(\frac{L_2}{L_1}e_{1,1}e_{1,1}+\frac{L_1}{L_2}c_{1,1}c_{1,1}+\frac{L_2}{L_1}f_{1,1}f_{1,1}+\frac{L_1}{L_2}d_{1,1}d_{1,1}\Big)$$

$$+\frac{\pi^2}{32}(4c_{2,1})\Big(\frac{L_2}{L_1}e_{1,2}e_{1,1}+2\frac{L_1}{L_2}c_{1,2}c_{1,1}+\frac{L_2}{L_1}f_{1,2}f_{1,1}+2\frac{L_1}{L_2}d_{1,2}d_{1,1}\Big)$$

$$+\frac{\pi^2}{64}(8c_{1,0}-12c_{1,2})\Big(2\frac{L_2}{L_1}e_{2,1}e_{1,1}+\frac{L_1}{L_2}c_{2,1}c_{1,1}+2\frac{L_2}{L_1}f_{2,1}f_{1,1}+\frac{L_1}{L_2}d_{2,1}d_{1,1}\Big)$$

$$+\frac{\pi^2}{64}(4c_{2,0}-2c_{2,2})\Big(\frac{L_2}{L_1}e_{1,2}e_{1,2}+4\frac{L_1}{L_2}c_{1,2}c_{1,2}+\frac{L_2}{L_1}f_{1,2}f_{1,2}+4\frac{L_1}{L_2}d_{1,2}d_{1,2}\Big)$$

$$+\frac{\pi^2}{32}(4c_{1,1})\Big(2\frac{L_2}{L_1}e_{2,2}e_{1,1}+2\frac{L_1}{L_2}c_{2,2}c_{1,1}+2\frac{L_2}{L_1}f_{2,2}f_{1,1}+2\frac{L_1}{L_2}d_{2,2}d_{1,1}\Big)$$

$$+\frac{\pi^2}{32}(4c_{1,1})\Big(2\frac{L_2}{L_1}e_{1,2}e_{2,1}+2\frac{L_1}{L_2}c_{1,2}c_{2,1}+2\frac{L_2}{L_1}f_{1,2}f_{2,1}+2\frac{L_1}{L_2}d_{1,2}d_{2,1}\Big)$$

$$+\frac{\pi^2}{64}(9c_{2,0}-12c_{2,2})\Big(4\frac{L_2}{L_1}e_{2,1}e_{2,1}+\frac{L_1}{L_2}c_{2,1}c_{2,1}+4\frac{L_2}{L_1}f_{2,1}f_{2,1}+\frac{L_1}{L_2}d_{2,1}d_{2,1}\Big)$$

$$+\frac{\pi^2}{32}(6c_{2,1})\Big(4\frac{L_2}{L_1}e_{2,1}e_{2,2}+2\frac{L_1}{L_2}c_{2,1}c_{2,2}+4\frac{L_2}{L_1}f_{2,1}f_{2,2}+2\frac{L_1}{L_2}d_{2,1}d_{2,2}\Big)$$

$$+\frac{\pi^2}{64}(8c_{1,0}-4c_{1,2})\Big(2\frac{L_2}{L_1}e_{1,2}e_{2,2}+4\frac{L_1}{L_2}c_{1,2}c_{2,2}+2\frac{L_2}{L_1}f_{1,2}f_{2,2}+4\frac{L_1}{L_2}d_{1,2}d_{2,2}\Big)$$

$$+\frac{\pi^2}{64}(6c_{2,0}-3c_{2,2})\Big(4\frac{L_2}{L_1}e_{2,2}e_{2,2}+4\frac{L_1}{L_2}c_{2,2}c_{2,2}+4\frac{L_2}{L_1}f_{2,2}f_{2,2}+4\frac{L_1}{L_2}d_{2,2}d_{2,2}\Big)=0;$$

$$-\frac{\pi^2}{2}\frac{L_2}{L_1}d_{1,0}+\Big[\Big(\frac{\pi}{L_1}\Big)^2+\Big(\frac{2\pi}{L_2}\Big)^2\Big]\frac{L_1L_2}{4}d_{1,2} \tag{C.3}$$

$$+\frac{\pi^2}{64}(9d_{1,0}-12d_{1,2})\Big(\frac{L_2}{L_1}e_{1,1}e_{1,1}+\frac{L_1}{L_2}c_{1,1}c_{1,1}+\frac{L_2}{L_1}f_{1,1}f_{1,1}+\frac{L_1}{L_2}d_{1,1}d_{1,1}\Big)$$

$$+\frac{\pi^2}{32}(6d_{1,1})\Big(\frac{L_2}{L_1}e_{1,2}e_{1,1}+2\frac{L_1}{L_2}c_{1,2}c_{1,1}+\frac{L_2}{L_1}f_{1,2}f_{1,1}+2\frac{L_1}{L_2}d_{1,2}d_{1,1}\Big)$$

$$+\frac{\pi^2}{64}(12d_{2,0}-16d_{2,2})\Big(2\frac{L_2}{L_1}e_{2,1}e_{1,1}+\frac{L_1}{L_2}c_{2,1}c_{1,1}+2\frac{L_2}{L_1}f_{2,1}f_{1,1}+\frac{L_1}{L_2}d_{2,1}d_{1,1}\Big)$$

$$+\frac{\pi^2}{64}(6d_{1,0}-3d_{1,2})\Big(\frac{L_2}{L_1}e_{1,2}e_{1,2}+4\frac{L_1}{L_2}c_{1,2}c_{1,2}+\frac{L_2}{L_1}f_{1,2}f_{1,2}+4\frac{L_1}{L_2}d_{1,2}d_{1,2}\Big)$$

$$+\frac{\pi^2}{32}(4d_{2,1})\Big(2\frac{L_2}{L_1}e_{2,2}e_{1,1}+2\frac{L_1}{L_2}c_{2,2}c_{1,1}+2\frac{L_2}{L_1}f_{2,2}f_{1,1}+2\frac{L_1}{L_2}d_{2,2}d_{1,1}\Big)$$

$$+\frac{\pi^2}{32}(4d_{2,1})\Big(2\frac{L_2}{L_1}e_{1,2}e_{2,1}+2\frac{L_1}{L_2}c_{1,2}c_{2,1}+2\frac{L_2}{L_1}f_{1,2}f_{2,1}+2\frac{L_1}{L_2}d_{1,2}d_{2,1}\Big)$$

$$+\frac{\pi^2}{64}(6d_{1,0}-8d_{1,2})\Big(4\frac{L_2}{L_1}e_{2,1}e_{2,1}+\frac{L_1}{L_2}c_{2,1}c_{2,1}+4\frac{L_2}{L_1}f_{2,1}f_{2,1}+\frac{L_1}{L_2}d_{2,1}d_{2,1}\Big)$$

$$+\frac{\pi^2}{32}(4d_{1,1})\Big(4\frac{L_2}{L_1}e_{2,1}e_{2,2}+2\frac{L_1}{L_2}c_{2,1}c_{2,2}+4\frac{L_2}{L_1}f_{2,1}f_{2,2}+2\frac{L_1}{L_2}d_{2,1}d_{2,2}\Big)$$

$$+\frac{\pi^2}{64}(8d_{2,0}-4d_{2,2})\Big(2\frac{L_2}{L_1}e_{1,2}e_{2,2}+4\frac{L_1}{L_2}c_{1,2}c_{2,2}+2\frac{L_2}{L_1}f_{1,2}f_{2,2}+4\frac{L_1}{L_2}d_{1,2}d_{2,2}\Big)$$

$$+\frac{\pi^2}{64}(4d_{1,0}-2d_{1,2})\Big(4\frac{L_2}{L_1}e_{2,2}e_{2,2}+4\frac{L_1}{L_2}c_{2,2}c_{2,2}+4\frac{L_2}{L_1}f_{2,2}f_{2,2}+4\frac{L_1}{L_2}d_{2,2}d_{2,2}\Big)=0;$$

$$-2\pi^2\frac{L_2}{L_1}d_{2,0}+\left[\left(\frac{2\pi}{L_1}\right)^2+\left(\frac{2\pi}{L_2}\right)^2\right]\frac{L_1L_2}{4}d_{2,2} \tag{C.4}$$

$$+\frac{\pi^2}{64}(6d_{2,0}-8d_{2,2})\Big(\frac{L_2}{L_1}e_{1,1}e_{1,1}+\frac{L_1}{L_2}c_{1,1}c_{1,1}+\frac{L_2}{L_1}f_{1,1}f_{1,1}+\frac{L_1}{L_2}d_{1,1}d_{1,1}\Big)$$

$$+\frac{\pi^2}{32}(4d_{2,1})\Big(\frac{L_2}{L_1}e_{1,2}e_{1,1}+2\frac{L_1}{L_2}c_{1,2}c_{1,1}+\frac{L_2}{L_1}f_{1,2}f_{1,1}+2\frac{L_1}{L_2}d_{1,2}d_{1,1}\Big)$$

$$+\frac{\pi^2}{64}(8d_{1,0}-12d_{1,2})\Big(2\frac{L_2}{L_1}e_{2,1}e_{1,1}+\frac{L_1}{L_2}c_{2,1}c_{1,1}+2\frac{L_2}{L_1}f_{2,1}f_{1,1}+\frac{L_1}{L_2}d_{2,1}d_{1,1}\Big)$$

$$+\frac{\pi^2}{64}(4d_{2,0}-2d_{2,2})\Big(\frac{L_2}{L_1}e_{1,2}e_{1,2}+4\frac{L_1}{L_2}c_{1,2}c_{1,2}+\frac{L_2}{L_1}f_{1,2}f_{1,2}+4\frac{L_1}{L_2}d_{1,2}d_{1,2}\Big)$$

$$+\frac{\pi^2}{32}(4d_{1,1})\Big(2\frac{L_2}{L_1}e_{2,2}e_{1,1}+2\frac{L_1}{L_2}c_{2,2}c_{1,1}+2\frac{L_2}{L_1}f_{2,2}f_{1,1}+2\frac{L_1}{L_2}d_{2,2}d_{1,1}\Big)$$

$$+\frac{\pi^2}{32}(4d_{1,1})\Big(2\frac{L_2}{L_1}e_{1,2}e_{2,1}+2\frac{L_1}{L_2}c_{1,2}c_{2,1}+2\frac{L_2}{L_1}f_{1,2}f_{2,1}+2\frac{L_1}{L_2}d_{1,2}d_{2,1}\Big)$$

$$+\frac{\pi^2}{64}(9d_{2,0}-12d_{2,2})\Big(4\frac{L_2}{L_1}e_{2,1}e_{2,1}+\frac{L_1}{L_2}c_{2,1}c_{2,1}+4\frac{L_2}{L_1}f_{2,1}f_{2,1}+\frac{L_1}{L_2}d_{2,1}d_{2,1}\Big)$$

$$+\frac{\pi^2}{32}(6d_{2,1})\Big(4\frac{L_2}{L_1}e_{2,1}e_{2,2}+2\frac{L_1}{L_2}c_{2,1}c_{2,2}+4\frac{L_2}{L_1}f_{2,1}f_{2,2}+2\frac{L_1}{L_2}d_{2,1}d_{2,2}\Big)$$

$$+\frac{\pi^2}{64}(8d_{1,0}-4d_{1,2})\Big(2\frac{L_2}{L_1}e_{1,2}e_{2,2}+4\frac{L_1}{L_2}c_{1,2}c_{2,2}+2\frac{L_2}{L_1}f_{1,2}f_{2,2}+4\frac{L_1}{L_2}d_{1,2}d_{2,2}\Big)$$

$$+\frac{\pi^2}{64}(6d_{2,0}-3d_{2,2})\Big(4\frac{L_2}{L_1}e_{2,2}e_{2,2}+4\frac{L_1}{L_2}c_{2,2}c_{2,2}+4\frac{L_2}{L_1}f_{2,2}f_{2,2}+4\frac{L_1}{L_2}d_{2,2}d_{2,2}\Big)=0;$$

$$-\frac{\pi^2}{2}\frac{L_1}{L_2}f_{0,1}+\left[\left(\frac{2\pi}{L_1}\right)^2+\left(\frac{\pi}{L_2}\right)^2\right]\frac{L_1L_2}{4}f_{2,1} \tag{C.5}$$

$$+\frac{\pi^2}{64}(9f_{0,1} - 12f_{2,1})\Big(\frac{L_2}{L_1}e_{1,1}e_{1,1} + \frac{L_1}{L_2}c_{1,1}c_{1,1} + \frac{L_2}{L_1}f_{1,1}f_{1,1} + \frac{L_1}{L_2}d_{1,1}d_{1,1}\Big)$$

$$+\frac{\pi^2}{64}(12f_{0,2} - 16f_{2,2})\Big(\frac{L_2}{L_1}e_{1,2}e_{1,1} + 2\frac{L_1}{L_2}c_{1,2}c_{1,1} + \frac{L_2}{L_1}f_{1,2}f_{1,1} + 2\frac{L_1}{L_2}d_{1,2}d_{1,1}\Big)$$

$$+\frac{\pi^2}{32}(6f_{1,1})\Big(2\frac{L_2}{L_1}e_{2,1}e_{1,1} + \frac{L_1}{L_2}c_{2,1}c_{1,1} + 2\frac{L_2}{L_1}f_{2,1}f_{1,1} + \frac{L_1}{L_2}d_{2,1}d_{1,1}\Big)$$

$$+\frac{\pi^2}{64}(6f_{0,1} - 8f_{2,1})\Big(\frac{L_2}{L_1}e_{1,2}e_{1,2} + 4\frac{L_1}{L_2}c_{1,2}c_{1,2} + \frac{L_2}{L_1}f_{1,2}f_{1,2} + 4\frac{L_1}{L_2}d_{1,2}d_{1,2}\Big)$$

$$+\frac{\pi^2}{32}(4f_{1,2})\Big(2\frac{L_2}{L_1}e_{2,2}e_{1,1} + 2\frac{L_1}{L_2}c_{2,2}c_{1,1} + 2\frac{L_2}{L_1}f_{2,2}f_{1,1} + 2\frac{L_1}{L_2}d_{2,2}d_{1,1}\Big)$$

$$+\frac{\pi^2}{32}(4f_{1,2})\Big(2\frac{L_2}{L_1}e_{1,2}e_{2,1} + 2\frac{L_1}{L_2}c_{1,2}c_{2,1} + 2\frac{L_2}{L_1}f_{1,2}f_{2,1} + 2\frac{L_1}{L_2}d_{1,2}d_{2,1}\Big)$$

$$+\frac{\pi^2}{64}(6f_{0,1} - 3f_{2,1})\Big(4\frac{L_2}{L_1}e_{2,1}e_{2,1} + \frac{L_1}{L_2}c_{2,1}c_{2,1} + 4\frac{L_2}{L_1}f_{2,1}f_{2,1} + \frac{L_1}{L_2}d_{2,1}d_{2,1}\Big)$$

$$+\frac{\pi^2}{64}(8f_{0,2} - 4f_{2,2})\Big(4\frac{L_2}{L_1}e_{2,1}e_{2,2} + 2\frac{L_1}{L_2}c_{2,1}c_{2,2} + 4\frac{L_2}{L_1}f_{2,1}f_{2,2} + 2\frac{L_1}{L_2}d_{2,1}d_{2,2}\Big)$$

$$+\frac{\pi^2}{32}(8f_{1,1})\Big(2\frac{L_2}{L_1}e_{1,2}e_{2,2} + 4\frac{L_1}{L_2}c_{1,2}c_{2,2} + 2\frac{L_2}{L_1}f_{1,2}f_{2,2} + 4\frac{L_1}{L_2}d_{1,2}d_{2,2}\Big)$$

$$+\frac{\pi^2}{64}(4f_{0,1} - 2f_{2,1})\Big(4\frac{L_2}{L_1}e_{2,2}e_{2,2} + 4\frac{L_1}{L_2}c_{2,2}c_{2,2} + 4\frac{L_2}{L_1}f_{2,2}f_{2,2} + 4\frac{L_1}{L_2}d_{2,2}d_{2,2}\Big) = 0;$$

$$-4\pi\frac{L_1}{L_2} - 2\pi^2\frac{L_1}{L_2}f_{0,2} + \Big[\Big(\frac{2\pi}{L_1}\Big)^2 + \Big(\frac{2\pi}{L_2}\Big)^2\Big]\frac{L_1L_2}{4}f_{2,2} \tag{C.6}$$

$$+\frac{\pi^2}{64}(6f_{0,2} - 8f_{2,2})\Big(\frac{L_2}{L_1}e_{1,1}e_{1,1} + \frac{L_1}{L_2}c_{1,1}c_{1,1} + \frac{L_2}{L_1}f_{1,1}f_{1,1} + \frac{L_1}{L_2}d_{1,1}d_{1,1}\Big)$$

$$+\frac{\pi^2}{64}(12f_{0,1} - 16f_{2,1})\Big(\frac{L_2}{L_1}e_{1,2}e_{1,1} + 2\frac{L_1}{L_2}c_{1,2}c_{1,1} + \frac{L_2}{L_1}f_{1,2}f_{1,1} + 2\frac{L_1}{L_2}d_{1,2}d_{1,1}\Big)$$

$$+\frac{\pi^2}{32}(4f_{1,2})\Big(2\frac{L_2}{L_1}e_{2,1}e_{1,1}+\frac{L_1}{L_2}c_{2,1}c_{1,1}+2\frac{L_2}{L_1}f_{2,1}f_{1,1}+\frac{L_1}{L_2}d_{2,1}d_{1,1}\Big)$$

$$+\frac{\pi^2}{64}(9f_{0,2}-12f_{2,2})\Big(\frac{L_2}{L_1}e_{1,2}e_{1,2}+4\frac{L_1}{L_2}c_{1,2}c_{1,2}+\frac{L_2}{L_1}f_{1,2}f_{1,2}+4\frac{L_1}{L_2}d_{1,2}d_{1,2}\Big)$$

$$+\frac{\pi^2}{32}(4f_{1,1})\Big(2\frac{L_2}{L_1}e_{2,2}e_{1,1}+2\frac{L_1}{L_2}c_{2,2}c_{1,1}+2\frac{L_2}{L_1}f_{2,2}f_{1,1}+2\frac{L_1}{L_2}d_{2,2}d_{1,1}\Big)$$

$$+\frac{\pi^2}{32}(4f_{1,1})\Big(2\frac{L_2}{L_1}e_{1,2}e_{2,1}+2\frac{L_1}{L_2}c_{1,2}c_{2,1}+2\frac{L_2}{L_1}f_{1,2}f_{2,1}+2\frac{L_1}{L_2}d_{1,2}d_{2,1}\Big)$$

$$+\frac{\pi^2}{64}(4f_{0,2}-2f_{2,2})\Big(4\frac{L_2}{L_1}e_{2,1}e_{2,1}+\frac{L_1}{L_2}c_{2,1}c_{2,1}+4\frac{L_2}{L_1}f_{2,1}f_{2,1}+\frac{L_1}{L_2}d_{2,1}d_{2,1}\Big)$$

$$+\frac{\pi^2}{64}(4f_{0,1}-4f_{2,1})\Big(4\frac{L_2}{L_1}e_{2,1}e_{2,2}+2\frac{L_1}{L_2}c_{2,1}c_{2,2}+4\frac{L_2}{L_1}f_{2,1}f_{2,2}+2\frac{L_1}{L_2}d_{2,1}d_{2,2}\Big)$$

$$+\frac{\pi^2}{32}(6f_{1,2})\Big(2\frac{L_2}{L_1}e_{1,2}e_{2,2}+4\frac{L_1}{L_2}c_{1,2}c_{2,2}+2\frac{L_2}{L_1}f_{1,2}f_{2,2}+4\frac{L_1}{L_2}d_{1,2}d_{2,2}\Big)$$

$$+\frac{\pi^2}{64}(6f_{0,2}-3f_{2,2})\Big(4\frac{L_2}{L_1}e_{2,2}e_{2,2}+4\frac{L_1}{L_2}c_{2,2}c_{2,2}+4\frac{L_2}{L_1}f_{2,2}f_{2,2}+4\frac{L_1}{L_2}d_{2,2}d_{2,2}\Big)=0;$$

$$-\frac{\pi^2}{2}\frac{L_1}{L_2}e_{0,1}+\Big[\Big(\frac{2\pi}{L_1}\Big)^2+\Big(\frac{\pi}{L_2}\Big)^2\Big]\frac{L_1L_2}{4}e_{2,1} \tag{C.7}$$

$$+\frac{\pi^2}{64}(9e_{0,1}-12e_{2,1})\Big(\frac{L_2}{L_1}e_{1,1}e_{1,1}+\frac{L_1}{L_2}c_{1,1}c_{1,1}+\frac{L_2}{L_1}f_{1,1}f_{1,1}+\frac{L_1}{L_2}d_{1,1}d_{1,1}\Big)$$

$$+\frac{\pi^2}{64}(12e_{0,2}-16e_{2,2})\Big(\frac{L_2}{L_1}e_{1,2}e_{1,1}+2\frac{L_1}{L_2}c_{1,2}c_{1,1}+\frac{L_2}{L_1}f_{1,2}f_{1,1}+2\frac{L_1}{L_2}d_{1,2}d_{1,1}\Big)$$

$$+\frac{\pi^2}{32}(6e_{1,1})\Big(2\frac{L_2}{L_1}e_{2,1}e_{1,1}+\frac{L_1}{L_2}c_{2,1}c_{1,1}+2\frac{L_2}{L_1}f_{2,1}f_{1,1}+\frac{L_1}{L_2}d_{2,1}d_{1,1}\Big)$$

$$+\frac{\pi^2}{64}(6e_{0,1}-8e_{2,1})\Big(\frac{L_2}{L_1}e_{1,2}e_{1,2}+4\frac{L_1}{L_2}c_{1,2}c_{1,2}+\frac{L_2}{L_1}f_{1,2}f_{1,2}+4\frac{L_1}{L_2}d_{1,2}d_{1,2}\Big)$$

$$+\frac{\pi^2}{32}(4e_{1,2})\Big(2\frac{L_2}{L_1}e_{2,2}e_{1,1}+2\frac{L_1}{L_2}c_{2,2}c_{1,1}+2\frac{L_2}{L_1}f_{2,2}f_{1,1}+2\frac{L_1}{L_2}d_{2,2}d_{1,1}\Big)$$

$$+\frac{\pi^2}{32}(4e_{1,2})\Big(2\frac{L_2}{L_1}e_{1,2}e_{2,1}+2\frac{L_1}{L_2}c_{1,2}c_{2,1}+2\frac{L_2}{L_1}f_{1,2}f_{2,1}+2\frac{L_1}{L_2}d_{1,2}d_{2,1}\Big)$$

$$+\frac{\pi^2}{64}(6e_{0,1}-3e_{2,1})\Big(4\frac{L_2}{L_1}e_{2,1}e_{2,1}+\frac{L_1}{L_2}c_{2,1}c_{2,1}+4\frac{L_2}{L_1}f_{2,1}f_{2,1}+\frac{L_1}{L_2}d_{2,1}d_{2,1}\Big)$$

$$+\frac{\pi^2}{64}(8e_{0,2}-4e_{2,2})\Big(4\frac{L_2}{L_1}e_{2,1}e_{2,2}+2\frac{L_1}{L_2}c_{2,1}c_{2,2}+4\frac{L_2}{L_1}f_{2,1}f_{2,2}+2\frac{L_1}{L_2}d_{2,1}d_{2,2}\Big)$$

$$+\frac{\pi^2}{32}(8e_{1,1})\Big(2\frac{L_2}{L_1}e_{1,2}e_{2,2}+4\frac{L_1}{L_2}c_{1,2}c_{2,2}+2\frac{L_2}{L_1}f_{1,2}f_{2,2}+4\frac{L_1}{L_2}d_{1,2}d_{2,2}\Big)$$

$$+\frac{\pi^2}{64}(4e_{0,1}-2e_{2,1})\Big(4\frac{L_2}{L_1}e_{2,2}e_{2,2}+4\frac{L_1}{L_2}c_{2,2}c_{2,2}+4\frac{L_2}{L_1}f_{2,2}f_{2,2}+4\frac{L_1}{L_2}d_{2,2}d_{2,2}\Big)=0;$$

$$-2\pi^2\frac{L_1}{L_2}e_{0,2}+\Big[\Big(\frac{2\pi}{L_1}\Big)^2+\Big(\frac{2\pi}{L_2}\Big)^2\Big]\frac{L_1L_2}{4}e_{2,2} \tag{C.8}$$

$$+\frac{\pi^2}{64}(6e_{0,2}-8e_{2,2})\Big(\frac{L_2}{L_1}e_{1,1}e_{1,1}+\frac{L_1}{L_2}c_{1,1}c_{1,1}+\frac{L_2}{L_1}f_{1,1}f_{1,1}+\frac{L_1}{L_2}d_{1,1}d_{1,1}\Big)$$

$$+\frac{\pi^2}{64}(12e_{0,1}-16e_{2,1})\Big(\frac{L_2}{L_1}e_{1,2}e_{1,1}+2\frac{L_1}{L_2}c_{1,2}c_{1,1}+\frac{L_2}{L_1}f_{1,2}f_{1,1}+2\frac{L_1}{L_2}d_{1,2}d_{1,1}\Big)$$

$$+\frac{\pi^2}{32}(4e_{1,2})\Big(2\frac{L_2}{L_1}e_{2,1}e_{1,1}+\frac{L_1}{L_2}c_{2,1}c_{1,1}+2\frac{L_2}{L_1}f_{2,1}f_{1,1}+\frac{L_1}{L_2}d_{2,1}d_{1,1}\Big)$$

$$+\frac{\pi^2}{64}(9e_{0,2}-12e_{2,2})\Big(\frac{L_2}{L_1}e_{1,2}e_{1,2}+4\frac{L_1}{L_2}c_{1,2}c_{1,2}+\frac{L_2}{L_1}f_{1,2}f_{1,2}+4\frac{L_1}{L_2}d_{1,2}d_{1,2}\Big)$$

$$+\frac{\pi^2}{32}(4e_{1,1})\Big(2\frac{L_2}{L_1}e_{2,2}e_{1,1}+2\frac{L_1}{L_2}c_{2,2}c_{1,1}+2\frac{L_2}{L_1}f_{2,2}f_{1,1}+2\frac{L_1}{L_2}d_{2,2}d_{1,1}\Big)$$

$$+\frac{\pi^2}{32}(4e_{1,1})\Big(2\frac{L_2}{L_1}e_{1,2}e_{2,1}+2\frac{L_1}{L_2}c_{1,2}c_{2,1}+2\frac{L_2}{L_1}f_{1,2}f_{2,1}+2\frac{L_1}{L_2}d_{1,2}d_{2,1}\Big)$$

$$+\frac{\pi^2}{64}(4e_{0,2}-2e_{2,2})\Big(4\frac{L_2}{L_1}e_{2,1}e_{2,1}+\frac{L_1}{L_2}c_{2,1}c_{2,1}+4\frac{L_2}{L_1}f_{2,1}f_{2,1}+\frac{L_1}{L_2}d_{2,1}d_{2,1}\Big)$$

$$+\frac{\pi^2}{64}(4e_{0,1}-4e_{2,1})\Big(4\frac{L_2}{L_1}e_{2,1}e_{2,2}+2\frac{L_1}{L_2}c_{2,1}c_{2,2}+4\frac{L_2}{L_1}f_{2,1}f_{2,2}+2\frac{L_1}{L_2}d_{2,1}d_{2,2}\Big)$$

$$+\frac{\pi^2}{32}(6e_{1,2})\Big(2\frac{L_2}{L_1}e_{1,2}e_{2,2}+4\frac{L_1}{L_2}c_{1,2}c_{2,2}+2\frac{L_2}{L_1}f_{1,2}f_{2,2}+4\frac{L_1}{L_2}d_{1,2}d_{2,2}\Big)$$

$$+\frac{\pi^2}{64}(6e_{0,2}-3e_{2,2})\Big(4\frac{L_2}{L_1}e_{2,2}e_{2,2}+4\frac{L_1}{L_2}c_{2,2}c_{2,2}+4\frac{L_2}{L_1}f_{2,2}f_{2,2}+4\frac{L_1}{L_2}d_{2,2}d_{2,2}\Big)=0;$$

$$e_{0,1}+e_{1,1}+e_{2,1}=-\frac{4}{\pi} \quad \text{(C.9)} \qquad c_{1,0}+c_{1,1}+c_{1,2}=0 \quad \text{(C.13)}$$

$$e_{0,2}+e_{1,2}+e_{2,2}=0 \quad \text{(C.10)} \qquad c_{2,0}+c_{2,1}+c_{2,2}=0 \quad \text{(C.14)}$$

$$e_{0,1}-e_{1,1}+e_{2,1}=\frac{4}{\pi} \quad \text{(C.11)} \qquad c_{1,0}-c_{1,1}+c_{1,2}=0 \quad \text{(C.15)}$$

$$e_{0,2}-e_{1,2}+e_{2,2}=0 \quad \text{(C.12)} \qquad c_{2,0}-c_{2,1}+c_{2,2}=0 \quad \text{(C.16)}$$

$$f_{0,1}+f_{1,1}+f_{2,1}=0 \quad \text{(C.17)} \qquad d_{1,0}+d_{1,1}+d_{1,2}=-\frac{4}{\pi} \quad \text{(C.21)}$$

$$f_{0,2}+f_{1,2}+f_{2,2}=0 \quad \text{(C.18)} \qquad d_{2,0}+d_{2,1}+d_{2,2}=0 \quad \text{(C.22)}$$

$$f_{0,1}-f_{1,1}+f_{2,1}=0 \quad \text{(C.19)} \qquad d_{1,0}-d_{1,1}+d_{1,2}=\frac{4}{\pi} \quad \text{(C.23)}$$

$$f_{0,2}-f_{1,2}+f_{2,2}=0 \quad \text{(C.20)} \qquad d_{2,0}-d_{2,1}+d_{2,2}=0 \quad \text{(C.24)}$$

To obtain a solution to Eqs. (C.1) – (C.24), let us first restrict the number of Fourier modes further by letting $0 \leq j_1, j_2, k_1, k_2 \leq 1$, then Eqs. (C.9) – (C.24) give us

$$\begin{cases} d_{1,1} = e_{1,1} = -\dfrac{4}{\pi} \\ c_{1,0} = c_{1,1} = d_{1,0} = e_{0,1} = f_{0,1} = f_{1,1} = 0 \\ c_{2,0} = c_{1,2} = c_{2,1} = c_{2,2} = 0 \\ d_{2,0} = d_{1,2} = d_{2,1} = d_{2,2} = 0 \\ e_{0,2} = e_{1,2} = e_{2,1} = e_{2,2} = 0 \\ f_{0,2} = f_{1,2} = f_{2,1} = f_{2,2} = 0 \end{cases} \tag{C.25}$$

which also satisfies Eqs. (C.1), (C.3) – (C.5), (C.7) and (C.8), but does not satisfy Eqs. (C.2) and (C.6). That means we need to include the Fourier modes with at least one of the indices

j_1, j_2, k_1, k_2 being 2. It is not difficult to show that one solution can satisfy

$$\begin{cases} d_{1,1} = e_{1,1} = -\dfrac{4}{\pi} \\ \\ c_{1,0} = c_{1,1} = d_{1,0} = e_{0,1} = f_{0,1} = f_{1,1} = 0 \\ \\ c_{1,2} = c_{2,1} = d_{1,2} = d_{2,1} = e_{1,2} = e_{2,1} = f_{1,2} = f_{2,1} = 0 \\ \\ \dfrac{L_2}{L_1} \cdot f_{0,2} - \dfrac{L_1}{L_2} \cdot c_{2,0} = \dfrac{\pi}{2} \cdot \left(\dfrac{L_1}{L_2} - \dfrac{L_2}{L_1}\right) \cdot c_{2,0} \cdot f_{0,2} \\ \\ \dfrac{L_2}{L_1} \cdot e_{0,2}^2 - \dfrac{L_1}{L_2} \cdot d_{2,0}^2 = \left(\dfrac{\pi^2}{2} - 1\right) \cdot \left(\dfrac{L_1}{L_2} - \dfrac{L_2}{L_1}\right) \cdot d_{2,0} \cdot e_{0,2} \\ \\ \pi \cdot d_{2,0} - c_{2,0} \cdot e_{0,2} = \left(\dfrac{L_1}{L_2}\right)^2 \cdot c_{2,0} \cdot d_{2,0} \\ \\ \dfrac{9}{16}\pi^2 \cdot \left(\dfrac{L_2}{L_1} e_{0,2}^2 + \dfrac{L_1}{L_2} c_{2,0}^2 + \dfrac{L_2}{L_1} f_{0,2}^2 + \dfrac{L_1}{L_2} d_{2,0}^2\right) = 4\pi \dfrac{L_2}{L_1} \cdot \dfrac{1}{c_{2,0}} + \left(3\pi^2 - \dfrac{7}{2}\right) \cdot \dfrac{L_2}{L_1} + \left(\pi^2 - \dfrac{7}{2}\right) \cdot \dfrac{L_1}{L_2} \\ \\ c_{2,0} = -c_{2,2},\ d_{2,0} = -d_{2,2},\ e_{0,2} = -e_{2,2},\ f_{0,2} = -f_{2,2} \end{cases} \tag{C.26}$$

If $L_1 = L_2 = L$, then considering the fact that the unit vector field $\mathbf{n}$ should be identical on the two copies, we find one solution to be

$$\begin{cases} d_{1,1} = e_{1,1} = -\dfrac{4}{\pi} \\ \\ c_{1,0} = c_{1,1} = d_{1,0} = e_{0,1} = f_{0,1} = f_{1,1} = 0 \\ \\ c_{1,2} = c_{2,1} = d_{1,2} = d_{2,1} = e_{1,2} = e_{2,1} = f_{1,2} = f_{2,1} = 0 \\ \\ c_{2,0} = -c_{2,2} = f_{0,2} = -f_{2,2} \approx -1.88 \\ \\ d_{2,0} = -d_{2,2} = e_{0,2} = -e_{2,2} = 0 \end{cases} \tag{C.27}$$

Substitute Eq. (C.27) into Eqs. (6.42) – (6.43), and we have

$$\begin{cases} n_x \sim -\dfrac{4}{\pi}\cos\dfrac{\pi x}{L}\sin\dfrac{\pi y}{L} \\ \\ n_y \sim -\dfrac{4}{\pi}\sin\dfrac{\pi x}{L}\cos\dfrac{\pi y}{L} \end{cases} \tag{C.28}$$

and,

$$\begin{cases} n_x \sim -1.88\cdot\sin\dfrac{2\pi x}{L} + 1.88\cdot\sin\dfrac{2\pi x}{L}\cos\dfrac{2\pi y}{L} \\ \\ n_y \sim -1.88\cdot\sin\dfrac{2\pi y}{L} + 1.88\cdot\cos\dfrac{2\pi x}{L}\sin\dfrac{2\pi y}{L} \end{cases} \tag{C.29}$$

which are shown in Fig. C.1.

Apparently, Equations (C.28) and (C.29) are not the correct solutions to our problem [in another word, they are not the solutions to Eqs. (6.44) – (6.59)], because they do not satisfy the constraint shown in Eq. (6.3). However, they are likely to be the first Fourier modes of the complete Fourier series (up to a possible change of the coefficients). This speculation comes from the above calculation process: when we add a higher-frequency mode to Eqs. (6.44) – (6.59) [restricted to finite number of lower-frequency modes], the original nonzero lower-frequency modes may still be nonzero, and the original zero lower-frequency modes may still be zero. We also speculate that these first Fourier modes determine the location of the defect core, and the rest of the Fourier modes make sure Eq. (6.3) is satisfied. If our speculations are correct, then Eqs. (C.28) and (C.29) correspond to two-dimensional nematics confined in a square with the defect core being at the center.

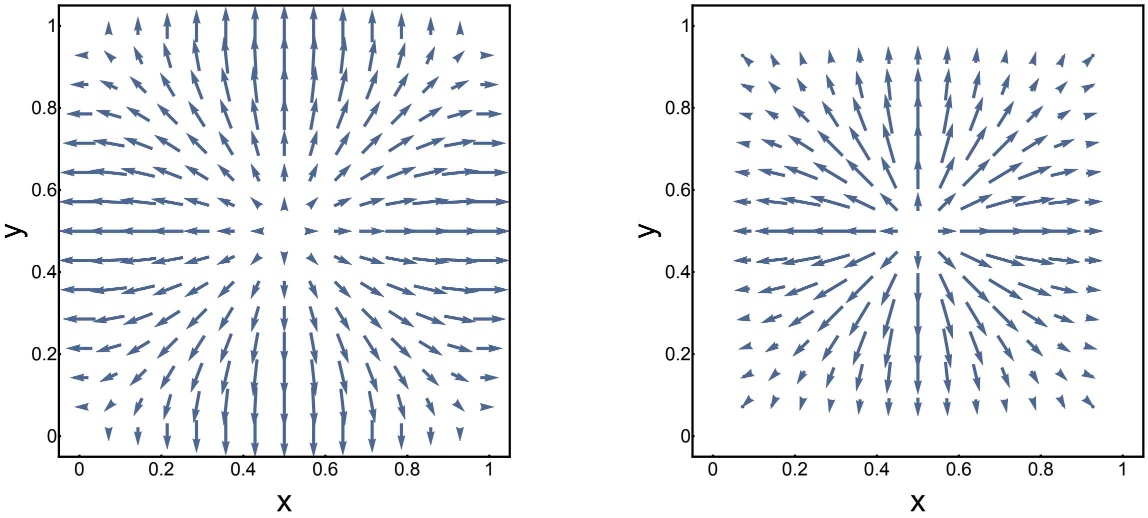

(a) First copy [i.e., Equation (C.28)]

(b) Second copy [i.e., Equation (C.29)]

Figure C.1: The first Fourier mode of the unit vector field $\mathbf{n}$

Furthermore, from this particular example, we suspect that $\sin(j\pi x/L_1)\cos(k\pi y/L_2)$ – representation for n_x corresponds to $\cos(j\pi x/L_1)\sin(k\pi y/L_2)$ – representation for n_y, and $\cos(j\pi x/L_1)\sin(k\pi y/L_2)$ – representation for n_x corresponds to $\sin(j\pi x/L_1)\cos(k\pi y/L_2)$ – representation for n_y.

APPENDIX D

METHOD (B) FOR A SIMPLE TWO-DIMENSIONAL EXAMPLE

Consider a charge-free rectangular region with fixed values of electric potential on the boundary as illustrated in Fig. D.1, and we want to know the electric potential inside the rectangle [105]. This boundary value problem is formulated explicitly as follows.

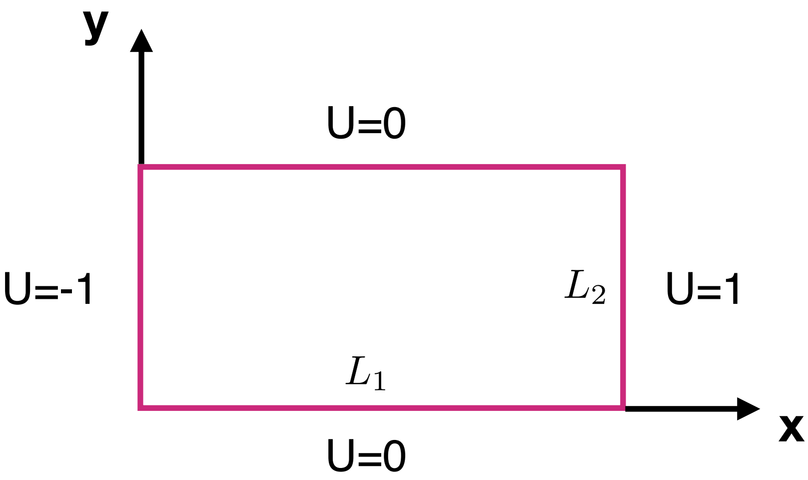

Figure D.1: Boundary conditions for the electric potential

The electric potential U satisfies Laplace's Equation

$$\frac{\partial^2 U}{\partial x^2} + \frac{\partial^2 U}{\partial y^2} = 0, \tag{D.1}$$

subject to the following boundary conditions

$$U(0, y) = -1 \tag{D.2}$$

$$U(L_1, y) = 1 \tag{D.3}$$

$$U(x, 0) = 0 \tag{D.4}$$

$$U(x, L_2) = 0 \tag{D.5}$$

By the method of separation of variables, we have

$$U = \frac{4}{\pi} \cdot \sum_{k=0}^{\infty} \frac{1}{2k+1} \cdot \frac{\sinh \frac{(2k+1)\pi x}{L_2} - \sinh \frac{(2k+1)\pi(L_1 - x)}{L_2}}{\sinh \frac{(2k+1)\pi L_1}{L_2}} \cdot \sin \frac{(2k+1)\pi y}{L_2}. \tag{D.6}$$

By Method (B), we first write U in terms of Fourier series, i.e.,

$$U = \sum_{j,k} a_{j,k} \sin \frac{j\pi x}{L_1} \sin \frac{k\pi y}{L_2}. \tag{D.7}$$

Then by the same procedure introduced in Chapter 5, we have

$$\int_0^{L_1} \mathrm{d}x \int_0^{L_2} \mathrm{d}y \left(\frac{\partial^2 U}{\partial x^2} + \frac{\partial^2 U}{\partial y^2} \right) \sin \frac{j\pi x}{L_1} \sin \frac{k\pi y}{L_2} = 0 \tag{D.8}$$

$$\Longrightarrow \frac{L_2}{L_1} \cdot \frac{j}{k} \cdot [-1 - \cos(j\pi) + \cos(k\pi) + \cos(j\pi) \cdot \cos(k\pi)]$$

$$- \left[\left(\frac{j\pi}{L_1} \right)^2 + \left(\frac{k\pi}{L_2} \right)^2 \right] \cdot \frac{L_1 L_2}{4} \cdot a_{j,k} = 0.$$

Therefore,

$$U = \sum_{j,k} \left(\frac{2}{L_1} \right)^2 \cdot \frac{j}{k} \left[\left(\frac{j\pi}{L_1} \right)^2 + \left(\frac{k\pi}{L_2} \right)^2 \right]^{-1} \tag{D.9}$$

$$\times [-1 + \cos(k\pi) - \cos(j\pi) + \cos(j\pi)\cos(k\pi)] \cdot \sin \frac{j\pi x}{L_1} \sin \frac{k\pi y}{L_2}.$$

Similarly, U can also be written as

$$U = \sum_{j=1}^{\infty} c_{j,0} \sin \frac{j\pi x}{L_1} + \sum_{j,k=1}^{\infty} c_{j,k} \sin \frac{j\pi x}{L} \cos \frac{k\pi y}{L_2}; \tag{D.10}$$

and we have the following algebraic equations

$$- (j\pi) \cdot \frac{L_2}{L_1} \cdot \cos(j\pi) - (j\pi) \cdot \frac{L_2}{L_1} - \frac{(j_1\pi)^2}{2} \cdot \frac{L_2}{L_1} \cdot c_{j,0} \tag{D.11}$$

$$+\int_0^{L_1} \mathrm{d}x\ \sin\frac{j\pi x}{L_1}\cdot\frac{\partial U}{\partial y}\Big|_{L_2} - \int_0^{L_1} \mathrm{d}x\ \sin\frac{j\pi x}{L_1}\cdot\frac{\partial U}{\partial y}\Big|_0 = 0$$

$$\cos(k\pi)\int_0^{L_1} \mathrm{d}x\ \sin\frac{j\pi x}{L_1}\cdot\frac{\partial U}{\partial y}\Big|_{L_2} - \int_0^{L_1} \mathrm{d}x\ \sin\frac{j\pi x}{L_1}\cdot\frac{\partial U}{\partial y}\Big|_0 \qquad \text{(D.12)}$$

$$-\Big[\Big(\frac{j\pi}{L_1}\Big)^2+\Big(\frac{k\pi}{L_2}\Big)^2\Big]\cdot\frac{L_1L_2}{4}\cdot c_{j,k}=0$$

$$c_{j,0}+\sum_{k=1}^{\infty}c_{j,k}=0 \qquad \text{(D.13)} \qquad c_{j,0}+\sum_{k=1}^{\infty}(-1)^k\cdot c_{j,k}=0 \quad \text{(D.14)}$$

Then U can also be written as

$$U=\sum_{m=1}^{\infty}\Big[\frac{2L_1}{(m\pi)^2L_2\cdot\coth\frac{\pi m L_2}{L_1}}-\frac{2}{m\pi}\Big]\cdot\sin\frac{2m\pi x}{L_1}+\sum_{m,n=1}^{\infty}\frac{16}{L_1L_2\cdot\coth\frac{\pi m L_2}{L_1}} \qquad \text{(D.15)}$$

$$\times\Big[\Big(\frac{2m\pi}{L_1}\Big)^2+\Big(\frac{2n\pi}{L_2}\Big)^2\Big]\cdot\sin\frac{2m\pi x}{L_1}\cos\frac{2n\pi y}{L_2}.$$

Here, Equations (D.6), (D.9) and (D.15) are equivalent. However, due to the possible Gibbs phenomenon at the boundary, when we substitute Eq. (D.9) or (D.15) into the energy functional

$$E=\int_0^{L_1}\mathrm{d}x\int_0^{L_2}\mathrm{d}y\ \Big[\Big(\frac{\partial U}{\partial x}\Big)^2+\Big(\frac{\partial U}{\partial y}\Big)^2\Big], \qquad \text{(D.16)}$$

we get an infinitely large value. According to the previous discussion, it is expected that the correct value can be acquired after a proper regularization.

REFERENCES

[1] P. G. de Gennes and J. Prost. *The physics of liquid crystals*. Oxford: Clarendon press, 1993.

[2] I. C. Khoo. *Liquid crystals*. Vol. 64. John Wiley & Sons, 2007.

[3] S. Kumar. *Liquid crystals: experimental study of physical properties and phase transitions*. Cambridge University Press, 2001.

[4] M. J. Stephen and J. P. Straley. "Physics of liquid crystals". In: *Reviews of Modern Physics* 46.4 (2014), p. 1974.

[5] N. J. Mottram and C. J. Newton. "Introduction to Q-tensor theory". In: *arXiv preprint* arXiv:1409.3542 (2014).

[6] P. M. Chaikin and T. C. Lubensky. *Principles of condensed matter physics*. Cambridge: Cambridge university press, 2000.

[7] D. Andrienko. "Introduction to liquid crystals". In: *IMPRS school, Bad Marienberg* (2006).

[8] V. Popa-Nita, V. Barna, and S. Repnik R.and Kralj. "Mixtures Composed of Liquid Crystals and Nanoparticles". In: *Syntheses and Applications of Carbon Nanotubes and Their Composites* (2013).

[9] P. Oswald and P. Pieranski. *Nematic and cholesteric liquid crystals: concepts and physical properties illustrated by experiments*. CRC press, 2005.

[10] M. Ravnik and S. Žumer. "Landau-de Gennes modelling of nematic liquid crystal colloids". In: *Liquid Crystals* 36.10-11 (2009), pp. 1201–1214.

[11] A. Zarnescu. "Topics in the Q-tensor theory of liquid crystals". In: *Topics in mathematical modeling and analysis* 7 (2012), pp. 187–252.

[12] D. W. Berreman and S. Meiboom. "Tensor representation of Oseen-Frank strain energy in uniaxial cholesterics". In: *Physical Review A* 30.4 (1984), p. 1955.

[13] H. Mori, J. R. Gartland Jr E. C.and Kelly, and P. J. Bos. "Multidimensional director modeling using the Q tensor representation in a liquid crystal cell and its application to the π cell with patterned electrodes". In: *Japanese journal of applied physics* 38.1R (1999), p. 135.

[14] S. Kralj and S. Žumer. "Saddle-splay elasticity of nematic structures confined to a cylindrical capillary". In: *Physical Review E* 51.1 (1995), p. 366.

[15] C. W. Oseen. "The theory of liquid crystals". In: *Transactions of the Faraday Society* 29.140 (1933), pp. 883–899.

[16] F. C. Frank. "I. Liquid crystals. On the theory of liquid crystals". In: *Discussions of the Faraday Society* 25 (1958), pp. 19–28.

[17] V. M. Pergamenshchik. "Phenomenological approach to the problem of the K_{13} surfacelike elastic term in the free energy of a nematic liquid crystal". In: *Physical Review E* 48.2 (1993), p. 1254.

[18] S. Faetti. "Theory of surfacelike elastic contributions in nematic liquid crystals". In: *Physical Review E* 49.5 (1994), p. 4192.

[19] J. M. Ball and S. J. Bedford. "Discontinuous order parameters in liquid crystal theories". In: *Molecular Crystals and Liquid Crystals* 612.1 (2015), pp. 1–23.

[20] J. M. Ball and A. Zarnescu. "Orientable and non-orientable line field models for uniaxial nematic liquid crystals". In: *Molecular Crystals and Liquid Crystals* 495.1 (2008), pp. 221–233.

[21] J. M. Ball and A. Zarnescu. "Orientability and energy minimization in liquid crystal models". In: *Archive for rational mechanics and analysis* 202.2 (2011), pp. 493–535.

[22] J. M. Ball and A. Majumdar. "Nematic liquid crystals: from Maier-Saupe to a continuum theory". In: *Molecular crystals and liquid crystals* 525.1 (2010), pp. 1–11.

[23] N. Schopohl and T. J. Sluckin. "Defect core structure in nematic liquid crystals". In: *Physical review letters* 59.22 (1987), p. 2582.

[24] N. Schopohl and T. J. Sluckin. "Hedgehog structure in nematic and magnetic systems". In: *Journal de Physique* 49.7 (1988), pp. 1097–1101.

[25] E. Penzenstadler and H. R. Trebin. "Fine structure of point defects and soliton decay in nematic liquid crystals". In: *Journal de Physique* 50.9 (1989), pp. 1027–1040.

[26] S. Kralj, E. G. Virga, and S. Žumer. "Biaxial torus around nematic point defects". In: *Physical Review E* 60.2 (1999), p. 1858.

[27] S. Kralj and E. G. Virga. "Universal fine structure of nematic hedgehogs". In: *Journal of Physics A: Mathematical and General* 34.4 (2001), p. 829.

[28] G. De Luca and A. D. Rey. “Ringlike cores of cylindrically confined nematic point defects”. In: *The Journal of chemical physics* 126.9 (2007), p. 094907.

[29] G. De Luca and A. D. Rey. “Point and ring defects in nematics under capillary confinement”. In: *The Journal of chemical physics* 127.10 (2007), p. 104902.

[30] N. D. Mermin. “The topological theory of defects in ordered media”. In: *Reviews of Modern Physics* 51.3 (1979), p. 591.

[31] H. Mori and H. Nakanishi. “On the stability of topologically non-trivial point defects”. In: *Journal of the Physical Society of Japan* 57.4 (1988), pp. 1281–1286.

[32] M. V. E. Kurik and O. D. Lavrentovich. “Defects in liquid crystals: homotopy theory and experimental studies”. In: *Physics-Uspekhi* 31.3 (1988), pp. 196–224.

[33] O. D. Lavrentovich. “Topological defects in dispersed words and worlds around liquid crystals, or liquid crystal drops”. In: *Liquid crystals* 24.1 (1998), pp. 117–126.

[34] G. P. Alexander et al. “Colloquium: Disclination loops, point defects, and all that in nematic liquid crystals”. In: *Reviews of Modern Physics* 84.2 (2012), p. 497.

[35] A Hatcher. *Algebraic Topology*. Cambridge University Press, 2002.

[36] R. Repnik et al. “Physics of defects in nematic liquid crystals”. In: *European Journal of Physics* 24.4 (2003), p. 481.

[37] Z. Bradač et al. “Annihilation of nematic point defects: postcollision scenarios”. In: *Physical Review E* 67.5 (2003), p. 050702.

[38] M. Svetec et al. “Hedgehog annihilation in a confined nematic liquid crystal”. In: *Milecular Crystals and Liquid Crystals* 413.1 (2004), pp. 43–51.

[39] M. Svetec et al. “Annihilation of nematic point defects: pre-collision and post-collision evolution”. In: *The European Physical Journal E* 20.1 (2006), pp. 71–79.

[40] B. J. Liang and S. H. Chen. “Discontinuous radial to axial transformation of director configuration in a cylindrical nematic cavity”. In: *Japanese journal of applied physics* 30.11B (1991), p. L1955.

[41] S. H. Chen and B. J. Liang. “Stability of a hedgehog nematic configuration in a small closed cylindrical cavity”. In: *Applied physics letters* 59.10 (1991), pp. 1173–1175.

[42] B. J. Liang and S. H. Chen. “Director-configuration diagram for a closed-cylinder nematic liquid crystal”. In: *Journal of applied physics* 71.5 (1992), pp. 2189–2194.

[43] J. M. Gilli et al. “Inversion walls in homeotropic nematic and cholesteric layers”. In: *Liquid crystals* 23.5 (1997), pp. 619–628.

[44] S. Thiberge et al. “Critical radius of loop defects in homeotropic nematic liquid crystals”. In: *Liquid crystals* 26.8 (1999), pp. 1225–1234.

[45] P. W. Ellis et al. “Defect transitions in nematic liquid-crystal capillary bridges”. In: *Physical Review E* 97.4 (2018), p. 040701.

[46] G. P. Crawford et al. “Escaped-radial nematic configuration in submicrometer-size cylindrical cavities: Deuterium nuclear-magnetic-resonance study”. In: *Physical Review A* 43.2 (1991), p. 835.

[47] I. Vilfan, M. Vilfan, and S. Žumer. “Defect structures of nematic liquid crystals in cylindrical cavities”. In: *Physical Review A* 43.12 (1991), p. 6875.

[48] G. P. Crawford, D. W. Allender, and J. W. Doane. “Surface elastic and molecular-anchoring properties of nematic liquid crystals confined to cylindrical cavities”. In: *Physical Review A* 45.12 (1992), p. 8693.

[49] M. Kleman and O. D. Lavrentovich. “Topological point defects in nematic liquid crystals”. In: *Philosophical Magazine* 86.25-26 (2006), pp. 4117–4137.

[50] R. Holyst and P. Oswald. “Annihilation of point defects on a line”. In: *Physical Review E* 65.4 (2002), p. 041711.

[51] E. M. Terentjev. “Disclination loops, standing alone and around solid particles, in nematic liquid crystals”. In: *Physical Review E* 51.2 (1995), p. 1330.

[52] R. Rosso and E. G. Virga. “Metastable nematic hedgehogs”. In: *Journal of Physics A: Mathematical and General* 29.14 (1996), p. 4247.

[53] O. D. Lavrentovich, T. Ishikawa, and E. M. Terentjev. “Disclination loop in Mori-Nakanishi ansatz: role of the divergence elasticity”. In: *Molecular Crystals and Liquid Crystals* 299.1 (1997), pp. 301–306.

[54] J. I. Fukuda and H. Yokoyama. “Stability of a hyperbolic disclination ring in a nematic liquid crysta”. In: *Physical Review E* 66.1 (2002), p. 012703.

[55] G. B. Arfken, H. J. Weber, and F. E. Harris. *Mathematical Methods for Physicists: A Comprehensive Guide*. Academic Press, 2011.

[56] T. C. Lubensky and J. Prost. “Orientational order and vesicle shape”. In: *Journal de Physique II* 2.3 (1992), pp. 371–382.

[57] J. Yan and A. D. Rey. “Theory and simulation of texture formation in mesophase carbon fibers”. In: *Carbon* 40.14 (2002), pp. 2647–2660.

[58] H. Brezis, J. M. Coron, and E. H. Lieb. “Harmonic maps with defects”. In: *Communications in Mathematical Physics* 107.4 (1986), pp. 649–705.

[59] D. R. Nelson and L. Peliti. “Fluctuations in membranes with crystalline and hexatic order”. In: *Journal de physique* 48.7 (1987), pp. 1085–1092.

[60] J. M. Park and T. C. Lubensky. “Topological defects on fluctuating surfaces: General properties and the Kosterlitz-Thouless transition”. In: *Physical Review E* 53.3 (1996), p. 2648.

[61] D. R. Nelson. *Defects and geometry in condensed matter physics*. Cambridge University Press, 2002.

[62] V. Vitelli and D. R. Nelson. “Nematic textures in spherical shells”. In: *Physical Review E* 74.2 (2006), p. 021711.

[63] M. J. Bowick and L. Giomi. “Two-dimensional matter: order, curvature and defects”. In: *Advances in Physics* 58.5 (2009), pp. 449–563.

[64] A. M. Turner, V. Vitelli, and D. R. Nelson. “Vortices on curved surfaces”. In: *Reviews of Modern Physics* 82.2 (2010), p. 1301.

[65] C. J. Lejdfors. *Surfaces of constant mean curvature*. Lund University, 2003.

[66] F. Hélein. *Constant mean curvature surfaces, harmonic maps and integrable systems*. Springer Science & Business Media, 2001.

[67] K. Kenmotsu. *Surfaces with constant mean curvature*. 221. American Mathematical Soc., 2003.

[68] J. Eells. “The surfaces of Delaunay”. In: *The Mathematical Intelligencer* 9.1 (1987), pp. 53–57.

[69] C. Tsakonas et al. “Multistable alignment states in nematic liquid crystal filled wells”. In: *Applied physics letters* 90.11 (2007), p. 111913.

[70] C. Luo, A. Majumdar, and R. Erban. “Multistability in planar liquid crystal wells”. In: *Physical Review E* 85.6 (2012), p. 061702.

[71] M. Cavallaro et al. “Exploiting imperfections in the bulk to direct assembly of surface colloids”. In: *Proceedings of the National Academy of Sciences* 110.47 (2013), pp. 18804–18808.

[72] D. A. Beller, M. A. Gharbi, and I. B. Liu. “Shape-controlled orientation and assembly of colloids with sharp edges in nematic liquid crystals”. In: *Soft Matter* 11.6 (2015), pp. 1078–1086.

[73] M. Conradi et al. “Janus nematic colloids”. In: *Soft Matter* 5.20 (2009), pp. 3905–3912.

[74] S. Čopar, M. Ravnik, and S. Žumer. “Janus nematic colloids with designable valence”. In: *Materials* 7.6 (2014), pp. 4272–4281.

[75] A. Majumdar et al. “Topology and bistability in liquid crystal devices”. In: *Physical Review E* 75.5 (2007), p. 051703.

[76] S. Kralj and A. Majumdar. “Order reconstruction patterns in nematic liquid crystal wells”. In: *Proceedings of the Royal Society A: Mathematical, Physical and Engineering Sciences* 470.2169 (2014), p. 20140276.

[77] I. C. Gârlea and B. M. Mulder. “Defect structures mediate the isotropic-nematic transition in strongly confined liquid crystals”. In: *Soft Matter* 11.3 (2015), pp. 608–614.

[78] Q. Hu and L. Yuan. “A Newton-penalty method for a simplified liquid crystal model”. In: *Advances in Computational Mathematics* 40.1 (2014), pp. 201–244.

[79] M. Stone and P. Goldbart. *Mathematics for physics: a guided tour for graduate students*. Cambridge University Press, 2009.

[80] C. Fox. *An introduction to the calculus of variations*. Courier Corporation, 1987.

[81] O. V. Kuksenok et al. “Director structure around a colloid particle suspended in a nematic liquid crystal”. In: *Physical Review E* 54.5 (1996), p. 5198.

[82] W. H. Press et al. *Numerical recipes in C: the art of scientific computing*. Cambridge: Cambridge university press, 1992.

[83] J. M. Ortega. *Numerical analysis: a second course*. Society for Industrial and Applied Mathematics, 1990.

[84] C. Pozrikidis. *Numerical computation in science and engineering*. Vol. 6. New York: Oxford university press, 1998.

[85] G. D. Smith. *Numerical solution of partial differential equations: finite difference methods*. Oxford university press, 1985.

[86] J. W. Thomas. *Numerical partial differential equations: finite difference methods*. Vol. 22. Springer Science & Business Media, 2013.

[87] L. A. Hageman and D. M. Young. *Applied iterative methods*. Courier Corporation, 2012.

[88] D. M. Young. *Iterative solution of large linear systems*. Elsevier, 2014.

[89] S. Huang. https://github.gatech.edu/shuang85/cylinder_case1. 2019 (accessed May 6, 2019).

[90] S. Huang. https://github.gatech.edu/shuang85/cylinder_case2. 2019 (accessed May 6, 2019).

[91] S. Huang. https://github.gatech.edu/shuang85/waist_shaped_nematic_bridges. 2019 (accessed May 6, 2019).

[92] S. Huang. https://github.gatech.edu/shuang85/barrel_shaped_nematic_bridges. 2019 (accessed May 6, 2019).

[93] U. Trottenberg, C. W. Oosterlee, and A. Schuller. *Multigrid*. Elsevier, 2000.

[94] W. Hackbusch. *Multi-grid methods and applications*. Vol. 4. Springer Science & Business Media, 2013.

[95] J. H. Bramble. *Multigrid methods*. Routledge, 2018.

[96] R. Cohen, S. Y. Lin, and M. Luskin. "Relaxation and gradient methods for molecular orientation in liquid crystals". In: *Computer Physics Communications* 53.1-3 (1989), pp. 455–465.

[97] S. Huang. https://github.gatech.edu/shuang85/multigrid_for_cylindrical_bridges. 2019 (accessed May 6, 2019).

[98] L. C. Evans. *Partial differential equations*. American Mathematical Society, 2010.

[99] W. Rudin. *Principles of mathematical analysis*. Vol. 3. New York: McGraw-hill, 1964.

[100] C. Lanczos. *Discourse on Fourier series*. SIAM, 2016.

[101] E. M. Stein and R. Shakarchi. *Fourier analysis: an introduction*. Vol. 1. Princeton University Press, 2011.

[102] J. Hadamard. *Le problème de Cauchy et les équations aux dérivées partielles linéaires hyperboliques*. Paris: Hermann, 1932.

[103] L. Blanchet and G. Faye. "Hadamard regularization". In: *Journal of Mathematical Physics* 41.11 (2000), pp. 7675–7714.

[104] F. Bethuel, H. Brezis, and F. Hélein. *Ginzburg-Landau Vortices*. Boston: Birkhuser, 1994.

[105] A. Zangwill. *Modern electrodynamics*. Cambridge University Press, 2013.